UNIVERSITÀ DEGLI STUDI DI PALERMO

PhD Course in Chemical, Environmental, Biomedical, Hydraulic and Materials Engineering

Dipartimento di Ingegneria

Settore Scientifico Disciplinare ING-IND/23

Fabrication And Characterization of Nanostructured Electrodes for Electrochemical Devices

PhD Candidate:

Sonia Carbone

Phd Course Coordinator:

Prof. Giorgio Domenico Maria Micale

Supervisor:

Prof. Rosalinda Inguanta

XXXVII CYCLE

GRADUATION YEAR 2025

Table of Contents

Introduction

One of the most pressing challenges of the 21st century, as the demand for clean and renewable energy sources has been brought forward, is strong needs both to mitigate climate change and reduce dependence on finite fossil fuel resources. Among different sustainable energy technologies, water splitting for hydrogen production is highly promising. To improve hydrogen production efficiency and lower production costs, extensive research has been conducted to identify the most effective electrocatalysts with enhanced activity and stability. A significant aspect of advancing water splitting technologies involves coupling electrolyzers with renewable energy sources such as wind or solar power. The intermittent nature of these energy sources presents challenges in maintaining consistent electrolyzer operation, making it essential to develop catalysts that can perform effectively under variable energy input. In addition, seawater electrolysis presents an attractive alternative to using purified water for hydrogen production, given the abundance of seawater. However, the presence of chloride ions and other impurities introduces some complications into seawater electrolysis due to their adverse effect on corrosion issues and the formation of unwanted by-products. A solution to overcome these challenges will be the development of robust and selective catalysts able to guarantee high performance and stability in a saline environment. This PhD thesis is part of this research area, concentrating on the fabrication and characterization of nanostructured electrodes for hydrogen production via seawater electrolysis. The first chapter provides an overview of the electrolysis process and the different electrolyzer technologies, with a particular focus on alkaline systems and the potential use of seawater as an electrolyte. The second chapter offers a summary of the various materials used as electrocatalysts, highlighting non-noble metals, and specifically nickel-based alloys, as an excellent alternative

to precious metals. Additionally, it is emphasized how nanostructured materials play a crucial role in enhancing catalytic activity. The third chapter delves into the focus of this research, identifying electrodeposition, and specifically template electrosynthesis, as an economical, scalable, and straightforward method. Furthermore, the main electrochemical tests used to evaluate the performance of the catalysts are presented. The fourth chapter focuses on the fabrication and characterization of NiFe NWs through template electrodeposition. NWs electrodes were characterized initially from a chemical-physical perspective, followed by electrochemical analysis. Various tests were conducted first in KOH, then in KOH+NaCl, also assessing their resistance at temperatures higher than ambient. Finally, the electrodes were used as both the anode and cathode in a prototype alkaline electrolyzer. To further enhance performance, a third element was added to the alloy, resulting in the development of Ni-Fe-P NWs, the subject of fifth chapter. These electrodes were initially tested in KOH, KOH+NaCl, and then in a solution able to better simulate seawater composition. At the end, in the sixth chapter, based on the results obtained, several attempts were made to deposit an alloy with five metals, in order to better harness the synergistic effect of the different elements, first on the nickel foam and then in the form of nanowires.

1. Hydrogen Production by Water Electrolysis: An Overview

It was the growing depletion of fossil fuels and the hostile effects of the emissions of global warming that started to turn the attention towards renewable sources of energy. Though these other renewable energies are truly sustainable and eco-friendly, they are neither at all practical to replace the conventional types of energy nor stable enough to continue an uninterrupted supply of energy. They are not available everywhere and thus can be tapped only in selected locations. In their turn, these sources need changes to overcome some problems. One of the promising ways is the transformation of renewable energy into chemical fuels that can easily be stored and delivered, for instance, green hydrogen. Green hydrogen has been in the limelight in recent years as a very promising energy carrier for the decarbonization of industries and one of the ways to store excess electricity [1], [2]. The process of electrolysis requires energy to convert water into hydrogen.

This input energy can be sourced from renewable resources [3], [4].

A possible scheme of Hydrogen Energy Cycle is shown in **figure 1.1**. It consists in the production of electrolytic hydrogen from the surplus electricity of renewable sources and is then used as fuel to produce energy when it is the most in demand. Focusing on hydrogen production through electrolysis, this cycle can be summarized in four steps:

- Production of hydrogen through electrolysers powered by renewable sources.
- Hydrogen storage.
- Transport of hydrogen from the point of production to the place of consumption.
- Conversion of Hydrogen into electricity or other forms of energy.

It has many advantages compared with other energy carriers. For example, unlike the use of fossil fuels, its use does not generate contaminants and pollution. Most importantly, it can be produced from different raw materials, which by implication makes it inexhaustible. In consequence, it does not have the problems associated with fossil fuels [5]. Many studies have examined the integration of renewable energy with hydrogen production. Moriarty and Honnery [6] explored various renewable energy types combined with electrolysis and concluded that wind turbines with electrolyzers offer a promising climate-neutral route for hydrogen production. They found that nuclear energy is an unsuitable source due to limited uranium resources, while hydro, geothermal, and biomass sources cannot produce sufficient electricity to meet demand. Although solar energy is abundant and widely available, its high cost and low energy density make it less practical. Acar and Dincer [7] compared the performance of biomass gasification, solar electrolysis, and wind electrolysis systems for hydrogen production in Turkey. Their study considered six criteria: energy efficiency, exergy efficiency, hydrogen production cost, acidification, social cost of carbon, and global warming potential. As shown in the work, biomass gasification offers better efficiency and cost but falls short in social and environmental performance. In contrast, solar and wind electrolysis perform better in these areas, with wind electrolysis being the most favourable option.

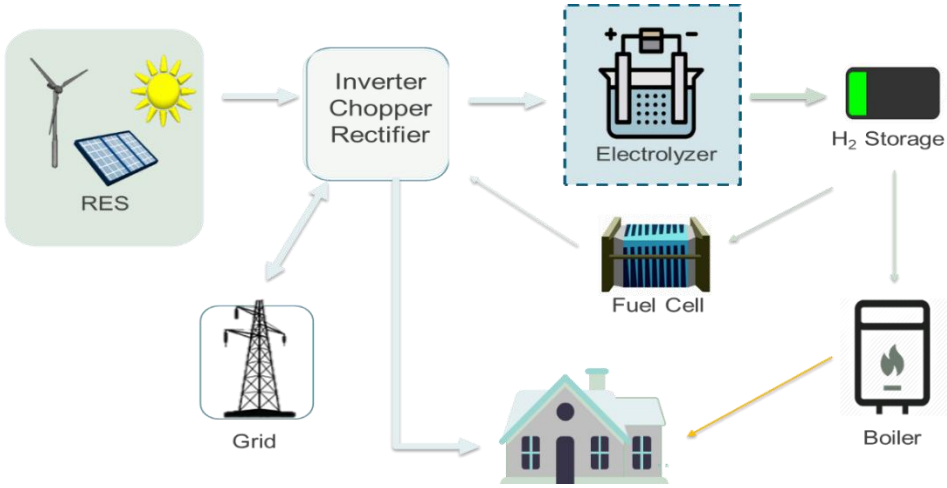

Fig. 1.1 *Hydrogen Energy Cycle*

1.1 Water Electrolysis

The fundamental equation for water electrolysis is given as Eq. 1.

$$\mathbf{H_2O} \rightarrow \frac{\mathbf{1}}{\mathbf{2}}\ \mathbf{O_2} + \mathbf{H_2} \quad \text{(Eq. 1)}$$

In electrolytic processes, a transformation of electrical work into chemical work is achieved: a redox reaction is made to proceed in the non-spontaneous direction ($\Delta G>0$) by exploiting the electromotive force of an external generator. The work the generator does in moving n moles of electrons under the potential difference, E, does the work equal to the product of their total charge and the potential difference. The charge of an electron is $-e$; that of one mole of electrons is $-eN_A$, where N_A is Avogadro's number. Therefore, the total charge will be $-neN_A$, and the work done is $L=-neN_AE$ where $N_A=6{,}022 \cdot 10^{23}$ mol^{-1}

Introducing the Faraday's constant F ($F= 9.6485\ 10^4\ C \cdot mol^{-1}$) as the product of e and N_A,

$$L = -nFE$$

For a reversible process ($T\Delta S=0$), we can therefore write:

$$\Delta G = -nFE$$

The minimum potential difference, that must be applied to the electrodes to drive the electrolysis reaction in an electrolytic cell is equal to the difference between the reduction potentials of the two half-reactions occurring at the cathode and anode. Under standard conditions, the standard cell potential, E°_{cell} ,can be calculated from the difference between the standard reduction potential of the cathode ($E°_{cathode}$) and the standard reduction potential of the anode ($E°_{anode}$):

$$E^{\circ}_{cell} = E^{\circ}_{cathode} - E^{\circ}_{anode}$$

Substituting this into the previous equation, we get:

$$\Delta G = -nF(E^{\circ}_{cathode} - E^{\circ}_{anode})$$

Under standard conditions, for water electrolysis reaction:

$$\Delta G° = 237.19\ \frac{kJ}{mol} \qquad \Delta H° = 285.53\ \frac{kJ}{mol} \qquad \Delta S° = 0.1631\ \frac{kJ}{mol\ K}$$

By substituting these values into the equations for the reversible cell potential and the thermoneutral cell potential, we obtain:

$$\Delta Erev = \frac{\Delta G°}{nF} = 1.229\ V \qquad \Delta Etn = \frac{\Delta H°}{nF} = 1.481\ V$$

The energy applied to the electrodes of any electrolyser to initiate the electrolysis reaction is higher than the reversible cell voltage. In fact, in a real (non-reversible) process, it is necessary to account for the entropy generated irreversibly and the energy dissipation that this entails. This term is also

known as "overpotential" (η) and includes various contributions of irreversibility, each associated with a specific physical phenomenon. Each of these phenomena represents an energy loss and causes an increase in the actual potential required to drive the electrolytic reaction [8]. Considering the typical cell overvoltages in a water electrolyzer, E_{cell} can be written**:**

$$\boldsymbol{E_{cell} = E_{rev} + E_{act} + E_{conc} + E_{ohm}}$$

The overvoltage E_{act}, resulting from electrochemical reactions at the anode and cathode surface, is known as activation losses. This overvoltage arises because it is necessary to overcome the activation energy for the transfer charge reactions. It is highly dependent on the electrocatalytic properties of the electrode materials [9] and is expressed by Tafel's equation:

$$\eta = a + b\log j$$

where a and b values are linked to the exchange current density and Tafel's curve slope.

Activation losses can be minimized by increasing the porosity of the electrodes (greater exchange surface), using effective catalysts (with high specific surface area), increasing the temperature (electrons more easily cross the energy barrier), increasing the concentration of reagents, and increasing the pressure (higher concentrations and pressures improve the occupation of catalytic sites by the reagents) [10]. The ohmic losses are due to the ionic resistance of the electrolyte and the electrical resistance of the external conductive circuit and electrodes. The resistances include anode resistance R_a, cathode resistance R_c, electrolyte resistance R_{ele}, bubble resistance R_{bubble}, diaphragm resistance R_{mem}, and external line resistance, among others. However, because the ohmic over-potential caused by external line resistance

is minimal, it is typically ignored in modeling analysis. Therefore, the total ohmic over-potential can be expressed as follows:

$$E_{ohm} = (R_c + R_a + R_{ele} + R_{mem} + R_{bubble}) \times I$$

Anode and Cathode resistance are linked to the material properties of the electrode itself. R_{ele} depends on the conductivity of the electrolyte σ_{ele}, and the distance of the electrodes from the membrane [11]. R_{mem} is related to its structure and to the conductivity of the electrolyte because ion transport primarily occurs through the diaphragm's pores which are filled with electrolyte solution [12].

During the reaction, bubbles continue to accumulate and grow on the electrode surface. Once their buoyancy and shear forces exceed the adhesion forces holding them to the electrode, the bubbles will detach. The detachment of bubbles from the electrode surface is influenced by factors such as the electrode's roughness, the contact angle, and the velocity of the electrolyte near the electrode surface. These bubbles obstruct the transport of reactive ions in the electrolyte and increase the length of the ion transmission path, thereby raising the overall resistance. Bubble resistance typically refers to the increase in electrolyte resistance caused by the bubbles entering the electrolyte from the electrode surface. Furthermore, bubbles on the electrode surface primarily affect the activation over-potential [13].

1.2 Water Electrolysis Technologies

Water electrolysis generates clean energy without emitting pollution by utilizing electricity. At room temperature, the splitting of water is minimal, approximately 10 moles/Liter, because pure water is a poor conductor of electricity. To improve conductivity, an acid or base is used. Solutions of KOH, NaOH, and H_2SO_4 are commonly used with water. These solutions

dissociate into positive and negative ions, which readily conduct electricity in the water solution by flowing from one electrode to the other. The technology can be divided based on the electrolyte used in the electrolysis cell [14]. Water electrolysis technologies can be categorized into four main types: Alkaline Water Electrolysis (**AWE**), Anion-Exchange Membrane (**AEM**), Polymer Exchange Membrane (**PEM**), and Solid Oxide Electrolysis (**SOE**). AWE and PEM have achieved high levels of technological readiness, whereas AEM and SOE, despite offering advantages like the use of low-concentration alkaline solutions and high operating temperatures for improved thermodynamics and reaction kinetics, are still in the developmental stage due to stability issues [15].

1.2.1 Alkaline water electrolysis (AWE)

AWE has been widely utilized since the early 20th century. Alkaline electrolysers, known for their safety and reliability, can last up to 15 years [16]. This proven technique is the most mature and commercially viable option among several technologies [17]. AWE has been a focus for large-scale industrial applications for several decades, recognized as a viable and cost-effective method for hydrogen production. Currently, alkaline water electrolysis plants can achieve megawatt capacities. A significant advantage of AWE over PEM electrolysis is its use of readily available and affordable alkaline electrolytes, contributing to a longer lifespan and cost-effectiveness for large-scale hydrogen production[18]. The most commonly used electrolytes are potassium hydroxide (KOH) and sodium hydroxide (NaOH) solutions, both serving as alkalis. These electrolytes operate with hydroxide ions at concentrations of 25-40 wt%, resulting in a pH of 13-14 [19]. A basic alkaline electrolyzer consists of two electrodes, a cathode and an anode, immersed in an aqueous electrolyte and separated by a separator, as shown in **Fig. 1.2.**

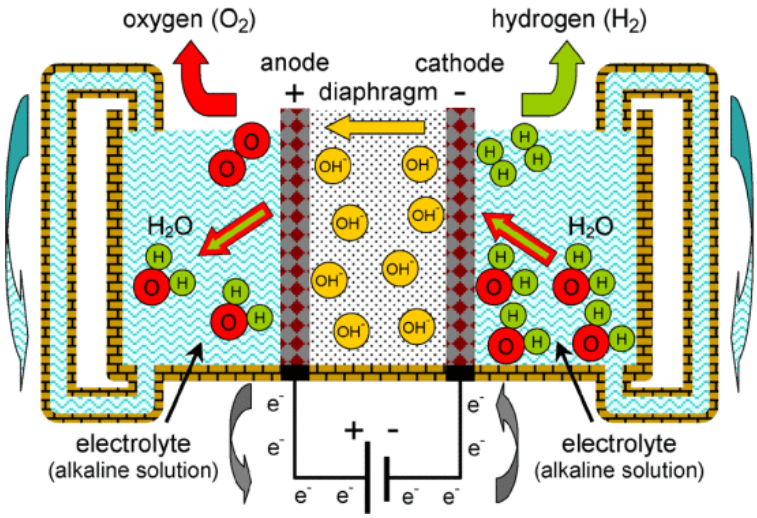

Fig. 1.2 *Scheme of an alkaline electrolysis cell [20]*

The separator has two functions: to physically separate the electrodes and to prevent the intermixing of the product gases released at the cathode and anode, allowing for the separate collection of hydrogen from the cathode side and oxygen from the anode side [21]. At the cathode, hydrogen gas is produced (HER) via water reduction, forming hydroxide anions that move across the diaphragm through the electrolyte to the anode under an electric field generated by an external power supply. At the anode, hydroxide anions are oxidized to form oxygen gas (OER), which bubbles up to the gas collector, releasing electrons that close the current circuit. The following are the chemical reactions occurring at the cathode and anode:

Cathode: $2H_2O + 2e^- \rightarrow H_2 + 2OH^-$

Anode: $2OH^- \rightarrow H_2O + \frac{1}{2}O_2 + 2e^-$

Alkaline Water Electrolysis is a well-established technology that can produce hydrogen with a high purity level of over 99.999% at ambient temperature. The use of non-noble materials, such as nickel and iron, as catalysts reduces the capital cost of electrolyzers to 900–1700 €/kW. However, AWE has several drawbacks, including a limited current density (less than 0.45 A/cm²), lower efficiency (60–70%) compared to other technologies, and the corrosive nature of the alkaline electrolyte [22], [23].

Zero-gap alkaline electrolysis operates by compressing two porous electrodes on either side of a hydroxide ion-conducting membrane or gas separator. This design minimizes the gap between the electrodes to the thickness of the membrane (less than 0.5 mm), compared to the traditional setup where the gap exceeds 2 mm, thereby significantly reducing the Ohmic resistance from the electrolyte between the electrodes. A gas diffusion layer ensures electrical connection between the porous electrode and the bipolar plate, while also allowing the flow of the electrolyte solution and the removal of gas products. The concept of zero-gap alkaline electrolysis was first introduced by Costa and Grimes in 1967, using mesh electrodes flanking a microporous gas separator. Extensive research during the 1980s demonstrated a substantial increase in current density. More recent research has focused on developing anion exchange membranes, which offer lower resistance and the potential for operation at differential pressures [24], [25], [26]. Additionally, novel cell designs have emerged, including the use of high surface area foam electrodes and fuel cell-type electrodes deposited directly onto the membrane [27]. The zero-gap design is more intricate compared to the traditional method, leading to some variations in the structural elements. Instead of a single flat plate used in finite gap electrolysis, the zero-gap cell features porous electrodes pressed against an engraved flow plate. In this design, the catalyst is either applied directly to the porous electrode or onto the membrane, whereas in the

traditional setup, it is placed on the flat electrode plate. Although the electrocatalytic materials from the traditional approach can still be utilized, the methods for applying them may need to be adjusted for porous surfaces. While both designs can incorporate the same gas separator, the zero-gap design also offers the possibility of using an anion exchange membrane. Porous electrodes made from nickel mesh or foam are widely used in various reported systems. Coated stainless steel is another option for the cathodic side, though it is prone to corrosion when exposed to high potentials in the presence of oxygen. Bipolar plates in these systems need to provide excellent electrical conductivity, low contact resistance, and resistance to corrosion. While titanium is commonly used in PEM cells, stainless steel and nickel-based plates are more cost-effective and attractive options for alkaline electrolysers.

1.2.2 Proton exchange membrane water electrolysis (PEM-WE)

The Proton Exchange Membrane electrolysis technology broke into hydrogen production on the 1960s. This was the great development in hydrogen production using as electrolyte a strong polimeric membrane for this process. Sometimes referred to as polymer electrolyte membrane electrolysis, PEM works as both a gas separator and an electrolyte. It operates using only deionized water without additives [28], [29]. Instead of the alkaline water electrolysis method, PEM uses an acidic membrane as a solid electrolyte, and it also acts as a separator between the anode and cathode compartments. This membrane generally consists of perfluorosulfonic acid (PFSA) polymers, such as Nafion® or Fumapem® [30], [31]. One of the major challenges for PEM electrolysers is the need for expensive noble materials in catalysts; specifically, at the cathode Pt or Pt-based materials and at the anode IrO_2 or RuO_2 are needed [32], [33]. The electrochemical reactions in a PEM-WE are

Cathode: $2H^+ + 2e^- \rightarrow H_2$

Anode: $H_2O \rightarrow \frac{1}{2}O_2 + 2H^+ + 2e^-$

PEM electrolysers can reach higher efficiency and high current density reaching up to 3 A/cm^2. Moreover, PEM systems can produce hydrogen with a purity level of 99.99% [34], [35]. The major disadvantage of PEM electrolysis is the high cost of noble metal catalysts like platinum and iridium that makes the significant capital cost of the PEM electrolysers in the range of 1,100-1,800 $/kWe according to the International Energy Agency's report in September 2022 [36]. This is being addressed through a range of studies focused on developing catalysts from more abundant materials and improving energy efficiency of the PEM electrolysis stacks to make this technology more competitive in investment and Levelized Cost of Hydrogen (LCOH)with Alkaline Water Electrolysis [37], [38]. **Figure 1.3** shows a scheme of PEM electrolyser cell.

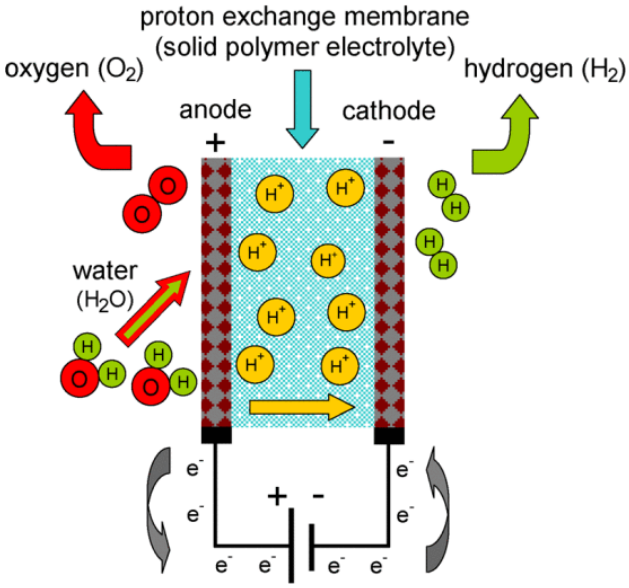

Fig. 1.3 *Scheme of a PEM Electrolysis cell [20]*

1.2.3 Anion exchange membrane water electrolysis (AEM-WE)

Mixing features of both AWE and PEM, Anion Exchange Membrane (AEM) water electrolysis emerges as a promising solution to address the limitations of both AWE and PEM. A scheme of AEM-WE is visible in **figure 1.4**. Like PEM electrolysis, AEM utilizes a solid polymer electrolyte that separates the anode and cathode compartments. However, unlike PEM, AEM operates under alkaline conditions rather than acidic ones. This approach aims to reduce the high capital costs associated with PEM by using non-precious metal catalysts such as cobalt, nickel, and iron [39], [40] instead of platinum group metals (PGM). Unlike the highly concentrated KOH used in Alkaline Electrolysis, AEM-WE employs distilled water or low-concentration alkaline solutions as electrolytes. These are less corrosive, thereby reducing the risk of leakage [41]. AEM electrolysers can use distilled water or a low-concentration alkaline solution, such as an optional dilute caustic or quaternary ammonia polysulfone solution [42]. In AEM electrolysis, a 1% KOH water-electrolyte circulates only in the anode half-cell and wets the membrane, while the cathode side of the cell remains dry and KOH-free. This results in hydrogen from the cathode half-cell having low moisture content. Water molecules cross the membrane and are reduced at the cathode to produce hydrogen. Although AEM-WE is still in the developmental stage and primarily under laboratory investigation, it is emerging as a promising low-temperature electrolysis technology with several advantages. Additionally, the zero-gap design of AEM-WE minimizes the crossover of H_2 and O_2, resulting in higher gas purity and increased energy density. The higher current density of AEM-WE, due to its lower ohmic resistance, implies a smaller volumetric footprint, using fewer materials and thus reducing the carbon footprint [43], [44]. However, AEM technology also has limitations. It is less established, with issues such as low activity and stability of oxygen evolution reaction (OER) catalysts, low ionic

conductivity of AEMs, and challenges in stabilizing these membranes with alkali. Designing and fabricating membrane electrode assemblies (MEAs) and operating them under real-world conditions remain significant challenges. Therefore, further research on the durability of AEM-WE is necessary, as current studies indicate that AEMs and ionomers developed so far are weak, leading to poor chemical stability [45].

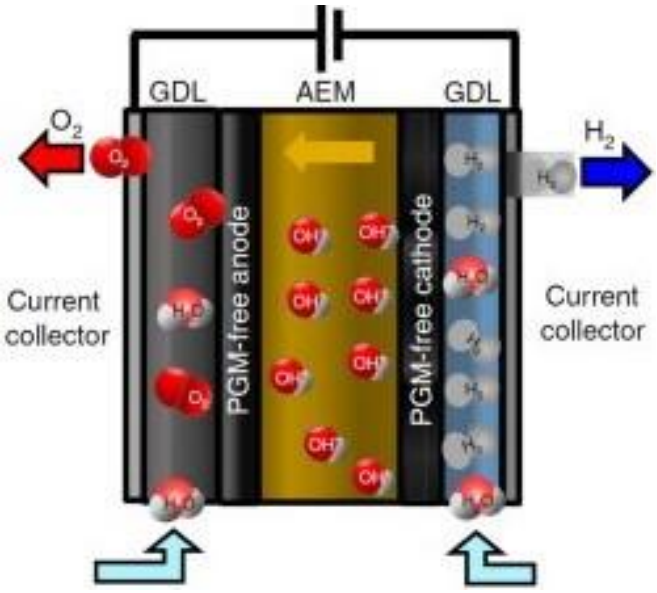

Fig. 1.4 *Scheme of an AEM cell [46]*

1.2.4 Solid oxide electrolysis cell (SOEC)

The technology of Solid Oxide Electrolysis Cells, still in the laboratory research stage, started intensive development during the last 15 years. This is a high-temperature process where steam is used instead of warm water, normally between 600–850°C. In the 1970s, SOEC technology began to emerge [47], [48]. A typical SOEC cell basically consists of two electrodes that can allow gas to pass through and a solid ceramic capable of conducting O_2^- ions [49]. Commonly, the electrolyte used in an SOEC is Yttrium-Stabilized Zirconia (YSZ), a solid solution of a few mol % of yttria (Y_2O_3) in

zirconia (ZrO_2) that has an efficient capability for oxygen ion conduction. Other material systems, such as Gadolinium-doped ceria known as CGO or GDC also hold promise as electrolyte materials [47]. In the hydrogen electrode, the most common applied material is a cermet of nickel and yttria-stabilized zirconia (Ni-YSZ) [50]. The interconnector may be fabricated from ferritic stainless steel or chromium alloys. Both types of materials create chromium oxides at high temperatures that mitigate breakaway oxidation. [47].

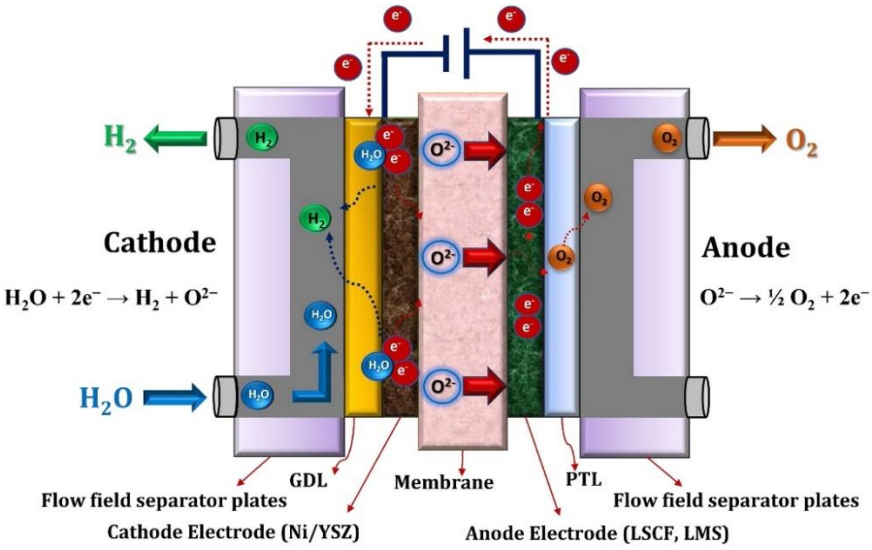

Fig. 1.5 *Scheme of SOEC cell [51]*

The system is supplied with steam at the cathode, where the reduction reaction converts into hydrogen gas and oxide ions. The oxide ions generated at the cathode migrate to the anode, where were converted into oxygen gas through the OER [52]. The partial reactions of the process are as follows:

Cathode : $H_2O + 2e^- \rightarrow H_2 + O^{2-}$

Anode : $O^{2-} \rightarrow 0.5O_2 + 2e^-$

Although SOEC technology for hydrogen production is not yet common, it has the advantage of building on knowledge from solid oxide fuel cells (SOFCs). Some SOECs can even operate reversibly as SOFCs under certain conditions, making them particularly versatile [53], [54]. SOECs are known for their high conversion efficiencies due to their operation at high temperatures, which reduces the thermodynamic potential and speeds up electrolysis reactions [49]. They can also harness heat from renewable or waste sources, which lowers the electrical energy required and boosts overall efficiency [55]. Additionally, SOEC technology can be integrated with chemical processes [47], [56]. However, SOEC technology faces significant challenges, such as high operating temperatures, unstable electrodes, safety issues, and relatively high costs. These factors limit the performance and durability of SOECs, which rely on solid oxide or ceramic materials to conduct electricity at elevated temperatures. To address these challenges, scientists are exploring new approaches, including improved materials, lower operating temperatures, the use of renewable energy sources, and large-scale demonstrations [34], [35], [57].

1.3 Alkaline electrolyser parameters optimization

Alkaline electrolysis is the most mature and widely developed technology for water electrolysis. Although it is the most mature technology, it is still the subject of research and optimization. Different parameters can be optimized, such as physical parameters (material conductivity, porosity, tortuosity) [11], operation parameters (temperature, pressure, flow rate) [58], and construction parameters (area, gaps, thickness) [59]. Abdin et al. [60] explored various physical characteristics of electrodes. Their simulations indicated that increasing the electrode surface roughness resulted in a higher exchange current density. However, excessive roughness caused gas trapping at the electrode surface, suggesting that moderate roughness is preferable, especially

for the cathode in hydrogen production applications. They also examined the effect of the wettability factor (the ratio between the volume of electrolyte absorbed inside the pores and the total pore volume) on separator resistance and current density. The results showed a significant increase in separator resistance at a wettability factor below 0.3, leading to a lower operation current density. Ding et al. [11] investigated the influence of diaphragm porosity on exergy efficiency. Their results were similar to those observed with variations in the wettability factor, with resistance increasing sharply for porosity below 0.3. As porosity increased, exergy efficiency also improved, though only slightly at high porosity levels. Conversely, increasing separator tortuosity led to a linear increase in separator resistance and a corresponding linear decrease in exergy efficiency. The study also assessed the electrical conductivity of electrode materials, finding that a six-fold increase in electrical conductivity resulted in only a 0.4% increase in exergy efficiency, likely due to the high initial conductivity used in the study. Adibi et al. [61] tested the impact of thermal resistance on cell performance. The results indicated that equilibrium temperature increased with higher thermal resistance, but further increases had a minimal effect. Consequently, cell voltage decreased with increasing thermal resistance due to the associated temperature variations. Operating parameters such as temperature, pressure, flow rate, and electrolyte concentration significantly impact the properties of the electrolyte, which in turn affect the electrolyzer performance in terms of cell voltage, energy efficiency, and exergy efficiency. Operating temperature is crucial because increasing it lowers the cell voltage, thereby reducing power consumption [61]. The reduction in cell voltage with rising temperature can be attributed to decreased electrolyte electric resistance, reduced separator resistance, and lower bubble coverage rate. Similarly, a reduction in bubble coverage rate lowers the cell voltage by reducing ohmic voltage. Additionally,

a low wettability factor of the separator can be somewhat mitigated by high operating temperatures. Conversely, increasing operating pressure has a minimal effect on cell voltage and can reduce the purity of produced hydrogen .[62]. Nonetheless, most alkaline electrolyzers are designed to operate at 30 bar to produce hydrogen at sufficient pressure [63]. Haug et al. [58] investigated the influence of electrolyte flow rate and concentration on electrolyzer performance. The results focused on the purity of the produced gas with variations in electrolyte flow rate and concentration. According to the mathematical findings, gas purity decreased as the mass flow rate increased. However, a low mass flow rate is not recommended because it increases the bubble coverage rate, which raises the cell voltage. Therefore, an appropriate electrolyte flow rate should be selected based on the priority of purity or energy consumption. Alternatively, increasing the electrolyte concentration improved gas purity, but excessive concentration reduced electrical conductivity, thereby increasing energy consumption [64]. Geometry parameters such as electrode gap, electrode thickness, and electrode shape have a major influence on electrolyzer performance as they directly affect electrical resistance and gas removal rate. Increasing the distance between the electrodes and the separator directly increases the ohmic electrolyte resistance. According to Ding et al.[11] , exergy efficiency decreases linearly with increasing gap due to a linear increase in electrical resistance. However, this study did not consider the impact of bubble coverage rate concerning the gap between the electrode and separator. Another study by Haverkort and Rajaei [65] showed that a gap of 0.2 mm reduces the ohmic resistance of the bubbles, making it more efficient than a zero-gap electrolyzer. Furthermore, electrode thickness influences cell voltage through increased ohmic resistance of the cathode and anode. However, thicker electrodes also increase thermal resistance, which raises equilibrium temperature and reduces cell voltage as

previously mentioned. Excessively high thermal resistance has a minimal effect on equilibrium temperature [61] , and moderate thickness only slightly affects electrical conductivity [66]. Therefore, a proper selection of electrode thickness is necessary to achieve appropriate cell voltage while withstanding electrolyzer pressure and mechanical stress

1.4 SeaWater Electrolysis

Currently, high-purity fresh water is used in commercial water electrolyzers for green hydrogen production. However, fresh water is a limited resource, with over 80% of the global population facing high water security risks [67]. With limited freshwater resources, the United Nations estimates that roughly one-third of the global population lives in areas experiencing water stress [68]. In contrast, seawater is abundant, covering approximately 71% of Earth's surface and constituting more than 96% of global water storage. Coastal regions with scarce fresh water, such as the Middle East, South Africa, the west coast of the Americas, and parts of Australia, have ample seawater and sufficient wind and solar resources [69]. Therefore, these arid coastal areas are the theoretically probable sites for splitting seawater into hydrogen using surplus renewable electricity. So far, the production of green hydrogen through seawater electrolysis has been investigated mainly in two ways: one-step and two-step seawater electrolysis. Others are of the opinion that seawater should be directly involved in the process of electrolysis, and the capability of the electrochemical industry to come up with seawater tolerant electrolyzers will be key enablers to the growth of green hydrogen applications [70], [71]. The notion behind this concept is that this process will be uncomplicated with no intervening processes that involve any kind of purification processes; such a system could be less expensive and less complicated. Some opponents claim the economic viability of direct seawater electrolysis is yet to be established. They argue that the cost of initial seawater purification, which typically

involves reverse osmosis, is relatively low compared to the expenses associated with seawater electrolysis. Current assessments suggest that reverse osmosis technology, when applied on a small scale, adds minimal cost to green hydrogen production—less than \$0.1 per kg H_2 [72]. However, the situation changes when considering large-scale applications. In such cases, the combined costs of seawater desalination and the use of renewable energy to drive the purification process can significantly increase, with estimates ranging from \$4–11 per m^3 for desalination and approximately \$12.1 per kg for green hydrogen production [73]. To address these cost concerns, it is essential to focus on reducing the expenses associated with water pretreatment while maintaining the high performance and longevity of electrolytic cells. Advancing the technology to enable effective electrolysis using water with purity levels lower than ultrapure could be a key factor in making seawater electrolysis more commercially viable. Overall, while the direct use of seawater in electrolysis presents an appealing theoretical advantage, practical considerations regarding cost and efficiency highlight the need for ongoing research and technological development. Progress in this field could significantly impact the future feasibility and adoption of seawater electrolysis for green hydrogen production.

1.4.1 Challenges of seawater electrolysis

Generally, seawater electrolysis (SWE) is conducted in an alkaline environment, which is favorable for the selectivity of OER and enables the use of non-noble metal catalysts. The most critical challenge for SWE comes from the complexity of seawater composition, comprising sediment, microorganisms, and all kinds of ions. Besides, the composition of seawater changes with geographical locations and seasonal variations, which also influences its physical and chemical properties. A significant challenge in SWE for HER is the substantial increase in local pH near the cathode surface.

To ensure the long-term viability of SWE, this issue of pH fluctuation must be resolved. This increase can lead to the formation of precipitates like $CaOH_2$ and $MgOH_2$ from the cations in the seawater, which can obstruct the HER active sites and reduce performance. This issue can be addressed through simple decantation and filtration processes, which yield a clear solution suitable for electrolysis [74]. Furthermore, certain metal ions present in seawater (e.g., Cu^{2+}, Cd^{2+}, and Pb^{2+}) can deposit on the cathode at specific potentials. These deposits not only interfere with HER but also considerably diminish the electrode longevity. Although sediment and microorganisms mainly affect seawater electrolyte cleanliness and can be filtered out by pretreatment, it is difficult to filter out various ions in seawater, for example, Cl^-, $SO4^{2-}$, Br^-, F^-, Na^+, Mg^{2+}, Ca^{2+}, K^+, Sr^{2+}, Cu^{2+}, Cd^{2+}, HCO_3^-, and CO_3^{2-}. These are ions that would be involved to a large extent in the process of electrolysis and therefore need to be taken into consideration.
Currently, two possible solutions exist:

1. Incorporating pH Buffers: Add a pH buffer to the SWE system to control pH fluctuations.

2. Developing Specialized Electrolysers: Design electrolyzers that effectively separate sediment from the cathode surface.

Thus, future catalyst designs should focus on preventing these undesirable electrochemical reactions to achieve high HER selectivity in SWE.

Additionally, seawater contains a significant number of electrochemically active halogen anions, such as Cl^- and Br^-. Unfortunately, chloride chemistry can compete with the anodic oxygen evolution reaction (OER) due to the corresponding standard redox potential of 0.9–1.6 V versus the standard hydrogen electrode (SHE). Peter et al. conducted an extensive study on anodic seawater electrolysis, producing a computed Pourbaix diagram that includes

both the OER and chloride chemistry [70], [75]. The **figure 1.6** shows a summary of the composition of seawater with the related challenges associated with the most common elements.

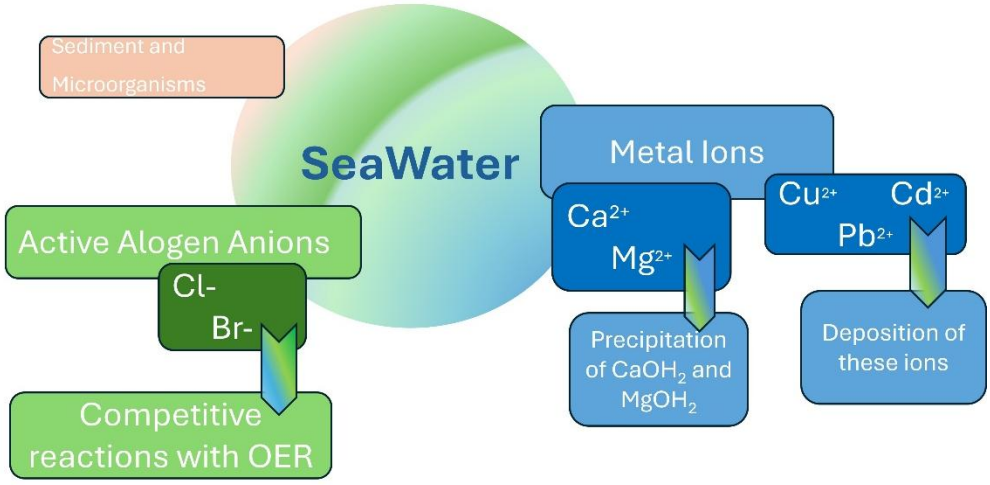

Fig. 1.6 *Scheme of Seawater composition*

Pourbaix diagram for simulated seawater model is shown in **figure 1.7a**, where the chlorine system containing the dissolved 0.5 M NaCl aqueous solution without other chlorine sources, with a total chlorine species (CT, Cl) of 0.5 M is used. In addition, **figure. 1.7b** shows the conditions to ensure 100% selective OER. The values have been obtained as difference between standard electrode potentials of the three relevant chloride oxidation reactions such as chlorine, hypochlorous acid, and hypochlorite formation, and the OER versus pH [75], [76].

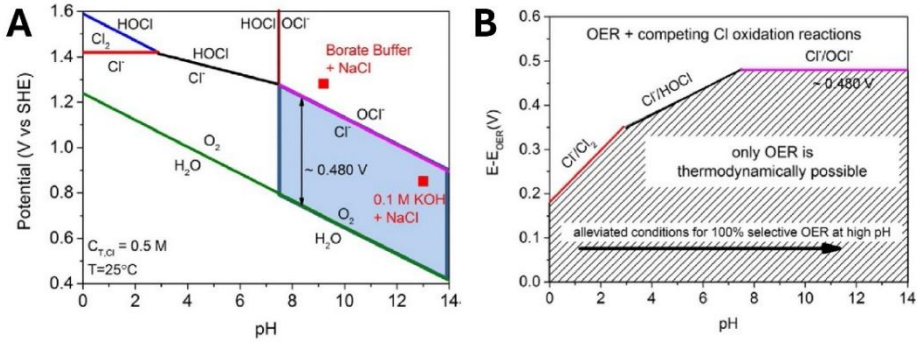

Fig. 1.7 (A) *Pourbaix diagram for simulated seawater model and* ***(B)*** *Maximum permitted for OER electrolyzer to ensure 100% selective OER [75], [76].*

The first diagram shows that at low pH (< 3) the reaction that competes with the OER is the chlorine evolution reaction (ClER), whilst at high pH (> 7.5) the hypochlorite production must be considered:

- **ClER (acidic conditions)**: $2Cl^{-} \rightarrow Cl_2 + 2e^{-}$ (E^0=1.36 V vs. SHE)
- **Hypochlorite production (alkaline conditions)**: $Cl^{-} + 2OH^{-} \rightarrow ClO^{-} + H_2O + 2e^{-}$ (E^0=0.89 V vs. SHE)

Although thermodynamics favour the OER, both ClER and hypochlorite production are two-electron reactions, which are kinetically more favourable compared to the four-electron OER. Interestingly, the oxidation product of Cl^{-} changes from HOCl to OCl- when the electrolyte is alkaline, maintaining a thermodynamic overpotential gap of 480 mV with OER. This means that using a high-performance OER catalyst under alkaline conditions and keeping the overpotential below 480 mV can theoretically prevent Cl^{-} oxidation entirely. This is referred to as the 'alkaline design criteria' for seawater electrolysis [70], [75].

1.5 The role of Electrocatalysts

To enhance hydrogen production efficiency and reduce production costs, researchers have conducted extensive studies to select the best electrocatalyst characterized by improved activity and stability. In particular, the development of inexpensive electrodes with high electrocatalytic features represents a promising approach to enhancing water electrolysis performance. The catalyst is essential for influencing the thermodynamic steps of water splitting reactions, improving overall reaction kinetics. It effectively reduces the activation energy needed for each stage, thereby facilitating both electron transfer and proton discharge [77]. Direct seawater electrolysis requires efficient and robust electrocatalysts that can prevent interference from competing reactions [78]. The undesired oxidation of Cl^- in seawater, as previously noted, not only decreases the efficiency of the OER but also leads to the formation of chlorine-containing species, which can damage the electrolyzer and raise environmental issues. One strategy to address this is by developing high-performance electrocatalysts that are selective for OER, which helps mitigate the ClER at the anode. A range of electrocatalysts, including transition metal compounds (e.g., oxides, phosphides, selenides, sulphides, and carbides), are being studied for their strong activity and suitability for SWE. Transition metals have proven highly effective at improving OER selectivity and resisting seawater corrosion, contributing to long-term durability during electrolysis. In contrast to the OER, the primary challenge for the HER is the formation of precipitates. To address this, researchers have investigated the use of blocking layers on catalyst surfaces to prevent the transfer of these species and enhance HER selectivity. However, this approach may also impede mass transfer, making it crucial to balance the trade-off between blocking layers and efficient mass transfer for effective SWE. While Pt and other noble metals remain the most effective catalysts for

HER, their high-cost limits widespread adoption. Alloying Pt with transition metals (such as Cr, Fe, Co, Ni, and Mo) offers a promising solution by maintaining comparable HER activity while reducing costs [79].

1.6 Alkaline Electrochemical Water Splitting

1.6.1 Thermodynamics of alkaline HER reaction

In alkaline media, the hydrogen evolution reaction (HER) occurs following the mechanism below reported [80], [81]:

- Volmer step: $H_2O + e^- \rightarrow OH^- + Had$
- Heyrovsky step: $H_2O + e^- + Had \rightarrow OH^- + H_2$
- Tafel step: $2Had \rightarrow H_2$

Each step can be connected to a typical Tafel Slope value. The first step, the Volmer step, with a value of 116 mV dec^{-1}; the second one with a value of 40 mV dec^{-1} and the last one with a value of 30 mV dec^{-1} [82], [83].

For HER, identifying the rate-determining step is crucial. If hydrogen adsorption is the rate-determining step, then electrode materials with more edges and cavities in their surface structure will facilitate electron transfer and create additional sites for hydrogen adsorption. On the other hand, if hydrogen desorption is the rate-determining step, then physical properties like surface roughness or perforation will help prevent bubbles from growing excessively. This, in turn, will increase electron transfer by expanding the reaction area, thereby enhancing the rate of electrolysis. When the overpotential is low, electron transfer is slower than desorption, making hydrogen adsorption the rate-determining step. Conversely, when the overpotential is sufficiently high, hydrogen desorption becomes the rate-determining step [10]. Thus, breaking the strong covalent H-O-H bond is necessary in alkaline conditions. The

rational design of electrocatalysts that can effectively dissociate water and bind hydrogen species will significantly enhance alkaline HER performance. Based on the reaction pathway involving the Volmer and Heyrovsky steps, four major factors can influence alkaline HER performance: **water adsorption** on active sites, **water dissociation** ability, **hydrogen binding energy**, and **aqueous OH^- adsorption** strength. Water adsorption, the first step of hydrogen evolution in alkaline media, is much weaker than H_3O^+ adsorption in acidic media. Strengthening the metal-H_2O bond can improve subsequent HER performance. Then, improving the dissociation ability of H_2O is crucial for enhancing hydrogen evolution performance in alkaline solutions. Some authors addressed this by designing a multistep system involving metal oxides and metals. In this system, the metal oxide provides sites for water dissociation, while the metal sites facilitate hydrogen adsorption and association [84]. Additionally, recent studies have indicated that hydrogen binding energy can serve as a key descriptor in alkaline media. OH^- adsorption could also significantly impact HER performance. According to the Sabatier principle, moderate binding strength is ideal for optimizing the overall reaction [85]. If OH^- adsorption is too strong, active sites may become occupied by final products, leading to higher HER overpotential. Baek and colleagues, supported by density functional theory calculations, found that the Ru/C_2N hybrid exhibits a low affinity for OH^-, resulting in improved HER performance in alkaline conditions [86]. However, Yan and coworkers offered a different perspective. Their findings suggested that OH^- adsorption does not directly participate in the reaction; instead, the concentration of OH^- in the medium alters hydrogen binding energy, thereby affecting HER performance. Additionally, Durst and coworkers proposed that the rapid recombination of H^+ and OH^- influences the Volmer and Heyrovsky steps, thus impacting alkaline HER performance [87].

1.6.2 Thermodynamics of alkaline OER reaction

OER process is more complex than the HER. It involves a 4-electron transfer. The possible mechanisms for OER in alkaline electrolytes have been proposed as follows [88]:

$M + OH^- \rightarrow M\text{-}OH + e^-$

$M\text{-}OH + OH^- \rightarrow M\text{-}O + H_2O + e^-$

Followed by either

$2M\text{-}O \rightarrow 2M + O_2$

Or

$M\text{-}O + OH^- \rightarrow M\text{-}OOH + e^-$

$M\text{-}OOH + OH^- \rightarrow M + O_2 + H_2O + e^-$

This mechanism is shown in the **Fig. 1.8a**. OER process primarily occurs on surface metal sites (M) and follows a general mechanism in alkaline environments. The process begins with the formation of M-OH through the 1-electron oxidation of an adsorbed hydroxide ion. This M-OH then transforms into M-O by losing protons and electrons. M-O can proceed along two pathways: it either combines with another M-O to produce O_2 and regenerate the active site or converts into M-OOH, which then undergoes further reactions to produce O_2 and regenerate the active site [89], [90]. Understanding the interaction between catalyst surfaces and OER intermediates is crucial for improving OER performance, although identifying the rate-determining steps (RDS) remains challenging due to the involvement of multiple intermediates. Density functional theory (DFT) calculations have been instrumental in analyzing individual reaction steps and understanding the thermodynamics of electrochemical reactions. These calculations help

determine the reaction energies of each step, identifying the step with the largest free energy as the RDS. DFT calculations reveal the thermodynamically unfavourable step in water splitting through free energy diagrams, which depict the reaction energies of consecutive steps based on differences in the adsorption energies of intermediates. The highest free energy in these diagrams determines the rate-limiting step, which can also be inferred from Tafel slope values. Various descriptors have been used to predict OER activity, including the energy difference between reaction steps (ΔG_O* - ΔG_{HO}*), M-OH bond energy, and electronic structural parameters such as d-orbital occupation, orbital filling, and oxygen binding energy. An ideal catalyst optimizes the (ΔG_O* - ΔG_{HO}*) value, where O* has two bonds to the surface, while HO* has only one bond [91]. A volcano plot **(Fig. 1.8b)** for OER using (ΔG_O* - ΔG_{HO}*) as a descriptor has been constructed for different metal oxides, including perovskites, spinels, rutiles, and transition metal oxides. Research has shown that the binding strength of oxygen on the surface significantly influences the formation of intermediates like MOOH and MO, which affects the overall OER mechanism [92]. If the surface binds oxygen too strongly, the potential is limited by the formation of HOO* from O*. If the binding is too weak, the potential is constrained by the oxidation of HO* to O*. Therefore, an optimal catalyst must achieve the right balance in (ΔG_O* - ΔG_{HO}*) for maximum performance.

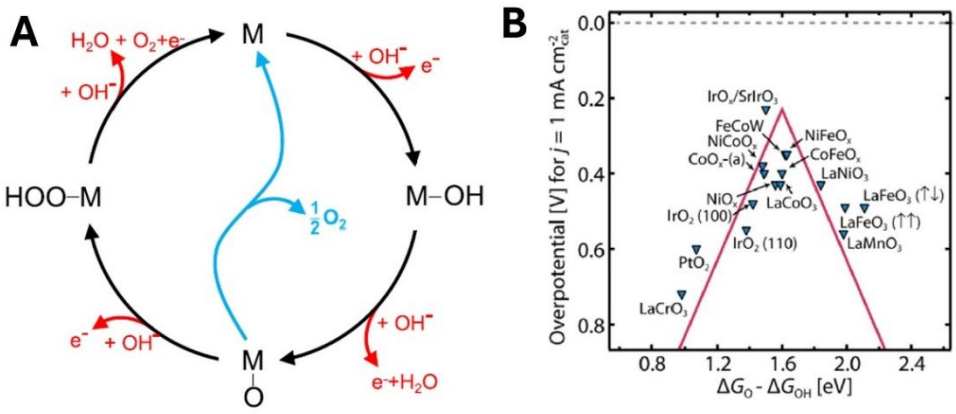

Fig. 1.8 *(**A**) The OER mechanism under alkaline conditions. The light blue route is for the direct reaction of two adjacent oxo (M-O) intermediates to produce oxygen. The black route represents the formation of a peroxide (M-OOH) intermediate during OER. (**B**) OER volcano plot for metal oxides using $\Delta G_O^* - \Delta G_{HO}^*$ as descriptor [93].*

References

[1] S. A. Sherif, F. Barbir, and T. N. Veziroglu, 'Towards a Hydrogen Economy', *The Electricity Journal*, vol. 18, no. 6, pp. 62–76, Jul. 2005, doi: 10.1016/j.tej.2005.06.003.

[2] C. Daoudi and T. Bounahmidi, 'Overview of alkaline water electrolysis modeling', *International Journal of Hydrogen Energy*, vol. 49, pp. 646–667, Jan. 2024, doi: 10.1016/j.ijhydene.2023.08.345.

[3] M. Alves, 'Hydrogen energy: Terceira island demonstration facility', *CI&CEQ*, vol. 14, no. 2, pp. 77–95, 2008, doi: 10.2298/CICEQ0802077A.

[4] R. E. Clarke, S. Giddey, and S. P. S. Badwal, 'Stand-alone PEM water electrolysis system for fail safe operation with a renewable energy source', *International Journal of Hydrogen Energy*, vol. 35, no. 3, pp. 928–935, Feb. 2010, doi: 10.1016/j.ijhydene.2009.11.100.

[5] H. Ibrahim, A. Ilinca, and J. Perron, 'Energy storage systems—Characteristics and comparisons', *Renewable and Sustainable Energy Reviews*, vol. 12, no. 5, pp. 1221–1250, Jun. 2008, doi: 10.1016/j.rser.2007.01.023.

[6] P. Moriarty and D. Honnery, 'Intermittent renewable energy: The only future source of hydrogen?', *International Journal of Hydrogen Energy*, vol. 32, no. 12, pp. 1616–1624, Aug. 2007, doi: 10.1016/j.ijhydene.2006.12.008.

[7] C. Acar and I. Dincer, 'Comparative assessment of hydrogen production methods from renewable and non-renewable sources', *International Journal of Hydrogen Energy*, vol. 39, no. 1, pp. 1–12, Jan. 2014, doi: 10.1016/j.ijhydene.2013.10.060.

[8] *Sustainable Hydrogen Production*. Elsevier, 2016. doi: 10.1016/C2014-0-00658-2.

[9] Ø. Ulleberg and S. O. Mørner, 'TRNSYS simulation models for solar-hydrogen systems', *Solar Energy*, vol. 59, no. 4–6, pp. 271–279, Apr. 1997, doi: 10.1016/S0038-092X(97)00015-7.

[10] D. M. F. Santos, C. A. C. Sequeira, and J. L. Figueiredo, 'Hydrogen production by alkaline water electrolysis', *Quím. Nova*, vol. 36, no. 8, pp. 1176–1193, 2013, doi: 10.1590/S0100-40422013000800017.

[11] S. Ding *et al.*, 'Analysis of the effect of characteristic parameters and operating conditions on exergy efficiency of alkaline water electrolyzer', *Journal of Power Sources*, vol. 537, p. 231532, Jul. 2022, doi: 10.1016/j.jpowsour.2022.231532.

[12] J. Rodríguez, S. Palmas, M. Sánchez-Molina, E. Amores, L. Mais, and R. Campana, 'Simple and Precise Approach for Determination of Ohmic Contribution of Diaphragms in Alkaline Water Electrolysis',

Membranes, vol. 9, no. 10, p. 129, Oct. 2019, doi: 10.3390/membranes9100129.
[13] C. Henao, K. Agbossou, M. Hammoudi, Y. Dubé, and A. Cardenas, 'Simulation tool based on a physics model and an electrical analogy for an alkaline electrolyser', *Journal of Power Sources*, vol. 250, pp. 58–67, Mar. 2014, doi: 10.1016/j.jpowsour.2013.10.086.
[14] M. Rashid, M. K. A. Mesfer, H. Naseem, and M. Danish, 'Hydrogen Production by Water Electrolysis: A Review of Alkaline Water Electrolysis, PEM Water Electrolysis and High Temperature Water Electrolysis', vol. 4, no. 3.
[15] D. Henkensmeier, M. Najibah, C. Harms, J. Žitka, J. Hnát, and K. Bouzek, 'Overview: State-of-the Art Commercial Membranes for Anion Exchange Membrane Water Electrolysis', *Journal of Electrochemical Energy Conversion and Storage*, vol. 18, no. 2, p. 024001, May 2021, doi: 10.1115/1.4047963.
[16] J. C. Ehlers, A. A. Feidenhans'l, K. T. Therkildsen, and G. O. Larrazábal, 'Affordable Green Hydrogen from Alkaline Water Electrolysis: Key Research Needs from an Industrial Perspective', *ACS Energy Lett.*, vol. 8, no. 3, pp. 1502–1509, Mar. 2023, doi: 10.1021/acsenergylett.2c02897.
[17] J. P. Viteri, S. Viteri, C. Alvarez-Vasco, and F. Henao, 'A systematic review on green hydrogen for off-grid communities –technologies, advantages, and limitations', *International Journal of Hydrogen Energy*, vol. 48, no. 52, pp. 19751–19771, Jun. 2023, doi: 10.1016/j.ijhydene.2023.02.078.
[18] R. Phillips and C. W. Dunnill, 'Zero gap alkaline electrolysis cell design for renewable energy storage as hydrogen gas', *RSC Adv.*, vol. 6, no. 102, pp. 100643–100651, 2016, doi: 10.1039/C6RA22242K.
[19] N. Heinemann *et al.*, 'Enabling large-scale hydrogen storage in porous media – the scientific challenges', *Energy Environ. Sci.*, vol. 14, no. 2, pp. 853–864, 2021, doi: 10.1039/D0EE03536J.
[20] A. Ursua, L. M. Gandia, and P. Sanchis, 'Hydrogen Production From Water Electrolysis: Current Status and Future Trends', *Proc. IEEE*, vol. 100, no. 2, pp. 410–426, Feb. 2012, doi: 10.1109/JPROC.2011.2156750.
[21] M. David, C. Ocampo-Martínez, and R. Sánchez-Peña, 'Advances in alkaline water electrolyzers: A review', *Journal of Energy Storage*, vol. 23, pp. 392–403, Jun. 2019, doi: 10.1016/j.est.2019.03.001.
[22] L. Vidas and R. Castro, 'Recent Developments on Hydrogen Production Technologies: State-of-the-Art Review with a Focus on Green-Electrolysis', *Applied Sciences*, vol. 11, no. 23, p. 11363, Dec. 2021, doi: 10.3390/app112311363.
[23] S. Sebbahi *et al.*, 'A comprehensive review of recent advances in alkaline water electrolysis for hydrogen production', *International Journal of*

Hydrogen Energy, vol. 82, pp. 583–599, Sep. 2024, doi: 10.1016/j.ijhydene.2024.07.428.
[24] H. Wendt and H. Hofmann, 'Ceramic diaphragms for advanced alkaline water electrolysis', *J Appl Electrochem*, vol. 19, no. 4, pp. 605–610, Jul. 1989, doi: 10.1007/BF01022121.
[25] Y. Leng, G. Chen, A. J. Mendoza, T. B. Tighe, M. A. Hickner, and C.-Y. Wang, 'Solid-State Water Electrolysis with an Alkaline Membrane', *J. Am. Chem. Soc.*, vol. 134, no. 22, pp. 9054–9057, Jun. 2012, doi: 10.1021/ja302439z.
[26] Z. Liu, S. D. Sajjad, Y. Gao, J. Kaczur, and R. Masel, 'An Alkaline Water Electrolyzer with Sustainion^{TM} Membranes: 1 A/cm^2 at 1.9V with Base Metal Catalysts', *ECS Trans.*, vol. 77, no. 9, pp. 71–73, May 2017, doi: 10.1149/07709.0071ecst.
[27] M. R. Kraglund, D. Aili, K. Jankova, E. Christensen, Q. Li, and J. O. Jensen, 'Zero-Gap Alkaline Water Electrolysis Using Ion-Solvating Polymer Electrolyte Membranes at Reduced KOH Concentrations', *J. Electrochem. Soc.*, vol. 163, no. 11, pp. F3125–F3131, 2016, doi: 10.1149/2.0161611jes.
[28] M. Carmo, D. L. Fritz, J. Mergel, and D. Stolten, 'A comprehensive review on PEM water electrolysis', *International Journal of Hydrogen Energy*, vol. 38, no. 12, pp. 4901–4934, Apr. 2013, doi: 10.1016/j.ijhydene.2013.01.151.
[29] T. Wang, X. Cao, and L. Jiao, 'PEM water electrolysis for hydrogen production: fundamentals, advances, and prospects', *Carb Neutrality*, vol. 1, no. 1, p. 21, Dec. 2022, doi: 10.1007/s43979-022-00022-8.
[30] E. Kuhnert, V. Hacker, and M. Bodner, 'A Review of Accelerated Stress Tests for Enhancing MEA Durability in PEM Water Electrolysis Cells', *International Journal of Energy Research*, vol. 2023, pp. 1–23, Feb. 2023, doi: 10.1155/2023/3183108.
[31] P. Staiti and F. Lufrano, 'Nafion® and Fumapem® polymer electrolytes for the development of advanced solid-state supercapacitors', *Electrochimica Acta*, vol. 206, pp. 432–439, Jul. 2016, doi: 10.1016/j.electacta.2015.11.103.
[32] S. Nur Ozdemir, I. Taymaz, E. Okumuş, F. Gül Boyacı San, and F. Akgün, 'Experimental investigation on performance evaluation of PEM electrolysis cell by using a Taguchi method', *Fuel*, vol. 344, p. 128021, Jul. 2023, doi: 10.1016/j.fuel.2023.128021.
[33] C. Fu *et al.*, 'Metallic-Ir-based anode catalysts in PEM water electrolyzers: Achievements, challenges, and perspectives', *Current Opinion in Electrochemistry*, vol. 38, p. 101227, Apr. 2023, doi: 10.1016/j.coelec.2023.101227.

[34] S. A. Grigoriev, V. N. Fateev, D. G. Bessarabov, and P. Millet, ‘Current status, research trends, and challenges in water electrolysis science and technology’, *International Journal of Hydrogen Energy*, vol. 45, no. 49, pp. 26036–26058, Oct. 2020, doi: 10.1016/j.ijhydene.2020.03.109.
[35] J. Chi and H. Yu, ‘Water electrolysis based on renewable energy for hydrogen production’, *Chinese Journal of Catalysis*, vol. 39, no. 3, Art. no. 3, Mar. 2018, doi: 10.1016/S1872-2067(17)62949-8.
[36] G. Squadrito, G. Maggio, and A. Nicita, ‘The green hydrogen revolution’, *Renewable Energy*, vol. 216, p. 119041, Nov. 2023, doi: 10.1016/j.renene.2023.119041.
[37] P. Shirvanian and F. Van Berkel, ‘Novel components in Proton Exchange Membrane (PEM) Water Electrolyzers (PEMWE): Status, challenges and future needs. A mini review’, *Electrochemistry Communications*, vol. 114, p. 106704, May 2020, doi: 10.1016/j.elecom.2020.106704.
[38] K. Zhang *et al.*, ‘Status and perspectives of key materials for PEM electrolyzer’, *Nano Research Energy*, vol. 1, p. e9120032, Dec. 2022, doi: 10.26599/NRE.2022.9120032.
[39] S. A. Lee, J. Kim, K. C. Kwon, S. H. Park, and H. W. Jang, ‘Anion exchange membrane water electrolysis for sustainable large-scale hydrogen production’, *Carbon Neutralization*, vol. 1, no. 1, pp. 26–48, Jun. 2022, doi: 10.1002/cnl2.9.
[40] R. Wang, M. Ohashi, M. Ishida, and H. Ito, ‘Water transport analysis during cathode dry operation of anion exchange membrane water electrolysis’, *International Journal of Hydrogen Energy*, vol. 47, no. 97, pp. 40835–40848, Dec. 2022, doi: 10.1016/j.ijhydene.2022.09.181.
[41] J. Yang *et al.*, ‘Non-precious electrocatalysts for oxygen evolution reaction in anion exchange membrane water electrolysis: A mini review’, *Electrochemistry Communications*, vol. 131, p. 107118, Oct. 2021, doi: 10.1016/j.elecom.2021.107118.
[42] C. Li and J.-B. Baek, ‘The promise of hydrogen production from alkaline anion exchange membrane electrolyzers’, *Nano Energy*, vol. 87, p. 106162, Sep. 2021, doi: 10.1016/j.nanoen.2021.106162.
[43] T. Naito, T. Shinagawa, T. Nishimoto, and K. Takanabe, ‘Gas Crossover Regulation by Porosity-Controlled Glass Sheet Achieves Pure Hydrogen Production by Buffered Water Electrolysis at Neutral pH’, *ChemSusChem*, vol. 15, no. 3, p. e202102294, Feb. 2022, doi: 10.1002/cssc.202102294.
[44] C. Santoro *et al.*, ‘What is Next in Anion-Exchange Membrane Water Electrolyzers? Bottlenecks, Benefits, and Future’, *ChemSusChem*, vol. 15, no. 8, p. e202200027, Apr. 2022, doi: 10.1002/cssc.202200027.

[45] J. E. Park *et al.*, 'High-performance anion-exchange membrane water electrolysis', *Electrochimica Acta*, vol. 295, pp. 99–106, Feb. 2019, doi: 10.1016/j.electacta.2018.10.143.
[46] D. Li *et al.*, 'Highly quaternized polystyrene ionomers for high performance anion exchange membrane water electrolysers', *Nat Energy*, vol. 5, no. 5, pp. 378–385, Mar. 2020, doi: 10.1038/s41560-020-0577-x.
[47] A. Nechache and S. Hody, 'Alternative and innovative solid oxide electrolysis cell materials: A short review', *Renewable and Sustainable Energy Reviews*, vol. 149, p. 111322, Oct. 2021, doi: 10.1016/j.rser.2021.111322.
[48] A. Nechache, M. Cassir, and A. Ringuedé, 'Solid oxide electrolysis cell analysis by means of electrochemical impedance spectroscopy: A review', *Journal of Power Sources*, vol. 258, pp. 164–181, Jul. 2014, doi: 10.1016/j.jpowsour.2014.01.110.
[49] A. Hauch *et al.*, 'Recent advances in solid oxide cell technology for electrolysis', *Science*, vol. 370, no. 6513, p. eaba6118, Oct. 2020, doi: 10.1126/science.aba6118.
[50] O. Schmidt, A. Gambhir, I. Staffell, A. Hawkes, J. Nelson, and S. Few, 'Future cost and performance of water electrolysis: An expert elicitation study', *International Journal of Hydrogen Energy*, vol. 42, no. 52, pp. 30470–30492, Dec. 2017, doi: 10.1016/j.ijhydene.2017.10.045.
[51] S. Shiva Kumar and H. Lim, 'An overview of water electrolysis technologies for green hydrogen production', *Energy Reports*, vol. 8, pp. 13793–13813, Nov. 2022, doi: 10.1016/j.egyr.2022.10.127.
[52] K. Kamlungsua, P. -C. Su, and S. H. Chan, 'Hydrogen Generation Using Solid Oxide Electrolysis Cells', *Fuel Cells*, vol. 20, no. 6, pp. 644–649, Dec. 2020, doi: 10.1002/fuce.202070602.
[53] M. Lang, S. Raab, M. S. Lemcke, C. Bohn, and M. Pysik, 'Long-Term Behavior of a Solid Oxide Electrolyzer (SOEC) Stack ▲ ', *Fuel Cells*, vol. 20, no. 6, pp. 690–700, Dec. 2020, doi: 10.1002/fuce.201900245.
[54] M. Shen, F. Ai, H. Ma, H. Xu, and Y. Zhang, 'Progress and prospects of reversible solid oxide fuel cell materials', *iScience*, vol. 24, no. 12, p. 103464, Dec. 2021, doi: 10.1016/j.isci.2021.103464.
[55] C. Acar and I. Dincer, '3.1 Hydrogen Production', in *Comprehensive Energy Systems*, Elsevier, 2018, pp. 1–40. doi: 10.1016/B978-0-12-809597-3.00304-7.
[56] Y. Zheng *et al.*, 'A review of high temperature co-electrolysis of H_2O and CO_2 to produce sustainable fuels using solid oxide electrolysis cells (SOECs): advanced materials and technology', *Chem. Soc. Rev.*, vol. 46, no. 5, pp. 1427–1463, 2017, doi: 10.1039/C6CS00403B.

[57] M. Ozturk and I. Dincer, ‘A comprehensive review on power-to-gas with hydrogen options for cleaner applications’, *International Journal of Hydrogen Energy*, vol. 46, no. 62, pp. 31511–31522, Sep. 2021, doi: 10.1016/j.ijhydene.2021.07.066.
[58] P. Haug, B. Kreitz, M. Koj, and T. Turek, ‘Process modelling of an alkaline water electrolyzer’, *International Journal of Hydrogen Energy*, vol. 42, no. 24, pp. 15689–15707, Jun. 2017, doi: 10.1016/j.ijhydene.2017.05.031.
[59] A. Zarghami, N. G. Deen, and A. W. Vreman, ‘CFD modeling of multiphase flow in an alkaline water electrolyzer’, *Chemical Engineering Science*, vol. 227, p. 115926, Dec. 2020, doi: 10.1016/j.ces.2020.115926.
[60] Z. Abdin, C. J. Webb, and E. MacA. Gray, ‘Modelling and simulation of an alkaline electrolyser cell’, *Energy*, vol. 138, pp. 316–331, Nov. 2017, doi: 10.1016/j.energy.2017.07.053.
[61] T. Adibi, A. Sojoudi, and S. C. Saha, ‘Modeling of thermal performance of a commercial alkaline electrolyzer supplied with various electrical currents’, *International Journal of Thermofluids*, vol. 13, p. 100126, Feb. 2022, doi: 10.1016/j.ijft.2021.100126.
[62] M. Sánchez, E. Amores, L. Rodríguez, and C. Clemente-Jul, ‘Semi-empirical model and experimental validation for the performance evaluation of a 15 kW alkaline water electrolyzer’, *International Journal of Hydrogen Energy*, vol. 43, no. 45, pp. 20332–20345, Nov. 2018, doi: 10.1016/j.ijhydene.2018.09.029.
[63] M. David, H. Alvarez, C. Ocampo-Martinez, and R. Sánchez-Peña, ‘Dynamic modelling of alkaline self-pressurized electrolyzers: a phenomenological-based semiphysical approach’, *International Journal of Hydrogen Energy*, vol. 45, no. 43, pp. 22394–22407, Sep. 2020, doi: 10.1016/j.ijhydene.2020.06.038.
[64] R. Gilliam, J. Graydon, D. Kirk, and S. Thorpe, ‘A review of specific conductivities of potassium hydroxide solutions for various concentrations and temperatures’, *International Journal of Hydrogen Energy*, vol. 32, no. 3, Art. no. 3, Mar. 2007, doi: 10.1016/j.ijhydene.2006.10.062.
[65] J. W. Haverkort and H. Rajaei, ‘Voltage losses in zero-gap alkaline water electrolysis’, *Journal of Power Sources*, vol. 497, p. 229864, Jun. 2021, doi: 10.1016/j.jpowsour.2021.229864.
[66] I. Firtina-Ertis, ‘Thermodynamic and electrochemical assessment of an alkaline electrolyzer (AE) at different operating parameters’, *Journal of Environmental Chemical Engineering*, vol. 10, no. 2, p. 107225, Apr. 2022, doi: 10.1016/j.jece.2022.107225.

[67] C. J. Vörösmarty *et al.*, 'Global threats to human water security and river biodiversity', *Nature*, vol. 467, no. 7315, pp. 555–561, Sep. 2010, doi: 10.1038/nature09440.
[68] K. N. Knust, D. Hlushkou, U. Tallarek, and R. M. Crooks, 'Electrochemical Desalination for a Sustainable Water Future', *ChemElectroChem*, vol. 1, no. 5, pp. 850–857, May 2014, doi: 10.1002/celc.201300236.
[69] S. Dresp, F. Dionigi, M. Klingenhof, and P. Strasser, 'Direct Electrolytic Splitting of Seawater: Opportunities and Challenges', *ACS Energy Lett.*, vol. 4, no. 4, Art. no. 4, Apr. 2019, doi: 10.1021/acsenergylett.9b00220.
[70] W. Tong *et al.*, 'Electrolysis of low-grade and saline surface water', *Nat Energy*, vol. 5, no. 5, Art. no. 5, May 2020, doi: 10.1038/s41560-020-0550-8.
[71] P. Farràs, P. Strasser, and A. J. Cowan, 'Water electrolysis: Direct from the sea or not to be?', *Joule*, vol. 5, no. 8, pp. 1921–1923, Aug. 2021, doi: 10.1016/j.joule.2021.07.014.
[72] M. A. Khan *et al.*, 'Seawater electrolysis for hydrogen production: a solution looking for a problem?', *Energy Environ. Sci.*, vol. 14, no. 9, pp. 4831–4839, 2021, doi: 10.1039/D1EE00870F.
[73] J. N. Hausmann, R. Schlögl, P. W. Menezes, and M. Driess, 'Is direct seawater splitting economically meaningful?', *Energy Environ. Sci.*, vol. 14, no. 7, pp. 3679–3685, 2021, doi: 10.1039/D0EE03659E.
[74] J. Juodkazytė *et al.*, 'Electrolytic splitting of saline water: Durable nickel oxide anode for selective oxygen evolution', *International Journal of Hydrogen Energy*, vol. 44, no. 12, pp. 5929–5939, Mar. 2019, doi: 10.1016/j.ijhydene.2019.01.120.
[75] F. Dionigi, T. Reier, Z. Pawolek, M. Gliech, and P. Strasser, 'Design Criteria, Operating Conditions, and Nickel-Iron Hydroxide Catalyst Materials for Selective Seawater Electrolysis', *ChemSusChem*, vol. 9, no. 9, Art. no. 9, May 2016, doi: 10.1002/cssc.201501581.
[76] J. Mohammed-Ibrahim and H. Moussab, 'Recent advances on hydrogen production through seawater electrolysis', *Materials Science for Energy Technologies*, vol. 3, pp. 780–807, 2020, doi: 10.1016/j.mset.2020.09.005.
[77] F. Sun, Q. Tang, and D. Jiang, 'Theoretical Advances in Understanding and Designing the Active Sites for Hydrogen Evolution Reaction', *ACS Catal.*, vol. 12, no. 14, pp. 8404–8433, Jul. 2022, doi: 10.1021/acscatal.2c02081.
[78] L. Zhuang *et al.*, 'Recent Advances on Hydrogen Evolution and Oxygen Evolution Catalysts for Direct Seawater Splitting', *Coatings*, vol. 12, no. 5, Art. no. 5, May 2022, doi: 10.3390/coatings12050659.

[79] J. N. Bamba, A. T. Dumlao, R. M. Lazaro, D. D. Matienzo, and J. Ocon, ‘Green Hydrogen from Seawater Electrolysis: Recent Developments and Future Perspectives’, *Current Opinion in Electrochemistry*, p. 101592, Sep. 2024, doi: 10.1016/j.coelec.2024.101592.
[80] N. M. Markovića, S. T. Sarraf, H. A. Gasteiger, and P. N. Ross, ‘Hydrogen electrochemistry on platinum low-index single-crystal surfaces in alkaline solution’, *J. Chem. Soc., Faraday Trans.*, vol. 92, no. 20, pp. 3719–3725, 1996, doi: 10.1039/FT9969203719.
[81] W. Sheng, H. A. Gasteiger, and Y. Shao-Horn, ‘Hydrogen Oxidation and Evolution Reaction Kinetics on Platinum: Acid vs Alkaline Electrolytes’, *J. Electrochem. Soc.*, vol. 157, no. 11, p. B1529, 2010, doi: 10.1149/1.3483106.
[82] K. E. Ramohlola, K. D. Modibane, M. M. Ndipingwi, and E. I. Iwuoha, ‘Polyaniline-based electrocatalysts for electrochemical hydrogen evolution reaction’, *European Polymer Journal*, vol. 213, p. 113125, Jun. 2024, doi: 10.1016/j.eurpolymj.2024.113125.
[83] H.-M. Zhang, J.-J. Wang, Y. Meng, and J. Sun, ‘Recent advances in amorphous metal phosphide electrocatalysts for hydrogen evolution reaction’, *International Journal of Hydrogen Energy*, vol. 47, no. 85, pp. 36084–36097, Oct. 2022, doi: 10.1016/j.ijhydene.2022.08.184.
[84] R. Subbaraman *et al.*, ‘Enhancing Hydrogen Evolution Activity in Water Splitting by Tailoring Li^+-$Ni(OH)_2$-Pt Interfaces’, *Science*, vol. 334, no. 6060, pp. 1256–1260, Dec. 2011, doi: 10.1126/science.1211934.
[85] A. J. Medford *et al.*, ‘From the Sabatier principle to a predictive theory of transition-metal heterogeneous catalysis’, *Journal of Catalysis*, vol. 328, pp. 36–42, Aug. 2015, doi: 10.1016/j.jcat.2014.12.033.
[86] J. Mahmood *et al.*, ‘An efficient and pH-universal ruthenium-based catalyst for the hydrogen evolution reaction’, *Nature Nanotech*, vol. 12, no. 5, pp. 441–446, May 2017, doi: 10.1038/nnano.2016.304.
[87] J. Durst, A. Siebel, C. Simon, F. Hasché, J. Herranz, and H. A. Gasteiger, ‘New insights into the electrochemical hydrogen oxidation and evolution reaction mechanism’, *Energy Environ. Sci.*, vol. 7, no. 7, pp. 2255–2260, 2014, doi: 10.1039/C4EE00440J.
[88] H. Jin *et al.*, ‘Emerging Two-Dimensional Nanomaterials for Electrocatalysis’, *Chem. Rev.*, vol. 118, no. 13, pp. 6337–6408, Jul. 2018, doi: 10.1021/acs.chemrev.7b00689.
[89] N.-T. Suen, S.-F. Hung, Q. Quan, N. Zhang, Y.-J. Xu, and H. M. Chen, ‘Electrocatalysis for the oxygen evolution reaction: recent development and future perspectives’, *Chem. Soc. Rev.*, vol. 46, no. 2, pp. 337–365, 2017, doi: 10.1039/C6CS00328A.

[90] S. Marini *et al.*, ‘Advanced alkaline water electrolysis’, *Electrochimica Acta*, vol. 82, pp. 384–391, Nov. 2012, doi: 10.1016/j.electacta.2012.05.011.
[91] J. Song *et al.*, ‘A review on fundamentals for designing oxygen evolution electrocatalysts’, *Chem. Soc. Rev.*, vol. 49, no. 7, pp. 2196–2214, 2020, doi: 10.1039/C9CS00607A.
[92] Á. Valdés *et al.*, ‘Solar hydrogen production with semiconductor metal oxides: new directions in experiment and theory’, *Phys. Chem. Chem. Phys.*, vol. 14, no. 1, pp. 49–70, 2012, doi: 10.1039/C1CP23212F.
[93] Y. Li, L. Zhou, and S. Guo, ‘Noble metal-free electrocatalytic materials for water splitting in alkaline electrolyte’, *EnergyChem*, vol. 3, no. 2, p. 100053, Mar. 2021, doi: 10.1016/j.enchem.2021.100053.

2. Overview of Electrocatalysts in Alkaline Medium

Quick progress in alkaline water electrolysis technology was already made prior the mid-20th century. The discovery some years ago that semiconductor oxides could be extremely efficient oxygen evolution catalysts in alkaline water electrolysis brought a fresh perspective to the body of work conducted with early evolving implementations. In 1981, Ni-based oxides were recognized as excellent candidates for catalyzing the OER. Today, Ru/Ir-based materials are the most efficient for OER catalysis, but their scarcity and high-cost limit their widespread use. To lower the production costs of electrode materials, numerous Earth-abundant OER catalyst candidates have been developed and explored. Significant progress has been made in recent years in the search and design of low-cost, high-performance OER catalysts, as reflected by the growing number of publications on this topic [1]. Several HER catalysts have been recognized for their significant role in accelerating these reactions. Platinum-based catalysts are particularly noteworthy, as they exhibit almost no overpotential at the onset and show a rapid increase in current with rising voltage. However, their limited availability and high cost restrict their large-scale use, prompting the development of more affordable alternatives with high activity and durability [2], [3]. While many non-precious metal-based compounds have shown excellent HER catalytic activity in acidic environments, the lack of non-precious alternatives for oxygen evolution catalysis has slowed the progress of developing cost-effective water-splitting devices in acidic solutions. The development of highly active oxygen evolution catalysts for alkaline conditions has driven the creation of novel non-precious metal structures for HER catalysis in alkaline media [4]. In addition to the catalyst composition, the morphology plays a significant role in influencing water-splitting reactions. To ensure high performance, electrodes need to have exceptionally large surface areas [5]. Additionally,

materials with a high active surface can increase electrolyzer performance even more [6], [7], [8], [9], [10], [11]. As a result, different types of nanostructured electrodes with high aspect ratios have been developed over the years, featuring 1D [12], 2D [13], and 3D morphologies [14]. One of the ways to increase electrocatalytic activity is by enhancing nanoporosity, since it will be able to enlarge an effective surface area for reactive surfaces and ionic transportation in a given material mass [15]. One is to increase the activity (or reaction rate) of an electrocatalyst system, which can be achieved by increasing either the density of active sites on the electrode through addition or structural optimization/conversion into highly reactive species per total mass, or intrinsic activity for each site. As illustrated in **Fig. 2.1** these strategies can be combined to achieve the greatest improvements in performance. However, there are physical limits to how much catalyst can be loaded onto an electrode without interfering with critical processes like charge and mass transport, leading to a plateau effect at high loadings. In contrast, enhancing intrinsic activity directly increases electrode performance while avoiding the transport challenges associated with high loadings. This also allows for reduced catalyst usage, lowering costs. Moreover, catalyst activity can vary widely; the difference in intrinsic activity between an effective and an ineffective catalyst can span over 10 orders of magnitude, whereas differences between high and low catalyst loadings typically range from only one to three orders of magnitude [16].

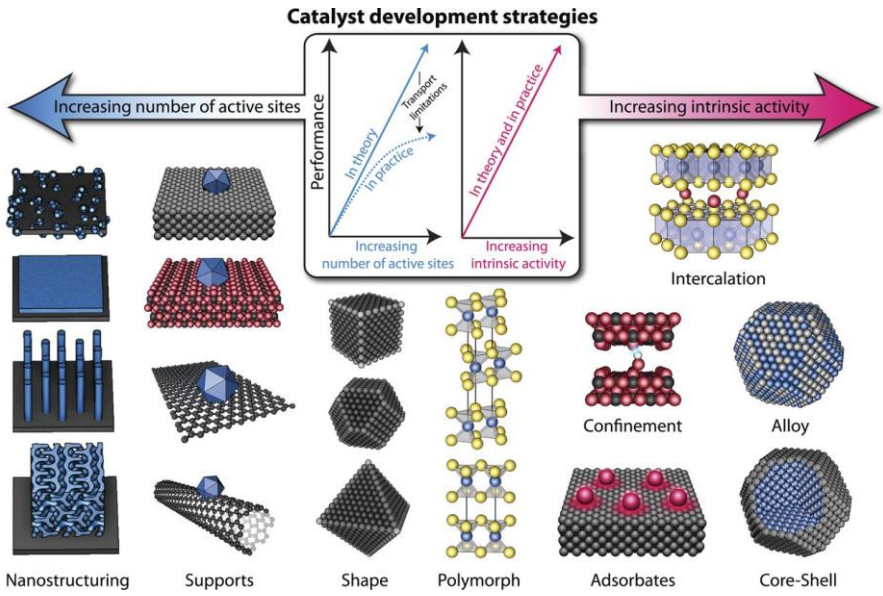

Fig. 2.1 *Schematic of various catalyst development strategies, which aim to increase the number of active sites and/or increase the intrinsic activity of each active site* [17]

2.1 Electrocatalysts materials: Noble Metals and their Alloys

Currently, the most advanced electrocatalysts, which are used to reduce overpotential and accelerate reaction kinetics, are based on expensive and scarce noble metals like Pt, IrO_2, and RuO [18]. The reactivity of a catalyst is closely linked to the number of d-electrons involved in coordination. Precious metals are effective as both catalysts and ligands, mainly due to their numerous empty d-electron orbitals, which allow for strong coordination bonds that facilitate reactions. These catalysts also have stable properties and excellent adsorption and desorption characteristics, enhancing the chemistry at the interface. Noble metal oxides like IrO_2 and RuO_2 are particularly active in catalysing OER and are considered among the most efficient materials for water electrolysis [19]. The performance of OER is significantly influenced by the redox behaviour of transition metals, with changes in their electronic structure playing a crucial role in adjusting catalytic activity. As shown in the

OER activity trend for various metal oxides, RuO_2 and IrO_2 demonstrate exceptional catalytic performance. Although their OER activities are similar, Ru is more abundant in nature compared to Ir. However, RuO_2 is more susceptible to deactivation in acidic and alkaline environments, while IrO_2 offers the best combination of catalytic activity and stability in both media. The number of efficient HER catalysts available for alkaline media is significantly lower compared to those for acidic environments. Therefore, research aimed at developing highly active and stable HER catalysts for alkaline media is both meaningful and promising for commercial viability. Platinum Group Metals (PGMs) generally exhibit the highest HER activity in both acidic and alkaline media, owing to their optimal hydrogen binding energies [20]. As discussed by Mahmood et al. [21], PGMs continue to demonstrate unparalleled HER activity in alkaline media. This has driven researchers to develop PGM alloys with transition metals to reduce costs and enhance performance by overcoming inherent limitations. For example, alloys of Pt/Fe [22], Pt/Ni/Co [23] were successfully obtained and have shown excellent catalytic properties. The faster HER kinetics of Pt/Ni/Co were attributed to a significant negative shift in the formation potential of $Pt–OH_{ad}$ and an increase in the charge related to hydrogen binding energy. This enhancement is a result of alloying and bifunctional effects [24]. Other noble metals such as Ru, Au, Ir, Pd, Ag, and their alloys with low-cost transition metals or doping with non-metal elements have been explored, leading to notable improvements in HER activity in alkaline media due to their favourable atomic structures and abundance of exposed active sites. Ru, a more affordable alternative to Pt, exhibits similar hydrogen binding energy but has been less studied as an HER catalyst. Recent efforts have enhanced Ru's activity in alkaline conditions by decorating Ru nanoparticles (NPs) on a nitrogenated holey 2D carbon structure (Ru@C2N)[25]. However, the high

cost and limited availability of these materials pose significant barriers to large-scale implementation. As a result, there is a critical need to develop low-cost, abundant, efficient, and stable electrocatalysts to facilitate the widespread adoption of clean energy technologies. Significant progress has been made in developing earth-abundant transition metal–based electrocatalysts. Among these, various transition metal–based candidates have gained attention due to their well-tuned electronic configurations, high electrical conductivity, and excellent electrochemical performance and durability [26]. Therefore, focusing on the development of cost-effective catalysts using non-noble metals or metal-free alternatives presents an effective strategy to address these challenges and achieve a balance between cost and performance.

2.2 Electrocatalysts materials: Non-Noble Metals and their Alloys

Although substantial advancements have been achieved in creating advanced catalysts using noble metals for water splitting, their high cost and limited availability continue to pose significant challenges to widespread adoption. Therefore, developing transition metal compound catalysts that offer high activity, affordability, long-term stability, and are abundant on Earth is crucial for the large-scale application of overall water splitting and to serve as viable alternatives to precious metal-based catalysts. Nickel (Ni) is one of the most popular non-noble catalysts for different applications due to its strong catalytic activity and relatively low susceptibility to poisoning. Nickel is an earth-abundant first-row transition metal with an atomic number of 28, and its abundance in Earth's crust exceeds 50 ppm and it possesses unique properties that make it widely useful in various applications, including coins, catalysts, and batteries. Nickel is known for its high ductility and corrosion resistance [27]. Almost a century ago, metallic nickel was found to catalyze HER in

alkaline solutions, leading researchers to invest significant efforts in understanding the catalytic mechanism and enhancing activity through electrode design. Nickel species have demonstrated promising performance for HER and OER in alkaline media, largely due to the strength of the metal-hydrogen (M-H) bond. Recently, there has been a focus on optimizing the chemical structures and morphology of Ni-based heterogeneous catalysts, which show promising HER catalytic activity for efficient water splitting. As described previously, in an alkaline environment, the Volmer step involves the formation of an adsorbed hydrogen atom and a negatively charged hydroxide anion through the reduction of a water molecule adsorbed on the electrocatalyst surface. Following this, two possible mechanisms can occur:

1. Tafel step: Two adsorbed hydrogen atoms, generated during the Volmer step, combine to form a hydrogen molecule, which then leaves the catalyst surface

2. Heyrovsky step: The adsorbed hydrogen atom from the Volmer step is attacked by another water molecule, resulting in the formation of a hydrogen molecule and a hydroxide anion

Some researchers suggest that the HER mechanisms on metallic Ni surfaces follow the Volmer-Tafel route, while others propose that they follow the Volmer-Heyrovsky route. However, the exact HER mechanisms on metallic Ni surfaces remain a topic of ongoing debate [28].

However, single-component transition metal catalysts have been found insufficient in meeting the demands for both activity and stability. Non-precious metals like Ni, Co, Fe, and Mo tend to form strong bonds with atomic hydrogen, making it difficult for H_2 to be released on the electrode surface, which results in lower activity for HER [29], [30].

In contrast, combined catalysts that effectively balance the properties of each component show significantly improved catalytic performance in water-splitting reactions. So, an effective approach for improving Ni catalytic performance is alloying it with other metals or incorporating non-metal species. To further enhance the catalytic activity and reduce the required overpotentials of Ni-based catalysts, a range of strategies has been developed [31]. The enhanced performance of Ni alloys mainly stems from their synergistic electronic properties which is crucial in influencing the adsorption and desorption kinetics in both HER and OER processes [32], [33]. Alloying Ni, known for its hyper d-electronic properties, with certain transition metals that are hypo d-electronic increases the d-band character. In particular, combining Ni with other metals boosts its intrinsic activity by adjusting the electron density and d-band character, key factors in enhancing electrocatalytic efficiency, improving its effectiveness in electrocatalytic water splitting [34]. Ni-based composites have garnered significant attention due to their abundance and impressive electrochemical efficiency. In particular, Ni-based catalysts with heterogeneous nanostructures have been extensively studied by researchers. These heterostructures are composite structures comprising interfaces formed by different materials. Significant progress has been made in the controlled design of materials with heterogeneous nanostructures, aiming to optimize surface properties and improve charge transfer between different components. These include modifying the microstructure of nanomaterials, configuring advanced materials with diverse active phases, and hybridizing them with conductive nanocarbon materials. Ni-based heterostructure catalysts are composed of two or more components linked through physical or chemical interactions [35]. Their exceptional activity is attributed to the increased number of active sites, unique physical and electronic structures, and strong interfacial effects.

Various Ni-based catalysts, such as Ni oxides/hydroxides [36], Ni chalcogenides[37], Ni phosphides [38], and Ni nitrides [39], have demonstrated remarkable electrochemical performance not only for HER or OER but also as bifunctional catalysts for overall water splitting. Alongside Ni-based catalysts, Co-based catalysts—such as metallic cobalt, its oxides, phosphides, and sulfides—have also attracted significant attention as innovative and efficient HER electrocatalysts for alkaline electrolytes. Cobalt phosphides, in particular, stand out due to their excellent electrical conductivity and durability. For instance, the development of 3D porous CoP_3 concave polyhedrons from metal-organic frameworks (MOFs) has shown remarkable electrocatalytic activity and enhanced stability in alkaline conditions. This highlights how designing open porous structures can be a key step forward in creating highly efficient electrocatalysts for alkaline HER. Additionally, structural and electronic modifications, like the use of Janus-like asymmetric nanoparticles, provide alternative ways to optimize the electronic distribution at the interface and improve catalytic performance [40], [41]. Other interesting catalysts are those based on Molybdenum (Mo) and Tungsten (W). These materials have so far shown greater activity for HER in acidic electrolytes compared to basic ones. Researchers are actively working to enhance the performance of Mo-based catalysts by developing variants like molybdenum carbides (e.g., Mo_2C/NCF) [42] or sulphides like MoS_2 [43]. **Transition metal oxides** (Ni, Co, Fe, Mn) are highly promising catalysts for the oxygen evolution reaction (OER) in alkaline media, with research primarily aimed at optimizing their microstructures. These oxides can be categorized into several structural types, including perovskite, spinel, amorphous, rock salt, and transition metal lithium oxides. Perovskite oxides are especially effective OER catalysts due to their ability to modify electrochemical potential and electronic properties by adjusting the valence

states of cations and controlling ion size [44]. Notably, certain transition metal-based compounds, such as sulphides and phosphides, tend to oxidize on their surfaces, forming an oxide layer when exposed to ambient conditions. This oxide layer can undergo restructuring under specific conditions, such as in the presence of an electrolyte or when a potential is applied [45], [46]. In the case of transition metal phosphides, chalcogenides, nitrides, and carbides, the incorporation of relatively electronegative atoms like P, S/Se, N, and C can adjust the electronic structure of the base metals by facilitating electron transfer from the transition metal to the non-metallic elements [47], [48]. On one hand, in transition metal phosphides and chalcogenides, the non-metallic elements reduce the concentration of the base metal and simultaneously act as proton acceptors, lowering hydrogen bond energy and giving them properties akin to those of active enzymatic centers. On the other hand, in transition metal nitrides and carbides, the addition of N and C atoms can expand the unoccupied portion of the d-band center in the parent metals, making their electronic structure more closely resemble that of platinum-group metals. Amorphous catalysts, in comparison to crystalline ones, offer a higher density of active catalytic sites, are easier to control in terms of composition, and can be synthesized under milder conditions. The porous surface of amorphous alloys helps prevent diffusion issues from interfering with surface reactions [49]. Amorphous metal oxides are made up of molecular-scale clusters with short-range order and abundant surface defects, which act as catalytic active sites. The disordered atomic structure of amorphous materials enhances electron interactions and interatomic bonding, supports the formation of hydroxy ion bridges and water terminal connections, and thus improves catalytic activity. Unlike crystalline materials, amorphous structures have numerous unsaturated bonds and defect sites that increase the availability of active sites, enhance electron transfer efficiency, and offer superior

mechanical and electrochemical stability. Additionally, they exhibit unique properties not found in crystalline alloys, such as superconductivity and excellent corrosion resistance. Other metal oxides, like rock salt and transition metal lithium oxides, are also effective OER catalysts. Notably, NiO has attracted considerable attention as a promising OER catalyst among rock salt metal oxides. Theoretical predictions indicate that the (100) crystal plane of NiO is the most stable and exhibits the highest adsorption energy. However, the actual efficiency of NiO has been lower than expected due to the absence of a perfect single-crystal structure. To boost its catalytic performance, doping NiO with other metals, such as Fe and Co, has been suggested as a way to enhance its catalytic activity [1].

2.2.1 Nickel-Iron Alloys

Several amorphous TM (Transition Metal)-Ni alloys have been identified and developed as affordable electrocatalysts. Additionally, combining multiple metals in amorphous catalysts shows promise, similar to the effective performance of polymetallic oxides in crystalline materials. The Ni-Fe amorphous alloy is particularly noteworthy, offering high intrinsic activity, abundant availability, low cost, and strong potential to accelerate the challenging OER process [50]. In 3D transition metal composites, Fe has been found to greatly enhance the OER efficiency of nickel and cobalt oxides, and researchers believe Fe may have a similar impact in amorphous systems. Due to the distinct advantages of amorphous structures, optimizing the composition of polymetallic amorphous catalysts has become a major research focus. Common synthesis methods include electrodeposition, photochemical metal-organic deposition, aerosol spray-assisted techniques, reactive magnetron co-sputtering, solvothermal processes, and thermal decomposition. FeNi-based catalysts exhibit superior performance in catalyzing both HER and OER due to the synergistic effect between Fe and Ni [51]. Ni and Fe are

naturally found together on Earth, and even trace amounts of Fe in the electrolyte can significantly enhance the HER and OER efficiency of Ni-based catalysts [52]. Extensive research has been conducted to investigate the synergistic effect between Fe and Ni in the FeNi system. Despite these efforts, the precise identification of active sites and the mechanism behind the water-splitting reaction in these catalysts remain contentious [53]. While there is general agreement on Fe contribution to improving efficiency in amorphous (Ni, Co)-based oxides, its exact role remains contentious. Debates have arisen regarding the roles of Fe and Ni active sites, with a common belief that Fe enhances Ni catalytic efficiency, even in small amounts [54]. It is still uncertain whether the reaction primarily occurs at Ni or Fe sites. Berlinguette et al suggested that Fe stabilizes higher oxidation states of Ni and Co, which is critical for the OER process, as the catalyst undergoes continuous redox reactions. This shift in oxidation states directly impacts catalytic activity. Li et al. also found that adding Fe improved the stability of nickel oxide in amorphous Ni-Fe oxides and increased the activity of Ni sites. However, Wang et al. argued that the Fe site, rather than the Ni site, is the active one in these oxides, while also noting that Fe helps stabilize Ni^{4+}. Although the exact mechanism is still under discussion, it is generally accepted that Fe improves the catalytic activity of Ni, particularly in the OER. Ni-based catalysts are thought to utilize high-valence NiOOH as active sites for OER, but pure NiOOH alone is not efficient at generating the O radical. The addition of Fe is believed to modify the electronic structure and coordination environment of active atoms, increase electron transfer by reducing kinetic barriers, and thus enhance the formation of active metal oxide or oxy(hydroxide) phases on the catalyst surface during OER [55]. For example, the synergy between Fe and Ni has led to NiFeOx exhibiting much better catalytic performance for OER compared to FeOx or NiOx alone [56]. NiFe-based catalysts also show great

promise for seawater electrolysis. Duan et al. [57] developed NiFe hydroxide nanosheets that demonstrated high stability in this application. More recently, Jiang et al. [58] proposed NiFe layered double hydroxide nanosheets for comprehensive seawater splitting, reporting a low cell voltage of 1.55 V at 10 mA cm^{-2} in alkaline simulated seawater (1.0 M KOH + 0.5 M NaCl) and maintaining operational stability over 105 hours at 100 mA cm^{-2}. These findings are particularly noteworthy since the reliance on deionized water, necessary to prevent catalyst poisoning and competitive reactions, is a major obstacle to green hydrogen production [2], [59], [60]. Extensive research has focused on optimizing the surface properties of NiFe alloys to further boost their OER performance [61]. To further optimize adsorption energy, researchers have explored incorporating non-3d transition metals into 3d transition metal-based amorphous catalysts to fine-tune their electronic structure. This includes efforts to adjust the composition, fine-tune the electronic structure, and employ in situ spectroscopic studies. The defect-induced strategy has shown great potential for enhancing OER performance. The increased number of edge sites in metal alloys, resulting from gaps or defects in the lattice, improves OER activity. This defect engineering approach offers a promising pathway for designing and developing efficient electrocatalysts [61]. The following figure, **Fig. 2.2**, summarizes what has been said so far. In particular, alloys are an excellent strategy for enhancing catalytic activity, with the main nickel- and iron-based catalysts being highlighted (fig. 2.2a); several modifications have been proposed for the Ni-based electrocatalyst to improve its activity (fig. 2.2b) and the essential characteristics of amorphous alloys are highlighted (fig. 2.2c).

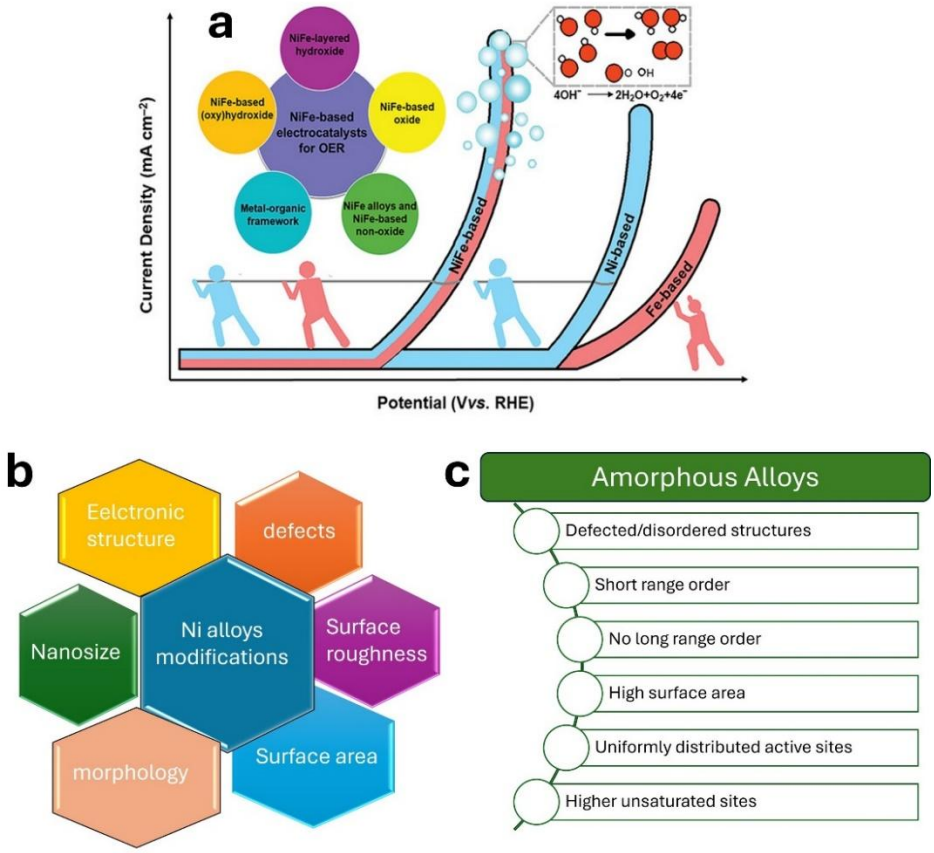

Fig. 2.2 *(**A**) Ni based electrocatalyst and their role in OER [57], (**B**) modifications in Ni-alloys and (**C**) features if amorphous alloys*

2.2.2 Metal Phosphides

Recently, transition metal-based phosphides (TMPs) have gained attention as cost-effective alternatives for catalysis. They are a notable class of metallic compounds with physical properties similar to metal carbides and nitrides, but with a distinct crystal structure. This difference is due to the larger radius of phosphorus atoms and the presence of numerous coordinatively unsaturated surface atoms, which contribute to their enhanced catalytic activity [62]. The phosphorus element plays a crucial role in modulating the electronic structure

of the transition metals. This is due to the difference in electronegativity between phosphorus and the transition metals, as revealed by both theoretical calculations and experimental characterizations [63]. These groundbreaking theoretical predictions and experimental findings have sparked extensive research into metal phosphides as catalysts for the hydrogen evolution reaction (HER). This adjustment balances the interaction between H* and the metal surface, thereby accelerating the hydrogen generation process. TMPs are formed by combining metallic or semi-metallic elements with phosphorus in various compositions, typically following the formula MxPy. Depending on the metal-to-phosphorus ratio, TMPs are classified as either metal-rich/stoichiometric phosphides ($x \approx y$) or phosphorus-rich phosphides. Their crystal structure and bonding vary widely based on composition and element type, with phosphorus content being a key factor in determining stability. In metal-rich TMPs, delocalized electron clouds indicate the presence of metallic bonds (M–M), which give rise to metallic or superconducting properties in some TMPs. For example, GaP and InP are recognized as semiconductors, while TiP, Fe_2P, and CoP display metallic behavior due to their strong metal–metal bonds. Superconducting properties are observed in TMPs like Mo_3P, W_3P, and Ni_3P. Partial ionic character also exists due to electron transfer within covalent bonds (Md+–Pd-), contributing to their overall stability. These metal-rich TMPs are thermally stable and resistant to chemical attack and oxidation. Because of their robust metal-phosphorus bonds, metal-rich TMPs are particularly suitable for water-splitting applications, showing stability in dilute acids and bases, and some can even withstand strong acids and alkaline conditions. However, their high metal content can result in moderate stability in acidic environments. In contrast, phosphorus-rich TMPs contain P–P bonded units, as phosphorus forms clusters and oligomers. For instance, NiP_2 and SiP_2 have pyrite-like structures that feature P–P dimers [64]. Transition

metal phosphides have garnered significant attention as effective catalysts for hydrodesulfurization and hydrogen production via the water-gas shift reaction. In 2005, Rodriguez et al. were the first to discover that Ni_2P (001) exhibited behavior in the hydrogen evolution reaction (HER) similar to NiFe hydrogenases. Based on density functional theory (DFT) calculations, they predicted that Ni_2P would be an excellent catalyst for HER. The remarkable activity of Ni_2P (001) in HER was attributed to an ensemble effect, where the introduction of phosphorus reduced the concentration of nickel, leading to moderate bonding with reaction intermediates and thereby enhancing the HER process. Following this, the first experimental study on nanostructured Ni_2P for HER performance was conducted, revealing that hollow Ni_2P nanoparticles demonstrated exceptional HER activity, consistent with theoretical predictions [30], [65]. Under alkaline HER conditions, the surface of transition metal-rich phosphides changes due to the generation of dissolved polyphosphate species and the reduction of oxidized phosphorus and metal species. In contrast, under alkaline OER conditions, the surface transforms into corresponding (ox)hydroxides or oxides with minimal phosphate residue due to strong oxidation and dissolution processes. Despite these surface restructurings, phosphide-based catalysts maintain their catalytic activity, as the bulk phosphide continues to contribute to the process [66]. Additionally, it has been reported that TMPs enhance water dissociation during the alkaline HER process by weakening the H–OH bond, with the metal center bonding to oxygen and phosphorus bonding to hydrogen. Beyond their excellent HER performance, recent studies have also shown that TMPs exhibit strong OER activity in alkaline solutions [67]. This is due to the rapid formation of NiOOH on the electrode surface during OER. Based on these findings, TMPs undergo structural reconstruction at the interface and can oxidize into corresponding oxides or hydroxides, which serve as active sites for OER, as demonstrated by

in situ and ex situ characterizations. This makes TMPs effective as bifunctional catalysts for overall water splitting, simplifying the design of water-splitting devices and reducing costs. This potential has sparked extensive research into the development of TMP-based bifunctional catalysts [68]. Sun's group made significant contributions to advancing TMPs for water splitting applications. They reported a variety of transition metal-based phosphides, including Ni, Co, Fe, Mo, and W, with different morphologies such as nanowires, nanosheets, nanorods, and nanoparticles. These materials were synthesized through a low-temperature topological transformation process starting from transition metal oxides or hydroxides as precursors [69], [70], [71].

2.2.3 High Entropy Alloys

In recent years, high entropy alloys (HEAs) have gained significant attention [72] due to their exceptional properties, including corrosion resistance [73], high hardness [74], wear resistance [75], and creep resistance[76]. Notably, recent studies have shown that HEAs also possess remarkable catalytic activity, driven by their four core effects: high entropy in thermodynamics [18], lattice distortion in structure, sluggish diffusion in dynamics, and the cocktail effect. Due to their large mixing entropy, HEAs tend to form simple face-centered cubic (FCC) or body-centered cubic (BCC) phases and can even exhibit amorphous states in some cases. In most HEAs, the elemental content of each component is nearly equal in molar proportion, allowing for easy regulation of alloy composition to maximize catalytic activity while maintaining stability. Additionally, HEAs can be tailored for various complex environments by introducing different elements. The synergistic effect between multiple components in multi-element catalysts has been proven to significantly enhance catalytic efficiency. Furthermore, porous nanostructures in HEAs provide higher surface areas, and nanoporous HEAs have shown

great potential as electrocatalysts, with excellent catalytic performance and stability. The current methods for producing HEAs are mostly limited to physical techniques. Recently, electrodeposition has been explored as a promising alternative for producing nanomaterials and alloys, offering advantages like strong adhesion, high density, and considerable potential for industrial application. Still, the challenge lies in the varying degrees of ion attraction, making it necessary to select appropriate complexing agents, adjust metal ion concentrations, and optimize electrodeposition parameters to achieve high-quality alloy coatings [77].

2.3 Morphology of Electrocatalysts

One route to decrease the production costs of hydrogen involves scaling up low-cost renewable electricity availability, increasing power output from renewable sources and boosting electrolyzer efficiency through advanced material usage. Besides the composition, an important aspect of improving water-splitting activity is nanostructure (e.g., nanoparticles, nanowires or nanoplates) in which a catalyst can expose more active surface. For example, nanostructured electrodes have shown excellent electrocatalytic activity as proven in many other studies of a variety of additional electrochemical systems; such as: batteries [15], [16], [17], [18], supercapacitors [82], [83], [84], [85], sensors [86], [87], fuel cells [88], [89], and solar cells [90]. These are a useful property of nanomaterials [91], [92] which have an extraordinarily large proportion of surface available for catalysis relative to conventional geometries and therefore many active sites for reactions [93], [94], [95], [96]. To improve the activity of Ni species, some methods have been devoted to increasing surface area, reducing particle size, regulating morphology and promoting surface roughness [61]. Nanostructures offer a larger surface area that is highly beneficial for electrocatalysis, and due to this porous nature of nanomaterials more current density can be provided at the same overpotential

since nanoarchitecture enhance electrolyte accessibility to active sites. At least of the two-to-three dimensions in their crystal structure is within the range 1–100 nanometers (nm) with optimized properties. In addition to the zero-dimensional (0D) and two-dimensional (2D) nanostructures including nanoparticles (NPs) and nanosheets, respectively: an ultimate definition of one-dimensional (1D) materials brings a variety of novel properties at play that can be controlled along defect-engineering strategies via utilization as metal-based platforms for strong basis both in facilitating or realizing different applications related with their specific setting architecture [97]. The main aspects are tied on the structure formation policy. Standardized behaviour is quite unfavoured when mentioning size limited structures. 1D nanostructures present special structural features that bring about unique processes in catalytic reactions. The following **figure 2.3** summarizes the advantages of alloys and 1D materials.

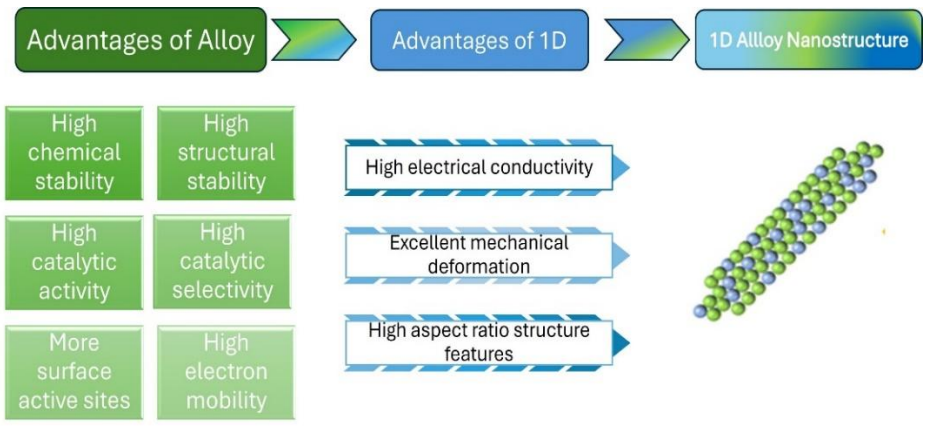

Fig. 2.3 *Schematics illustrating the advantages of 1D metal alloy nanostructures*

Among the different 1D nanostructures, nanowires have attracted much attention. The unique structural properties of nanowires offer several advantages in catalytic reactions, as discussed in various recent reviews. First, the high aspect ratio of nanowires results in substantial surface areas, providing many active sites for electrochemical reactions. While the surface area of nanowires may be smaller than that of nanoparticles of equivalent volume and diameter, they often have more accessible surface area during electrochemical processes because nanoparticles are more prone to aggregation during catalyst loading and cycling. This leads to a second benefit of nanowires: they typically exhibit greater structural stability, being more resistant to dissolution, aggregation, which enhances their durability in catalytic reactions. As reported by Darband et al. [98], the specific morphology of nanostructures reduces the reaction potential, partly due to the super aero-phobic nature of nanowire (NW) surfaces, which facilitates rapid gas bubble detachment, thereby increasing the availability of active catalytic sites [99], [100].

Metal alloy nanowires, which combine the advantages of 1D nanostructures and alloy materials, present themselves as promising candidates for electrocatalysts. On one hand, these materials benefit from the structural characteristics of 1D nanostructures, offering a substantial number of active surface sites, improved structural stability, and high electron mobility during electrochemical processes. Nanowire synthesis can be achieved through either templating techniques or self-assembly processes. A schematic illustration of some of the methods used to produce nanowires is shown in **Figure 2.4**. Tubular hard templates, combined with deposition methods, can be used to create 1D nanostructures. In solution-based methods, one or more structure-directing agents, are often required to promote 1D growth of metal nanostructures. Some of these agents are believed to form micellar structures

that guide linear metal growth, though in certain cases, the precise mechanisms behind this 1D growth remain incompletely understood. In templating methods, the primary challenge for successful co-precipitation is overcoming the differences in the reduction potentials of various metal precursors. Direct synthesis of metal alloy nanowires usually follows similar mechanisms that form pristine metal nanowires, but with simultaneous co-precipitation of all alloy compositions [101].

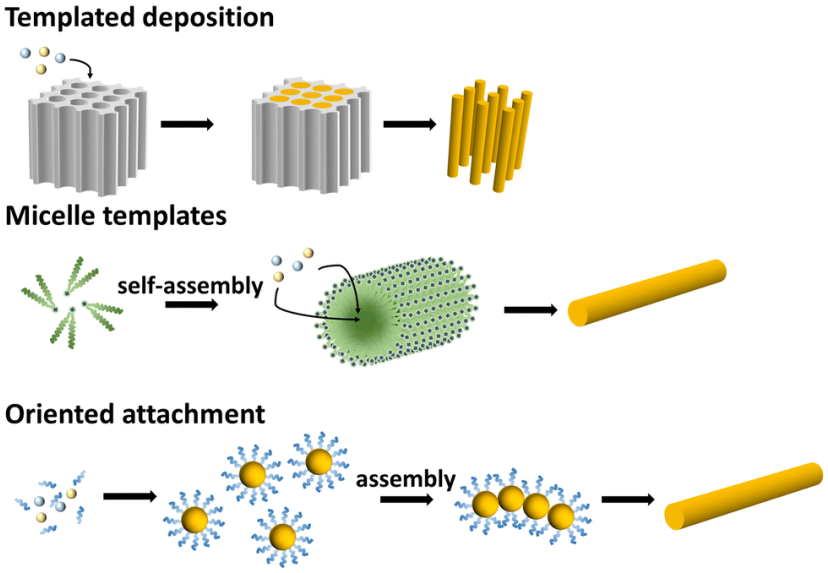

Fig. 2.4 *Schematics illustrating the formation mechanisms that form the metal alloy nanowires directly with chemical methods* [101].

Moreover, surface wettability is closely linked to surface roughness; by creating a micro-nanostructure on a flat surface, the wetting state can shift from hydrophilic (or hydrophobic) to superhydrophilic (or superhydrophobic) [102]. Consequently, novel three-dimensional (3D) porous metallic materials with high specific surface areas and open-pore hierarchical structures have

garnered significant interest due to their ability to reduce ion diffusion lengths, thereby improving both ionic and electronic conductivity. To date, various substrates such as metal foams, meshes, foils, and fabrics have been explored as current collectors for electrochemical applications, including lithium-ion batteries, supercapacitors, solar cells, and, most notably, water splitting. As a result, a promising future direction in electrocatalyst design is the integration of different structural dimensionalities to create nanostructured catalyst–support composites. These composites would offer enhanced conductivity, a larger surface area, and greater stability, making them ideal for advanced catalytic applications. **Nickel foam**, in particular, offers a low-cost, conductive metal framework with a large electroactive surface area, making it an excellent substrate for catalyst loading and enhancing the availability of active sites [103]. For example, the electrodeposition of some iron group metals on nickel foam was investigated and their performances as bifunctional catalysts for both HER and OER reactions were evaluated by Zhao et al. [104]. Additionally, the microholes and zigzag flow channels within nickel foams (NFs) provide excellent mass transport and a high surface area per unit, making them highly efficient. While nickel foam is widely used in supercapacitor and battery electrodes, studies have shown that electrode materials deposited on NF demonstrate superior OER activity compared to those deposited on nickel foil or mesh [105]. **Figure 2.5** shows, by SEM images, how the surface morphology of NF changes after the deposition of the catalyst **(a)** and the mechanism of the catalyst towards OER/HER.

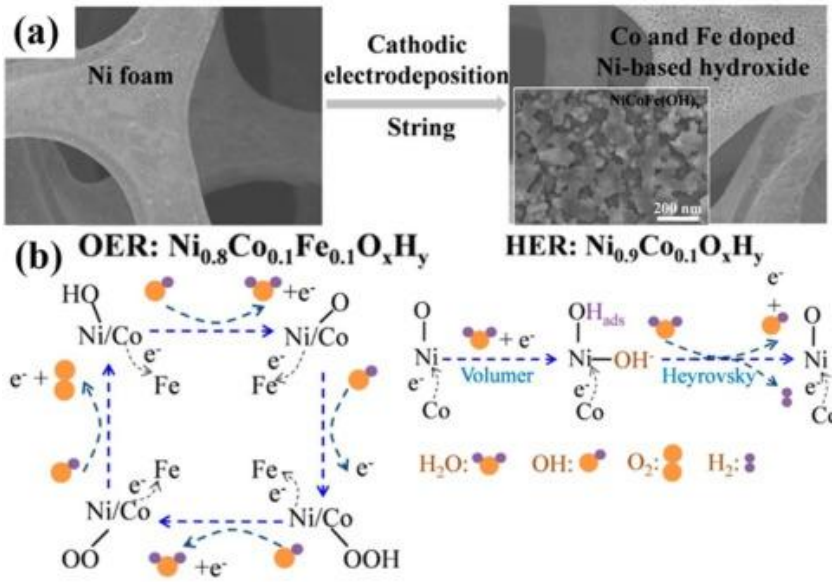

Fig*.2.5 *A*)** *The synthesis scheme and SEM images of NiCoFeOxHy.* ***(B) *Schematic diagram of the reaction mechanism of the catalyst HER and OER* [104]

References

[1] Y. Liu *et al.*, «Research Progress of Oxygen Evolution Reaction Catalysts for Electrochemical Water Splitting», *ChemSusChem*, vol. 14, fasc. 24, pp. 5359–5383, dic. 2021, doi: 10.1002/cssc.202101898.

[2] K. Zeng e D. Zhang, «Recent progress in alkaline water electrolysis for hydrogen production and applications», *Progress in Energy and Combustion Science*, vol. 36, fasc. 3, pp. 307–326, giu. 2010, doi: 10.1016/j.pecs.2009.11.002.

[3] N. Danilovic, R. Subbaraman, D. Strmcnik, V. Stamenkovic, e N. Markovic, «Electrocatalysis of the HER in acid and alkaline media», *J Serb Chem Soc*, vol. 78, fasc. 12, pp. 2007–2015, 2013, doi: 10.2298/JSC131118136D.

[4] M. D. Merrill e R. C. Dougherty, «Metal Oxide Catalysts for the Evolution of O 2 from H 2 O», *J. Phys. Chem. C*, vol. 112, fasc. 10, pp. 3655–3666, mar. 2008, doi: 10.1021/jp710675m.

[5] E. López-Fernández, J. Gil-Rostra, J. P. Espinós, A. R. González-Elipe, A. De Lucas Consuegra, e F. Yubero, «Chemistry and Electrocatalytic Activity of Nanostructured Nickel Electrodes for Water Electrolysis», *ACS Catal.*, vol. 10, fasc. 11, pp. 6159–6170, giu. 2020, doi: 10.1021/acscatal.0c00856.

[6] Y. Peng *et al.*, «Recent Advances Regarding Precious Metal-Based Electrocatalysts for Acidic Water Splitting», *Nanomaterials*, vol. 12, fasc. 15, p. 2618, lug. 2022, doi: 10.3390/nano12152618.

[7] D. M. F. Santos, C. A. C. Sequeira, e J. L. Figueiredo, «Hydrogen production by alkaline water electrolysis», *Quím. Nova*, vol. 36, fasc. 8, pp. 1176–1193, 2013, doi: 10.1590/S0100-40422013000800017.

[8] P. M. Bodhankar, P. B. Sarawade, G. Singh, A. Vinu, e D. S. Dhawale, «Recent advances in highly active nanostructured NiFe LDH catalyst for electrochemical water splitting», *J. Mater. Chem. A*, vol. 9, fasc. 6, pp. 3180–3208, 2021, doi: 10.1039/D0TA10712C.

[9] G. Maduraiveeran, M. Sasidharan, e W. Jin, «Earth-abundant transition metal and metal oxide nanomaterials: Synthesis and electrochemical applications», *Progress in Materials Science*, vol. 106, p. 100574, dic. 2019, doi: 10.1016/j.pmatsci.2019.100574.

[10] K. Su *et al.*, «Three-Dimensional Nickel Cobalt Phosphide Nanocrosses with Well-Defined Axial Arms for Efficient Oxygen Evolution Reaction», *Chemistry A European J*, vol. 29, fasc. 32, p. e202300398, giu. 2023, doi: 10.1002/chem.202300398.

[11] L. Bruno, M. Scuderi, F. Priolo, L. Falciola, e S. Mirabella, «Enlightening the bimetallic effect of Au@Pd nanoparticles on Ni oxide nanostructures with enhanced catalytic activity», *Sci Rep*, vol. 13, fasc. 1, p. 3203, feb. 2023, doi: 10.1038/s41598-023-29679-6.

[12] Y. Wei *et al.*, «CoC $_2$ O $_4$ ·2H $_2$ O derived Co $_3$ O $_4$ nanorods array: a high-efficiency 1D electrocatalyst for alkaline oxygen evolution reaction», *Chem. Commun.*, vol. 54, fasc. 12, pp. 1533–1536, 2018, doi: 10.1039/C7CC08423D.

[13] S. Chandrasekaran *et al.*, «Electronic structure engineering on two-dimensional (2D) electrocatalytic materials for oxygen reduction, oxygen evolution, and hydrogen evolution reactions», *Nano Energy*, vol. 77, p. 105080, nov. 2020, doi: 10.1016/j.nanoen.2020.105080.

[14] Y. Yan *et al.*, «Construction of Efficient 3D Gas Evolution Electrocatalyst for Hydrogen Evolution: Porous FeP Nanowire Arrays on Graphene Sheets», *Adv. Sci.*, vol. 2, fasc. 8, Art. fasc. 8, ago. 2015, doi: 10.1002/advs.201500120.

[15] Z. Wu *et al.*, «Morphology effects on electrocatalysis of anodic water splitting on nickel (II) oxide», *Microporous and Mesoporous Materials*, vol. 333, p. 111734, mar. 2022, doi: 10.1016/j.micromeso.2022.111734.

[16] J. D. Benck, T. R. Hellstern, J. Kibsgaard, P. Chakthranont, e T. F. Jaramillo, «Catalyzing the Hydrogen Evolution Reaction (HER) with Molybdenum Sulfide Nanomaterials», *ACS Catal.*, vol. 4, fasc. 11, pp. 3957–3971, nov. 2014, doi: 10.1021/cs500923c.

[17] Z. W. Seh, J. Kibsgaard, C. F. Dickens, I. Chorkendorff, J. K. Nørskov, e T. F. Jaramillo, «Combining theory and experiment in electrocatalysis: Insights into materials design», *Science*, vol. 355, fasc. 6321, p. eaad4998, gen. 2017, doi: 10.1126/science.aad4998.

[18] K. Wang *et al.*, «Wrinkled Rh $_2$ P Nanosheets as Superior pH-Universal Electrocatalysts for Hydrogen Evolution Catalysis», *Advanced Energy Materials*, vol. 8, fasc. 27, p. 1801891, set. 2018, doi: 10.1002/aenm.201801891.

[19] E. Fabbri, A. Habereder, K. Waltar, R. Kötz, e T. J. Schmidt, «Developments and perspectives of oxide-based catalysts for the oxygen evolution reaction», *Catal. Sci. Technol.*, vol. 4, fasc. 11, pp. 3800–3821, 2014, doi: 10.1039/C4CY00669K.

[20] Z. Huang, J. Wang, Y. Peng, C. Jung, A. Fisher, e X. Wang, «Design of Efficient Bifunctional Oxygen Reduction/Evolution Electrocatalyst: Recent Advances and Perspectives», *Advanced Energy Materials*, vol. 7, fasc. 23, Art. fasc. 23, dic. 2017, doi: 10.1002/aenm.201700544.

[21] N. Mahmood, Y. Yao, J. Zhang, L. Pan, X. Zhang, e J. Zou, «Electrocatalysts for Hydrogen Evolution in Alkaline Electrolytes: Mechanisms, Challenges, and Prospective Solutions», *Advanced Science*, vol. 5, fasc. 2, p. 1700464, feb. 2018, doi: 10.1002/advs.201700464.

[22] L. Huang *et al.*, «Pt/Fe-NF electrode with high double-layer capacitance for efficient hydrogen evolution reaction in alkaline

media», *International Journal of Hydrogen Energy*, vol. 42, fasc. 15, pp. 9458–9466, apr. 2017, doi: 10.1016/j.ijhydene.2017.02.055.

[23] A. Oh *et al.*, «Rational design of Pt–Ni–Co ternary alloy nanoframe crystals as highly efficient catalysts toward the alkaline hydrogen evolution reaction», *Nanoscale*, vol. 8, fasc. 36, pp. 16379–16386, 2016, doi: 10.1039/C6NR04572C.

[24] R. Subbaraman *et al.*, «Enhancing Hydrogen Evolution Activity in Water Splitting by Tailoring Li^+-$Ni(OH)_2$-Pt Interfaces», *Science*, vol. 334, fasc. 6060, Art. fasc. 6060, dic. 2011, doi: 10.1126/science.1211934.

[25] J. Mahmood *et al.*, «An efficient and pH-universal ruthenium-based catalyst for the hydrogen evolution reaction», *Nature Nanotech*, vol. 12, fasc. 5, Art. fasc. 5, mag. 2017, doi: 10.1038/nnano.2016.304.

[26] C. Tan *et al.*, «Preparation of High-Percentage 1T-Phase Transition Metal Dichalcogenide Nanodots for Electrochemical Hydrogen Evolution», *Advanced Materials*, vol. 30, fasc. 9, p. 1705509, mar. 2018, doi: 10.1002/adma.201705509.

[27] N. Yabuuchi, K. Kubota, M. Dahbi, e S. Komaba, «Research Development on Sodium-Ion Batteries», *Chem. Rev.*, vol. 114, fasc. 23, pp. 11636–11682, dic. 2014, doi: 10.1021/cr500192f.

[28] M. Gong, D.-Y. Wang, C.-C. Chen, B.-J. Hwang, e H. Dai, «A mini review on nickel-based electrocatalysts for alkaline hydrogen evolution reaction», *Nano Res.*, vol. 9, fasc. 1, pp. 28–46, gen. 2016, doi: 10.1007/s12274-015-0965-x.

[29] B. Hinnemann *et al.*, «Biomimetic Hydrogen Evolution: MoS_2 Nanoparticles as Catalyst for Hydrogen Evolution», *J. Am. Chem. Soc.*, vol. 127, fasc. 15, pp. 5308–5309, apr. 2005, doi: 10.1021/ja0504690.

[30] P. Liu e J. A. Rodriguez, «Catalysts for Hydrogen Evolution from the [NiFe] Hydrogenase to the Ni_2P(001) Surface: The Importance of Ensemble Effect», *J. Am. Chem. Soc.*, vol. 127, fasc. 42, pp. 14871–14878, ott. 2005, doi: 10.1021/ja0540019.

[31] M. Gong e H. Dai, «A mini review of NiFe-based materials as highly active oxygen evolution reaction electrocatalysts», *Nano Res.*, vol. 8, fasc. 1, pp. 23–39, gen. 2015, doi: 10.1007/s12274-014-0591-z.

[32] Y. Zhu, T. Liu, L. Li, S. Song, e R. Ding, «Nickel-based electrodes as catalysts for hydrogen evolution reaction in alkaline media», *Ionics*, vol. 24, fasc. 4, pp. 1121–1127, apr. 2018, doi: 10.1007/s11581-017-2270-z.

[33] L. Angely, G. Bronoel, e G. Peslerbe, «Relation between nickel crystalline structures and their electrocatalytic properties», *Journal of Electroanalytical Chemistry and Interfacial Electrochemistry*, vol. 96, fasc. 2, pp. 203–208, feb. 1979, doi: 10.1016/S0022-0728(79)80377-0.

[34] C. Wei *et al.*, «Surface Composition Dependent Ligand Effect in Tuning the Activity of Nickel–Copper Bimetallic Electrocatalysts toward Hydrogen Evolution in Alkaline», *J. Am. Chem. Soc.*, vol. 142, fasc. 17, pp. 7765–7775, apr. 2020, doi: 10.1021/jacs.9b12005.

[35] G. Zhao, K. Rui, S. X. Dou, e W. Sun, «Heterostructures for Electrochemical Hydrogen Evolution Reaction: A Review», *Adv. Funct. Mater.*, vol. 28, fasc. 43, p. 1803291, ott. 2018, doi: 10.1002/adfm.201803291.

[36] J. Luo *et al.*, «Water photolysis at 12.3% efficiency via perovskite photovoltaics and Earth-abundant catalysts», *Science*, vol. 345, fasc. 6204, pp. 1593–1596, set. 2014, doi: 10.1126/science.1258307.

[37] S. Anantharaj, J. Kennedy, e S. Kundu, «Microwave-Initiated Facile Formation of Ni $_3$ Se $_4$ Nanoassemblies for Enhanced and Stable Water Splitting in Neutral and Alkaline Media», *ACS Appl. Mater. Interfaces*, vol. 9, fasc. 10, pp. 8714–8728, mar. 2017, doi: 10.1021/acsami.6b15980.

[38] X. Bai *et al.*, «In-situ structure reconstitution of NiCo2P for enhanced electrochemical water oxidation», *Science Bulletin*, vol. 62, fasc. 22, pp. 1510–1518, nov. 2017, doi: 10.1016/j.scib.2017.10.019.

[39] F. Yan *et al.*, «Highly Stable Three-Dimensional Porous Nickel-Iron Nitride Nanosheets for Full Water Splitting at High Current Densities», *Chemistry A European J*, vol. 23, fasc. 42, pp. 10187–10194, lug. 2017, doi: 10.1002/chem.201701662.

[40] X. Yang *et al.*, «CoP nanosheet assembly grown on carbon cloth: A highly efficient electrocatalyst for hydrogen generation», *Nano Energy*, vol. 15, pp. 634–641, lug. 2015, doi: 10.1016/j.nanoen.2015.05.026.

[41] T. Wu, M. Pi, X. Wang, D. Zhang, e S. Chen, «Three-dimensional metal–organic framework derived porous CoP $_3$ concave polyhedrons as superior bifunctional electrocatalysts for the evolution of hydrogen and oxygen», *Phys. Chem. Chem. Phys.*, vol. 19, fasc. 3, pp. 2104–2110, 2017, doi: 10.1039/C6CP07294A.

[42] Y. Huang *et al.*, «Mo $_2$ C Nanoparticles Dispersed on Hierarchical Carbon Microflowers for Efficient Electrocatalytic Hydrogen Evolution», *ACS Nano*, vol. 10, fasc. 12, pp. 11337–11343, dic. 2016, doi: 10.1021/acsnano.6b06580.

[43] Z. Xing, X. Yang, A. M. Asiri, e X. Sun, «Three-Dimensional Structures of MoS $_2$ @Ni Core/Shell Nanosheets Array toward Synergetic Electrocatalytic Water Splitting», *ACS Appl. Mater. Interfaces*, vol. 8, fasc. 23, pp. 14521–14526, giu. 2016, doi: 10.1021/acsami.6b02331.

[44] X. Li *et al.*, «Exceptional oxygen evolution reactivities on CaCoO $_3$ and SrCoO $_3$», *Sci. Adv.*, vol. 5, fasc. 8, p. eaav6262, ago. 2019, doi: 10.1126/sciadv.aav6262.

[45] Z. Wu, L. Huang, H. Liu, M. Li, e H. Wang, «Erratum to: Surface oxidation of transition metal sulfide and phosphide nanomaterials», *Nano Res.*, vol. 14, fasc. 7, pp. 2463–2463, lug. 2021, doi: 10.1007/s12274-021-3296-0.

[46] Z. Wu, Q. Gan, X. Li, Y. Zhong, e H. Wang, «Elucidating Surface Restructuring-Induced Catalytic Reactivity of Cobalt Phosphide Nanoparticles under Electrochemical Conditions», *J. Phys. Chem. C*, vol. 122, fasc. 5, pp. 2848–2853, feb. 2018, doi: 10.1021/acs.jpcc.7b11843.

[47] T. F. Jaramillo, K. P. Jørgensen, J. Bonde, J. H. Nielsen, S. Horch, e I. Chorkendorff, «Identification of Active Edge Sites for Electrochemical H $_2$ Evolution from MoS $_2$ Nanocatalysts», *Science*, vol. 317, fasc. 5834, pp. 100–102, lug. 2007, doi: 10.1126/science.1141483.

[48] D. J. Ham e J. S. Lee, «Transition Metal Carbides and Nitrides as Electrode Materials for Low Temperature Fuel Cells», *Energies*, vol. 2, fasc. 4, pp. 873–899, ott. 2009, doi: 10.3390/en20400873.

[49] J. Van Wonterghem, S. Mørup, C. J. W. Koch, S. W. Charles, e S. Wells, «Formation of ultra-fine amorphous alloy particles by reduction in aqueous solution», *Nature*, vol. 322, fasc. 6080, pp. 622–623, ago. 1986, doi: 10.1038/322622a0.

[50] H. Wang *et al.*, «Recent advances in NiFe layered double hydroxide electrocatalysts for seawater oxidation», *Journal of Alloys and Compounds*, vol. 1002, p. 175368, ott. 2024, doi: 10.1016/j.jallcom.2024.175368.

[51] H. Wang *et al.*, «Template-free solvothermal preparation of ternary FeNi $_2$ S $_4$ hollow balloons as RuO $_2$ -like efficient electrocatalysts for the oxygen evolution reaction with superior stability», *J. Mater. Chem. A*, vol. 6, fasc. 40, pp. 19417–19424, 2018, doi: 10.1039/C8TA06051G.

[52] R. Xiang *et al.*, «Hierarchical coral-like FeNi(OH) /Ni via mild corrosion of nickel as an integrated electrode for efficient overall water splitting», *Chinese Journal of Catalysis*, vol. 39, fasc. 11, pp. 1736–1745, nov. 2018, doi: 10.1016/S1872-2067(18)63150-X.

[53] M. Zeng e Y. Li, «Recent advances in heterogeneous electrocatalysts for the hydrogen evolution reaction», *J. Mater. Chem. A*, vol. 3, fasc. 29, pp. 14942–14962, 2015, doi: 10.1039/C5TA02974K.

[54] D. Lim, E. Oh, C. Lim, S. E. Shim, e S.-H. Baeck, «Bimetallic NiFe alloys as highly efficient electrocatalysts for the oxygen evolution reaction», *Catalysis Today*, vol. 352, pp. 27–33, ago. 2020, doi: 10.1016/j.cattod.2019.09.046.

[55] B. J. Trześniewski *et al.*, «In Situ Observation of Active Oxygen Species in Fe-Containing Ni-Based Oxygen Evolution Catalysts: The

Effect of pH on Electrochemical Activity», *J. Am. Chem. Soc.*, vol. 137, fasc. 48, pp. 15112–15121, dic. 2015, doi: 10.1021/jacs.5b06814.
[56] D. A. Corrigan, «The Catalysis of the Oxygen Evolution Reaction by Iron Impurities in Thin Film Nickel Oxide Electrodes», *J. Electrochem. Soc.*, vol. 134, fasc. 2, pp. 377–384, feb. 1987, doi: 10.1149/1.2100463.
[57] S. Duan *et al.*, «Hydrochloric acid corrosion induced bifunctional free-standing NiFe hydroxide nanosheets towards high-performance alkaline seawater splitting», *Nanoscale*, vol. 12, fasc. 42, pp. 21743–21749, 2020, doi: 10.1039/D0NR05458E.
[58] K. Jiang *et al.*, «NiFe Layered Double Hydroxide/FeOOH Heterostructure Nanosheets as an Efficient and Durable Bifunctional Electrocatalyst for Overall Seawater Splitting», *Inorg. Chem.*, vol. 60, fasc. 22, pp. 17371–17378, nov. 2021, doi: 10.1021/acs.inorgchem.1c02903.
[59] G. Liu, Y. Xu, T. Yang, e L. Jiang, «Recent advances in electrocatalysts for seawater splitting», *Nano Materials Science*, vol. 5, fasc. 1, pp. 101–116, mar. 2023, doi: 10.1016/j.nanoms.2020.12.003.
[60] S. Jiang *et al.*, «Recent Advances in Seawater Electrolysis», *Catalysts*, vol. 12, fasc. 2, p. 123, gen. 2022, doi: 10.3390/catal12020123.
[61] R. A. Mir, D. W. Kirk, e S. J. Thorpe, «Recent progress and advances in nickel (Ni) based amorphous metal alloys towards alkaline water splitting: A review», *Journal of Alloys and Compounds*, vol. 976, p. 173211, mar. 2024, doi: 10.1016/j.jallcom.2023.173211.
[62] X. Zou e Y. Zhang, «Noble metal-free hydrogen evolution catalysts for water splitting», *Chem. Soc. Rev.*, vol. 44, fasc. 15, pp. 5148–5180, 2015, doi: 10.1039/C4CS00448E.
[63] Y. Shi e B. Zhang, «Recent advances in transition metal phosphide nanomaterials: synthesis and applications in hydrogen evolution reaction», *Chem. Soc. Rev.*, vol. 45, fasc. 6, pp. 1529–1541, 2016, doi: 10.1039/C5CS00434A.
[64] A. Ray, S. Sultana, L. Paramanik, e K. M. Parida, «Recent advances in phase, size, and morphology-oriented nanostructured nickel phosphide for overall water splitting», *J. Mater. Chem. A*, vol. 8, fasc. 37, Art. fasc. 37, 2020, doi: 10.1039/D0TA05797E.
[65] E. J. Popczun *et al.*, «Nanostructured Nickel Phosphide as an Electrocatalyst for the Hydrogen Evolution Reaction», *J. Am. Chem. Soc.*, vol. 135, fasc. 25, pp. 9267–9270, giu. 2013, doi: 10.1021/ja403440e.
[66] R. Beltrán-Suito, P. W. Menezes, e M. Driess, «Amorphous outperforms crystalline nanomaterials: surface modifications of molecularly derived CoP electro(pre)catalysts for efficient water-

splitting», *J. Mater. Chem. A*, vol. 7, fasc. 26, pp. 15749–15756, 2019, doi: 10.1039/C9TA04583J.

[67] L.-A. Stern, L. Feng, F. Song, e X. Hu, «Ni $_2$ P as a Janus catalyst for water splitting: the oxygen evolution activity of Ni $_2$ P nanoparticles», *Energy Environ. Sci.*, vol. 8, fasc. 8, pp. 2347–2351, 2015, doi: 10.1039/C5EE01155H.

[68] S. Jin, «Are Metal Chalcogenides, Nitrides, and Phosphides Oxygen Evolution Catalysts or Bifunctional Catalysts?», *ACS Energy Lett.*, vol. 2, fasc. 8, pp. 1937–1938, ago. 2017, doi: 10.1021/acsenergylett.7b00679.

[69] J. Tian, Q. Liu, A. M. Asiri, e X. Sun, «Self-Supported Nanoporous Cobalt Phosphide Nanowire Arrays: An Efficient 3D Hydrogen-Evolving Cathode over the Wide Range of pH 0–14», *J. Am. Chem. Soc.*, vol. 136, fasc. 21, pp. 7587–7590, mag. 2014, doi: 10.1021/ja503372r.

[70] J. Tian, Q. Liu, N. Cheng, A. M. Asiri, e X. Sun, «Self-Supported Cu $_3$ P Nanowire Arrays as an Integrated High-Performance Three-Dimensional Cathode for Generating Hydrogen from Water», *Angewandte Chemie*, vol. 126, fasc. 36, pp. 9731–9735, set. 2014, doi: 10.1002/ange.201403842.

[71] Z. Xing, Q. Liu, A. M. Asiri, e X. Sun, «High-Efficiency Electrochemical Hydrogen Evolution Catalyzed by Tungsten Phosphide Submicroparticles», *ACS Catal.*, vol. 5, fasc. 1, pp. 145–149, gen. 2015, doi: 10.1021/cs5014943.

[72] H. Kamaruddin, Z. Jianghong, L. Yu, W. Yuefan, e H. Yizhong, «A review of noble metal-free high entropy alloys for water splitting applications», *J. Mater. Chem. A*, vol. 12, fasc. 17, pp. 9933–9961, 2024, doi: 10.1039/D4TA00690A.

[73] A. Aliyu e C. Srivastava, «Phase constitution, surface chemistry and corrosion behavior of electrodeposited MnFeCoNiCu high entropy alloy-graphene oxide composite coatings», *Surface and Coatings Technology*, vol. 429, p. 127943, gen. 2022, doi: 10.1016/j.surfcoat.2021.127943.

[74] L.-A. Chen, Y.-S. Lu, Y.-T. Lin, e Y.-L. Lee, «Preparation and characterization of cerium-based conversion coating on a Fe50Mn30Co10Cr10 dual-phase high-entropy alloy», *Applied Surface Science*, vol. 562, p. 150200, ott. 2021, doi: 10.1016/j.apsusc.2021.150200.

[75] P. Gao *et al.*, «Influence of Plasma Arc Current on the Friction and Wear Properties of CoCrFeNiMn High Entropy Alloy Coatings Prepared on CGI through Plasma Transfer Arc Cladding», *Coatings*, vol. 12, fasc. 5, p. 633, mag. 2022, doi: 10.3390/coatings12050633.

[76] C. Nagarjuna *et al.*, «Strengthening the mechanical properties and wear resistance of CoCrFeMnNi high entropy alloy fabricated by powder metallurgy», *Advanced Powder Technology*, vol. 33, fasc. 4, p. 103519, apr. 2022, doi: 10.1016/j.apt.2022.103519.
[77] H. Bian *et al.*, «Facile electrodeposition synthesis and super performance of nano-porous Ni-Fe-Cu-Co-W high entropy alloy electrocatalyst», *Surface and Coatings Technology*, vol. 459, p. 129407, apr. 2023, doi: 10.1016/j.surfcoat.2023.129407.
[78] L. Silipigni *et al.*, «Template Electrochemical Growth and Properties of Mo Oxide Nanostructures», *J. Phys. Chem. C*, vol. 118, fasc. 38, pp. 22299–22308, set. 2014, doi: 10.1021/jp505819j.
[79] P. G. Bruce, B. Scrosati, e J. Tarascon, «Nanomaterials for Rechargeable Lithium Batteries», *Angew Chem Int Ed*, vol. 47, fasc. 16, pp. 2930–2946, apr. 2008, doi: 10.1002/anie.200702505.
[80] R. Inguanta, E. Rinaldo, S. Piazza, e C. Sunseri, «Lead Nanowires for Microaccumulators Obtained Through Indirect Electrochemical Template Deposition», *Electrochem. Solid-State Lett.*, vol. 13, fasc. 1, p. K1, 2010, doi: 10.1149/1.3246944.
[81] M. G. Insinga, R. L. Oliveri, C. Sunseri, e R. Inguanta, «Template electrodeposition and characterization of nanostructured Pb as a negative electrode for lead-acid battery», *Journal of Power Sources*, vol. 413, pp. 107–116, feb. 2019, doi: 10.1016/j.jpowsour.2018.12.033.
[82] G. Mineo, M. Scuderi, G. Pezzotti Escobar, S. Mirabella, e E. Bruno, «Engineering of Nanostructured WO3 Powders for Asymmetric Supercapacitors», *Nanomaterials*, vol. 12, fasc. 23, p. 4168, nov. 2022, doi: 10.3390/nano12234168.
[83] M. Urso, F. Priolo, e S. Mirabella, «Investigating the charge-discharge behaviour of Ni(OH)2 nanowalls», *Applied Surface Science*, vol. 534, p. 147585, dic. 2020, doi: 10.1016/j.apsusc.2020.147585.
[84] P. Perret, Z. Khani, T. Brousse, D. Bélanger, e D. Guay, «Carbon/PbO2 asymmetric electrochemical capacitor based on methanesulfonic acid electrolyte», *Electrochimica Acta*, vol. 56, fasc. 24, pp. 8122–8128, ott. 2011, doi: 10.1016/j.electacta.2011.05.125.
[85] P. G. Perret, P. R. L. Malenfant, C. Bock, e B. MacDougall, «Electro-Deposition and Dissolution of MnO_2 on a Graphene Composite Electrode for Its Utilization in an Aqueous Based Hybrid Supercapacitor», *J. Electrochem. Soc.*, vol. 159, fasc. 9, pp. A1554–A1561, 2012, doi: 10.1149/2.064208jes.
[86] X. Qu, P. J. J. Alvarez, e Q. Li, «Applications of nanotechnology in water and wastewater treatment», *Water Research*, vol. 47, fasc. 12, pp. 3931–3946, ago. 2013, doi: 10.1016/j.watres.2012.09.058.

[87] C. Zhu, G. Yang, H. Li, D. Du, e Y. Lin, «Electrochemical Sensors and Biosensors Based on Nanomaterials and Nanostructures», *Anal. Chem.*, vol. 87, fasc. 1, pp. 230–249, gen. 2015, doi: 10.1021/ac5039863.

[88] W. Xia, A. Mahmood, Z. Liang, R. Zou, e S. Guo, «Earth-Abundant Nanomaterials for Oxygen Reduction», *Angew Chem Int Ed*, vol. 55, fasc. 8, pp. 2650–2676, feb. 2016, doi: 10.1002/anie.201504830.

[89] C. Zhu, H. Li, S. Fu, D. Du, e Y. Lin, «Highly efficient nonprecious metal catalysts towards oxygen reduction reaction based on three-dimensional porous carbon nanostructures», *Chem. Soc. Rev.*, vol. 45, fasc. 3, pp. 517–531, 2016, doi: 10.1039/C5CS00670H.

[90] R. Inguanta *et al.*, «An electrochemical route towards the fabrication of nanostructured semiconductor solar cells», in *SPEEDAM 2010*, Pisa, Italy: IEEE, giu. 2010, pp. 1166–1171. doi: 10.1109/SPEEDAM.2010.5542264.

[91] E. Roduner, «Size matters: why nanomaterials are different», *Chem. Soc. Rev.*, vol. 35, fasc. 7, p. 583, 2006, doi: 10.1039/b502142c.

[92] A. B. Asha e R. Narain, «Nanomaterials properties», in *Polymer Science and Nanotechnology*, Elsevier, 2020, pp. 343–359. doi: 10.1016/B978-0-12-816806-6.00015-7.

[93] B. Ni e X. Wang, «Face the Edges: Catalytic Active Sites of Nanomaterials», *Advanced Science*, vol. 2, fasc. 7, p. 1500085, lug. 2015, doi: 10.1002/advs.201500085.

[94] H. Zhang, Z. Feng, L. Wang, D. Li, e P. Xing, «Bifunctional nanoporous Ni-Zn electrocatalysts with super-aerophobic surface for high-performance hydrazine-assisted hydrogen production», *Nanotechnology*, vol. 31, fasc. 36, p. 365701, set. 2020, doi: 10.1088/1361-6528/ab9396.

[95] L. Bruno, S. Battiato, M. Scuderi, F. Priolo, A. Terrasi, e S. Mirabella, «Physical insights into alkaline overall water splitting with NiO microflowers electrodes with ultra-low amount of Pt catalyst», *International Journal of Hydrogen Energy*, vol. 47, fasc. 80, pp. 33988–33998, set. 2022, doi: 10.1016/j.ijhydene.2022.08.005.

[96] L. Bruno, M. Scuderi, F. Priolo, e S. Mirabella, «Enhanced electrocatalytic activity of low-cost NiO microflowers on graphene paper for the oxygen evolution reaction», *Sustainable Energy Fuels*, vol. 6, fasc. 19, pp. 4498–4505, 2022, doi: 10.1039/D2SE00829G.

[97] D. Huo, M. J. Kim, Z. Lyu, Y. Shi, B. J. Wiley, e Y. Xia, «One-Dimensional Metal Nanostructures: From Colloidal Syntheses to Applications», *Chem. Rev.*, vol. 119, fasc. 15, pp. 8972–9073, ago. 2019, doi: 10.1021/acs.chemrev.8b00745.

[98] G. B. Darband, «Recent advances in methods and technologies for enhancing bubble detachment during electrochemical water splitting», *Renewable and Sustainable Energy Reviews*, p. 21, 2019.
[99] R. Wen, S. Xu, X. Ma, Y.-C. Lee, e R. Yang, «Three-Dimensional Superhydrophobic Nanowire Networks for Enhancing Condensation Heat Transfer», *Joule*, vol. 2, fasc. 2, pp. 269–279, feb. 2018, doi: 10.1016/j.joule.2017.11.010.
[100] S. H. Ahn *et al.*, «Effect of morphology of electrodeposited Ni catalysts on the behavior of bubbles generated during the oxygen evolution reaction in alkaline water electrolysis», *Chem. Commun.*, vol. 49, fasc. 81, Art. fasc. 81, 2013, doi: 10.1039/c3cc44891f.
[101] S. Li, H. Jin, e Y. Wang, «Recent progress on the synthesis of metal alloy nanowires as electrocatalysts», *Nanoscale*, vol. 15, fasc. 6, pp. 2488–2515, 2023, doi: 10.1039/D2NR06090F.
[102] Y. Li *et al.*, «Under-Water Superaerophobic Pine-Shaped Pt Nanoarray Electrode for Ultrahigh-Performance Hydrogen Evolution», *Adv Funct Materials*, vol. 25, fasc. 11, pp. 1737–1744, mar. 2015, doi: 10.1002/adfm.201404250.
[103] Y. Li *et al.*, «Electrodeposited ternary iron-cobalt-nickel catalyst on nickel foam for efficient water electrolysis at high current density», *Colloids and Surfaces A: Physicochemical and Engineering Aspects*, vol. 506, pp. 694–702, ott. 2016, doi: 10.1016/j.colsurfa.2016.07.047.
[104] Q. Zhao *et al.*, «Tuning Electronic Push/Pull of Ni-Based Hydroxides To Enhance Hydrogen and Oxygen Evolution Reactions for Water Splitting», *ACS Catal.*, vol. 8, fasc. 6, pp. 5621–5629, giu. 2018, doi: 10.1021/acscatal.8b01567.
[105] N. K. Chaudhari, H. Jin, B. Kim, e K. Lee, «Nanostructured materials on 3D nickel foam as electrocatalysts for water splitting», *Nanoscale*, vol. 9, fasc. 34, pp. 12231–12247, 2017, doi: 10.1039/C7NR04187J.

3. Fabrication and Characterization of Electrocatalysts

The special properties of nanomaterial — size, composition or structure related — make them especially interesting for numerous energy, environmental and medical technologies. Due to their remarkable and fascinating characteristics, they have attracted a great deal of interest among scientists. The unique electrical, electrochemical, optical and magnetic behavior of nanostructured materials have motivated increasing attention in the academic and industrial fields. These nanostructures are already being used, or can be employed for different applications (nanomedicine, sensing, catalysis and etc.). The wide range of applications is also attributed to the diverse methods available for fabricating nanostructures, which are typically categorized into "bottom-up" and "top-down" approaches:

- **Top-down manufacturing** involves scaling down the patterning of materials to the nanometer range. This method enables the creation of materials with a continuous and coherent structure, ordered from the macroscopic level down to the nanoscale.
- **Bottom-up manufacturing** focuses on atomically precise assembly of entities that grow in size. This approach is central to macromolecular and supramolecular chemistry (such as dendrimers and engineered DNA) and to cluster and surface physics (such as epitaxy and self-assembly) [1].

In this PhD thesis, the attention is focused on the nanostructures obtained by electrodeposition processes. After the fabrication phase, the electrodes are characterized both from a physicochemical standpoint to evaluate morphology and composition, for example, and then from electrochemical point to study

their catalytic activity towards the HER and OER reactions**. Figure 3.1** provides an overview of the methodology followed during the research activity.

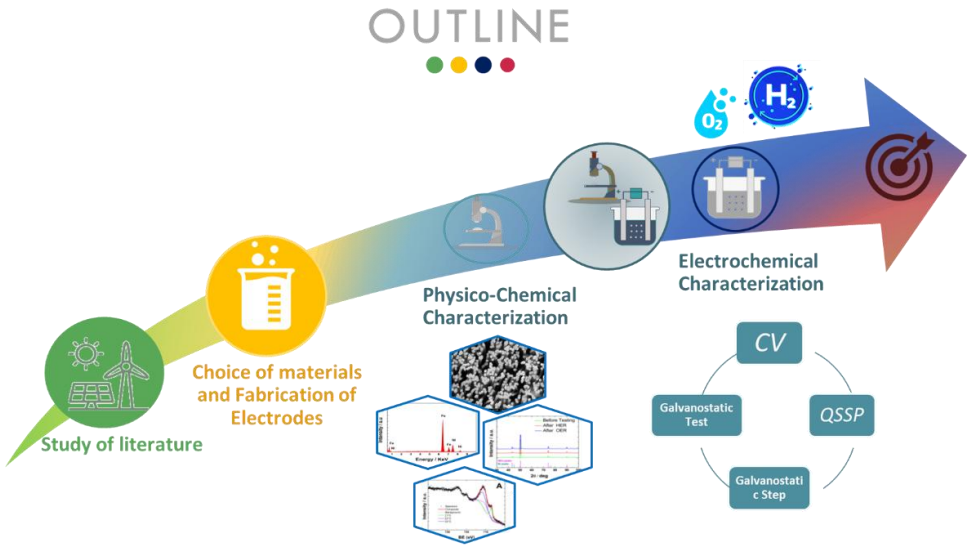

Figure 3.1 *Outline of Research Activity*

3.1 Electrodeposition

In accordance with data in the literature, most electrocatalysts are obtained by processes that require large amounts of energy and time. Finding a simple and efficient method to produce catalysts with high electrocatalytic activity at a low cost and minimal damage is essential. Compared to other methods for producing non-noble metal catalysts, electrodeposition stands out for its simplicity, affordability, and the advantage of not requiring conductive agents or binders between the catalyst material and the substrate [2]. The electrodeposition of a pure metal and alloys is widely studied and applied in

various industries. A general scheme of electrodeposition system is shown in **figure 3.2**.

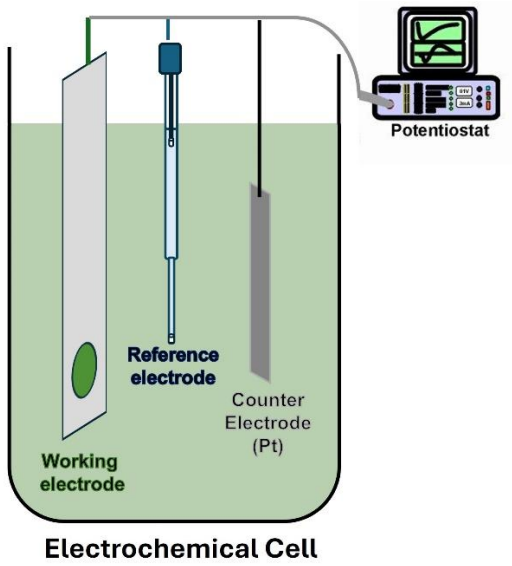

Fig. 3.2. *Scheme of Electrodeposition system*

The **solution bath** serves as a metal source for deposition, containing metal ions that facilitate conductivity. To successfully carry out electrodeposition, several chemical and operational parameters must be carefully controlled, such as current density, electrolyte concentration, complexing agents, pH, temperature, electrolyte stirring, substrate characteristics, and cleaning procedures. It includes stabilizers to protect against hydrolysis and to maintain a stable pH, acting as a buffer. This bath regulates the morphology of the deposit and assists in the dissolution of the anodes. Additionally, it alters the properties of either the solution or the deposit. Complex ions are created to stabilize the cation, becoming significantly more stable when bonded to ligands or metal atoms through coordinate bonding. Furthermore, complex

ions help maintain the equated form at a suitably low concentration, enabling better control over the uniformity of the plating [3].

Co-deposition of metal alloys presents a challenge because the optimal conditions for depositing one metal may differ from those needed for the other constituent metals. Each metal has its deposition potential, which is influenced by the concentration of its ions in the bath, its standard reduction potential, and the presence of complexing agents. For successful electrodeposition of an alloy, the deposition potentials of the constituent metals need to be close to each other. In some cases, there is the so-called anomalous co-deposition where the less noble metal deposits preferentially at a higher ratio in the deposit than in the electrolyte. An example is Nickel-Zinc alloy. This anomalous co-deposition can lead to the simultaneous formation of multiple phases, which can have significant technological applications. In general, zinc-nickel deposition follows a normal process at low current densities but transitions to anomalous deposition beyond a certain current threshold. This transition current density is influenced by various factors such as the nature of the electrolyte anion, temperature, nickel ion concentration, Ni/Zn concentration ratio, electrode substrate, and electrolyte agitation. Another interesting alloy known for its anomalous co-deposition is Nickel-Iron alloy. Some researchers have attributed anomalous codeposition primarily to the formation of an oxide or hydroxide of the less noble metal. In the case of NiFe alloy, codeposition anomalies arise from $Fe(OH)_2$ adsorption [4]. For Zinc-Iron group metals, the electrodeposition of the latter is often suppressed in the presence of inhibitory zinc hydroxide, similar to the suppression observed with hydrogen. The phenomenon where the electrochemically less noble zinc deposits preferentially over more noble iron-group metals has been explained by the inhibitory action of adsorbed zinc hydroxide, a concept known as the hydroxide suppression mechanism [5]. This can be achieved by adjusting the

ion concentrations or adding appropriate complexing agents. Complexing agents convert the simple ions of more noble metals into complex ions with lower potentials, thus aligning their deposition potentials. When a complexing agent coordinates with only one metal, it shifts its deposition potential to a more negative value, allowing the second metal to remain as a simple ion. In cases where a single complexing agent forms complexes with both types of metal ions, the potentials of both metals are shifted to more negative values, reducing the difference between them. Sometimes, two different complexing agents are used to coordinate with different metals. These agents must be non-toxic and non-corrosive. To ensure stability, complexing agents are often added to the electrolyte solution in excess, leaving some free agents in the solution, which helps achieve the desired stoichiometric composition [6]. Boric acid has traditionally been regarded as a buffering agent in the electrodeposition process. Recent studies, however, highlight its catalytic role in metal electrodeposition, suggesting that boric acid improves metal deposition by reducing over-potential and increasing current efficiency. It forms complexes with metal ions in aqueous solutions, such as the nickel-borate complex. These complexes influence the shape of the deposited nickel nanostructures by adjusting the local concentration of Ni^{2+} ions near the pore walls. Graham et al. reported the effect of boric acid on nickel nanotubes (NT) formation suggesting its crucial role in the growth of the nanostructures [7]. Another additive widely used in electrodeposition process is citric acid. It is used to avoid ferric hydroxide formation. Additionally, citric acid can form stable complexes with Ni^{2+} ions, which affects the electrodeposition process of Ni alloys [8]. There are numerous electrochemical methods to synthesize the electrocatalysts. In this part, a summary of the different electricity input is described and shown in the following **figure 3.3**.

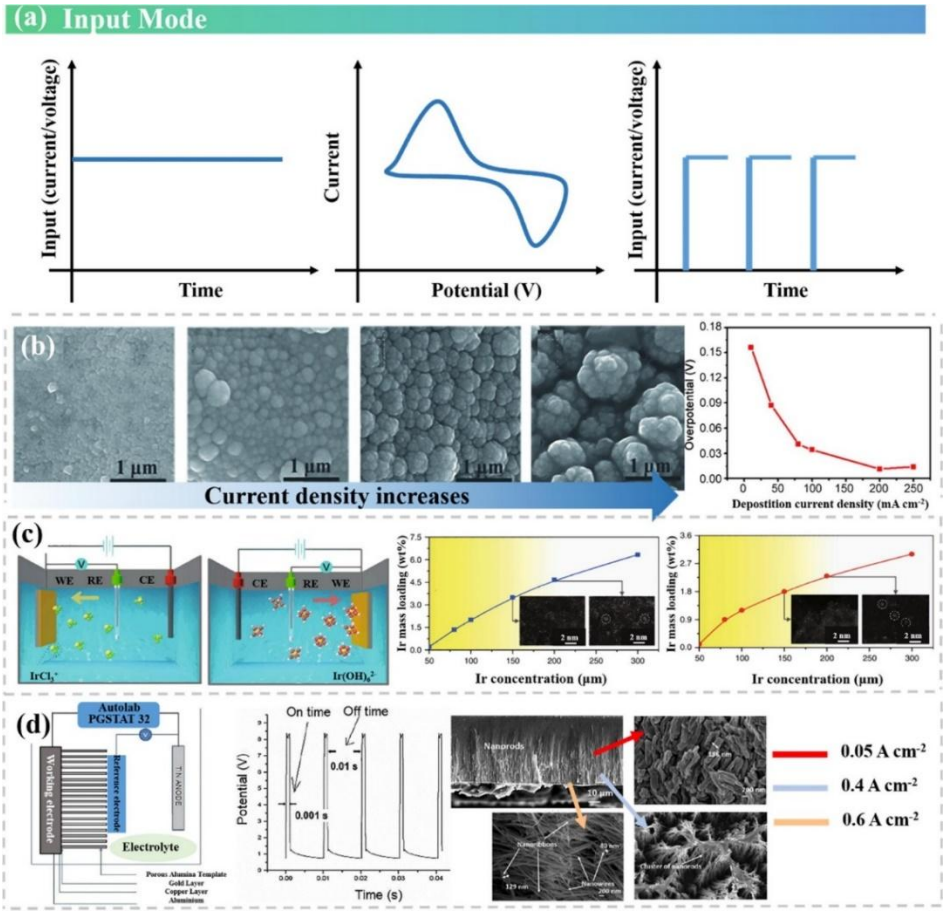

Fig. 3.3. *Schematic diagram of typical power input with different modes* [9] *(potentiostatic and galvanostatic, cyclic voltammetry, pulse current/voltage) . (b) Surface morphologies of the Ni-Mo catalysts electrodeposited on Cu foam at increasing cathodic current densities. Right is the relationship between Mo content and deposited current density* [10] *(c) Schematic illustration of cathodic and anodic doping of Ir species by electrodeposition*[11] *(d) Schematic diagram of pulse deposition system* [12]

In this research, **pulsed electrodeposition** was used to fabricate the electrocatalyst. Pulsed current or voltage applied in electrodeposition systems offers several advantages, such as promoting a more compact structure with increased nucleation. Recently, many studies [12], [13], [14] have synthesized films using pulsed input and examined the effects of pulsed deposition. To enhance catalytic performance, regulating pulse parameters enables controlled material morphology and increased reactive sites. In sum, pulsed deposition governs the crystal nucleation process through adjustments in frequency, current, and voltage, directly influencing catalytic performance while moderating diffusion resistance, controlling chemical composition and microstructure, and reducing side reactions.

3.2 Template Electrosynthesis

Template-directed synthesis is a simple, scalable and efficient method for creating 1D nanostructures, especially various types of nanowires. In this approach, the template acts as a scaffold within or around which a different material is formed in situ, resulting in a nanostructure that mirrors the template's shape. By filling a porous template that features numerous straight cylindrical pores with a narrow size distribution, arrays on nanowires can be produced. The filling of the pores can be done using various techniques, but the most common and commercially available methods are electrochemical deposition or polymerization reactions [15]. When the template serves only a physical role, it often needs to be selectively removed through post-synthesis treatments like chemical etching or calcination to retrieve the nanostructures. In chemical processes, the template is usually consumed during the reaction, allowing the nanostructures to be obtained directly in pure form. Template-directed synthesis is generally recognized as a straightforward, high-throughput, and cost-effective technique that can replicate complex surface features of the template in a single step [16]. Many types of templates have

been successfully demonstrated by research groups, including step edges on solid substrates, channels in porous materials. The most frequently used substrates for the electrodeposition of one-dimensional nanomaterials are nanoporous membranes made from polycarbonate (PC) [17], [18] or anodic alumina membrane (AAM). AAM is considered an ideal template due to its morphology, which consists of a well-organized array of cylindrical pores oriented perpendicular to the surface. A key benefit of these membranes is the ability to fine-tune their structural properties by adjusting anodization parameters such as the aluminium surface treatment, applied voltage, anodization time, and the type and composition of the electrolyte. Moreover, these membranes are both cost-effective and easy to manufacture [19], [20]. PC membranes offer a wider range of pore diameters (from 15 nm to 12 mm) compared to AAM templates, allowing for the use of various PC membrane templates to create nanostructures of different diameters [21]. The primary benefits of using polycarbonate membranes are their high density of interconnected pores and ease of dissolution in solvents like dichloromethane or chloroform. Additionally, after dissolution, the polycarbonate can be recovered from etching process. In this work the attention was focused on the fabrication of the nanostructured electrodes through polycarbonate membrane. In particular, commercial Whatman Cyclopore membrane were used as template. A Typical morphology is shown in the following **figure 3.4**. These membranes are characterized by a pore density of 10^{12} pori/m^2, a pore diameter of 200-250 nm, and a thickness of 20 μm.

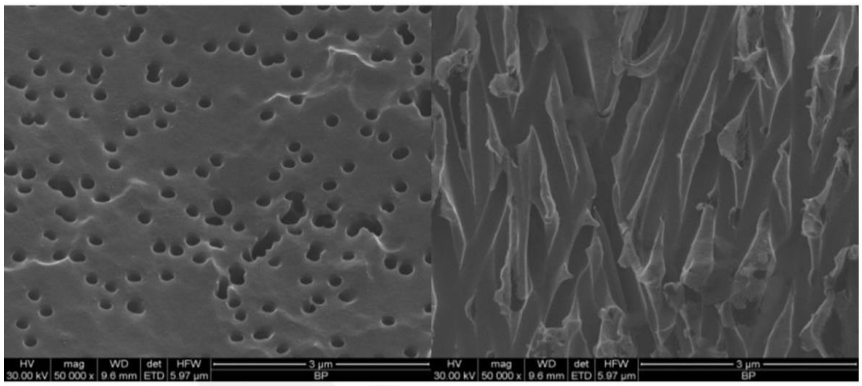

Fig. 3.4 *Polycarbonate Membrane SEM images:*
left) top view; right) section view

In the following **figure 3.5**, a scheme of the synthesis of nanostructures by template electrosynthesis is shown.

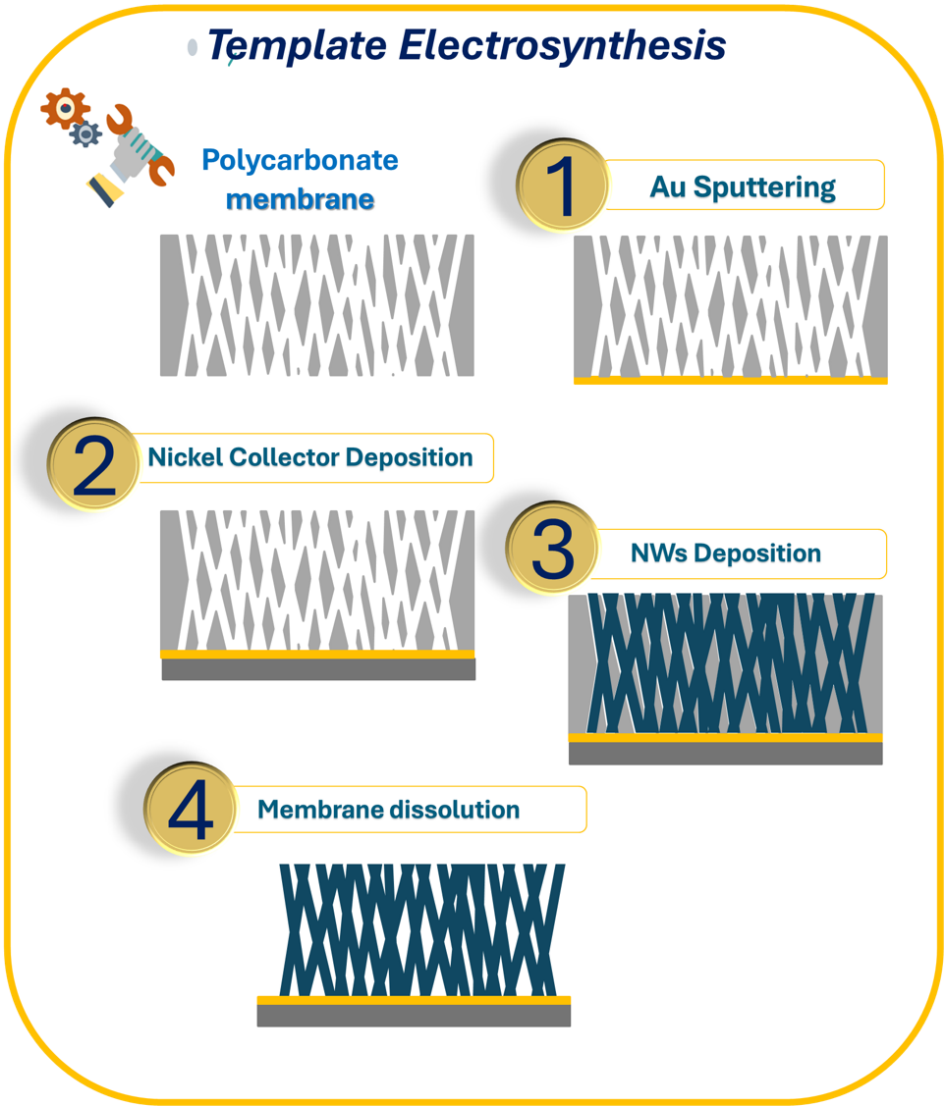

Fig. 3.5 *Schematic representation of template electrosynthesis*

Starting from a porous polycarbonate membrane, a thin layer of gold, approximately 30 nanometers thick, is deposited on one side of the membrane to make it conductive, through a sputtering process. On this gold-coated side, a layer of nickel is electrodeposited using a potentiostatic technique, with the standard Watt's bath (300 g/L $NiSO_4*6H_2O$, 45 g/L $NiCl_2*6H_2O$, 45g/L

H_3BO_3) as the electrolyte solution. This nickel layer provides mechanical strength to the electrode and ensures electrical connectivity between all the nanowires that will be deposited later. A typical 3 electrode-cell configuration was used. A Platinum sheet was used as a counter-electrode, a standard calomel electrode (SCE) was used as a reference and the gold membrane was the working electrode. The following **figure 3.6** shows electrodeposition configuration. The copper ring serves to have electrical connection between the golden membrane and the potentiostat.

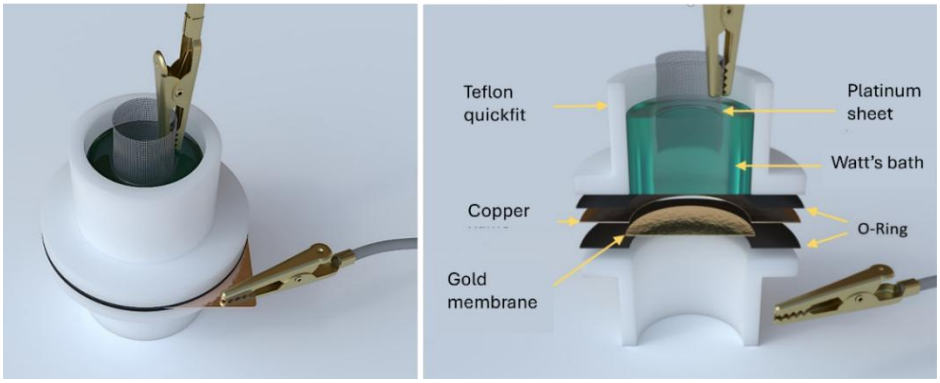

Fig. 3.6 *Electrodeposition configuration*

Nickel is electrodeposited applying a potential of -1.5 V vs. SCE for 1.5 hours

$$Ni^{2+} + 2e^{-} \rightarrow Ni$$

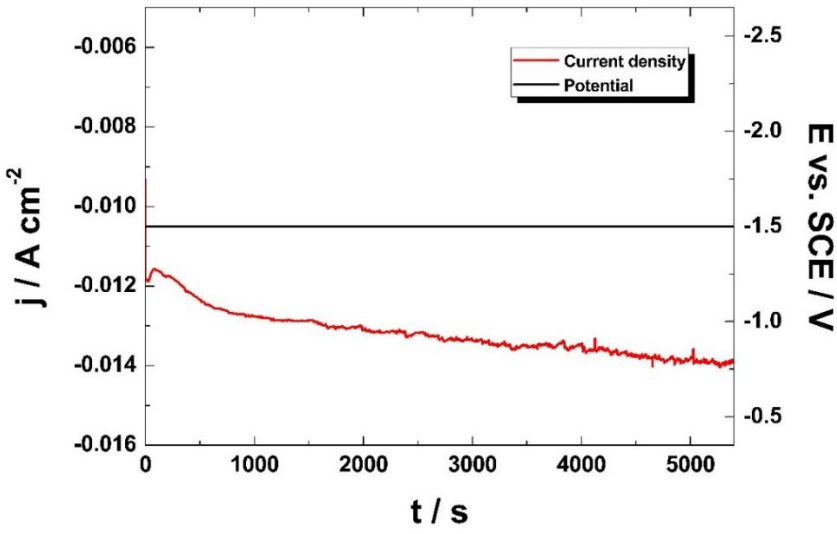

***Fig. 3.7** Nickel layer electrodeposition*

The **figure 3.7** shows the nickel electrodeposition curve, where the black line represents the applied potential, which is constant, and the red curve represents the current density trend over time.

The electrodeposited Ni layer was later used as a current collector to deposit nanostructures within the template. The details of nanowires electrodeposition will be shown in the next chapters. The technique, operating parameters, electrodeposition bath etc., depend on which metals you want to deposit. After nanowires deposition, the membrane was etched in pure chloroform in four consecutive baths of five minutes each.

3.3 Chemical and Physical Characterization

Various advanced characterization techniques are employed to thoroughly study electrocatalysts. X-ray diffraction (XRD) and electron diffraction spectroscopy (EDS) are commonly used for phase identification and composition analysis. Morphological studies are conducted using scanning

electron microscopy (SEM). Surface composition details are investigated through X-ray photoelectron spectroscopy (XPS). In particular, morphology was investigated using a FEG-ESEM microscope (model: QUANTA 200 by FEI), equipped with Energy Disperse Spectroscopy (EDS) probe. The crystallographic structure was investigated by a RIGAKU X-ray diffractometer (model: D-MAX 25600 HK). Diffraction patterns were obtained in the 2θ range from 5° to 100° with a sampling width of 0.01° and a scan speed of 0.5 step/sec, using Ni-filtered Cu Kα radiation (λ= 1.54 Å). The tube voltage and current were set at 40 kV and 40 mA, respectively. The surface of the nanowires (NWs) was characterized using X-ray photoelectron spectroscopy (XPS) with a PHI5000 VersaProbe II (ULVACPHI). This system operates with an Al anode (Al Kα = 1486.6 eV), employing a 200 μm diameter beam (50 W) and collecting electrons ejected at a 45° angle from the surface, while neutralizing charges using both electron and ion guns.

3.4 Electrochemical Characterization

To better evaluate the water-splitting performance of a given catalyst, several important parameters have been established. Today, widely recognized measurement criteria include total catalytic activity (e.g., overpotential at a given current density), Tafel slope, exchange current density, turnover frequency (TOF), and long-term stability. Total activity, Tafel slope, and exchange current density can be directly estimated using linear sweep voltammetry (LSV) and the derived Tafel plots. In any electrolyte used for water splitting, the thermodynamic equilibrium potentials are 0 V and 1.23 V vs. RHE for catalyzing the HER and OER, respectively. A smaller overpotential required to reach a given current density indicates better catalytic activity. The Tafel slope is a crucial parameter for estimating the reaction mechanism. It is a valuable tool for assessing the kinetic rate of an electrocatalyst and understanding the reaction mechanism. A smaller Tafel

slope indicates that achieving the same increase in current density requires a lower overpotential, which suggests faster charge transfer kinetics. By plotting overpotential (η) as a function of log current density (j), the Tafel equation $\eta = a + b \log j$ is obtained, where b is the Tafel slope. The exchange current density j_0 is derived by assuming η is zero, making it a key kinetic parameter for assessing the intrinsic catalytic activity of a catalyst under equilibrium conditions. It is only related to the catalyst material, electrolyte and temperature. Higher values of j_0 mean greater activity of the catalyst. Briefly, an ideal catalyst should exhibit a small Tafel slope (b) and a high exchange current density j_0 [22].

TOF is defined as the total number of reactants converted into the desired product per catalytic site per unit of time. It is calculated using the equation $TOF = jA/(xnF)$ where j is the current density, A is the area of the working electrode, x is the number of transferred electrodes for each molecule of gas produced (x=2 for HER, x=4 for OER), n is the number of moles of active material and F is the Faraday's constant [23]. However, obtaining a precise TOF value for most heterogeneous catalysts is challenging because not all surface atoms are catalytically active or easily accessible. Despite this imprecision, the calculated TOF still provides a valuable comparative measure of catalytic activity.

Stability is another critical parameter for evaluating catalyst performance in practical applications. It is used to assess the ability of the catalyst to catalyze a water-splitting reaction for a long-term operation period. There are two common methods for measuring catalyst stability:

1. **Monitoring Current or Potential Variation:** The variation of current (or potential) over time at a given overpotential (or current density) is observed. Small variations indicate good stability.

2. **Comparing Cyclic Voltammetry (CV) or LSV Curves Before and After Cycling:** Small shifts in onset potential and overpotential at a constant current density after cycling experiments suggest good durability of the catalyst [24], [25].

Overall, these parameters—when properly measured and analyzed—provide a comprehensive evaluation of a catalyst's effectiveness in water splitting applications [26].

To assess water-splitting performance, both the conventional three-electrode and two-electrode systems are utilized. The three-electrode system consists of a working electrode, a reference electrode, and a counter electrode. The reference electrode must be stable during the catalysis, and the commonly used reference electrodes include Ag/AgCl, the saturated calomel electrode (SCE), the Hg–HgO electrode referred to the reversible hydrogen electrode (RHE).

3.4.1 Cyclic Voltammetry (CV)-Electrochemically Surface Area (ECSA)

Cyclic voltammetry (CV), or potentiodynamic cycling, is an extensively employed electrochemical technique used to analyze electrode reactions and to characterize electrode surfaces in the field of electrocatalysis**.** CVs can be conducted to obtain information about the electrochemically active surface area of an electrode. By analyzing the double-layer capacitance, which depends on the electrode surface, it is possible to estimate the actual area involved in electrochemical reactions. This is particularly useful for studying porous materials or catalysts, where the real surface area can significantly differ from the geometric area [27]. The electrical double layer describes the variation in electric potential near the surface of an electrode. Generally, this double layer is less than 10 nm thick when the electrolyte concentration is above 0.001 M. Despite its thinness, it can store a significant amount of

electrical charge, with the double layer capacitance being dependent on the electrode's surface area. Consequently, measuring double layer capacitance provides an estimate of the actual surface area of solid metal electrodes. The double layer capacitance (measured in mF), is calculated using the equation:

$C=\Delta I/v$

where ΔI (in mA) denote the change in current during the charge/discharge cycle, and v (in V/s) represents the scan rate. The change in current is obtained by measuring the difference between the upper and lower lines in the voltammogram [28]. Using the double-layer capacitance method, the specific capacitance can be calculated. It is directly linked to the real active surface area of the electrode [27]. To calculate the specific capacitance, CVs at increasing scan rates were carried out in a small range of potential where no Faradic reactions occur. Then, at fixed potential value, for each scan rate, the difference between anodic and cathodic current density was calculated. This difference is plotted with the scan rate values and a linear fitting is carried out. The slope value (Capacitance/Area) represents the specific capacitance. This value is particularly useful in the case of nanostructured catalysts because it allows us to determine how much the actual surface area is greater than the geometric area. This is important because nanostructured materials often exhibit a much larger effective surface area due to their morphology, which enhances their catalytic performance by providing more active sites for reactions.

3.4.2 Quasi Steady-State Polarization (QSSP)

Quasi Steady-state Polarization were conducted for both water splitting reactions. A range of approximately 0.7 V respect to the thermodynamic values of hydrogen and oxygen evolution is analyzed. Many insights can be obtained from these tests. The current response at a given potential can

indicate the activity of the catalyst. By comparing curves from different catalysts under identical conditions, one can evaluate which catalyst is more efficient or effective for a given reaction. Higher current densities suggest higher catalytic activity. Moreover, analyzing the curve can help identify any mass transport limitations that may affect the performance of the catalyst at higher current densities. By fitting the linear range of these curves, it is possible to derive the Tafel parameters, thus gaining information into the catalytic activity of the catalysts and to understand which stage is kinetically determining. The test can also be repeated after a long-term stability test to determine if the catalyst has degraded over time. Additionally, at a specific potential value, the corresponding current value can be obtained from the curves, allowing for the calculation of the TOF value.

3.4.3 Galvanostatic Test

Different types of galvanostatic tests are conducted at constant current values to study the behavior of the catalysts. **Galvanostatic step polarization** was carried out to study the behavior of the catalysts at different current densities. In particular, in this work, six increasing different current densities were imposed for a fixed time and the average potential value for each step was measured. This value allows us to compare various catalysts and understand which one, in terms of the obtained overpotential, is the best for working under certain applied current conditions, from laboratory-scale values like 10 mA cm^{-2} to industrial-scale values like 500 mA cm^{-2}. Then, the stability of the electrodes was studied at a constant current value. Initially, the mid-term stability was investigated by applying a certain current for 6 hours, and then for 125 hours, evaluating the overpotential trend over time. A nearly constant overpotential trend indicates an excellent ability of the catalyst to catalyze the target reactions.

For the tests conducted in simulated seawater, the potential value mustn't reach the level where hypochlorite formation occurs [29]. In this case, the catalyst would become non-selective towards the Oxygen Evolution Reaction. In addition, coupling galvanostatic tests with OCP (open circuit potential) cycles can be a useful method to simulate the operation of an electrolyzer powered by renewable energy sources. This technique allows replicating the dynamic conditions to which an electrolyzer might be exposed when powered by intermittent energy sources, such as solar or wind. In a system powered by renewable energy, the electrolyzer can be frequently turned on and off due to variations in energy availability (such as solar radiation or wind speed). The combination of OCP cycles and galvanostatic tests allows the reproduction of this dynamic. For example:

- During a **peak in energy production** (sunny day or strong wind), a constant galvanostatic current can be applied to simulate the stable operation of the electrolyzer.
- During a **drop in production** (clouds, lack of wind), OCP cycles can be used to simulate the idle or inactive period of the electrolyzer.

It allows for a realistic study of the effects of energy variability and the on-off cycling on the efficiency, lifetime, and stability of electrode materials. It also helps evaluate how electrode materials degrade during inactivity periods and transition phases [30].

References

[1] F. Charra, S. Gota-Goldmann, e H. Warlimont, «Nanostructured Materials», in *Springer Handbook of Materials Data*, H. Warlimont e W. Martienssen, A c. di, in Springer Handbooks. , Cham: Springer International Publishing, 2018, pp. 1041–1080. doi: 10.1007/978-3-319-69743-7_28.

[2] S. Esmailzadeh, T. Shahrabi, Gh. Barati Darband, e Y. Yaghoubinezhad, «Pulse electrodeposition of nickel selenide nanostructure as a binder-free and high-efficient catalyst for both electrocatalytic hydrogen and oxygen evolution reactions in alkaline solution», *Electrochimica Acta*, vol. 334, p. 135549, feb. 2020, doi: 10.1016/j.electacta.2019.135549.

[3] S. A. M. Al-Bat'hi, «Electrodeposition of Nanostructure Materials», in *Electroplating of Nanostructures*, M. Aliofkhazraei, A c. di, InTech, 2015. doi: 10.5772/61389.

[4] T. Akiyama e H. Fukushima, «Recent Study on the Mechanism of the Electrodeposition of Iron-group Metal Alloys.», *ISIJ Int.*, vol. 32, fasc. 7, pp. 787–798, 1992, doi: 10.2355/isijinternational.32.787.

[5] R. Albalat, E. G□mez, C. M□ller, M. Sarret, E. Vall□s, e J. Pregonas, «Electrodeposition of zinc-nickel alloy coatings: influence of a phenolic derivative», *J. Appl. Electrochem.*, vol. 20, fasc. 4, pp. 635–639, lug. 1990, doi: 10.1007/BF01008875.

[6] E. M. Mkawi, K. Ibrahim, M. K. M. Ali, M. A. Farrukh, A. S. Mohamed, e N. K. Allam, «Effect of complexing agents on the electrodeposition of Cu–Zn–Sn metal precursors and corresponding Cu2ZnSnS4-based solar cells», *J. Electroanal. Chem.*, vol. 735, pp. 129–135, dic. 2014, doi: 10.1016/j.jelechem.2014.10.021.

[7] L. M. Graham, S. Cho, S. K. Kim, M. Noked, e S. B. Lee, «Role of boric acid in nickel nanotube electrodeposition: a surface-directed growth mechanism», *Chem Commun*, vol. 50, fasc. 5, pp. 527–529, 2014, doi: 10.1039/C3CC47183G.

[8] W. Wu, Z. Wang, P. Jiang, e Z. Tang, «Effect of Electroplating Variables on Electrodeposition of Ni Rich Ni-Ir Alloys from Citrate Aqueous Solutions», *J. Electrochem. Soc.*, vol. 164, fasc. 14, pp. D985–D993, 2017, doi: 10.1149/2.0771714jes.

[9] R. Li *et al.*, «Electrodeposition: Synthesis of advanced transition metal-based catalyst for hydrogen production via electrolysis of water», *J. Energy Chem.*, vol. 57, pp. 547–566, giu. 2021, doi: 10.1016/j.jechem.2020.08.040.

[10] Y. Wang *et al.*, «A 3D Nanoporous Ni–Mo Electrocatalyst with Negligible Overpotential for Alkaline Hydrogen Evolution», *ChemElectroChem*, vol. 1, fasc. 7, pp. 1138–1144, lug. 2014, doi: 10.1002/celc.201402089.

[11] Z. Zhang *et al.*, «Electrochemical deposition as a universal route for fabricating single-atom catalysts», *Nat. Commun.*, vol. 11, fasc. 1, p. 1215, mar. 2020, doi: 10.1038/s41467-020-14917-6.
[12] A. Sharma, S. Bhattacharya, S. Das, e K. Das, «Fabrication of Sn nanostructures by template assisted pulse electrodeposition», *Surf. Eng.*, vol. 32, fasc. 5, pp. 378–384, mag. 2016, doi: 10.1179/1743294415Y.0000000091.
[13] Kh. M. S. Youssef, C. C. Koch, e P. S. Fedkiw, «Improved corrosion behavior of nanocrystalline zinc produced by pulse-current electrodeposition», *Corros. Sci.*, vol. 46, fasc. 1, pp. 51–64, gen. 2004, doi: 10.1016/S0010-938X(03)00142-2.
[14] M. H. Allahyarzadeh, M. Aliofkhazraei, A. R. S. Rouhaghdam, e V. Torabinejad, «Electrodeposition of Ni–W–Al2O3 nanocomposite coating with functionally graded microstructure», *J. Alloys Compd.*, vol. 666, pp. 217–226, mag. 2016, doi: 10.1016/j.jallcom.2016.01.031.
[15] C. Schönenberger *et al.*, «Template Synthesis of Nanowires in Porous Polycarbonate Membranes: Electrochemistry and Morphology», *J. Phys. Chem. B*, vol. 101, fasc. 28, pp. 5497–5505, lug. 1997, doi: 10.1021/jp963938g.
[16] Y. Xia *et al.*, «One-Dimensional Nanostructures: Synthesis, Characterization, and Applications», *Adv. Mater.*, vol. 15, fasc. 5, pp. 353–389, mar. 2003, doi: 10.1002/adma.200390087.
[17] Bernardo Patella, Rosalinda Inguanta, Salvatore Piazza, e Carmelo Sunseri, «Nanowire ordered arrays for electrochemical sensing of h2o2», *Chem. Eng. Trans.*, vol. 47, pp. 19–24, mar. 2016, doi: 10.3303/CET1647004.
[18] A. Moncada, S. Piazza, C. Sunseri, e R. Inguanta, «Recent improvements in PbO2 nanowire electrodes for lead-acid battery», *J. Power Sources*, vol. 275, pp. 181–188, feb. 2015, doi: 10.1016/j.jpowsour.2014.10.189.
[19] R. Inguanta, S. Piazza, e C. Sunseri, «Influence of electrodeposition techniques on Ni nanostructures», *Electrochimica Acta*, vol. 53, fasc. 19, pp. 5766–5773, ago. 2008, doi: 10.1016/j.electacta.2008.03.045.
[20] R. Inguanta, S. Piazza, e C. Sunseri, «Synthesis of self-standing Pd nanowires via galvanic displacement deposition», *Electrochem. Commun.*, vol. 11, fasc. 7, pp. 1385–1388, lug. 2009, doi: 10.1016/j.elecom.2009.05.012.
[21] J. Li *et al.*, «Template electrosynthesis of tailored-made helical nanoswimmers», *Nanoscale*, vol. 6, fasc. 16, pp. 9415–9420, 2014, doi: 10.1039/C3NR04760A.
[22] J. Wang *et al.*, «Earth-abundant transition-metal-based bifunctional catalysts for overall electrochemical water splitting: A review», *J. Alloys*

Compd., vol. 819, p. 153346, apr. 2020, doi: 10.1016/j.jallcom.2019.153346.
[23] V. D. Silva, T. A. Simões, J. P. F. Grilo, E. S. Medeiros, e D. A. Macedo, «Impact of the NiO nanostructure morphology on the oxygen evolution reaction catalysis», *J. Mater. Sci.*, vol. 55, fasc. 15, pp. 6648–6659, mag. 2020, doi: 10.1007/s10853-020-04481-1.
[24] X. Zou e Y. Zhang, «Noble metal-free hydrogen evolution catalysts for water splitting», *Chem. Soc. Rev.*, vol. 44, fasc. 15, pp. 5148–5180, 2015, doi: 10.1039/C4CS00448E.
[25] K. Liu, H. Zhong, F. Meng, X. Zhang, J. Yan, e Q. Jiang, «Recent advances in metal–nitrogen–carbon catalysts for electrochemical water splitting», *Mater. Chem. Front.*, vol. 1, fasc. 11, pp. 2155–2173, 2017, doi: 10.1039/C7QM00119C.
[26] Y. Li, L. Zhou, e S. Guo, «Noble metal-free electrocatalytic materials for water splitting in alkaline electrolyte», *EnergyChem*, vol. 3, fasc. 2, p. 100053, mar. 2021, doi: 10.1016/j.enchem.2021.100053.
[27] A. J. Bard, L. R. Faulkner, e H. S. White, *Electrochemical methods: fundamentals and applications*, Third edition. Hoboken, NJ, USA Chichester, West Sussex, UK: Wiley, 2022.
[28] K. K. Diao, Z. Xiao, e Y. Y. Zhao, «Specific surface areas of porous Cu manufactured by Lost Carbonate Sintering: Measurements by quantitative stereology and cyclic voltammetry», *Mater. Chem. Phys.*, vol. 162, pp. 571–579, lug. 2015, doi: 10.1016/j.matchemphys.2015.06.031.
[29] S. Dresp, T. Ngo Thanh, M. Klingenhof, S. Brückner, P. Hauke, e P. Strasser, «Efficient direct seawater electrolysers using selective alkaline NiFe-LDH as OER catalyst in asymmetric electrolyte feeds», *Energy Environ. Sci.*, vol. 13, fasc. 6, pp. 1725–1729, 2020, doi: 10.1039/D0EE01125H.
[30] S. Dresp *et al.*, «Direct Electrolytic Splitting of Seawater: Activity, Selectivity, Degradation, and Recovery Studied from the Molecular Catalyst Structure to the Electrolyzer Cell Level», *Adv. Energy Mater.*, vol. 8, fasc. 22, p. 1800338, ago. 2018, doi: 10.1002/aenm.201800338.

4. Fabrication and Characterization of NiFe NWs for water electrolysis

4.1 Introduction

Harnessing renewable energy sources for electricity generation is a crucial step in reducing greenhouse gas emissions [1], [2]. Integrating them with energy storage systems, like green hydrogen, is essential to ensure grid stability and improve overall efficiency [3], [4]. Nevertheless, green hydrogen is currently not cost-competitive as an energy carrier, primarily due to the high costs associated with materials and electricity used in its production [5], [6]. Electrocatalysts tailored for efficient hydrogen production tend to operate most effectively in highly purified freshwater systems. This dependence could result in resource scarcity and water allocation problems if electrolysis becomes the primary means of electricity generation in the future. Seawater, constituting over 96% of Earth's water, presents as a promising feedstock for electrolysis [7]. The main challenges in seawater water splitting are the large quantities of chloride anions existing at about 0.5 M in seawater [8], [9]. In this regard, various nanomaterials of oxides and alloys containing precious and non-precious metals [10], [11], [12], have been explored for applications in water electrolysis for both HER [13], [14], [15] and OER [16], [17]. Unique properties of the nanomaterials are the high specific surface area and increased edge-to-face ratio, contributing to the increased electrochemical performance of the electrocatalysts [24]. Among the different tested nanomaterials, NiFe alloys are well studied because they are inexpensive electrocatalysts that can enhance both HER and OER reactions [19], [20], [21], [22], [23], [24]. The aim is to achieve performance comparable to that obtained from the noble metals based on Ir and Ru [25]. Starting from earlier research [17], [26], this chapter regards the fabrication and characterization of nanostructured electrodes composed of NiFe alloy nanowires.

The nanostructured electrodes were fabricated using template electrosynthesis. To examine their behavior in simulated seawater, electrodes were tested in KOH + 0.5 M NaCl solution. Electrochemical tests were performed at different temperatures. Also long-term galvanostatic tests (±50 mA cm^2 for 125 hours) were carried out to assess electrode stability. Before and after the long-term tests, the electrodes were characterized using various techniques to evaluate any changes in their morphology and composition. The overall water-splitting performance was also evaluated using a two-electrode configuration in a 30% KOH aqueous solution.

4.2 Materials & Methods

NiFe nanowire (NWs) electrodes were fabricated using template electrosynthesis, with a polycarbonate membrane serving as the template. The initial steps of the fabrication process were described in detail in the previous chapter in the paragraph “3.4 Template Electrosynthesis”. For the deposition of the Ni-Fe nanowires, a Watt's bath with 0.44 M $FeSO_4 \cdot 7H_2O$ was employed. A pulse electrodeposition method was used switching the potential between –1.35 and –0.65 V versus SCE for 6 and 4 s, respectively, for 100 cycles. Electrodeposition was performed at room temperature in a standard three-electrode cell containing a platinum mesh as the counter electrode and a SCE as the reference electrode. In **Figure 4.1**, some deposition cycles are shown, highlighting the typical current density (red curve) response recorded during the electrodeposition of nanowires.

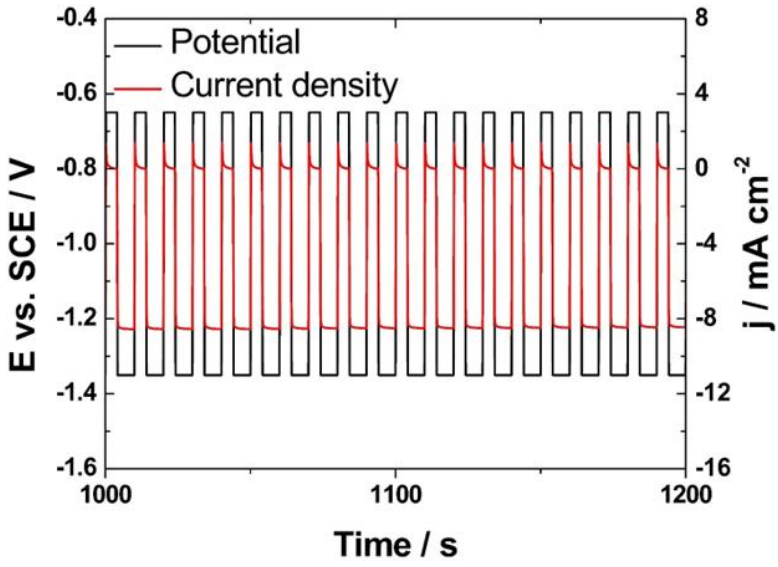

Fig.4.1 *Pulse potential and measured current density vs. time plots for NiFe NWs electrodeposition.*

Pulsed polarization is used to restore the double layer by reversing the current polarity [27]. In the context of nanostructure deposition, it is crucial for managing the buildup of hydrogen gas within the template channels. This is important because excessive gas accumulation can result in the formation of nanotubes, which have lower mechanical strength than nanowires. In addition, the polarity reversal of the current density enables control over the composition and morphology of the nanostructure, leading to the formation of nanowires with uniform lengths and composition evenly distributed across the entire surface of the current collector. The chemical composition of the nanowires remains consistent, irrespective of their length. The morphology and composition of the NiFe nanowire electrodes before and after the long galvanostatic tests were characterized by SEM, EDS, XRD and XPS. Electrochemical characterizations were conducted in a 30% w/w KOH aqueous solution containing 0.5 M NaCl (referred to as KOH+NaCl) and, for comparison, in a 30% KOH aqueous solution (referred to as KOH). A nickel

sheet was used as the counter-electrode, and a Hg/HgO 0.1 M NaOH electrode served as the reference. All potentials are reported relative to the Reversible Hydrogen Electrode (RHE) at pH 14. The experiments were carried out at room temperature, without stirring,

UV tests of the solutions for hypochlorite (ClO) and hypochlorous acid (HClO) were carried out in search of the possible chlorine compound generation during galvanostatic tests using Agilent Cary 60 UV spectrophotometer, scan rate 600 nm/min (detection wavelengths for HClO were 235 and 289 nm, and 294 nm for ClO), calibration curves prepared from sodium hypochlorite pentahydrate $NaClO{\cdot}5H_2O$ provided by TCI. Ion chromatography analysis was done to measure chlorate (ClO_3^-) and perchlorate (ClO_4^-) concentrations. Analyses were done on a Metrohm 882 compact IC system fitted with a Metrosep A Supp 5–250/4.0 column. The standard eluent consisted of 1 mM $NaHCO_3$ and 3.2 mM Na_2CO_3 flowing at 0.7 mL/min. Calibration curves were constructed using pure ClO_3^- and ClO_4^- standards ICCLO31 and ICCLO41 respectively, 1000 ppm each, ISO certified and provided by Inorganic Ventures.

The NiFe nanowire load on the nickel current collector was determined through gravimetric analysis, using a Sartorius microbalance (Premium Microbalance ME36S) to measure the specific load with respect to the geometrical area of the electrode, of about 3.31 mg/cm^3.

4.3 Physico-Chemical and Electrochemical Characterizations

NiFe NWs were realized using an electrolyte composition of about 67% Ni and 33% Fe, which was chosen since this composition has yielded the best-performing NiFe alloy nanowires consistently. EDS performed before the long-term stability test detected only the Fe and Ni peaks, as shown in **Fig.**

4.4, where the iron content is estimated to be about 79%. This composition was confirmed by EDS analysis and also by inductively coupled plasma optical emission spectrometry (ICP). For a more precise estimation of NWs composition, they were pealed from the current collector using copper tape. The results are presented in Table 4.1.

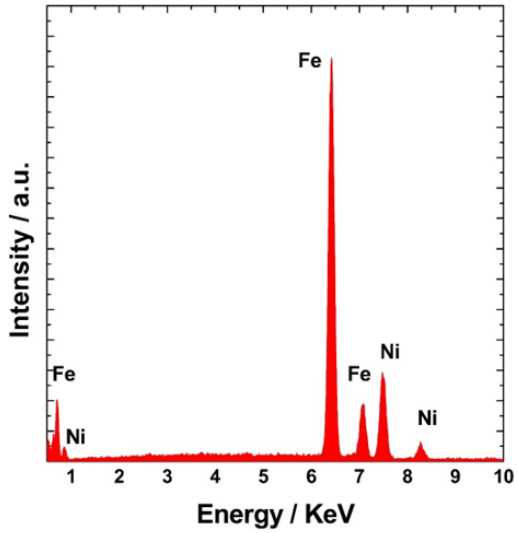

Fig.4.2 *EDS of NiFe NWs electrode before long-term stability test.*

Table. 4.1 *NWs atomic composition measured by EDS and ICP*

	%w/w Electrolyte		***%w/w EDS***		***%w/w ICP***	
NiFe NWs	*Ni*	*Fe*	*Ni*	*Fe*	*Ni*	*Fe*
	66.67	33.33	21.05	78.95	20.20	79.80

The iron content is around 2.85 times higher than that of nickel, consistent with the well-known anomalous co-deposition of these two elements [28].

Although iron is the less noble metal, its concentration exceeds that of the bath solution. This finding aligns with literature reports, as the electrodeposition of iron alloys is recognized as anomalous co-deposition, where the less noble metal deposits preferentially over the more noble one, complicating the control of alloy composition [29]. Various mechanisms have been proposed to explain this behavior [30], [31] and as shown by Llavona et al., the effect is intensified when electrodeposition occurs within nanoporous templates [32]. The most widely accepted explanation for anomalous co-deposition in iron alloys was proposed by Matlosz [31], who demonstrated that the inhibition of nickel deposition in the presence of iron arises from the preferential adsorption of intermediate iron species on the electrode surface.

In **Figure 4.3,** the SEM images of the electrode before testing were reported. The morphology is characteristic of nanowires (NWs), which exhibit an almost uniform cylindrical shape that replicates the nanochannel of the polycarbonate membrane used as the template. **Figure 4.3A** shows the top view of the nanostructured electrode, **Figures 4.3B and 4.3C** the cross-sectional views, and **Figure 4.3D** the tilted top view. In Figure 4.3A, it can be observed that the Ni current collector is evenly covered by NiFe NWs. The Ni collector, approximately 12 μm thick, is continuous, uniform, and free of cracks or fractures. The interconnections between different wires, seen in Figures 4.3A and 4.3D, are characteristic of the polycarbonate template. Figures 4.3B and 4.3C reveal that the NWs are firmly anchored to the current collector. These NWs have low surface roughness, with diameters ranging from 220 to 250 nm and lengths of 12 μm. Some broken NWs, as seen in Figure 4.3C, are due to the sample preparation for SEM analysis, where a section of the sample was simply torn off.

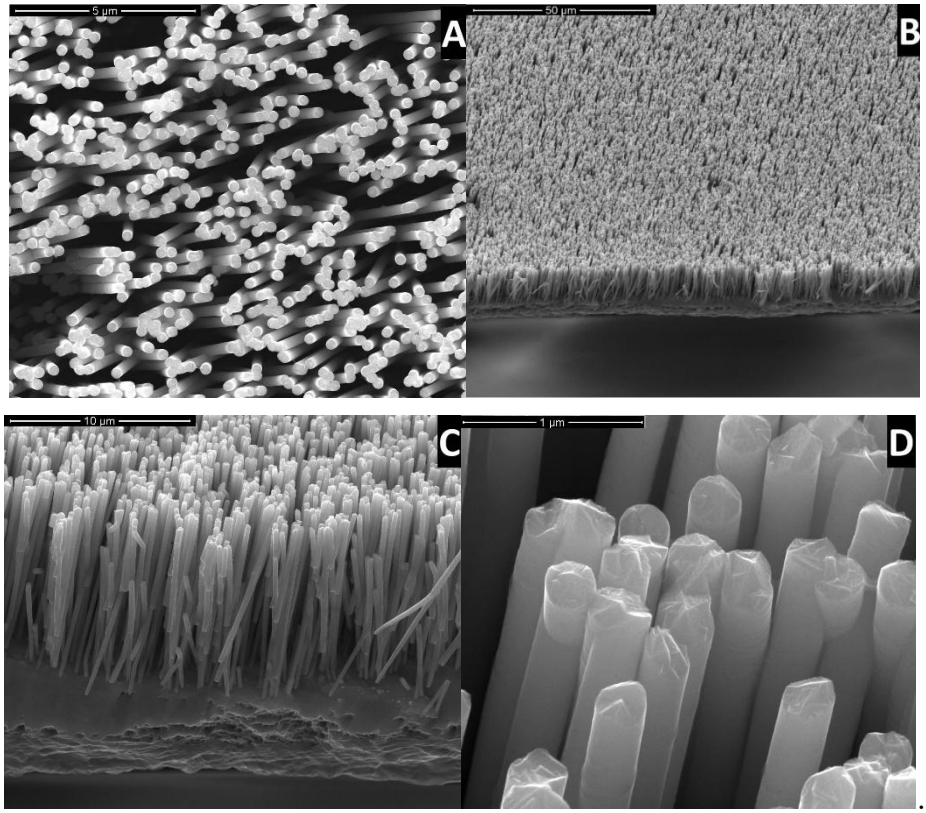

***Fig. 4.3**. (**A-D**) SEM images of NiFe NWs electrode before long-term stability test. (**A**) top view; (**B-C**) tilted cross-sectional view and (**D**) tilted top view*

The electrochemical and electrocatalytic behavior of NiFe-based electrodes was studied in KOH+NaCl to evaluate the possible use of the NiFe NWs electrodes in seawater, and the results were compared with those obtained in KOH. First of all, CVs at different scan rates were performed to calculate the specific capacitance by the double-layer capacitance method [33]. CVs were carried out with a scan rate from 20 to 40 mV s^{-1} in the potential range from 0.82 V to 1.02 V vs RHE, where no reactions occurred. An example of CVs curves in this potential range is shown in **Figure 4.4A**. This test was also carried out on a Ni planar sheet, for comparison. For each scan rate, the anodic

and cathodic current density at 0.975 V vs. RHE, were measured, and the difference was calculated and plotted vs. the scan rate. The slope of the linear fit represents the specific capacitance that is related to the real active surface area of the electrode.

Figure 4.4B shows that the slope for NiFe is greater than the slope of Ni sheet, both for KOH and KOH+NaCl. Comparable values were obtained in both solutions. Thus, from planar electrodes to nanostructured ones, the real electrode surface area increases (about 7.8 times). This value is plausible because it is comparable (the total surface area of NWs is 6.26 cm^2, 10.4 times higher than the geometrical one) with the value calculated using the method proposed in [34] based on the analysis of SEM images. Considering the result obtained with the double-layer capacitance method, a specific load on the total surface area of about 0.424 mg/cm2 can be qualitatively estimated. From the result of **Fig. 4.4B**, it can be concluded that the NiFe NWs are able to provide higher electrochemical active surface area and, thus more active sites than planar electrodes, improving electrode catalytic activity [35].

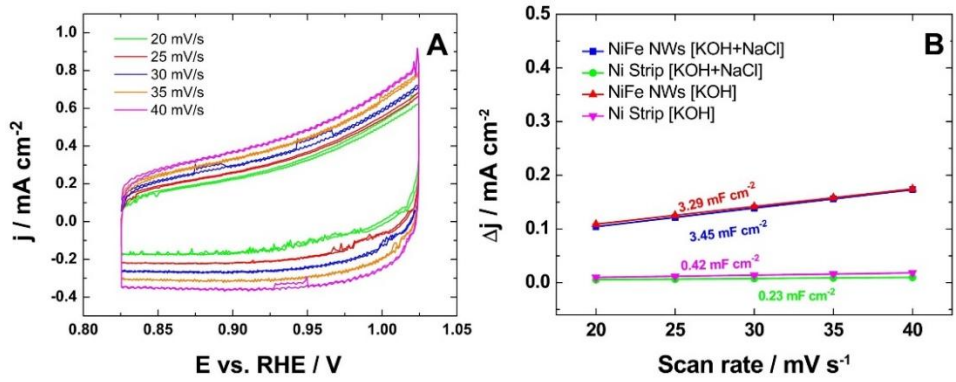

Fig. 4.4 *(**A**) Example of CVs in the range 0.82-1.02 V vs. RHE; (**B**)Specific capacitance of the electrodes evaluated by double layer capacitance method: pink) Ni Strip in KOH and green) in KOH+NaCl; red) NiFe NWs in KOH and blue) in KOH+NaCl.*

QSSP tests were performed for both HER (**Fig. 4.5A**) and OER (**Fig. 4.5B**), analyzing a potential range of 0.7 V with a scan rate of 0.1667 mV s^{-1}. The QSSP curves recorded in the KOH+NaCl solution show minimal differences compared to those recorded in the pure KOH solution. These slight variations can be attributed to the increased conductivity of the solution caused by the addition of NaCl. The overpotentials (η) required to achieve current densities of 10 mA cm^{-2} (η10) and 100 mA cm^{-2} (η100) for both HER and OER were also measured and are presented in **Fig. 4.5C and 4.5D**. These values are significant as they are commonly used to assess and compare the electrocatalytic activity of different catalysts [15]. In particular, to reach a current density of 10 mA cm^{-2} (often considered the benchmark for comparison) the overpotential values in the KOH+NaCl solution were found to be -211 mV for HER and 289 mV for OER. These values are slightly lower than those recorded in the KOH solution alone. Additionally, when compared to the literature (see **Table 4.3**), the results are consistent with many other NiFe-based electrodes and exhibit better performance than a planar Ni strip. This indicates that the nanostructured electrodes fabricated in this study exhibit good catalytic activity.

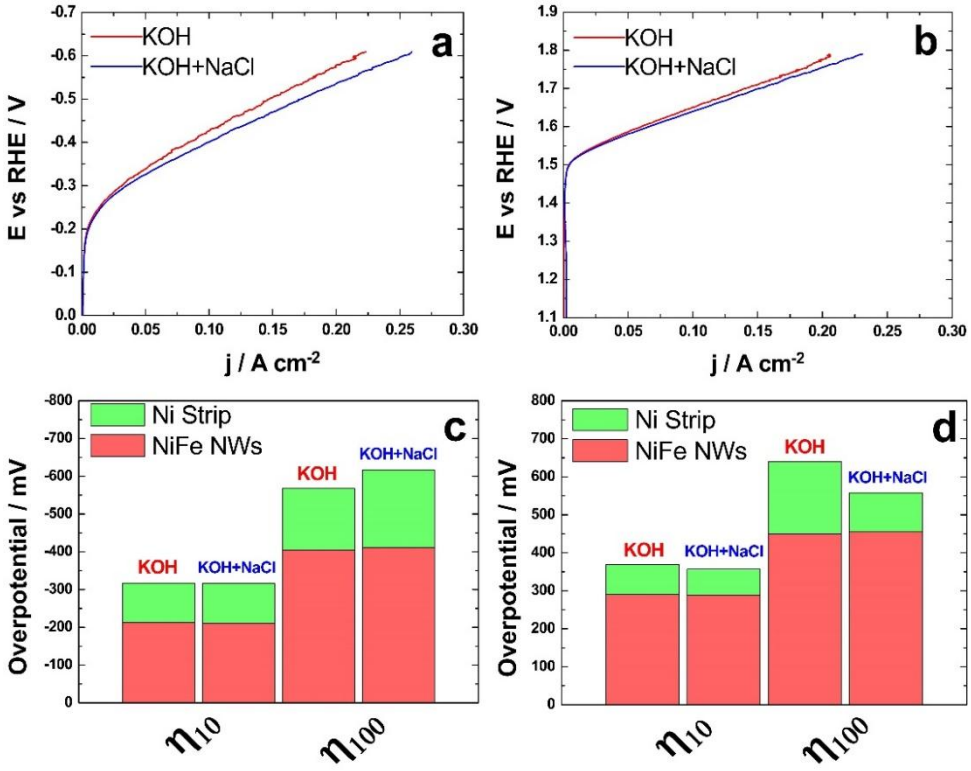

Fig.4.5 *QSSP for (**A**) HER and (**B**) OER at 0.1667 mV s^{-1} in KOH+NaCl (blue) and in KOH (red) aqueous solution. Values of η10 and η100 for HER (**C**) and OER (**D**).*

The linear range of the QSSP curves (**Fig.4.6**) was fitted using the Tafel's equation:

$\eta = a + b \log i$

where *a* corresponds to the exchange current density, and *b* represents the slope of the Tafel curve. The fitting procedure follows the approach outlined in previous studies[14]. The Tafel slope is a key indicator of catalyst performance.

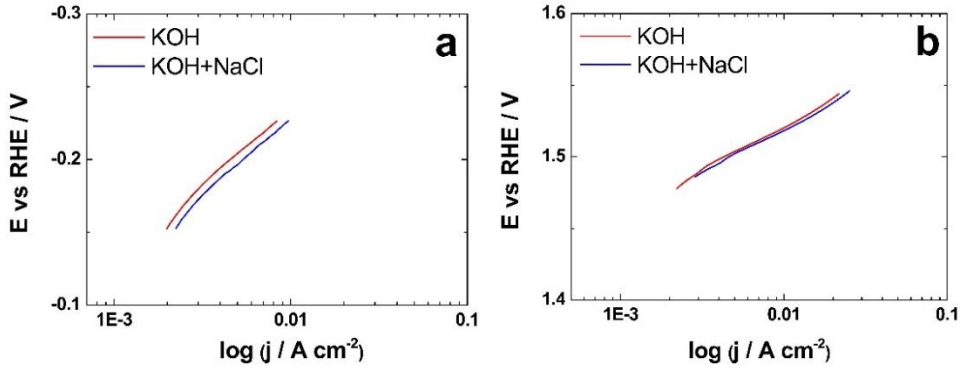

Fig. 4.6 *Linearity range of QSSP curves for both (**A**) HER and (**B**) OER in KOH+NaCl (blue) and in KOH (red) aqueous solution.*

The Tafel parameters are listed in **Table 4.2**, and they indicate strong performance for both HER and OER. These values align well with those of NiFe-based catalysts reported in the literature [36], [37], [38] (see **Table 4.3**). Additionally, as demonstrated in [17], the nanostructured NiFe alloy shows superior performance compared to pure nickel or iron nanowires (NWs), and significantly outperforms a flat nickel sheet. In the case of the Ni sheet, the improved results with NWs are largely due to the increased active surface area, which ensures a greater number of active sites for electrochemical reactions [39], [40], [41]. The nanostructured alloy also exhibits better performance than its pure components. This is particularly notable for OER, where a lower Tafel slope indicates higher catalytic activity [42]. As noted by Louie et al. [22], the presence of Fe in the alloy influences the redox properties of Ni, which catalyzes OER. They observed that higher Fe content shifts the redox potential of the $Ni(OH)_2/NiOOH$ reaction to more anodic values, which lowers the average oxidation state of Ni and enhances its activity for OER.

Importantly, the Tafel parameters in KOH+NaCl solution are nearly identical to those in pure KOH, suggesting that the addition of NaCl does not adversely affect the electrocatalytic behavior of the NiFe nanostructured electrodes. The Tafel slope for HER, around 120 mV, indicates that the Volmer step is the rate-limiting step [39]. For OER, a slope of approximately 50 mV suggests that the adsorption of hydroxide ions onto the active sites is the rate-determining step [42].

Table 4.2 *Fitted Tafel's parameters for HER and OER in KOH and KOH+NaCl solutions*

Solution	***HER***			***OER***		
	a (V)	**b (V)**	**R^2 (%)**	**a (V)**	**b (V)**	**R^2 (%)**
KOH	-0.46	-0.114	99.2	1.62	0.055	99.6
KOH+NaCl	-0.45	-0.110	99.4	1.63	0.053	99.8

Table 4.3 *Comparison between the state of the art on NiFe-based electrodes and our nanostructured NiFe electrode*

Catalysts	**Reaction**	**KOH** Working Temperature	**Tafel Slope**	**Catalyst loading [$mgcm^{-2}$]**	**OverPotential for 10 $mAcm^{-2}$ [mV]**	**Mass activity at 10 mA cm^{-2} [A mg^{-1}]**	**Ref.**
Ni_2Fe	HER	1 M Room temperature	162	0.2	-231	0.05	[43]
$NiFe_2O_4$	HER	0.1 M 22 ± 2°C	130	2.2	-330	0.0045	[44]
NiFe LDH/NF	HER	1 M	-138	2	-250	0.005	[45]

		Room temperature					
Ni-$Fe(OH)_x$/ NF	HER	1 M Room temperature	-135	8	-170	0.00125	[46]
NiFe-LDH@$FeNi_3$	HER	1M Room temperature	-175.8	0.84	-157	0.00012	[47]
NiFe NWs	HER	30 % w/w Room temperature	-114	3.31	-210	0.003	TW
FeNiP-NP	OER	1 M Room Temperature	76	4.12	180	0.00243	[48]
Ni2Fe1-O	OER	1 M 70°C	39	0.15	244	0.0667	[49]
NiFe-NS	OER	1 M	45	1	302	0.143	[50]
NiFeOx/ CFP	OER	1 M	85	1.6	230	0.00625	[51]
NiFe Oxide	OER	0.1 M Room temperature	40	-	300	-	[22]
NiFe LDH	OER	1 M	31	0.2	260	0.05	[21]

FexNi1–xO	OER	0.5 M	37	-	277	-	[20]
nNiFe LDH/NGF	OER	1 M Room Temperature	47	8	260	0.00125	[46]
NiFe LDH	OER	1 M 50° C	60	2.5	400	0.004	[52]
FeNi/$NiFe_2O_4$@NC−800	OER	1M	91	0.13	310	0.076	[53]
$NiFe_2O_4$	OER	1 M Room temperature	40	-	350	-	[54]
NiFe LDH	OER	0.1 M Room temperature	50	0.1	359	0.1	[37]
NiFe LDH	OER	0.1M KOH+ 0.5M NaCl Room temperature	51	0.1	360	0.1	[37]
NiFe NWs	**OER**	**30 % w/w** Room Temperature	**45**	**3.31**	**290**	**0.003**	**TW**
NiFe NWs	**OER**	**30 %w/w +0.5M NaCl**	**43**	**3.31**	**289**	**0.003**	**TW**

		Room Temperature					

The turnover frequency (TOF) values, listed in **Table 4.4**, were calculated using the following equation:

$$TOF = iA/xnF$$

where i represents the current density (A/cm²) measured at a specific overpotential, A is the geometric surface area of the electrode (cm²), F is the Faraday constant (96,485 C/mol), and x is the number of electrons transferred per molecule of gas produced (x = 2 for HER, x = 4 for OER). For comparison, the TOF values for both HER and OER on a flat nickel sheet were also reported.

Table 4.4 *TOF values for NiFe NWs and Ni planar strip.*

	TOF $[s^{-1}]$ *HER per* η*=400 mV*	***TOF*** $[s^{-1}]$ *OER per* η*=400 mV*
Ni strip KOH	$6.62*10^{-5}$	$2.5*10^{-5}$
Ni strip KOH+NaCl	$2.28*10^{-5}$	$3.31*10^{-5}$
NiFe NWs KOH	0.007	0.00366
NiFe NWs KOH+NaCl	0.0089	0.0041

The TOF is a key metric for evaluating the impact of catalyst morphology on its activity [55], [56], as it is directly related to the number of active sites in the electrocatalyst. The calculated TOF for the nanostructured NiFe alloy was found to be higher than that of the flat Ni sheet. According to Silva et al. [55],

this improvement is attributed to the significantly higher availability of active sites in the nanostructured alloy. The TOF values calculated at η400 are comparable to those reported for other NiFe-based electrodes [56].

Galvanostatic step polarization tests were also conducted to investigate electrode behavior at different current densities. Various constant current densities (0.01, 0.02, 0.05, 0.1, 0.2, and 0.5 A/cm²) were applied for five minutes each. The average potential value for each current density is plotted, providing insights into the overall performance under different operating conditions. As shown in **Fig.4.7**, the NiFe NWs catalyst demonstrates excellent catalytic activity for both the hydrogen evolution reaction (HER) and oxygen evolution reaction (OER). The performance of the catalyst in the KOH+NaCl solution is nearly identical to its performance in pure KOH electrolyte. For the anodic reaction (OER), this result suggests selective oxygen evolution in the tested conditions. At a current density of 10 mA/cm², the potentials in KOH+NaCl are approximately -0.21 V and 1.53 V vs. RHE for HER and OER, respectively.

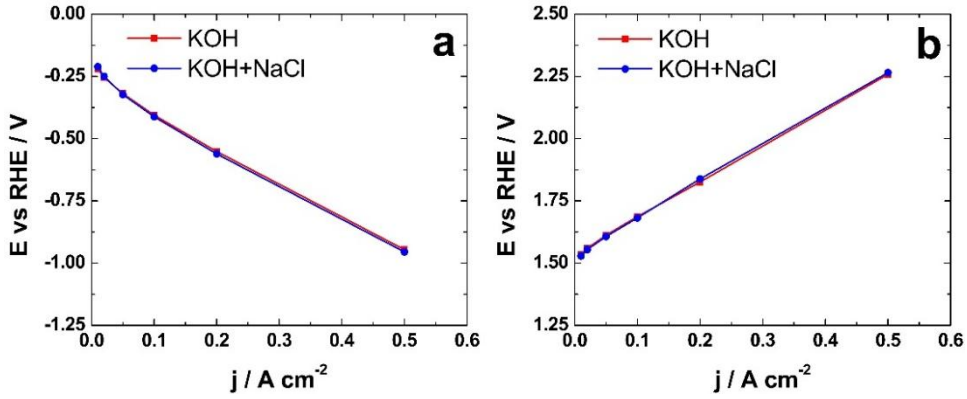

Fig. 4.7 *Galvanostatic-step polarization for (**A**) HER and (**B**) OER in KOH+NaCl (blue) and in KOH (red) aqueous solution.*

To assess the mid-term behavior of the nanostructured electrodes, a constant current density of -50 mA/cm² for HER and 50 mA/cm² for OER was applied over 6 hours. The results, **Fig. 4.8**, show that the potential remained stable throughout the test. For HER in KOH+NaCl, the potential began at -0.32 V vs. RHE and concluded at -0.335 V vs. RHE, reflecting a minor loss of 15 mV, which indicates promising stability. The OER test also showed good electrode stability, with only a 10 mV loss and a final potential of 1.61 V.

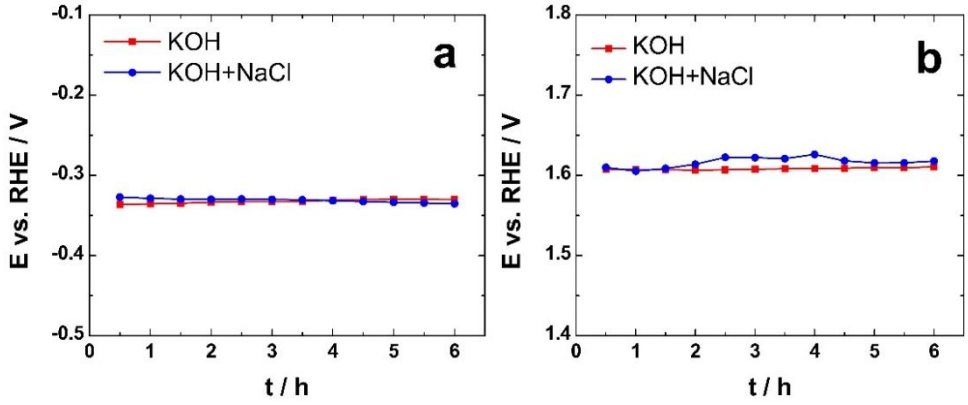

Fig. 4.8 *Mid-term stability test for 6 hours for (**A**) HER at −50 mA cm^{-2} and (**B**) OER at 50 mA cm^{-2} in KOH+NaCl (blue) and in KOH (red) aqueous solution.*

For a more thorough evaluation of electrode stability, the test was extended to 125 hours. As shown in **Fig. 4.9A**, the cathodic potential for HER in KOH+NaCl remained nearly constant at -0.33 V vs. RHE throughout the experiment. Similarly, the OER potential started with closely overlapping curves in both solutions. After 75 hours, the potential in KOH+NaCl became slightly higher than in KOH, with a final value of 1.63 V vs. RHE (**Fig. 4.9B**). Importantly, this value is lower than the standard reduction potential for hypochlorite formation. Specifically, at pH 14, the standard electrode potential for the following reaction is 1.714 V vs. RHE [57].

$2OH^- + Cl^- \rightarrow ClO^- + H_2O + 2e^-$

Therefore, the potential for Cl^- oxidation was not reached, and only OER occurred in the KOH+NaCl solution [9].

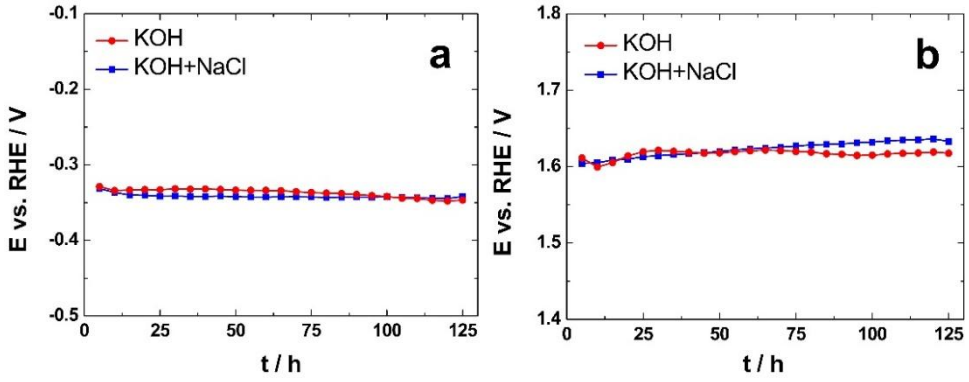

Fig.4.9 *Long-term stability test for 125 hours for (**A**) HER at -50 mA cm^{-2} and (**B**) OER at 50 mA cm^{-2} in KOH+NaCl (blue) and in KOH (red) aqueous solution.*

The electrolytic solution after the long-term stability tests was analysed to verify the absence of hypochlorite, ClO^-, and other chlorine compounds such as hypochlorous acid, HClO, chlorate, ClO_3^-, and perchlorate, ClO_4^-, in. As presented in **Fig. 4.10**, standard solutions of ClO^- and HClO, and the electrolytic solution before and after the long-term stability test, were analysed. In agreement with literature reports [58] wavelengths for ClO^- and $HClO^-$ absorbance were 294 nm and 235/289 nm, correspondingly. As expected, no absorbance for ClO^- or HClO was detected, confirming that they were not formed.

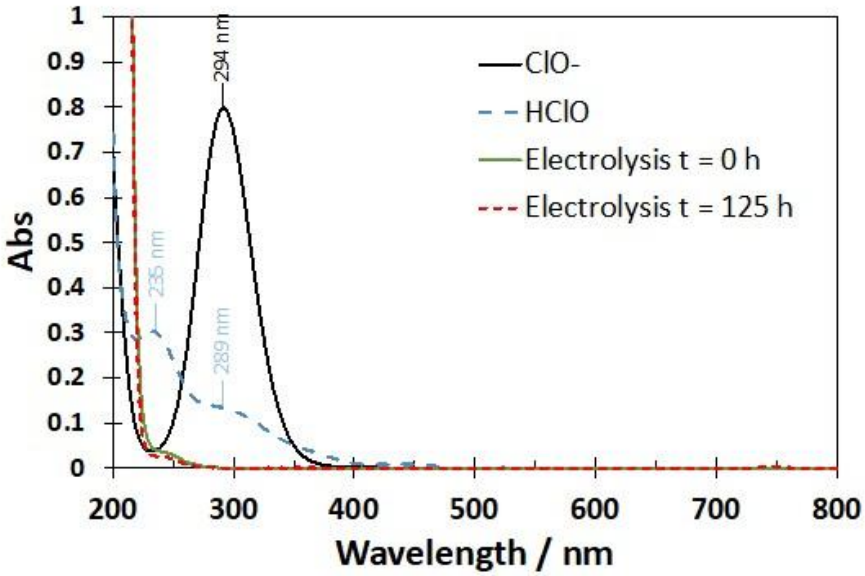

Fig. 4.10 *UV-Vis spectra of water solution of ClO^-, HClO and of the electrolytic solution before (t = 0 hours) and after (t = 125 hours) the long-term galvanostatic tests.*

Fig. 4.11 shows the chromatograms of the standard ClO_3^- and ClO_4^- solutions alongside the electrolytic solution before and after the long-term test. The only observed peak, at approximately 9 minutes retention time, corresponded to chloride ions, with no evidence of ClO_3^- or ClO_4^-. These findings confirm the selectivity of NiFe NWs electrodes for OER in seawater electrolysis and are consistent with other studies of NiFe-based catalysts [37], [59], [60].

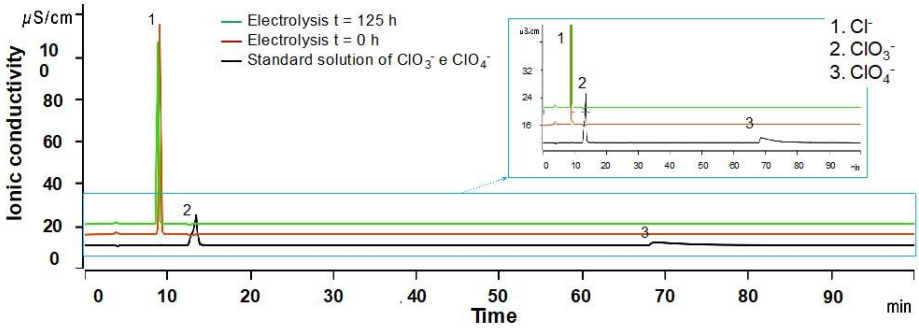

***Fig. 4.11**. IC chromatogram of aqueous solution of ClO_3^- and ClO_4^- and of the electrolytic solution before (t = 0 hours) and after (t = 125 h) the long-term galvanostatic tests.*

After the long-term stability test in the KOH+NaCl solution, no significant changes were observed in either the morphology or composition of the NWs, both for the electrodes used in HER (**Fig. 4.12A and C**) and OER (**Fig. 4.12B and D**). SEM images (**Fig. 4.12A and B**) revealed that the morphology of NWs remained stable without any signs of collapse, indicating that these nanostructured arrays are highly stable. Additionally, only Ni and Fe peaks were detected in the EDS spectra (**Fig. 4.12C and D**). The potassium peak in Fig. 4.12D results from traces of KOH precipitated on the electrode when it was removed from the electrolysis cell and dried in air. These findings suggest that the NiFe NW-based electrodes exhibit long-term durability.

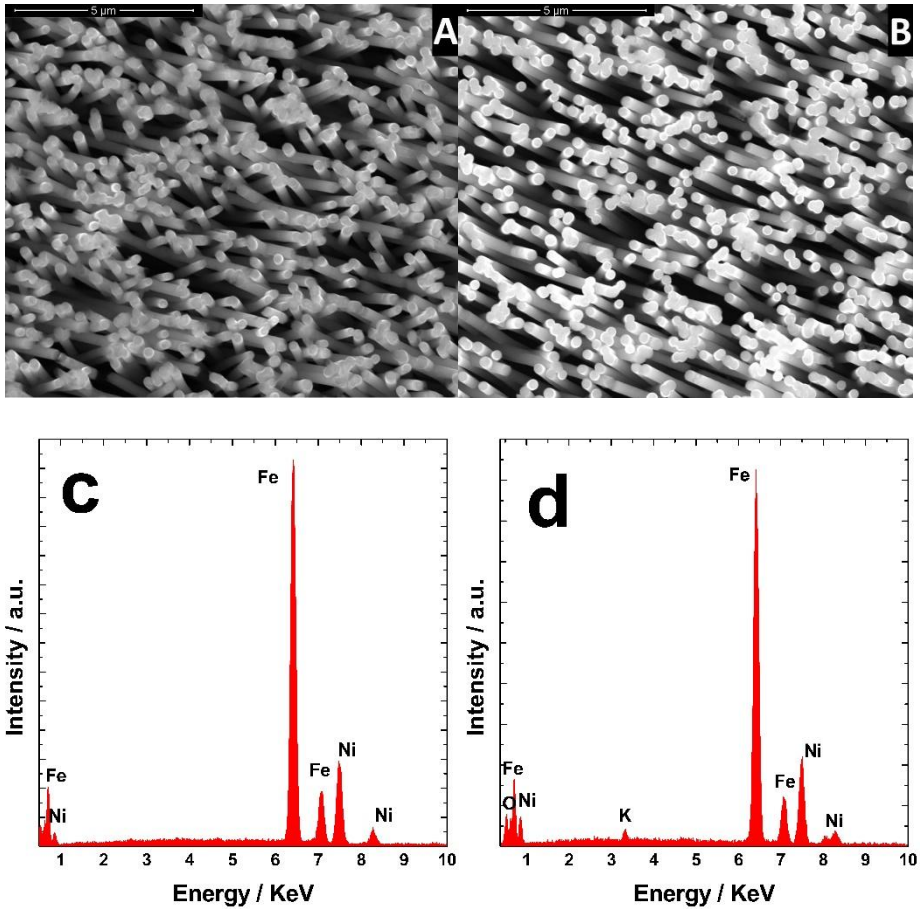

Fig. 4.12. *SEM images and EDS of NiFe NWs electrodes after long-term stability test in KOH+NaCl: (**A,C**) HER and (**B,D**) OER*

Further confirmation can be seen in the XRD analysis of the nanostructured electrodes in **Fig. 4.13**. The peaks of the as-prepared electrode appeared at about 43.23°, 50.38°, 74.18°, and 90.16° corresponding to reflections from the (111), (200), (220), and (311) planes of the face-centered cubic structure of the Fe-Ni alloy (card no. 47-1405) [28], [61], [62]. The high intensity of the (200) reflection indicates a preferred orientation of NiFe NWs in the 〈100〉 direction. This behavior was also predicted and confirmed by theoretical calculations for Au and Cu NWs produced by pulsed electrodeposition into

polycarbonate membranes [63]. As described in the experimental section, NiFe NWs were fabricated by switching the potential between −1.35 V and −0.65 V vs. SCE, which causes a reversal of the deposition current density and promotes preferential growth in the 〈100〉 direction. This orientation is driven by the preferential dissolution of surfaces in other directions during the anodic current pulse. Peaks from the Ni current collector were also detected at 44.53°, 51.86°, and 76.37°, corresponding to the α-Ni face-centered cubic structure (card no. 04-850) and the reflections from (111), (200), and (220) planes. The XRD spectra remained essentially unchanged after long-term stability testing, confirming the findings from SEM and EDS and further demonstrating the stability of the nanostructured NiFe electrodes

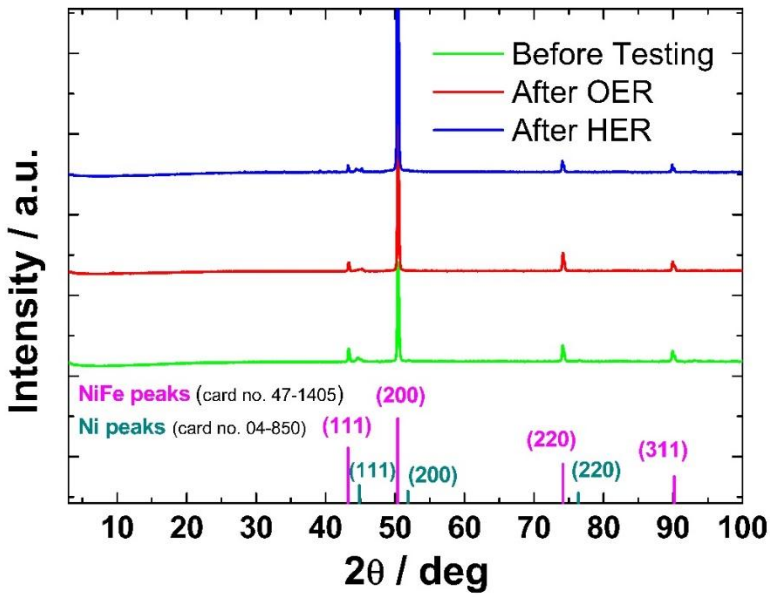

Fig. 4.13 *XRD patterns of NiFe NWs electrodes: green) before testing; red) after long-term stability test HER in KOH+NaCl; and blue) after a long-term stability test OER in KOH+NaCl*

The surface of NWs was characterized using XPS both before and after the long-term stability test for the OER in a KOH+NaCl solution (**Fig. 4.14, Table 4.5**). Both electrons and ion guns were used for charge neutralization. Survey spectra (Pass Energy = 117.400 eV; resolution = 1.0 eV) and high-resolution spectra (Pass Energy = 29.350 eV; resolution = 0.05 eV) were recorded in the Ni $2p_{3/2}$, Fe $2p_{3/2}$, and C 1s regions for the NiFe samples before and after the tests. A direct comparison of the quantitative surface analysis is challenging, primarily due to differences in air exposure of the samples, which affects the adventitious carbon content, and due to the non-homogeneous nature of the samples. The presence of NWs may influence the inelastic mean free path of the electrons within the analyzed samples, allowing the collection of electrons from deeper layers.

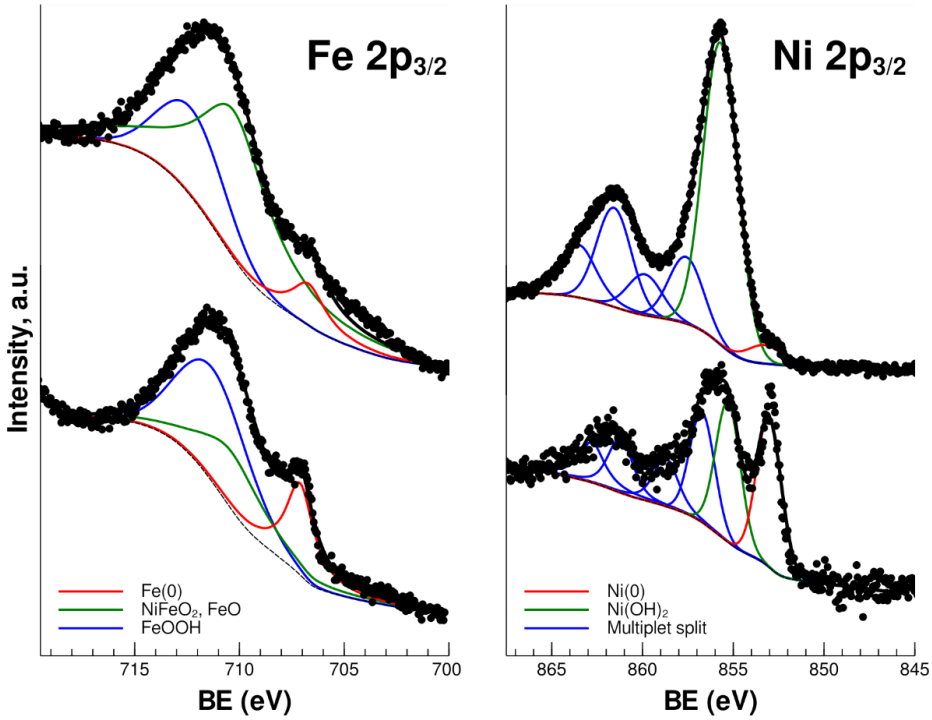

Fig. 4.14 *XPS spectra in the Fe $2p_{3/2}$ (left) and Ni $2p_{3/2}$ (right) regions, before (bottom) and after the long-term stability test (top).*

***Table 4.5**. XPS results.*

Quantitative (at%)

	C	O	Cl	K	Fe	Ni
NiFe-pre	11 ± 2	61 ± 12	0.38 ± 0.08	1.5 ± 0.3	7 ± 1	19 ± 4
NiFe-post	54 ± 11	35 ± 7			6 ± 1	4.5 ± 0.9

C 1s

	BE (eV)	%	Assignment
NiFe-pre	282.95	10.61	Metal carbide
	284.80	70.09	C−C/C−H
	286.28	9.86	C−O
	288.85	5.64	O=C−O
	290.87	3.80	Carbonate
NiFe-post	284.80	28.34	C−C/C−H
	285.48	54.58	C−O
	289.05	17.08	Carbonate

O 1s

	BE (eV)	%	Assignment
NiFe-pre	528.51	0.90	Chemisorbed O_2
	530.28	40.97	FeO, NiO, $NiFeO_2$
	531.73	32.29	$Ni(OH)_2$, FeOOH
	532.76	17.66	Physisorbed H_2O
	533.92	8.18	

NiFe-post	528.63	3.15	Chemisorbed O_2
	530.03	30.09	FeO, NiO, $NiFeO_2$
	531.38	61.77	$Ni(OH)_2$, FeOOH
	532.66	5.00	Physisorbed H_2O

Cl 2p

	BE (eV)	**%**	**Assignment**
NiFe-post	198.09, 199.69	100	Chloride

Fe $2p_{3/2}$

	BE (eV)	**%**	**Assignment**
NiFe-pre	707.11	23.11	Fe(0)
	710.32	29.09	$NiFeO_2$, FeO
	711.25	47.80	FeOOH
NiFe-post	706.70	9.4	Fe(0)
	710.25	66.56	$NiFeO_2$, FeO
	712.28	24.40	FeOOH

Ni $2p_{3/2}$

	BE (eV)	**%**	**Assignment**
NiFe-pre	853.03	25.72	Ni(0)
	855.29	24.14	$Ni(OH)_2$
	856.71	19.03	Multiplet split
	858.71	9.88	
	861.21	11.23	
	862.78	9.99	
NiFe-post	853.28	3.15	Ni(0)
	855.70	51.18	$Ni(OH)_2$
	857.60	11.32	Multiplet split

859.87	6.95
861.57	16.80
863.49	10.61

Results showed that, after the long-term stability test in KOH+NaCl, both K and Cl were present on the electrode surface. The detected chlorine was exclusively in the form of chloride. The C 1s region also indicated carbonate species that precipitated on the electrode surface after the stability test. In the case of metallic components, the Fe and Ni were in different chemical environments. The as-prepared electrode showed a distribution of metallic Fe (about 23%), Fe(II) (FeO, NiFeO2), and Fe(III) (FeOOH) species. The satellite feature around 720 eV also indicated the presence of high-spin Fe(III) compounds. Distribution of this nature remained after the long-term stability test in KOH+NaCl to a limited extent; overall Fe distribution shifted upon decreasing the Fe(0) content to about 9% and diminishing the intensity of the satellite feature, which suggested a reduction of Fe(III) content.In the Ni $2p^{3/2}$ spectra (**Fig. 4.14, right**), it can be observed that after the long-term stability test, the surface of the electrode nanowires is primarily composed of oxidized Ni, predominantly in the form of $Ni(OH)_2$. To avoid introducing calculation artifacts, the spectral analysis focused mainly on the principal peaks of the species, while the expected multiplet pattern of Ni was regarded as a combination of contributions from all observed species. The observed changes in the multiplet pattern before and after the long-term stability test can be attributed to a non-homogeneous distribution of Ni-oxidized sites. Our findings are further supported by the O 1s region analysis, which also indicated the presence of physisorbed H_2O and chemisorbed O_2.

4.4 Behaviour of NiFe NWs electrodes at different Temperature

QSSP, CVs, Galvanostatic Step and Mid-Term Stability Test were carried out at 40°C and 60°C in a 30 wt% potassium hydroxide aqueous solution and the performances were compared with those obtained at room temperature, 25°C. CVs were carried out from 10 to 35 mV s^{-1} in a very small potential range, 0.64-0.74 V vs. RHE where no faradic reaction takes place. While the temperature does not influence the electrochemically active area, the tests were performed at three different temperatures to further examine the stability of the nanowires under different temperatures. As expected, ECSA of NWs is independent of temperature, and for the three cases, the slope is around 3.37 mF cm^{-2}, see **figure 4.15**. The CVs were repeated over a different potential range compared to the previous test (see Figure 4.4), but the results obtained are very similar, suggesting good reliability of the data obtained.

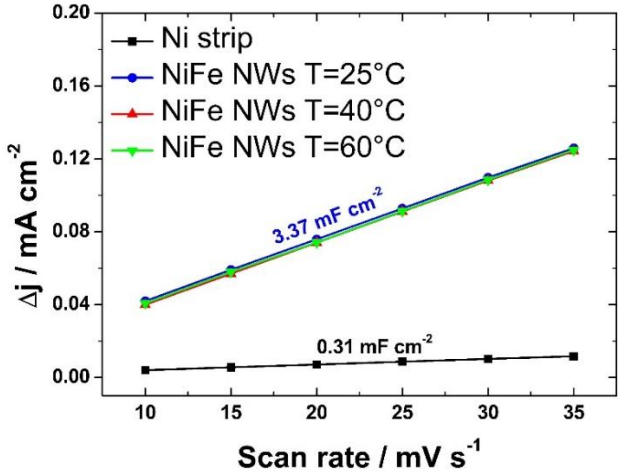

***Fig.4.15**. Specific capacitance of the electrodes evaluated by double layer capacitance method: black) Ni strip; blue) NiFe NWs at 25°C; red) NiFe NWs at 40°C; green) NiFe NWs at 60°C.*

Each QSSP, Galvanostatic step polarization and mid-term stability tests were conducted at progressively increasing temperatures of 25°C, 40°C, and 60°C for both HER and OER, **Figures 4.16A** and **4.16B**. The temperature rise significantly influences the current density response this is due to both the increase in electrolyte conductivity and the reaction kinetics [64], [65].

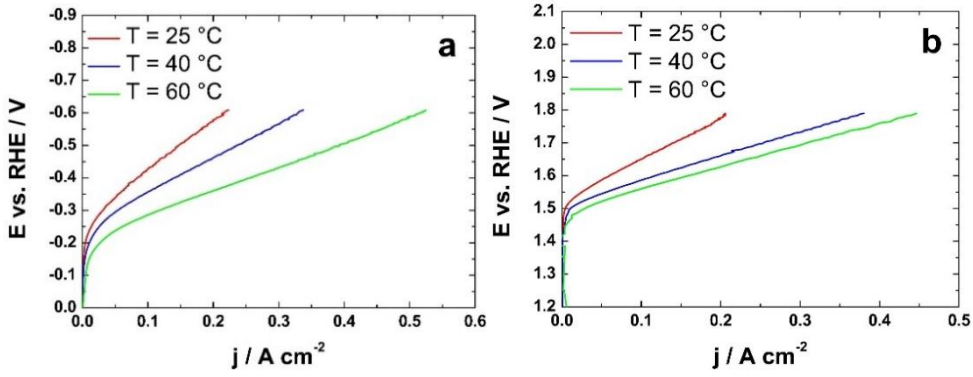

Fig. 4.16 *QSSP for (**A**) HER and (**B**) OER at 0.1667 mV s^{-1} relative to the three temperatures*

The linear range of the curves was plotted on a logarithmic scale (log j vs. V) to facilitate a fitting operation within the linear range of the curves. The Tafel parameters, **Table 4.6**, across the different tests, show minimal variation. This can be attributed to the fact that the temperature rise significantly reduces ohmic losses, which are particularly pronounced at high current densities. At lower current densities, the curves remain closely aligned; however, at higher current densities, a distinct separation emerges. Specifically, for a given applied potential, the recorded current density increases with temperature, peaking for the test conducted at 60°C.

Tab. 4.6 *Fitted Tafel's parameters*

Temperature	**HER**			**OER**		
	a (V)	**b (V)**	**R^2 (%)**	**a (V)**	**b (V)**	**R^2 (%)**
25 °C	-0.47	-0.120	99.17	1.62	0.055	99.6
40 °C	-0.44	0.119	99.6	1.56	0.053	98.7
60 °C	-0.41	0.118	99.8	1.55	0.049	99.1

The galvanostatic step test, **figure 4.17**, showed that, at the same current density, the potential decreases with rising temperature, reaching a minimum for the tests at 60°C, [66]. This decrease in overvoltage makes the process more thermodynamically feasible, as it lowers the energy requirement for the system while simultaneously enhancing its efficiency.

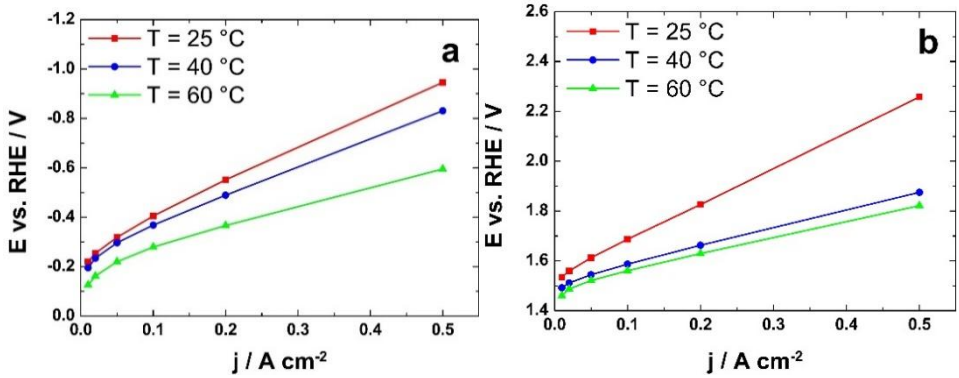

Fig. 4.17 *Galvanostatic Step polarization for (**A**) HER and (**B**) OER relative to the three temperatures*

The galvanostatic tests at a constant current density of 50 mA cm^{-2} for 6 hours were also performed. As expected, a notable reduction in recorded potential is anticipated with increasing temperature, **Figure 4.18.** The electrodes demonstrate excellent medium-term stability, with the curves remaining nearly constant and showing minimal potential drops. According to Nagai et al, [67] the higher electrolyte temperature leads to increased bubble volume and reduced reversible potential. The increase in bubble volume is associated with both a direct rise in void fraction and a decrease in bubble rise velocity. Compared to the tests at room temperature, at 60°C, a decrease of the potential value of about 70 mV and about 90 mV was measured for HER for OER, respectively.

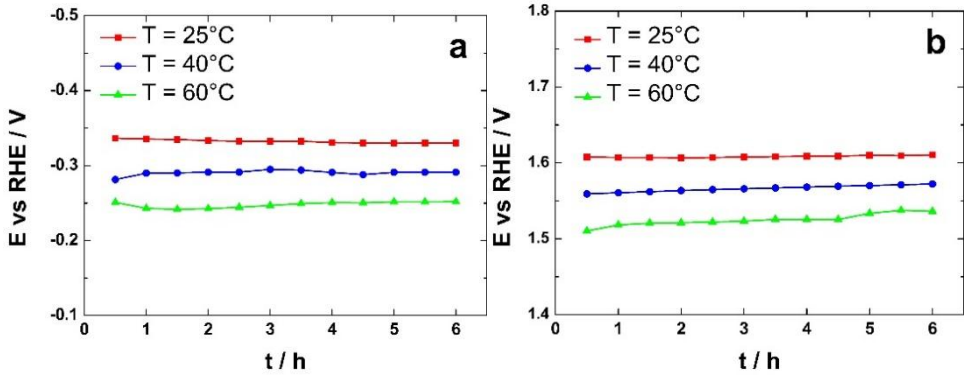

***Fig.4.18**. Mid-term stability test for 6 hours for (**A**) HER at -50 mA cm^{-2} and (**B**) OER at +50 mA cm^{-2} relative to the three temperatures.*

SEM images of the electrodes after the tests carried out at 60°C are shown in **Figure 4.19**. In both cases, the nanostructure remained perfectly intact. The operation temperature did not damage the electrodes. The mechanical and electrochemical stability of the electrode at medium-high temperatures allows us to hypothesize possible applications of these electrodes in industrial

alkaline electrolyzers, usually working at temperatures other than room temperature.

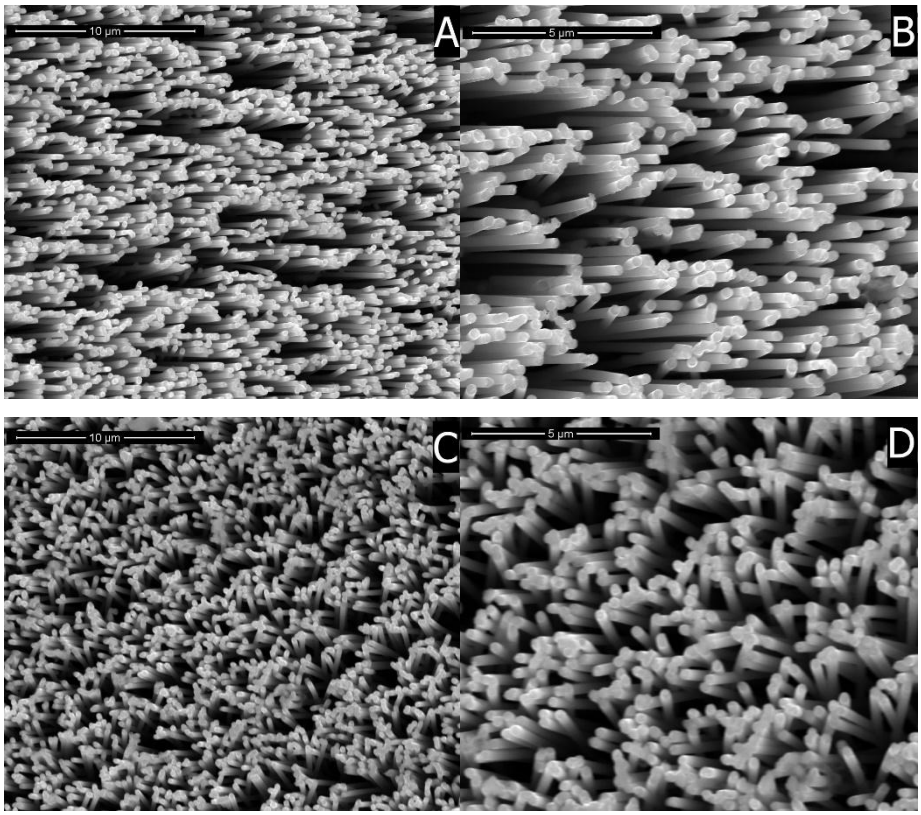

Fig. 4.19 *SEM images of NiFe NWs after galvanostatic test performed at 60°C (**A**) HER (10000x); (**B**) HER (20000x); (**C**) OER (10000x); (**D**) OER (20000x)*

Nanostructured electrodes were also characterized by XRD in the range 2θ 3-100°, after a galvanostatic test performed at 60°C**, Figure 4.20**. XRD spectra remains practically unchanged after long-term stability testing, confirming SEM results and thus the stability of the nanostructured NiFe electrodes.

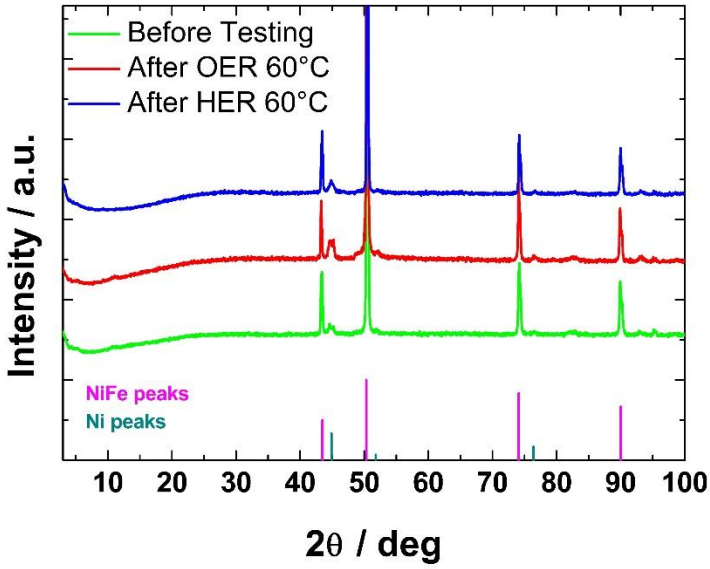

Fig. 4.20 *XRD pattern of NiFe NWs: green) before testing; red) After mid-term galvanostatic test OER at 60°C; blue) After mid-term galvanostatic test HER at 60°C*

The findings from this study indicate that raising the operating temperature of alkaline electrolyzers can significantly enhance both device performance and hydrogen output. However, increasing the temperature requires additional energy to exceed ambient levels

.

4.5 Overall Water Splitting

A scale-lab alkaline electrolyzer was constructed to test the overall water splitting. The scheme of the water electrolysis cell system is shown in the following image, **Fig. 4.21.** The system consists of an alkaline electrolyzer connected to a potentiostat to apply the desired current or potential, along with a pump that circulates the KOH solution, which is then recirculated through appropriate connections.

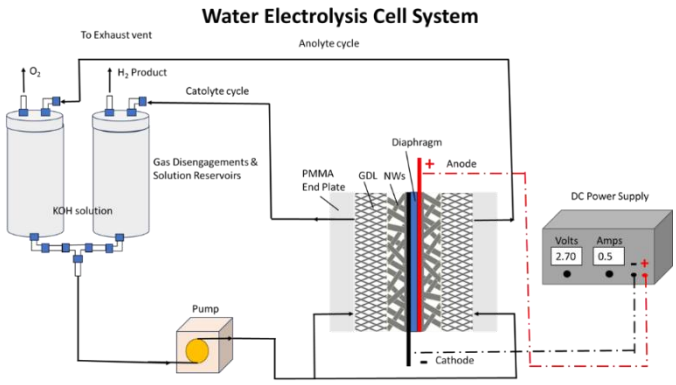

Fig. 4.21 *Water electrolysis cell system*

A small-gap electrolysis cell (AE) with an effective active area of 4 cm², as shown in **Figure 4.22** was fabricated from poly-methyl methacrylate (PMMA) plates which were designed and shaped with a laser cutter**.**

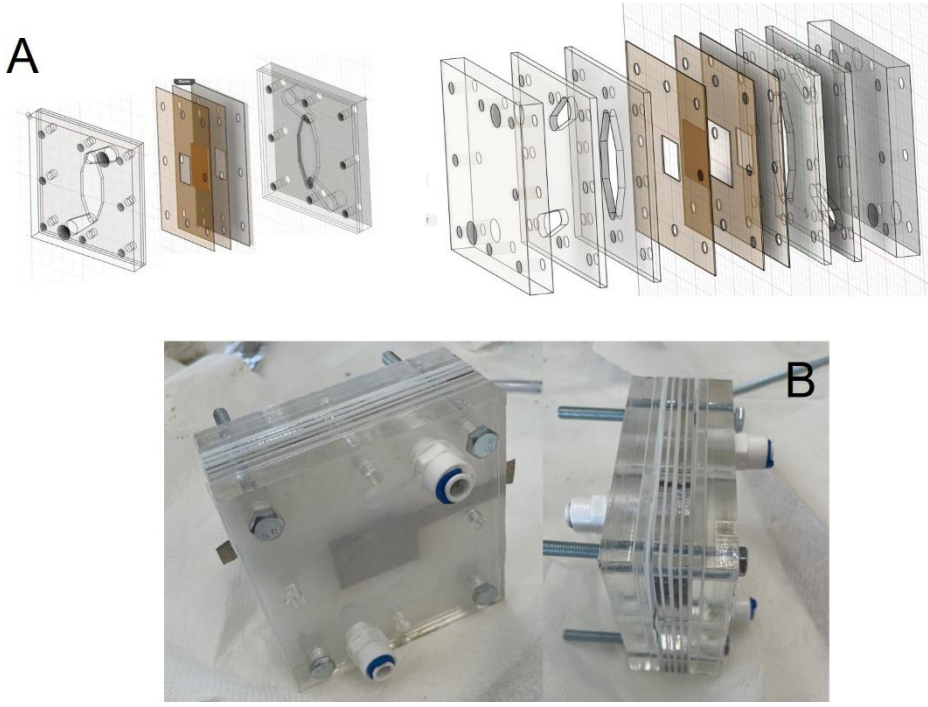

Fig. 4.22 *(**A**) Design and (**B**)Photograph of assembled PMMA electrolysis cell*

The laboratory prototype is shown in the following figures, **Figures 4.23,** where the system has been completed by connecting the electrolyzer to a gas separation and temperature control system.

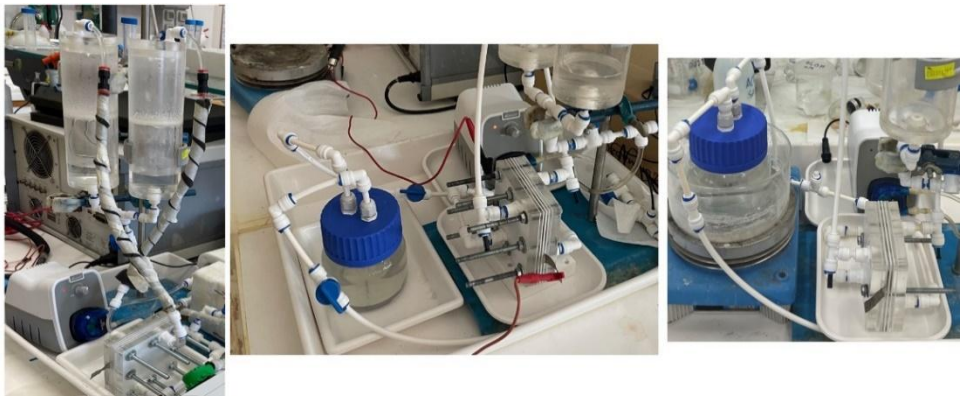

Fig. 4.23 *Scale-lab alkaline electrolyzer*

Two Ni plates were used as current collectors, while NiFe NWs served as both the anode and cathode electrodes. A Zirfon® diaphragm (Agfa Zirfon Perl UTP 500) was employed as a separator, and the gasket was made from polytetrafluoroethylene (PTFE) and shaped with a laser cutter. The electrolyte was circulated through the cell at a constant flow rate with the assistance of peristaltic pumps.

To test the functionality and sealing of the system, several electrochemical tests were conducted, including QSSP, GS, and stability tests at three different temperatures, 25°C. 40°C and 60°C. All these tests are shown in the **figure 4.24**.

QSSP curves were obtained in the potential range 1.3-3 V at 10 mV s^{-1}. The galvanostatic step curves replicate the trend of the QSSP curves. To reach a

current density of 500 mA cm^{-2}, the potential required decreases from 3V to 2.48 V, from 25 °C to 60°C. To study the stability of the electrodes and the ability of the lab-scale electrolyzer to work for a continuous operation, a current density of 50 mA cm^{-2} was imposed at the beginning for 6 hours. After the first hour, the potential reaches a constant value in all three tests, moving from 1.92 to 1.85 V. These results are very similar to those obtained when NiFe NWs were tested individually.

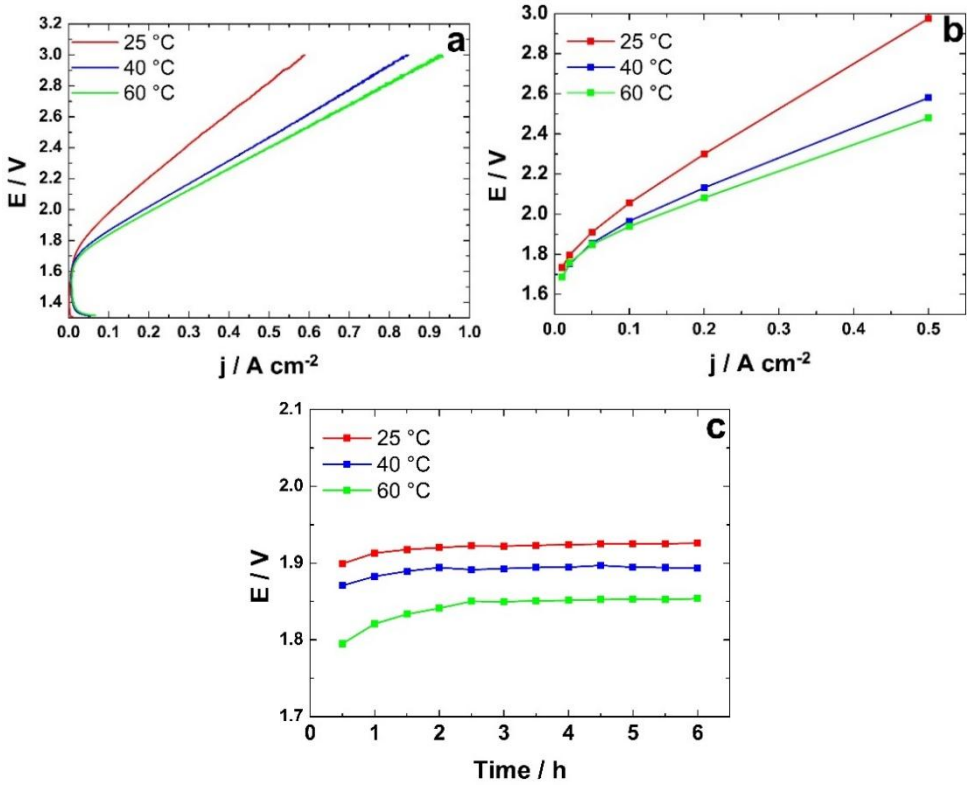

Fig. 4.24 *Electrochemical test of lab-scale electrolyzer (**A**) QSSP (**B**)Galvanostatic Step (**C**)Mid-term stability test*

4.6 Conclusions

In this section, nanostructured NiFe alloy electrodes were prepared by template electrosynthesis, a simple and cheap method. The alloy with a composition of about 79% Fe was used as both the cathode and anode. Electrodes were investigated in a 30% w/w KOH + 0.5 M NaCl solution for their possible applications in seawater electrolysis. For comparison, the behavior of electrodes in pure KOH is also tested. The electrochemical performance was evaluated through CV, QSSP and galvanostatic test polarization. Medium- and long-term galvanostatic tests have been carried out to investigate nanostructured electrode stability. Chemical and physical characterizations have been performed after long-term tests in order to highlight any change in the morphology or composition of the electrodes. Finally, KOH + 0.5 M NaCl solution, after testing was analyzed for the eventual formation of chlorine compounds at the anode.

The analysis indicates that the performance of the NiFe NWs described here is comparable to that of other NiFe-based electrodes reported in the literature. Moreover, the presence of NaCl did not significantly affect the electrocatalytic performance, as the results in KOH+NaCl were comparable to those in pure KOH. Additionally, post-experiment chemical and physical characterizations following long-term galvanostatic testing demonstrated that the nanostructured electrodes maintained stability in both morphology and composition. The electrolyte used in the galvanostatic tests was also analyzed to detect any potential formation of chlorine compounds. The absence of such compounds, along with the lower observed potential for the oxygen evolution reaction compared to the thermodynamic redox potential for hypochlorite formation, supports the conclusion that these electrodes show promise for use in seawater electrolysis.

In order to enhance the performance and evaluate the possible use of these electrodes in an industrial electrolyzer, the electrochemical tests were repeated at higher temperatures. As expected, a better result was obtained at 60°C confirming also good mechanical stability. In addition, NiFe NWs were tested in a lab-scale alkaline electrolyzer for overall water spitting. The prototype alkaline electrolyzer has demonstrated promising results, particularly in reproducing the performance of its electrodes when tested in a single-cell configuration. The system was designed to facilitate the efficient electrolysis of water while maintaining consistent hydrogen and oxygen production rates.

References

[1] D. Gielen, F. Boshell, D. Saygin, M. D. Bazilian, N. Wagner, e R. Gorini, «The role of renewable energy in the global energy transformation», *Energy Strategy Reviews*, vol. 24, pp. 38–50, apr. 2019, doi: 10.1016/j.esr.2019.01.006.

[2] P. A. Owusu e S. Asumadu-Sarkodie, «A review of renewable energy sources, sustainability issues and climate change mitigation», *Cogent Engineering*, vol. 3, fasc. 1, p. 1167990, dic. 2016, doi: 10.1080/23311916.2016.1167990.

[3] A. Baldinelli, L. Barelli, G. Bidini, G. Cinti, A. Di Michele, e F. Mondi, «How to Power the Energy–Water Nexus: Coupling Desalination and Hydrogen Energy Storage in Mini-Grids with Reversible Solid Oxide Cells», *Processes*, vol. 8, fasc. 11, p. 1494, nov. 2020, doi: 10.3390/pr8111494.

[4] D. Falabretti, M. Lindholm, M. Merlo, e G. Scapeccia, «Energy storage coupling in a high efficiency household scenario: A real life experimental application», *Journal of Energy Storage*, vol. 17, pp. 496–506, giu. 2018, doi: 10.1016/j.est.2018.04.010.

[5] K. Oshiro e S. Fujimori, «Role of hydrogen-based energy carriers as an alternative option to reduce residual emissions associated with mid-century decarbonization goals», *Applied Energy*, vol. 313, p. 118803, mag. 2022, doi: 10.1016/j.apenergy.2022.118803.

[6] H. Nami, O. B. Rizvandi, C. Chatzichristodoulou, P. V. Hendriksen, e H. L. Frandsen, «Techno-economic analysis of current and emerging electrolysis technologies for green hydrogen production», *Energy Conversion and Management*, vol. 269, p. 116162, ott. 2022, doi: 10.1016/j.enconman.2022.116162.

[7] J. N. Bamba, A. T. Dumlao, R. M. Lazaro, D. D. Matienzo, e J. Ocon, «Green Hydrogen from Seawater Electrolysis: Recent Developments and Future Perspectives», *Current Opinion in Electrochemistry*, p. 101592, set. 2024, doi: 10.1016/j.coelec.2024.101592.

[8] S. Dresp, F. Dionigi, M. Klingenhof, e P. Strasser, «Direct Electrolytic Splitting of Seawater: Opportunities and Challenges», *ACS Energy Lett.*, vol. 4, fasc. 4, Art. fasc. 4, apr. 2019, doi: 10.1021/acsenergylett.9b00220.

[9] Y. Kuang *et al.*, «Solar-driven, highly sustained splitting of seawater into hydrogen and oxygen fuels», *Proc. Natl. Acad. Sci. U.S.A.*, vol. 116, fasc. 14, Art. fasc. 14, apr. 2019, doi: 10.1073/pnas.1900556116.

[10] N. Tian *et al.*, «Pt-group bimetallic nanocrystals with high-index facets as high performance electrocatalysts», *Faraday Discuss.*, vol. 162, p. 77, 2013, doi: 10.1039/c3fd20146e.

[11] H. Wang, Y. Yang, F. J. DiSalvo, e H. D. Abruña, «Multifunctional Electrocatalysts: Ru–M (M = Co, Ni, Fe) for Alkaline Fuel Cells and Electrolyzers», *ACS Catal.*, vol. 10, fasc. 8, pp. 4608–4616, apr. 2020, doi: 10.1021/acscatal.9b05621.
[12] W. Sheng *et al.*, «Non-precious metal electrocatalysts with high activity for hydrogen oxidation reaction in alkaline electrolytes», *Energy Environ. Sci.*, vol. 7, fasc. 5, pp. 1719–1724, 2014, doi: 10.1039/C3EE43899F.
[13] J. Mohammed-Ibrahim e X. Sun, «Recent progress on earth abundant electrocatalysts for hydrogen evolution reaction (HER) in alkaline medium to achieve efficient water splitting – A review», *Journal of Energy Chemistry*, vol. 34, pp. 111–160, lug. 2019, doi: 10.1016/j.jechem.2018.09.016.
[14] F. Ganci *et al.*, «Ni alloy nanowires as high efficiency electrode materials for alkaline electrolysers», *International Journal of Hydrogen Energy*, vol. 46, fasc. 72, Art. fasc. 72, ott. 2021, doi: 10.1016/j.ijhydene.2020.11.208.
[15] J. Zhu, L. Hu, P. Zhao, L. Y. S. Lee, e K.-Y. Wong, «Recent Advances in Electrocatalytic Hydrogen Evolution Using Nanoparticles», *Chem. Rev.*, vol. 120, fasc. 2, pp. 851–918, gen. 2020, doi: 10.1021/acs.chemrev.9b00248.
[16] M.-I. Jamesh e X. Sun, «Recent progress on earth abundant electrocatalysts for oxygen evolution reaction (OER) in alkaline medium to achieve efficient water splitting – A review», *Journal of Power Sources*, vol. 400, pp. 31–68, ott. 2018, doi: 10.1016/j.jpowsour.2018.07.125.
[17] B. Buccheri, F. Ganci, B. Patella, G. Aiello, P. Mandin, e R. Inguanta, «Ni-Fe alloy nanostructured electrodes for water splitting in alkaline electrolyser», *Electrochimica Acta*, vol. 388, p. 138588, ago. 2021, doi: 10.1016/j.electacta.2021.138588.
[18] B. Ni e X. Wang, «Face the Edges: Catalytic Active Sites of Nanomaterials», *Advanced Science*, vol. 2, fasc. 7, p. 1500085, lug. 2015, doi: 10.1002/advs.201500085.
[19] I. Flis-Kabulska e J. Flis, «Electroactivity of Ni–Fe cathodes in alkaline water electrolysis and effect of corrosion», *Corrosion Science*, vol. 112, pp. 255–263, nov. 2016, doi: 10.1016/j.corsci.2016.07.017.
[20] K. Fominykh *et al.*, «Iron-Doped Nickel Oxide Nanocrystals as Highly Efficient Electrocatalysts for Alkaline Water Splitting», *ACS Nano*, vol. 9, fasc. 5, pp. 5180–5188, mag. 2015, doi: 10.1021/acsnano.5b00520.
[21] M. Gong *et al.*, «An Advanced Ni–Fe Layered Double Hydroxide Electrocatalyst for Water Oxidation», *J. Am. Chem. Soc.*, vol. 135, fasc. 23, pp. 8452–8455, giu. 2013, doi: 10.1021/ja4027715.

[22] M. W. Louie e A. T. Bell, «An Investigation of Thin-Film Ni–Fe Oxide Catalysts for the Electrochemical Evolution of Oxygen», *J. Am. Chem. Soc.*, vol. 135, fasc. 33, pp. 12329–12337, ago. 2013, doi: 10.1021/ja405351s.
[23] E. Gonzalez, L. Avaca, A. Carubelli, A. Tanaka, e G. Tremiliosifilho, «The hydrogen evolution reaction on mild steel and nickel-iron codeposits in alkaline media», *International Journal of Hydrogen Energy*, vol. 9, fasc. 8, pp. 689–693, 1984, doi: 10.1016/0360-3199(84)90266-0.
[24] J. De Carvalho, G. Tremiliosi Filho, L. A. Avaca, e E. R. Gonzalez, «Electrodeposits of iron and nickel-iron for hydrogen evolution in alkaline solutions», *International Journal of Hydrogen Energy*, vol. 14, fasc. 3, pp. 161–165, gen. 1989, doi: 10.1016/0360-3199(89)90049-9.
[25] L. Yi *et al.*, «Electronic interaction boosted electrocatalysis of iridium nanoparticles on nitrogen-doped graphene for efficient overall water splitting in acidic and alkaline media», *Chemical Engineering Journal*, vol. 415, p. 129034, lug. 2021, doi: 10.1016/j.cej.2021.129034.
[26] S. Carbone *et al.*, «Behavior of a forest of NiFe nanowires in KOH and NaCl solution for water electrolysis», *Electrochimica Acta*, vol. 467, p. 143120, nov. 2023, doi: 10.1016/j.electacta.2023.143120.
[27] F. Ganci *et al.*, «Electrodeposited nickel–zinc alloy nanostructured electrodes for alkaline electrolyzer», *International Journal of Hydrogen Energy*, vol. 47, fasc. 21, pp. 11302–11315, mar. 2022, doi: 10.1016/j.ijhydene.2021.09.221.
[28] O. Dragos, H. Chiriac, N. Lupu, M. Grigoras, e I. Tabakovic, «Anomalous Codeposition of *fcc* NiFe Nanowires with 5–55% Fe and Their Morphology, Crystal Structure and Magnetic Properties», *J. Electrochem. Soc.*, vol. 163, fasc. 3, pp. D83–D94, 2016, doi: 10.1149/2.0771603jes.
[29] D. Kim, D.-Y. Park, B. Y. Yoo, P. T. A. Sumodjo, e N. V. Myung, «Magnetic properties of nanocrystalline iron group thin film alloys electrodeposited from sulfate and chloride baths», *Electrochimica Acta*, vol. 48, fasc. 7, pp. 819–830, feb. 2003, doi: 10.1016/S0013-4686(02)00773-9.
[30] S. N. Srimathi e S. M. Mayanna, «Electrolytic preparation of Fe-Ni alloy», *J Mater Sci Lett*, vol. 4, fasc. 7, pp. 904–907, lug. 1985, doi: 10.1007/BF00720535.
[31] M. Matlosz, «Competitive Adsorption Effects in the Electrodeposition of Iron-Nickel Alloys», *J. Electrochem. Soc.*, vol. 140, fasc. 8, Art. fasc. 8, ago. 1993, doi: 10.1149/1.2220807.
[32] Á. Llavona, L. Pérez, M. C. Sánchez, e V. De Manuel, «Enhancement of anomalous codeposition in the synthesis of Fe–Ni alloys in nanopores»,

Electrochimica Acta, vol. 106, pp. 392–397, set. 2013, doi: 10.1016/j.electacta.2013.05.116.
[33] A. J. Bard, L. R. Faulkner, e H. S. White, *Electrochemical methods: fundamentals and applications*, Third edition. Hoboken, NJ, USA Chichester, West Sussex, UK: Wiley, 2022.
[34] F. Schröper, D. Brüggemann, Y. Mourzina, B. Wolfrum, A. Offenhäusser, e D. Mayer, «Analyzing the electroactive surface of gold nanopillars by electrochemical methods for electrode miniaturization», *Electrochimica Acta*, vol. 53, fasc. 21, pp. 6265–6272, set. 2008, doi: 10.1016/j.electacta.2008.03.068.
[35] K. I. Siwek, S. Eugénio, D. M. F. Santos, M. T. Silva, e M. F. Montemor, «3D nickel foams with controlled morphologies for hydrogen evolution reaction in highly alkaline media», *International Journal of Hydrogen Energy*, vol. 44, fasc. 3, Art. fasc. 3, gen. 2019, doi: 10.1016/j.ijhydene.2018.11.070.
[36] J. Choi, A. Nkhama, A. Kumar, S. R. Mishra, F. Perez, e R. K. Gupta, «A facile preparation of sulfur doped nickel–iron nanostructures with improved HER and supercapacitor performance», *International Journal of Hydrogen Energy*, vol. 47, fasc. 12, Art. fasc. 12, feb. 2022, doi: 10.1016/j.ijhydene.2021.12.117.
[37] F. Dionigi, T. Reier, Z. Pawolek, M. Gliech, e P. Strasser, «Design Criteria, Operating Conditions, and Nickel-Iron Hydroxide Catalyst Materials for Selective Seawater Electrolysis», *ChemSusChem*, vol. 9, fasc. 9, Art. fasc. 9, mag. 2016, doi: 10.1002/cssc.201501581.
[38] Y. Wu, «Ni2P nanoparticles-inserted NiFeP nanosheets with rich interfaces as efficient catalysts for the oxygen evolution reaction», *Journal of Alloys and Compounds*, p. 10, 2022.
[39] G. B. Darband, «Recent advances in methods and technologies for enhancing bubble detachment during electrochemical water splitting», *Renewable and Sustainable Energy Reviews*, p. 21, 2019.
[40] R. Wen, S. Xu, X. Ma, Y.-C. Lee, e R. Yang, «Three-Dimensional Superhydrophobic Nanowire Networks for Enhancing Condensation Heat Transfer», *Joule*, vol. 2, fasc. 2, pp. 269–279, feb. 2018, doi: 10.1016/j.joule.2017.11.010.
[41] S. H. Ahn *et al.*, «Effect of morphology of electrodeposited Ni catalysts on the behavior of bubbles generated during the oxygen evolution reaction in alkaline water electrolysis», *Chem. Commun.*, vol. 49, fasc. 81, Art. fasc. 81, 2013, doi: 10.1039/c3cc44891f.
[42] L. Negahdar, F. Zeng, S. Palkovits, C. Broicher, e R. Palkovits, «Mechanistic Aspects of the Electrocatalytic Oxygen Evolution Reaction over Ni−Co Oxides», *ChemElectroChem*, vol. 6, fasc. 22, pp. 5588–5595, nov. 2019, doi: 10.1002/celc.201901265.

[43] Y. Chen, C. Dong, J. Zhang, C. Zhang, e Z. Zhang, «Hierarchically porous Mo-doped Ni–Fe oxide nanowires efficiently catalyzing oxygen/hydrogen evolution reactions», *J. Mater. Chem. A*, vol. 6, fasc. 18, pp. 8430–8440, 2018, doi: 10.1039/C8TA00447A.
[44] A. Y. Faid, A. O. Barnett, F. Seland, e S. Sunde, «Optimized Nickel-Cobalt and Nickel-Iron Oxide Catalysts for the Hydrogen Evolution Reaction in Alkaline Water Electrolysis», *J. Electrochem. Soc.*, vol. 166, fasc. 8, pp. F519–F533, 2019, doi: 10.1149/2.0821908jes.
[45] H. Zhang *et al.*, «Bifunctional Heterostructure Assembly of NiFe LDH Nanosheets on NiCoP Nanowires for Highly Efficient and Stable Overall Water Splitting», *Adv. Funct. Mater.*, vol. 28, fasc. 14, p. 1706847, apr. 2018, doi: 10.1002/adfm.201706847.
[46] C. Zhang *et al.*, «Ternary nickel iron phosphide supported on nickel foam as a high-efficiency electrocatalyst for overall water splitting», *International Journal of Hydrogen Energy*, vol. 43, fasc. 15, pp. 7299–7306, apr. 2018, doi: 10.1016/j.ijhydene.2018.02.157.
[47] Q. Li, W. Zhang, J. Shen, X. Zhang, Z. Liu, e J. Liu, «Trimetallic nanoplate arrays of Ni-Fe-Mo sulfide on FeNi3 foam: A highly efficient and bifunctional electrocatalyst for overall water splitting», *Journal of Alloys and Compounds*, vol. 902, p. 163670, mag. 2022, doi: 10.1016/j.jallcom.2022.163670.
[48] M. Qian, S. Cui, D. Jiang, L. Zhang, e P. Du, «Highly Efficient and Stable Water-Oxidation Electrocatalysis with a Very Low Overpotential using FeNiP Substitutional-Solid-Solution Nanoplate Arrays», *Adv. Mater.*, vol. 29, fasc. 46, p. 1704075, dic. 2017, doi: 10.1002/adma.201704075.
[49] C. Dong, T. Kou, H. Gao, Z. Peng, e Z. Zhang, «Eutectic-Derived Mesoporous Ni-Fe-O Nanowire Network Catalyzing Oxygen Evolution and Overall Water Splitting», *Adv. Energy Mater.*, vol. 8, fasc. 5, p. 1701347, feb. 2018, doi: 10.1002/aenm.201701347.
[50] F. Song e X. Hu, «Exfoliation of layered double hydroxides for enhanced oxygen evolution catalysis», *Nat Commun*, vol. 5, fasc. 1, p. 4477, lug. 2014, doi: 10.1038/ncomms5477.
[51] L. Yang, H. Qi, C. Zhang, e X. Sun, «An efficient bifunctional electrocatalyst for water splitting based on cobalt phosphide», *Nanotechnology*, vol. 27, fasc. 23, p. 23LT01, giu. 2016, doi: 10.1088/0957-4484/27/23/23LT01.
[52] S. Dresp *et al.*, «Direct Electrolytic Splitting of Seawater: Activity, Selectivity, Degradation, and Recovery Studied from the Molecular Catalyst Structure to the Electrolyzer Cell Level», *Adv. Energy Mater.*, vol. 8, fasc. 22, Art. fasc. 22, ago. 2018, doi: 10.1002/aenm.201800338.
[53] Y. Ma *et al.*, «Strongly Coupled FeNi Alloys/NiFe $_2$ O $_4$ @Carbonitride Layers-Assembled Microboxes for Enhanced Oxygen Evolution

Reaction», *ACS Appl. Mater. Interfaces*, vol. 8, fasc. 50, pp. 34396–34404, dic. 2016, doi: 10.1021/acsami.6b11821.
[54] Z. Angeles-Olvera, A. Crespo-Yapur, O. Rodríguez, J. Cholula-Díaz, L. Martínez, e M. Videa, «Nickel-Based Electrocatalysts for Water Electrolysis», *Energies*, vol. 15, fasc. 5, p. 1609, feb. 2022, doi: 10.3390/en15051609.
[55] V. D. Silva, T. A. Simões, J. P. F. Grilo, E. S. Medeiros, e D. A. Macedo, «Impact of the NiO nanostructure morphology on the oxygen evolution reaction catalysis», *J Mater Sci*, vol. 55, fasc. 15, pp. 6648–6659, mag. 2020, doi: 10.1007/s10853-020-04481-1.
[56] J. Kibsgaard e I. Chorkendorff, «Considerations for the scaling-up of water splitting catalysts», *Nat Energy*, vol. 4, fasc. 6, pp. 430–433, mag. 2019, doi: 10.1038/s41560-019-0407-1.
[57] S. Dresp, T. Ngo Thanh, M. Klingenhof, S. Brückner, P. Hauke, e P. Strasser, «Efficient direct seawater electrolysers using selective alkaline NiFe-LDH as OER catalyst in asymmetric electrolyte feeds», *Energy Environ. Sci.*, vol. 13, fasc. 6, Art. fasc. 6, 2020, doi: 10.1039/D0EE01125H.
[58] N. Kishimoto, «State of the Art of UV/Chlorine Advanced Oxidation Processes: Their Mechanism, Byproducts Formation, Process Variation, and Applications», *J. of Wat. & Envir. Tech.*, vol. 17, fasc. 5, pp. 302–335, 2019, doi: 10.2965/jwet.19-021.
[59] K. Jiang *et al.*, «NiFe Layered Double Hydroxide/FeOOH Heterostructure Nanosheets as an Efficient and Durable Bifunctional Electrocatalyst for Overall Seawater Splitting», *Inorg. Chem.*, vol. 60, fasc. 22, pp. 17371–17378, nov. 2021, doi: 10.1021/acs.inorgchem.1c02903.
[60] H. Yang, M. Driess, e P. W. Menezes, «Self-Supported Electrocatalysts for Practical Water Electrolysis», *Advanced Energy Materials*, vol. 11, fasc. 39, p. 2102074, ott. 2021, doi: 10.1002/aenm.202102074.
[61] P. Jing *et al.*, «Dependence of phase configurations, microstructures and magnetic properties of iron-nickel (Fe-Ni) alloy nanoribbons on deoxidization temperature in hydrogen», *Sci Rep*, vol. 6, fasc. 1, p. 37701, nov. 2016, doi: 10.1038/srep37701.
[62] Y. Gao *et al.*, «Partially reduced Ni2+, Fe3+-layered double hydroxide for ethanol electrocatalysis», *J Mater Sci*, vol. 54, fasc. 23, pp. 14515–14523, dic. 2019, doi: 10.1007/s10853-019-03964-0.
[63] F. Maurer, J. Brötz, S. Karim, M. E. T. Molares, C. Trautmann, e H. Fuess, «Preferred growth orientation of metallic fcc nanowires under direct and alternating electrodeposition conditions», *Nanotechnology*, vol. 18, fasc. 13, p. 135709, apr. 2007, doi: 10.1088/0957-4484/18/13/135709.

[64] E. Amores, J. Rodríguez, e C. Carreras, «Influence of operation parameters in the modeling of alkaline water electrolyzers for hydrogen production», *International Journal of Hydrogen Energy*, vol. 39, fasc. 25, Art. fasc. 25, ago. 2014, doi: 10.1016/j.ijhydene.2014.07.001.
[65] Department of Interface Chemistry and Surface Engineering, Max-Planck-Institut für Eisenforschung GmbH, Max-Planck-Strasse 1, 40237 Düsseldorf, Germany e M. Schalenbach, «A Perspective on Low-Temperature Water Electrolysis – Challenges in Alkaline and Acidic Technology», *Int. J. Electrochem. Sci.*, pp. 1173–1226, feb. 2018, doi: 10.20964/2018.02.26.
[66] S. Marini *et al.*, «Advanced alkaline water electrolysis», *Electrochimica Acta*, vol. 82, pp. 384–391, nov. 2012, doi: 10.1016/j.electacta.2012.05.011.
[67] N. Nagai, «Existence of optimum space between electrodes on hydrogen production by water electrolysis», *International Journal of Hydrogen Energy*, vol. 28, fasc. 1, Art. fasc. 1, gen. 2003, doi: 10.1016/S0360-3199(02)00027-7.

5. Fabrication and Characterization of NiFeP NWs for SeaWater Electrolysis

5.1 Introduction

As already discussed, Nickel-based materials are the most electrocatalysts employed in AWE because of their corrosion resistance and good catalytic properties in alkaline solutions. Notably, nickel alloys, especially Ni-Fe, are promising bifunctional catalysts for water splitting. To enhance its properties, the efficient catalytic activity of phosphides in the electrochemical studies have recently attracted a lot of researchers. Transition metal phosphides (TMPs) are gaining attention as efficient catalysts due to their unique properties which enhance catalytic activity and stability [1] and "ensemble effect" [2]. The negative charge of the phosphorus in the system with the metal catalyst facilitates the capturing of more H^+ ions and releases it as H_2 [3], [4]. The combined activity of nickel, iron, and phosphorus has demonstrated significant efficiency in water-splitting reactions. Studies indicate that specific nickel-iron phosphide alloys display excellent performance and stability, which can be further enhanced by adjusting the alloy composition and utilizing nanostructured materials. However, obtaining electrocatalysts with at least 3 elements to enhance the intrinsic activities of the individual is extremely challenging [5]. In accordance with data in the literature, most phosphorus-containing electrocatalysts are obtained by processes that require large amounts of energy and time. Direct-current electrodeposition has attracted considerable attention due to its ease of use, mild conditions, and straightforward operation. This study explores the performance of NiFeP alloy nanowires, focusing on their synthesis through a scalable and cheap method. Initially, the performance of the ternary alloys was compared with that of the binary alloy in a solution containing only KOH. The research builds on previous findings regarding their effectiveness in KOH+NaCl electrolyte with

a particular emphasis on long-term stability through galvanostatic tests. Various characterization techniques were employed to assess morphological and compositional changes in the electrodes. Subsequently, electrochemical tests were conducted in a solution better able to simulate the composition of seawater. Using NiFeP nanostructured electrodes, a lab-scale electrolyzer was fabricated and tested. Additionally, a Life Cycle Assessment was carried out to evaluate the environmental impact of electrode production by electrodeposition.

5.2 Materials and methods

This chapter focuses on the fabrication of nanostructured NiFeP electrodes to enhance the well-established performance of NiFe nanowires (NWs) developed previously. The electrodes were synthesized using template electrosynthesis, with a nanoporous polycarbonate membrane serving as the template. The method, described in detail in "3.4 Template Electrosynthesis" is a multi-step process. The resulting electrodes were characterized by SEM using a FEG-ESEM microscope (QUANTA 200 by FEI), complemented by EDS and XRD using a RIGAKU X-ray diffractometer (D-MAX 25600 HK). The surface characterization of NWs was also performed using XPS with a PHI5000 VersaProbe. Various electrochemical measurements were made in a conventional three-electrode cell. All the potentials were referred to the RHE at pH 14. The electrochemical characterization was performed using a Solartron Multichannel Cell Test System (Mod. 1470 E), and data were recorded with MultiStat Software. Initially, the NiFeP electrodes were then tested as both cathodes and anodes in a 30% w/w KOH aqueous solution at room temperature, without stirring. Their performance was compared to that of the binary NiFe alloy, focusing on the influence of phosphorus on electrocatalytic behaviour to determine the optimal alloy composition. Long-term

electrochemical characterization was also carried out in an alkaline KOH solution with 0.5 M NaCl to simulate seawater conditions in terms of chlorine content [46]. Later, to better simulate the seawater conditions, electrochemical tests were performed in 30% w/w KOH aqueous solution with different anions and cations like chloride, magnesium, calcium, and potassium. An artificial seawater solution was prepared by the addition of NaCl, $MgSO_4$, $CaCl_2$, and KCl to a 30 % w/w KOH aqueous solution to obtain the same concentration as natural seawater: 0.5 M Na^+, 0.5 M Cl^-, 0.057 M SO_4^{2-}, 0.057 M Mg^{2+}, 0.01 M Ca^{2+}, and 0.01 M K^+. The addition caused the precipitation of $Mg(OH)_2$. Then, the precipitate was allowed to stand overnight. The clear solution was carefully decanted and filtered, then used for electrolysis experiments.

As for the synthesis of NiFeP NWs, the starting electrodeposition bath was prepared by Watt's solution comprising 300 g/L $NiSO_4 \cdot 6H_2O$, 45 g/L $NiCl_2 \cdot 6H_2O$, 45 g/L H_3BO_3 to which 0.44 M $FeSO_4 \cdot 7H_2O$ was added, allowing to obtain NWs with an optimal Fe content of ca. 79%. To this bath, further additions of various concentrations of the phosphorus precursor $NaH_2PO_2 \cdot H_2O$ were made: +20 g/L (labelled NiFeP/1), +30 g/L (labelled NiFeP/2), and +50 g/L (labelled NiFeP/3). The formation of metal phosphides using sodium hypophosphite as the phosphorus source [6] can be represented by the following reactions:

$$H_2PO_{2-} + 2H^+ + e^- \rightarrow P + 2H_2O$$

$$M^{z+}P + ze^- \rightarrow MP$$

A uniform array of nanowires was deposited within the pores of the membrane using a pulsed electrodeposition technique, with voltage cycling between -1.2 V (for 6 seconds) and -0.75 V (for 4 seconds) versus SCE, for a total of 70 cycles. The optimized parameters were initially derived from reference [7] and

subsequently refined. Achieving homogenous nanowires with the desired elemental composition requires precise control of these parameters. During deposition at -1.2 V, material forms within the pores, while partial dissolution occurs at -0.75 V, making the current density positive and allowing for fine regulation of the composition of the nanostructures and morphology while avoiding gas bubble formation [8]. The electrodeposition was performed at room temperature in a standard three-electrode cell setup, using a Pt mesh as the counter electrode and an SCE as the reference electrode. **Figure 5.1** illustrates the pulse potential and the resulting current density for NiFeP NW deposition.

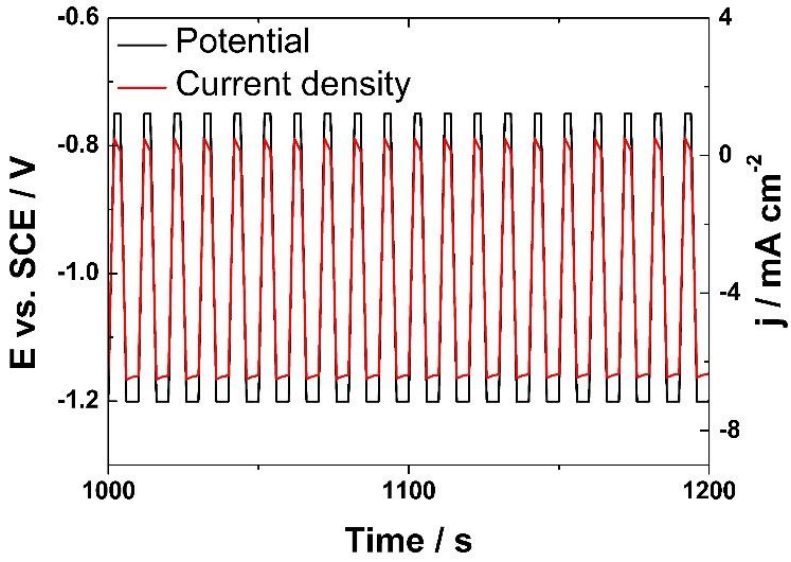

Fig. 5.1 *Pulse potential and measured current density vs. time plots for NiFeP NWs electrodeposition*

5.3 Physico-Chemical and Electrochemical Characterizations

SEM was employed to examine the morphology of the nanowire (NW) electrodes. **Figure 5.2** shows several top-view images of a NiFeP/3 NW electrode at different magnifications. It is important to note that, for all

fabricated electrodes, the SEM images appear nearly identical, as the NW morphology is dictated solely by the shape of the template and not by the phosphorus content. Due to the structure of the nanoporous template, the nanowires have a cylindrical shape, with a smooth and uniform surface, and are evenly distributed over the entire surface of the nickel collector, as depicted in Figure **5.2A**. Figure **5.2B** shows a cluster of fallen nanowires with a length of about 15 µm. Figure **5.2D** highlights the interconnections between NWs, caused by the typical pore interconnection found in polycarbonate membranes. SEM analysis was also performed with a tilt angle of 30°, showcasing the three-dimensional structure of NWs (**Figure 5.3**). The average diameter of the NWs was about 250 nm.

EDS was performed to quantify the atomic percentages of each element in the NWs. For this analysis, the NWs were detached from the nickel collector using copper (Cu) tape to ensure more accurate measurements of the composition. **Figure 5.4** presents the EDS spectra of electrodes obtained from deposition baths with varying phosphorus concentrations. All the elements of the ternary alloy are visible. The presence of Cu is attributed to the copper tape. For comparison, the EDS spectrum of the NiFe binary alloy is also displayed. As expected, the NWs exhibit a high iron content (with an Fe ratio of about 3.3). This confirms the occurrence of anomalous iron deposition, which is typical of Fe alloy electrodeposition [9]. Additionally, the phosphorus content was found to increase slightly with its concentration in the deposition bath, with a weight percentage ranging from 6-8%.

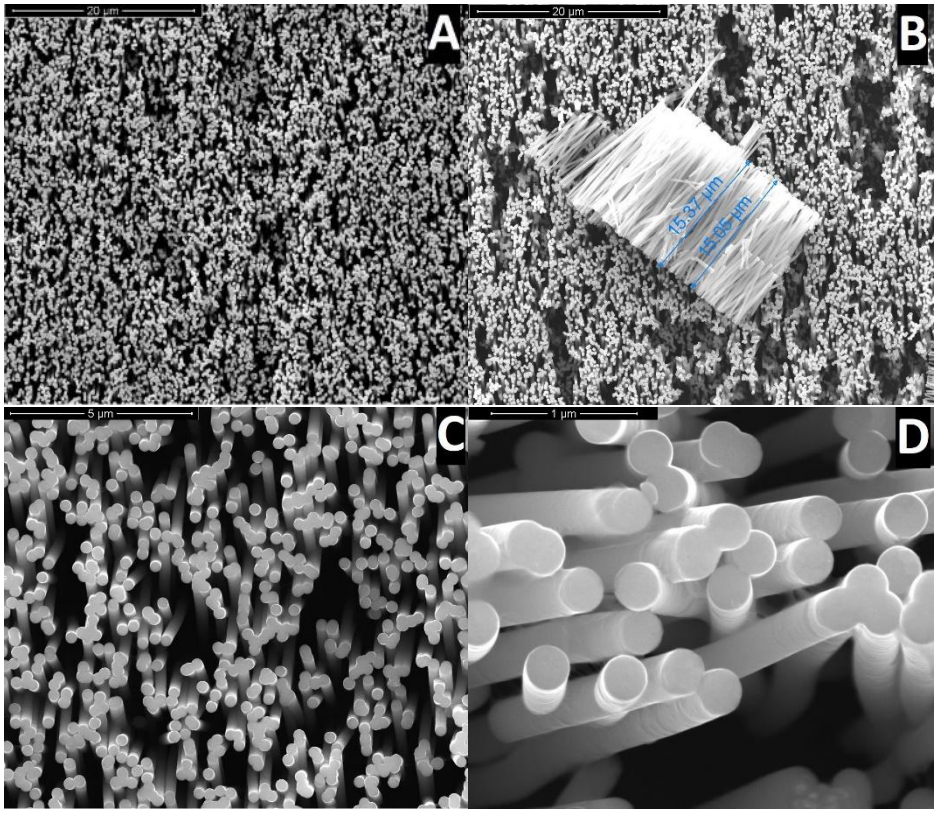

Fig. 5.2 *SEM top-view images of NiFeP/3 NWs electrode at increasing magnification.*

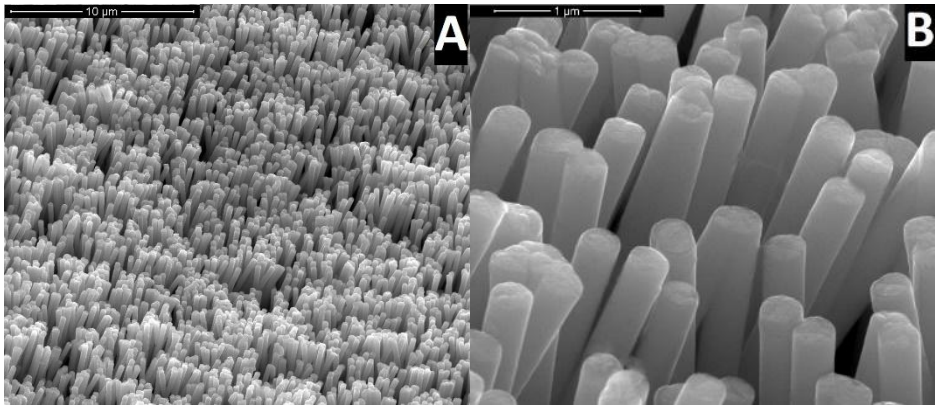

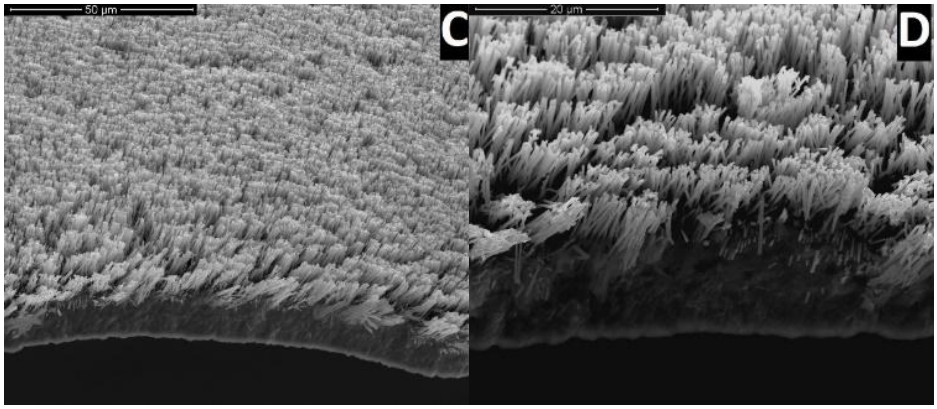

Fig. 5.3 *SEM tilted top-view images of NiFeP/3 NWs electrodes at increasing magnification*

The composition of the 3 electrodes is reported in **Table 5.1**. In agreement with literature data, the presence of phosphorus in the deposition bath depresses the deposition of iron even if slightly [10].

Table 5.1 *Composition of NiFeP electrodes measured throughout EDS analyses*

Electrocatalyst	***Ni***	***Fe***	***P***
NiFeP/1	20.85	73.22	5.93
NiFeP/2	20.69	72.60	6.71
NiFeP/3	19.41	72.92	7.67

Phosphorus, being a nonmetal, cannot be deposited in its pure form from aqueous solutions. However, it can be easily co-deposited from solutions containing iron group elements through a process known as "induced co-deposition." In this process, hydrogen can act as an inducing element, particularly when the reduction of iron group metals is also taking place. The reduction of phosphorus is closely tied to the reduction of the inducing

element, as for each electron used in the reduction of the inducing element, only one electron is available for phosphorus reduction. As a result, only half of the total current is available for phosphorus deposition [11]. This explains why, despite increasing its concentration in the deposition bath, the phosphorus content in the electrodes remains relatively low compared to other alloying elements.

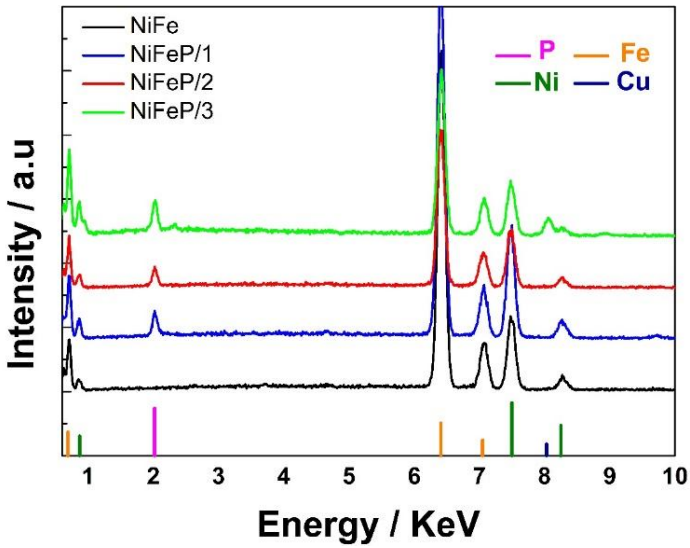

Fig. 5.4 *EDS spectra of NiFeP NWs with different phosphorus concentrations. For comparison, the spectrum of NiFe NWs was also reported.*

As shown in **Figure 5.5**, EDS analysis was also performed along the length of the NWs (**Fig. 5.5A**) to assess the variation in the composition (**Fig. 5.5B**) of the three elements (Ni, Fe, P).

The results suggest that the composition within the nanowires is uniform, exhibiting an almost constant distribution throughout.

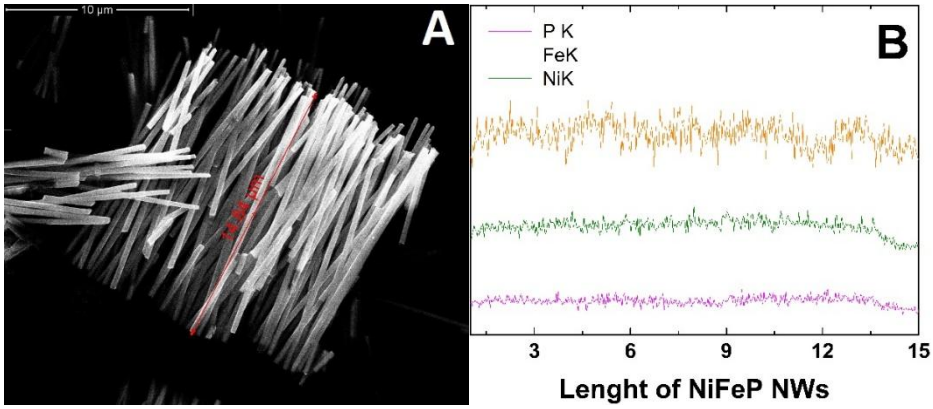

***Fig. 5.5**. EDS-line analysis of NiFeP/3 NWs*

Figure 5.6 presents the X-ray diffraction (XRD) patterns of NiFeP NWs. Based on the XRD database [12] , the NiFe alloy peaks were identified at approximately 2θ values of 43.5°, 50.3°, 74.1°, and 89.9° (**Figure 5.6A**). Among these, the peak at 2θ= 50.3° showed the highest intensity. These results confirm the deposition of a crystalline alloy, consistent with the findings in [11], which demonstrated that alloys containing around 7% phosphorus exhibit a crystalline structure. Specifically, it has been noted that alloys with about 7% phosphorus are crystalline but tend to become amorphous as the phosphorus content increases. In this work, all alloys remain crystalline; however, the reduction in peak intensity with increasing phosphorus content, as seen in the main diffraction peak in **Figure 5.6B,** indicates a shift toward an amorphous phase.

The peaks located at 44.5°, 51.8°, 76.3°, and 92.8° can be attributed to crystalline Ni, likely originating from the Ni current collector. The average grain size of the alloy, **d**, was calculated using the Scherrer equation:

$$d = \frac{0.94\lambda}{\beta\cos\theta}$$

where **λ** is the wavelength of the radiation, **θ** is the diffraction angle, and **β** is the full-width half maximum (FWHM) of the main intensity peak in radians. According to [13] the XRD patterns of all NiFeP alloys show no presence of phosphide phases. However, the phosphorus added into the alloy structure introduces distortions in the crystalline lattice that latter changes the grain size, as shown in Figure 5.6B. The mean grain sizes increase from ~ 31 ± 1.1 nm in the NiFe alloy to ~ 40 ± 1.7 nm in the NiFeP alloy. Since the phosphorus content in the alloy varies slightly, ranging from 6 to 8%, the grain size in the NiFeP alloy shows minimal variation, generally falling between 37 and 40 nm.

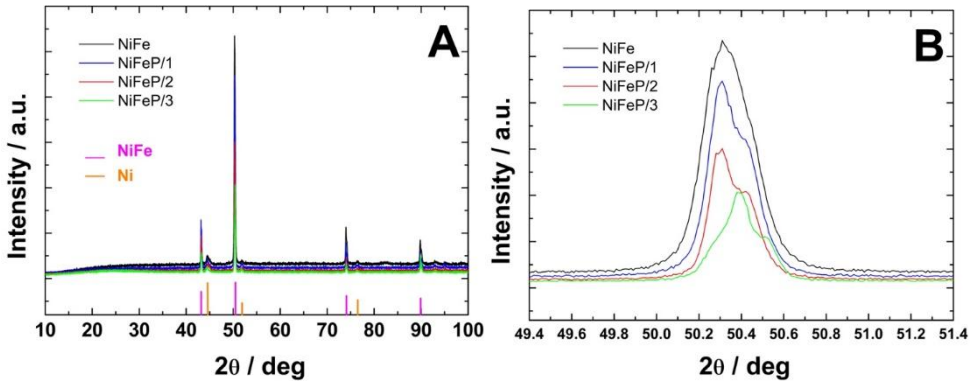

***Fig. 5.6**. **(A)** XRD patterns of NiFeP NWs with different phosphorus concentrations. For comparison also the pattern of NiFe NWs was reported. **(B)** Detail of the main peak*

To highlight the advantages of their nanostructured morphology, both NiFeP/3 and a planar Nickel strip were tested in 30% KOH using cyclic voltammetry (CV) at different scan rates. The specific capacitance was

estimated through the double-layer capacitance method, which correlates with the electrochemically active surface area. Cyclic voltammetry was conducted within the non-Faradaic region, spanning from 0.64 to 0.74 V versus the Reversible Hydrogen Electrode (RHE). For accurate determination of the double-layer capacitance, it is crucial that the data be collected within a potential range where the charging of the double layer is the primary contributor to the measured net current, while contributions from other electrochemical processes, including redox reactions and adsorption/desorption, are minimal. The inset of **Figure 5.7** presents the CVs of NiFeP NWs, by way of example. For each scan rate, the difference between the anodic and cathodic current density at 0.7 V versus RHE was calculated and plotted against the scan rate. The slope of the resulting linear fit represents the double-layer capacitance. The slope for NiFeP/3 was significantly higher than that of the planar Nickel strip, reflecting the much larger surface area of the nanowires. This enhanced surface area is anticipated to improve electrocatalytic performance. The slope value for NiFeP is consistent with findings in the literature [14] and aligns well with the value derived from the SEM image analysis using the equation proposed in [15].

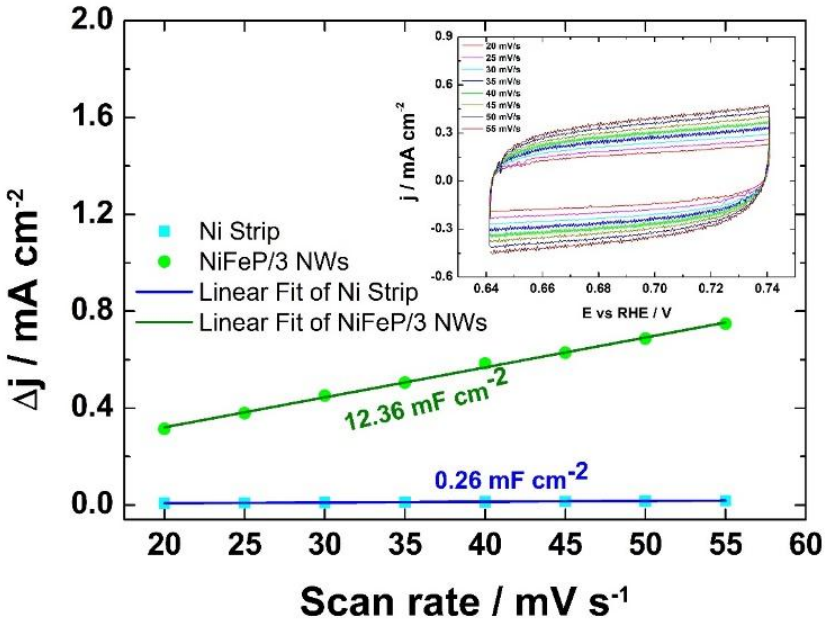

Fig. 5.7 *Specific capacitance of the electrodes is evaluated by double layer capacitance method.*

QSSP tests were carried out for both HER and OER. A range of 0.7 V has been analyzed with a scan rate of 0.1667 mV s^{-1}, as shown in **Figure 5.8A and 5.8B.** From this figure, the effect of the improvement in performance thanks to the presence of P in the alloy can be observed. For HER, performance also increases as the P content increases, while for OER different P concentrations lead to practically the same result. The values of η_{10} and η_{100} [16] for HER and OER were also measured and reported in **Figure 5.8C and D**. At a current density of 10 mA/cm^2 (the most common parameter used for the comparison), the η values for NiFeP/3 electrode are −123 mV for HER and 270 mV OER, respectively. These values are better than those measured for the binary NiFe alloy and a planar Ni strip and are in line with many NiFe-based electrodes, and thus the electrodes obtained herein have good catalytic properties.

The linear range of QSSP curves was fitted, as shown in **Figure 5.9**, with Tafel's equation

$$\eta = a + b \log i$$

where *a* and *b* values are an exchange current density and Tafel's curve slope, respectively. A Tafel slope is an intrinsic property of the catalyst that is linked to the kinetically decisive stage of HER and OER processes. A smaller Tafel slope means faster formation of the two gases. Calculated Tafel parameters are listed in **Table 5.2.**

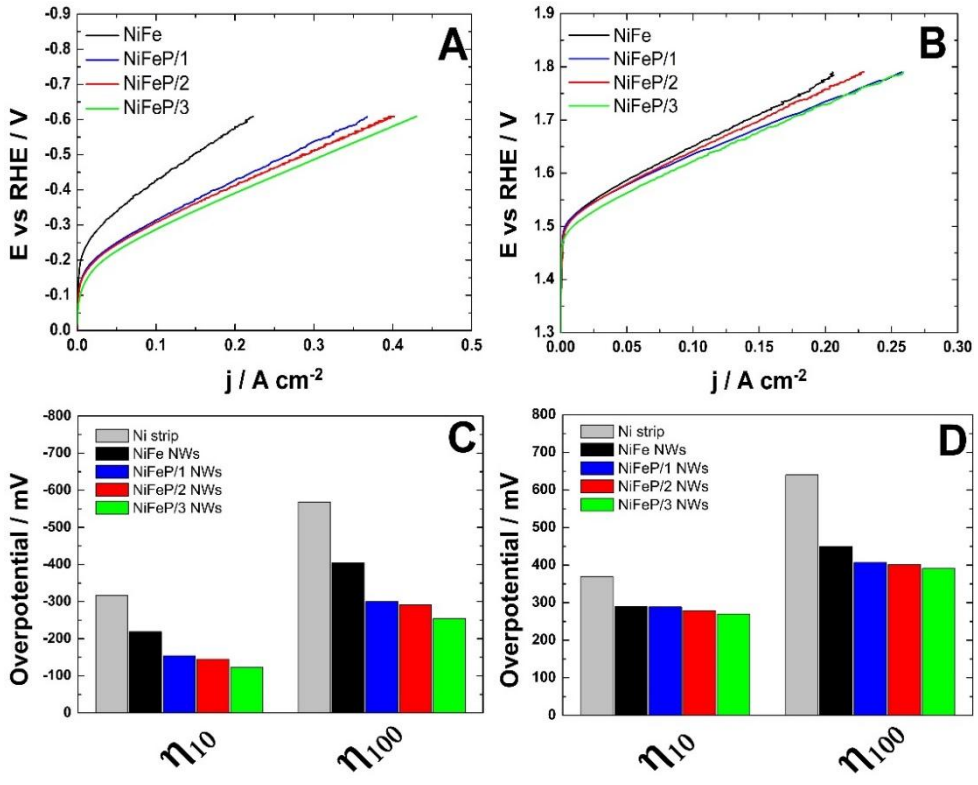

Fig. 5.8 *QSSP for (**A**) HER and (**B**) OER at 0.1667 mV s^{-1} in KOH aqueous solution. (**C**) and (**D**) values of overpotential for HER and OER respectively.*

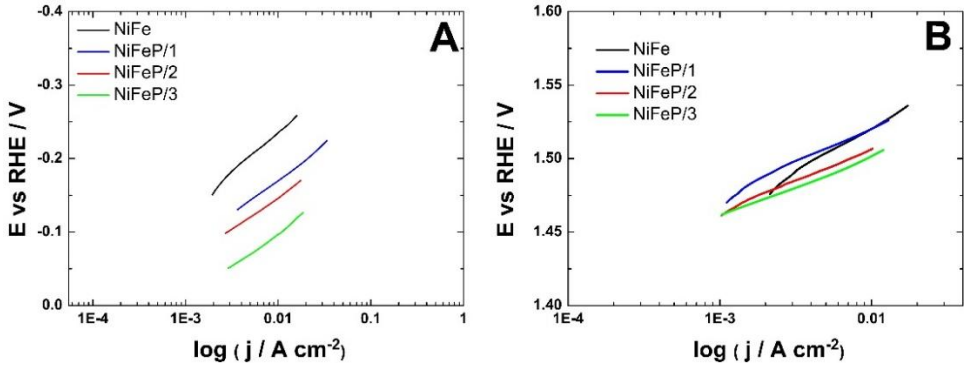

Fig. 5.9 *Linearity range of QSSP curves for (A) HER and (B) OER*

Table 5. 2 *– Fitted Tafel's parameters for HER and OER*

Electrocatalyst	***HER***			***OER***		
	a (V)	**b (V)**	**R^2 (%)**	**a (V)**	**b (V)**	**R^2 (%)**
NiFe	-0.46	-0.114	99.2	1.62	0.055	99.6
NiFeP/1	-0.36	-0.096	99.74	1.61	0.049	98.7
NiFeP/2	-0.322	-0.089	99.84	1.592	0.043	98.8
NiFeP/3	-0.271	-0.088	99.81	1.581	0.042	99.2

For the cathodic side, the Tafel slope for NiFeP electrodes is lower than that for NiFe electrodes, indicating that the ternary alloy exhibits faster HER kinetics. The optimal performance was observed for NiFeP/3 electrodes, which contain a phosphorus amount similar to the other alloys but display less intense diffraction peaks, suggesting a lower degree of crystallinity [17]. The Tafel slope values range between 116 and 40 mV dec^{-1} indicating that the HER kinetics follow the Volmer-Heyrovsky mechanism value [18], [19].

Volmer step: $M+H_2O+e^- \rightarrow M\text{-}H^*+OH^-$ **120 mV/dec**

Heyrovsky step: $H_2O+M\text{-}H^*+e^- \rightarrow M+H_2+OH^-$ **40 mV/dec**

Tafel step: $2M\text{-}H^* \rightarrow 2M+H_2$ **30 mV/dec**

For the NiFeP electrocatalyst, the proposed oxygen evolution reaction (OER) mechanism consists of four steps involving various intermediates [14], [20], [21]

$M+OH^- \rightarrow M{-}OH^*+e^-$ **120 mV/dec**

$M{-}OH^*+OH^- \rightarrow M\text{-}O^-+H_2O$ **60 mV/dec**

$M\text{-}O^- \rightarrow M\text{-}O+e^-$ **45 mV/dec**

$2M\text{-}O \rightarrow 2M+O_2$ **19 mV/dec**

For the anodic side, the Tafel slopes of all nanostructured electrodes exhibit a close relationship of approximately 45 mV/dec, suggesting that the rate-controlling step is linked to the formation of M−O. The ternary alloy outperforms the binary alloy, with all three alloys demonstrating similar performance, regardless of phosphorus concentration. The Tafel slope values for both HER and OER are comparable to or exceed those of similar catalysts containing iron-group elements and phosphorus [20], [22], [23].

The TOF values were calculated at a specific overpotential of 400 mV for both reactions using this equation: TOF= $\frac{iA}{xnF}$

The TOF value for the optimal NiFeP ternary alloy was calculated based on an electrocatalyst amount of 2.53 mg/cm². This TOF value was then compared with those of the Ni planar sheet and the binary Ni-Fe alloy. The values are listed in the following table.

Table 5.3 *– TOF Values*

Electrocatalyst	***TOF*** *[s^{-1}] HER per η=400 mV*	***TOF*** *[s^{-1}] OER per η=400 mV*
Ni Sheet	$6.62*10^{-5}$	$2.5*10^{-5}$
NiFe NWs	0.007	0.004
NiFeP NWs	0.0234	0.0059

Multistep chronopotentiometry tests were carried out to investigate the behaviour of the nanostructured electrodes at varying current densities. Each applied current density (0.01, 0.02, 0.05, 0.1, 0.2, 0.5 A/cm^2) was maintained for five minutes, after which the average value of potential was measured. **Figure 5.10** displays the average potential for each step.

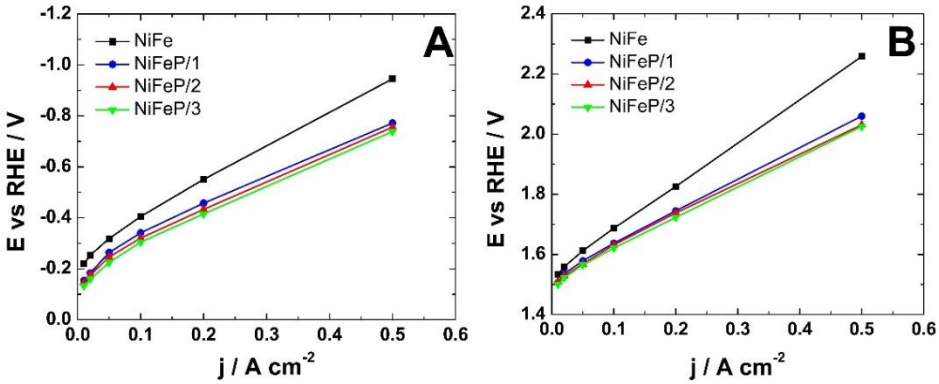

Fig. 5.10*. Galvanostatic-step polarization for (**A**) HER and (**B**) OER*

Multistep chronopotentiometry tests corroborate the earlier findings, demonstrating that the catalysts composed of the ternary alloy exhibit superior performance compared to those made from the binary alloy. When assessing high current densities of 0.5 A/cm², a significant energy gain of 300 mV and

230 mV was observed for the cathodic and anodic reactions, respectively, when transitioning from the binary alloy to the optimal ternary alloy.

To investigate the stability, a current density of ±50 mA/cm² was imposed for six hours. In **Figure 5.11**, each data point on the graph represents the average potential recorded every half hour. The potential exhibited minimal variation from the start to the end of the experiment. NiFeP electrodes outperformed the NiFe electrodes, with NiFeP/3 demonstrating the most exemplary results. The inclusion of phosphorus significantly enhanced both HER and OER performance, with electrodes containing higher phosphorus concentrations yielding the best outcomes. Specifically, the HER and OER potentials decreased from -0.33 to -0.21 V vs. RHE and from 1.61 to 1.57 V vs. RHE, respectively, when using NiFeP/3 in place of NiFe.

Although the effect of phosphorus is more pronounced on the cathode side, it generally influences the performance of the ternary NiFeP alloy. Phosphorus, being negatively charged, acts as a proton acceptor, which ultimately weakens the bond strength between the positively charged metal and the hydrogen, facilitating hydrogen desorption. Additionally, alloys typically exhibit a synergistic effect among their constituent elements, which enhances electron transfer rates and leads to optimized electrocatalytic activity [24].

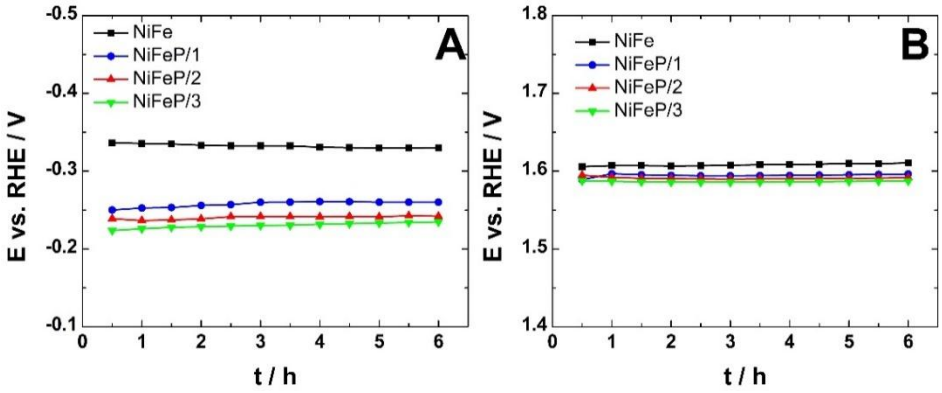

Fig. 5.11 *Mid-term stability test for 6 hours for (**A**) HER at −50 mA/cm^2 and **B**) OER at 50 mA/cm^2 in KOH aqueous solution*

Galvanostatic-step polarization, **Figure 5.12A,** and mid-term stability tests, **Figure 5.12B,** were performed on three different electrodes obtained in the same deposition conditions to verify the reproducibility of the fabrication method. As shown, the reproducibility is quite strong.

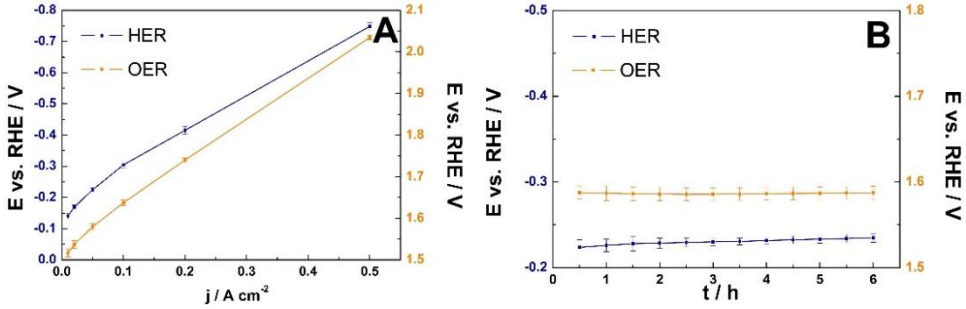

Figure 5.12 *Galvanostatic-step polarization (**A**) and (**B**) mid-term stability test (6 h) for three NiFeP/3 electrodes obtained using identical deposition parameters.*

To further examine the durability of the electrode, the stability test was extended to 125 hours. The lifespan of the electrode is closely associated with its electrocatalytic durability. Additionally, we evaluated the NiFeP/3 alloy in a solution of 30% KOH + 0.5 M NaCl, aiming to assess its potential as a

bifunctional catalyst for seawater electrolyzers. The results were then compared with those obtained in a KOH solution alone. **Figure 5.13** illustrates the performance comparison of the binary alloy in both solutions. It is clear that the ternary alloy significantly outperforms the binary alloy over the long term, with only a negligible difference in performance between the NaCl solution and the KOH solution. Notably, for the OER, the potential is lower than the hypochlorite standard reduction potential (which is 1.714 V vs. RHE at pH 14). Therefore, we can conclude that these electrodes exhibit selectivity for the OER.

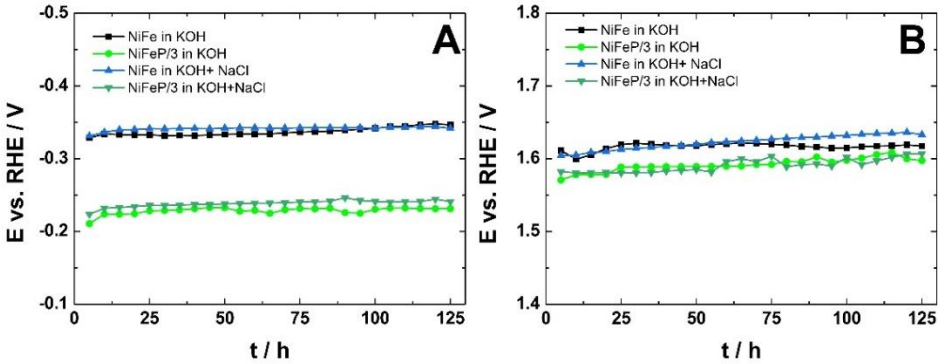

Fig. 5.13 *Long-term stability test for 125 hours for (**A**) HER at -50 mA/cm^2 and (**B**) OER at 50 mA/cm^2*

QSSP tests were conducted again after the long-term stability test to further investigate the stability of the catalysts. As illustrated (**Figure 5.14**), there is only a slight difference between the two curves and thus the electrodes have a very good stability.

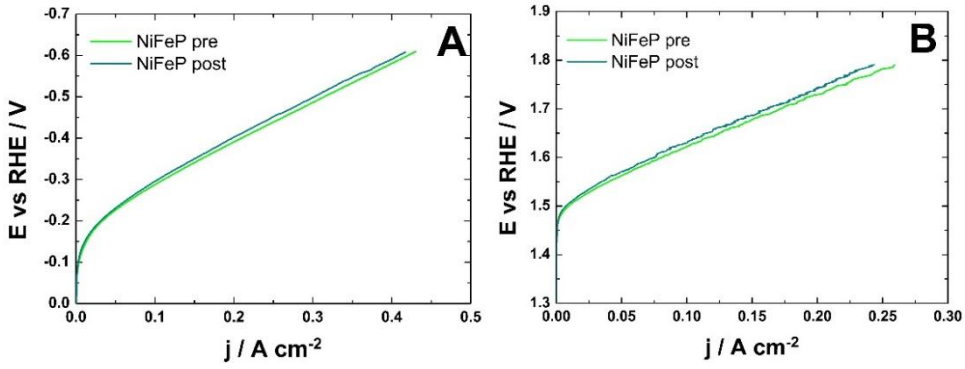

Fig. 5.14 *QSSP test before and after 125 hours for (**A**) HER at -50 mA/cm^2 and (**B**) OER at 50 mA/cm^2*

After the long-term stability test in the KOH + NaCl solution, the morphology of the NiFeP nanowires (NWs) was examined using SEM. The images in **Figures 5.15A and 5.15B** reveal that the nanostructural morphology remains largely unchanged, indicating that these nanostructure arrays are stable.

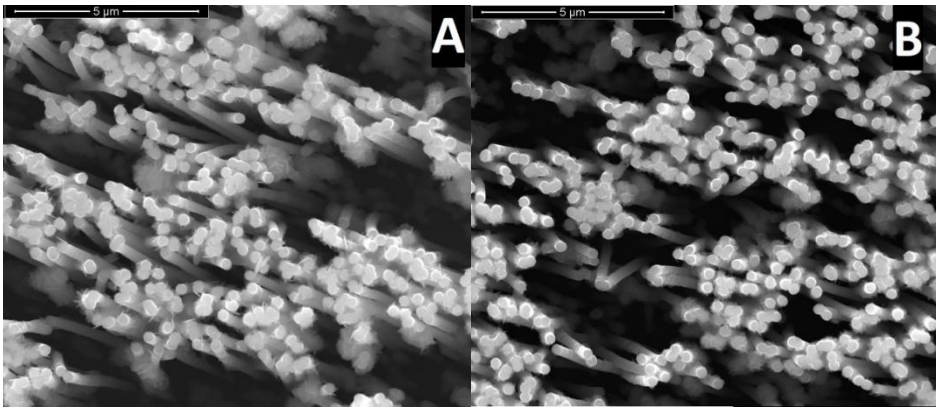

Fig. 5.15 *SEM images of NiFeP NWs electrodes after long-term stability test in KOH+NaCl: **A**) HER and **B**) OER.*

Additionally, the surface of the nanostructures was chemically characterized using XPS before and after the long-term stability test for OER in KOH + NaCl, as shown in **Figure 5.16**.

High-resolution spectra were collected in the regions of the Fe 2p3/2, Ni 2p3/2 and C 1s regions, the latter being used as reference for the binding energy scale due to adventitious carbon at 284.8 eV. The samples were analyzed before and after alkaline treatment. It can be clearly seen that in the Ni 2p3/2 region, the green line multiplet at 854.9 eV, 855.7 eV, 857.7 eV, 860.5 eV, and 861.5 eV corresponds to the $Ni(OH)_2$ species, while the blue line multiplet at 852.6 eV, 856.3 eV, and 858.7 eV corresponds to Ni(0). In the region of Fe 2p3/2, the difference between Fe(III) multiplet-bound bottom-710.0 eV, 711.0 eV, 711.9 eV, 713.0 eV, and 714.1 eV-and top-bound FeOOH 710.3 eV, 711.3 eV, 712.2 eV, 713.3 eV, and 714.4 eV is established.

Finally, in the P 2p region, there is a noticeable disappearance of the phosphide peak (green line) after the stability test. Before the stability test, surface analysis revealed a superficial composition with relatively comparable abundances of Ni, Fe, and P, with a ratio of P:Fe= 1:1.39:1.45. Phosphorus was identified in two forms: as metal phosphide (at 129.8 eV, accounting for 34%) and as phosphate (at 133.3 eV). The Fe 2p3/2 and Ni 2p3/2 regions were analyzed using peak envelopes, as suggested in the literature [25]. The Fe 2p3/2 region was found to be entirely composed of Fe(III). While it is plausible that Fe(0) was present, the low abundance and signal-to-noise ratio (SNR) made quantification difficult. In contrast, the Ni analysis indicated the co-presence of metallic Ni (13.6%) and $Ni(OH)_2$. After the stability test, the changes in surface composition became more pronounced. The P:Fe ratio shifted significantly to 1:8.32:17.69, with phosphide species completely disappearing from the P 2p region, leaving only phosphate species and demonstrating a steep decrease in relative abundance. Concurrently, metallic

Ni appeared to be completely oxidized to $Ni(OH)_2$, while Fe(III) seemed to have been converted to FeOOH.

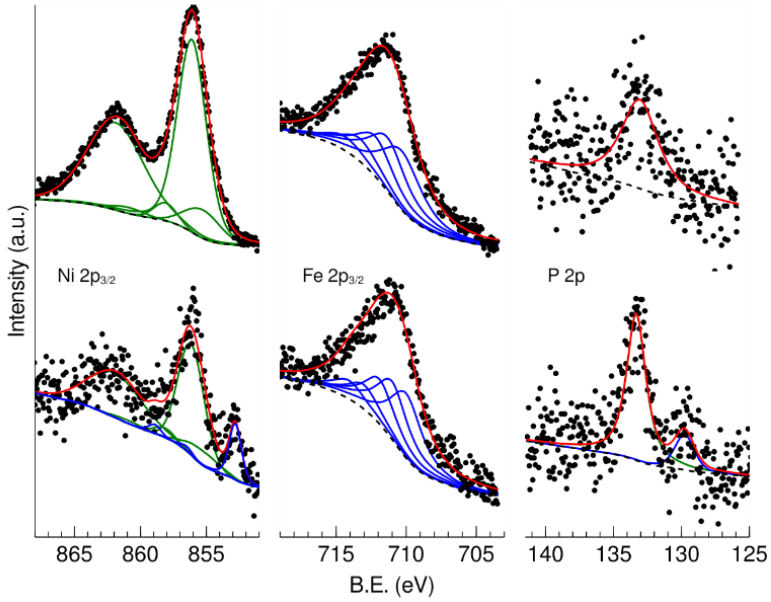

Fig. 5.16 *XPS analysis comparison before (bottom) and after (top) long-term stability test*

To use these electrodes as catalysts for seawater electrolysis, and considering the good performance obtained in the NaCl solution, the previous tests were repeated in a solution simulating the seawater. **Figures 5.17 - 5.20**, show the comparison between the performance obtained in 30% w/w KOH solution (green curve, labelled KOH) and the performance in a 30% w/w KOH solution containing also Na^+, Cl^-, SO_4^{2-}, Mg^{2+}, Ca^{2+} and K^+ (blue curve, labelled Simulated SeaWater).

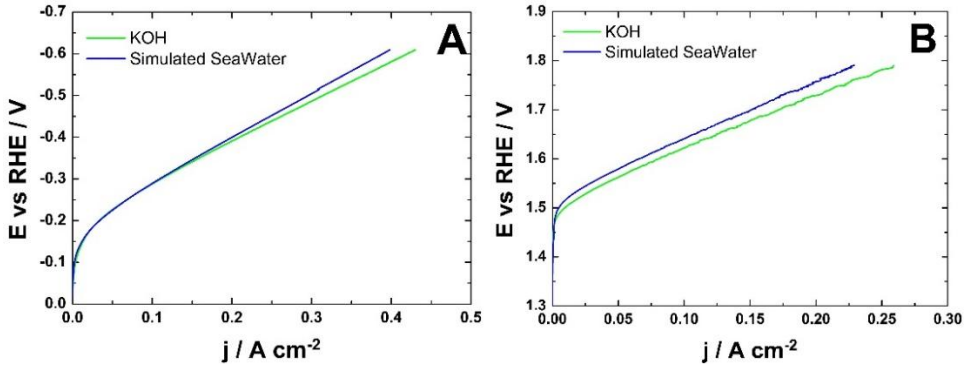

Fig. 5.17 *QSSP for (**A**) HER and (**B**) OER*

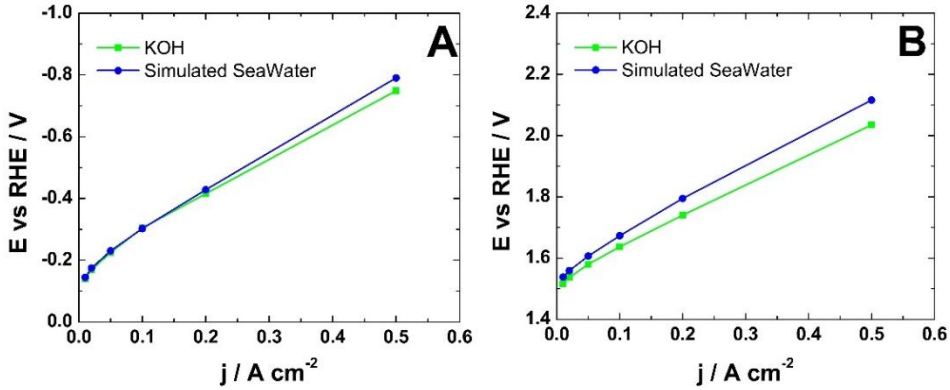

Fig. 5.18 *Galvanostatic step polarization (**A**) HER and (**B**) OER*

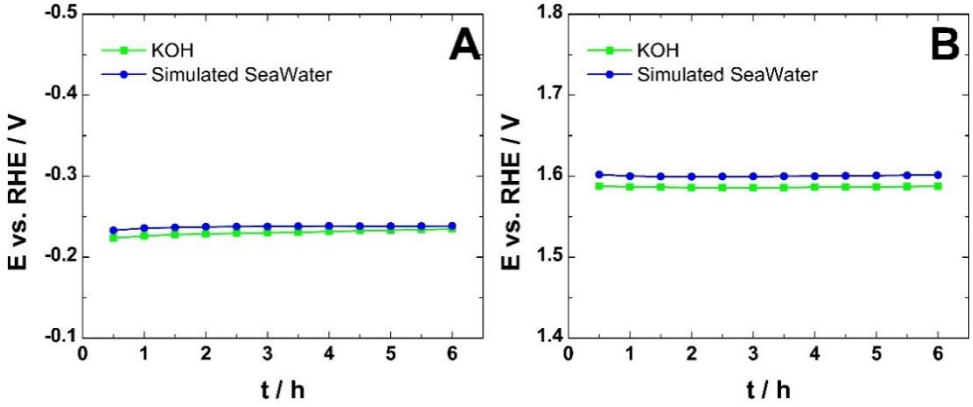

Fig. 5.19 *Mid-term stability test for 6 hours for (**A**) HER at −50 mA/cm^2 and **B**) OER at 50 mA/cm^2*

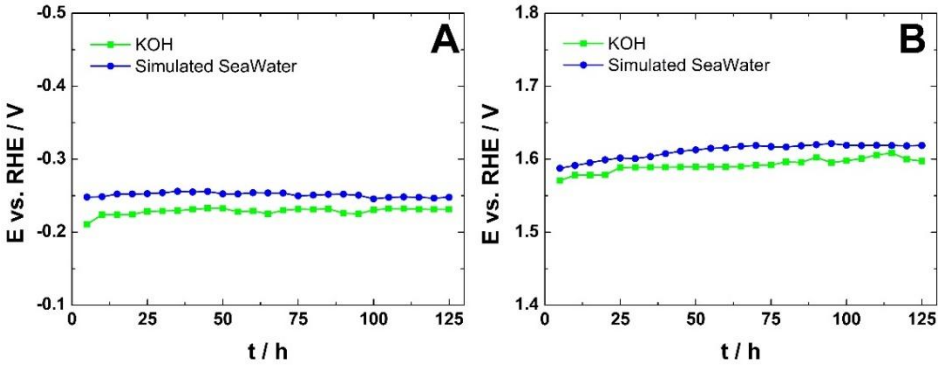

Fig. 5.20 *Long-term stability test for 125 hours for (**A**) HER at −50 mA/cm^2 and (**B**) OER at 50 mA/cm^2*

In both solutions, the performance of the electrodes is comparable suggesting a good stability and selectivity towards the desired water splitting reactions. Focusing on the stability test, the difference on cell potential is only 20-30 mV. For the test performed in simulated seawater, the final potential is 1.615 and -0.247 V vs. RHE, for HER and OER.

To further evaluate the catalyst stability, QSSP tests were conducted again after the long-term stability test in simulated seawater, **Figure 5.21**. The two curves are practically superimposable, confirming the results obtained previously.

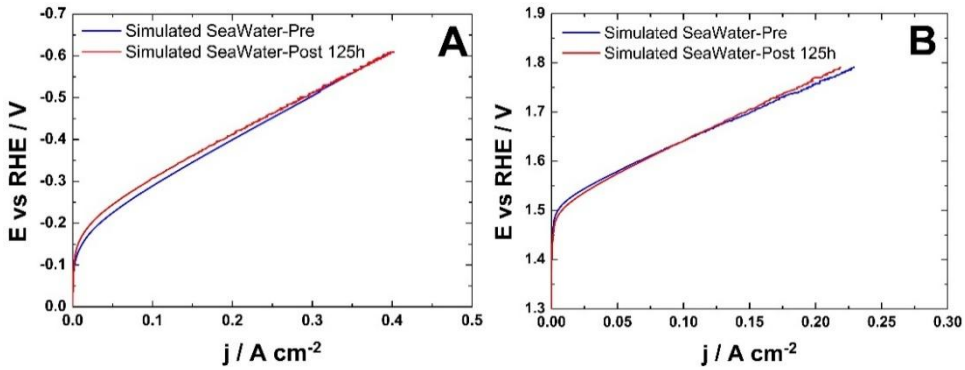

Fig. 5.21 *QSSP test before and after 125 hours for (**A**) HER and (**B**) OER*

To the production of green hydrogen, water electrolysis system must be coupled with renewable energy sources (RES). This means that the electrolyser may be subject to variable power supplies and even periods of inactivity. To replicate such intermittent functioning, the NiFeP electrodes were tested in a single-cell electrolyzer (using "Simulated SeaWater" as electrolyte) in long-term trials with intermittent power supply, alternating hours of constant current with hours when the electrolyzer was left in open-circuit mode. Since, RES exhibit significant fluctuations (such as the day-night cycle), the system was subjected to two different discontinuous functioning [26]:

- Solar Power-Seawater Electrolyzer: 20 hours of operation at ±50 mA/cm^2 and 4 hours at open-circuit potential, **figure 5.22**;
- Wind Power- Seawater Electrolyzer: 8 hours of operation at ±50 mA/cm^2 and 16 hours at open-circuit potential, **figure 5.23**.

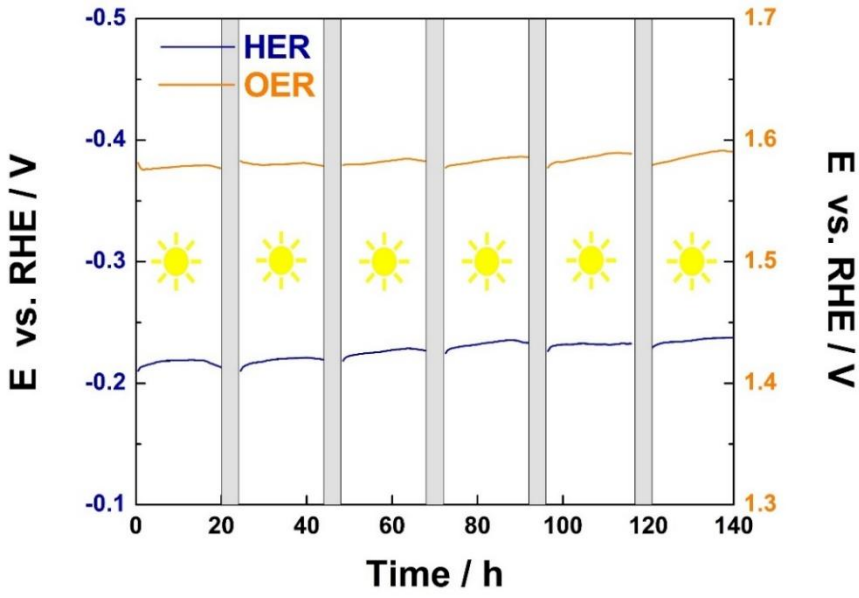

Fig. 5.22 *Intermittent functioning: Solar Power-Seawater Electrolyzer*

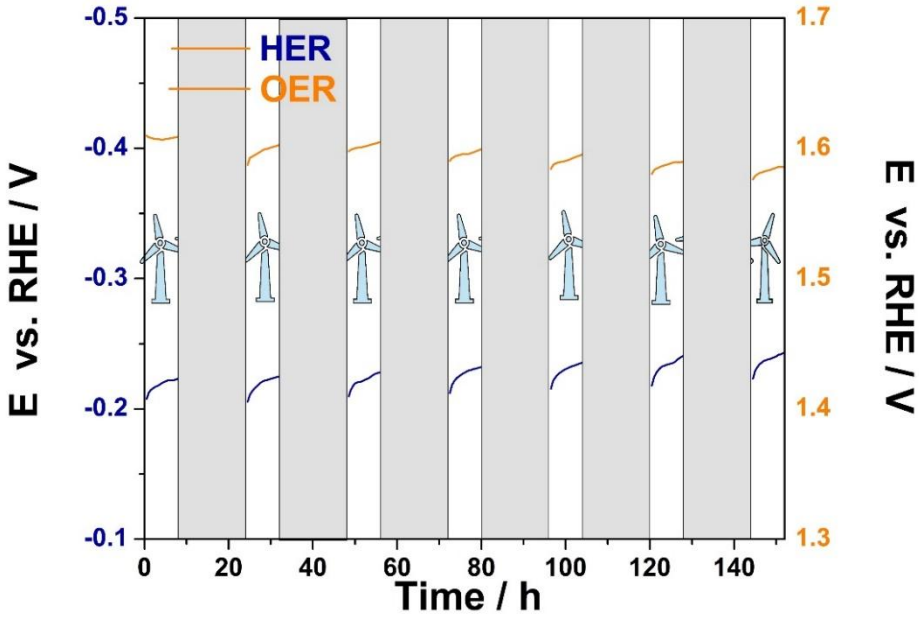

Fig. 5.23 *Intermittent functioning: Wind Power-Seawater Electrolyzer*

For both intermittent operations, the curves were obtained by averaging the potential every half hour. In the first graph, the potential for both reactions is almost constant. The potential shifts approximately from -0.213 to -0.235 V for HER and 1.58 to 1.59 V for OER. For the second intermittent functioning, the performance are also good but especially for the cathodic side, the potential during the 8 hours of operation not reach a stable value, but the values are still comparable to those obtained in the previous test. The potential achieved during the various operating hours is comparable to that of continuous operation. These results are promising because suggest a good behaviour of the nanostructured electrodes.

5.4 Overall Water Splitting

To test the overall water splitting, the scale-lab electrolyzer described in the previous chapter (4.5) was used. In a first phase, NiFeP NWs electrodes were tested by QSSP, Galvanostatic step polarization at room temperature, 25°C, and the results were compared with those obtained using NiFe as anode and cathode. In the following images (**Figure 5.24**), the comparison between two electrodes is shown. As we can see, using the ternary alloy for both anodic and cathodic side, the performance is better, confirming the results obtained with the three-electrode configuration. At a current density of 500 mA/cm^2 moving to the binary to the ternary alloy, an energy gain of about 320 mV is obtained.

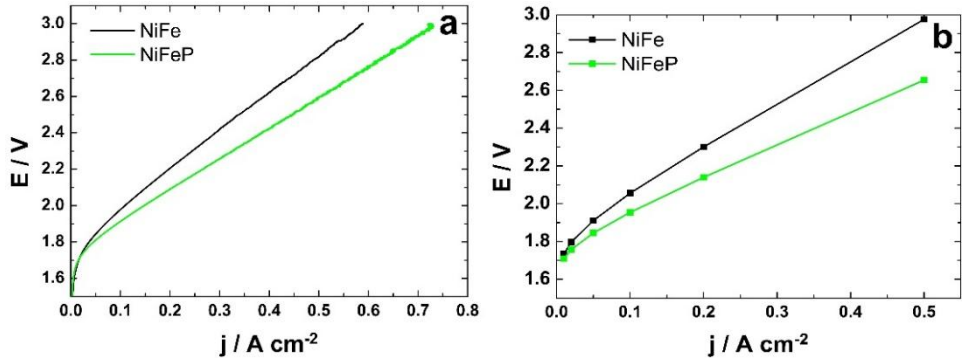

Fig. 5.24 *Comparison of NiFe (black curve) and NiFeP (green curve) in a lab-scale electrolyzer at 25 °C (**A**) QSSP (**B**)Galvanostatic Step polarization*

From the results obtained in the 125-hour stability test, **Figure 5.25**, the potential changes from 1.92 to 1.95 V. Considering that the electrolyzer prototype is only in the initial design and assembly phase, these results are very promising.

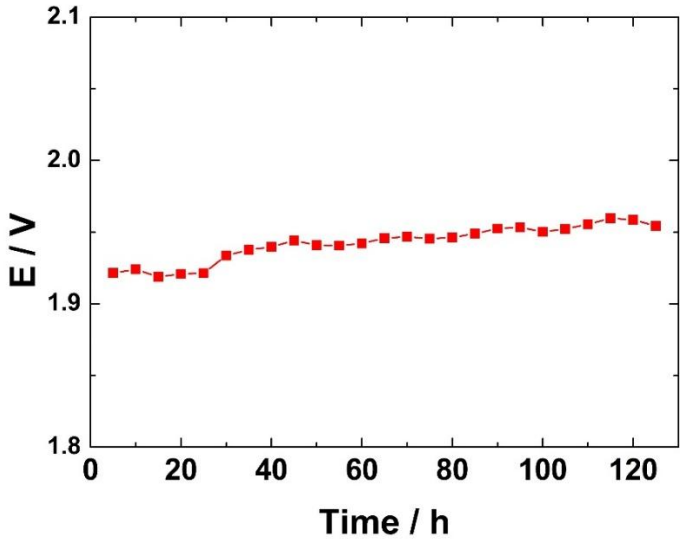

Fig. 5.25 *Long-term stability test in a lab-scale electrolyzer at* 50 mA cm^{-2} *and 25 °C*

Considering the superior performance of the ternary alloy, these electrodes were further characterized. QSSP and Galvanostatic step were performed at different temperatures and compared with those obtained at room temperature. **The figure 5.26** shows this comparison. As expected, the best performance is obtained at 60 °C. Moving to room temperature to 60 °C, the activity increases. Considering the lower and higher current density, 10 mA/cm^2 and 500 mA/cm^2, moving to room temperature to 60 °C, an energy gain of about 120 mV and 420 mV is obtained.

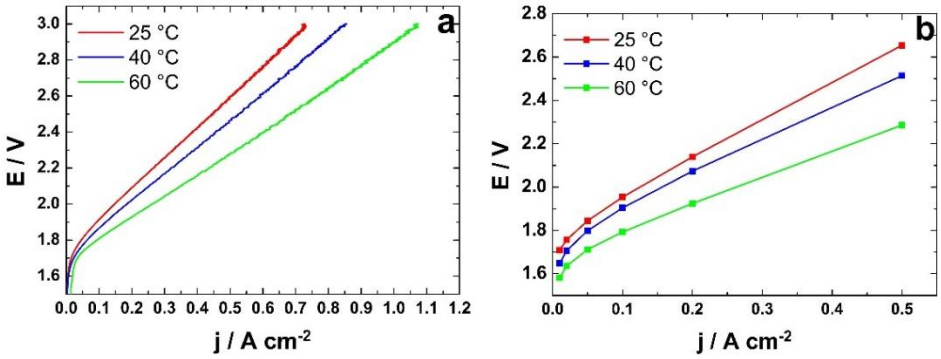

Fig. 5.26 *Electrochemical test of lab-scale electrolyzer at different temperatures (**A**) QSSP (**B**)Galvanostatic Step polarization*

In the meanwhile, the stability in the mid-term period was evaluated in different conditions, two different current density were imposed 50 and 100 mA cm^2 at 25 °C and at 40 °C. The comparison between these different tests is shown in the following **Figure 5.27**. The results are very promising, especially for the test performed at 40°C with a current density of 100 mA cm^2, where an almost stable potential value was measured.

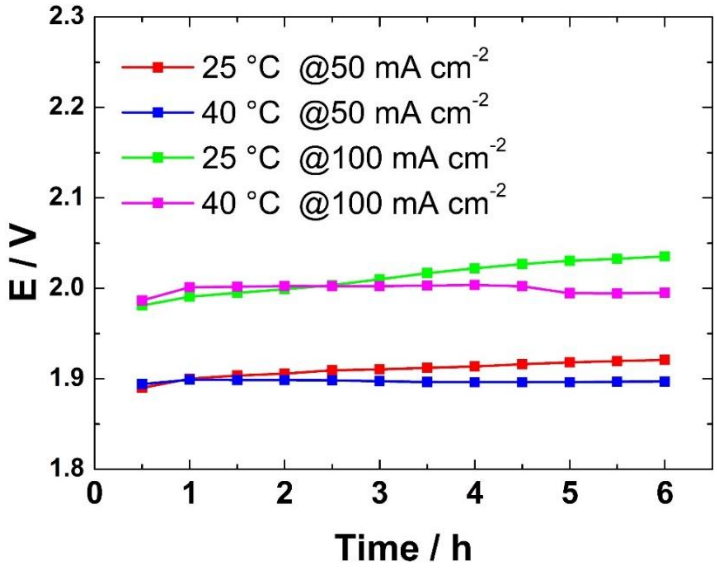

Fig. 5.27 *Mid-term stability test in a lab-scale electrolyzer at different conditions*

5.5 Life Cycle Assessment

Life Cycle Assessment (LCA) is an effective methodology for evaluating the potential environmental impacts of a product throughout its lifecycle. By analysing the entire life cycle, LCA reveals hidden environmental impacts, identifies areas for improvement, and helps prevent burden shifting. This study was carried out in collaboration with the research group of Professor Maurizio Cellura of the University of Palermo, and it is conducted in accordance with international standards UNI EN ISO 14040 [27] and 14044 [28], using an attributional approach.

The LCA process is divided into four phases [27]:

1. **Goal and Scope Definition:** This initial phase outlines the aims of the study, defines system boundaries, establishes the functional unit, describes allocation procedures, and identifies impact categories and methodologies for the impact assessment.

2. **Life Cycle Inventory Analysis:** This phase involves data collection and calculations to assess resource consumption, direct emissions, and waste generation throughout the product's lifecycle.

3. **Life Cycle Impact Assessment:** Building on the data collected, this phase calculates the potential environmental impacts associated with the product.

4. **Life Cycle Interpretation:** In this final phase, the results from the impact assessment are summarized and analyzed to draw conclusions and make recommendations.

The primary objectives of the assessment are to evaluate the energy and environmental impacts of the examined electrode across three different scenarios and to identify the contributions of each manufacturing stage to the total impacts. The inventory includes sputtering, electrodeposition, and etching with trichloromethane, with data collected for three scenarios varying in NaH_2PO_2 concentration. For each of these sub-steps, primary data regarding the input and output flows are collected at the lab scale. The inventory analysis focuses on an electrode with a surface area of 17.35 cm^2.

All eco-profiles for the materials and energy sources, which provide secondary data for modelling the supply chains involved in the materials and energy used, are derived from the Ecoinvent database [29]. To fill gaps in the available secondary data within the environmental database, several assumptions were made:

1. Standard polycarbonate was used in place of track-etched polycarbonate membranes.

2. Nickel chloride ($NiCl_2$) and sodium hypophosphite (NaH_2PO_2) were modeled based on their stoichiometric reactions.

3. Deionized water was utilized instead of distilled water.

These assumptions contribute to a more accurate assessment of the environmental impacts associated with the manufacturing process.

5.5.1 Life Cycle Impact Assessment and Interpretation

The analysis shows negligible differences among the three scenarios, suggesting that the phosphorus precursor used in the electrodeposition step has a minimal contribution to overall environmental impacts. Therefore, increasing the concentration of this precursor leads to only a slight increase in environmental effects. A detailed contribution analysis of the electrodeposition process reveals that $NiSO_4$ and $NiCl_2$ are the materials with the most significant environmental impact, contributing approximately 45% and 52%, respectively. To identify which processes in the manufacturing stage are responsible for the majority of the impacts, a contribution analysis was conducted for the NiFePe/3 scenario, with similar findings applicable to the other scenarios. **Figure 5.28** illustrates that the sputtering and etching processes using trichloromethane result in the highest impacts across nearly all impact categories. This is mainly due to the use of gold in the sputtering process and trichloromethane in the etching process. In contrast, the electrodeposition process ranks higher than the other steps only in the categories of "water use" and "acidification."

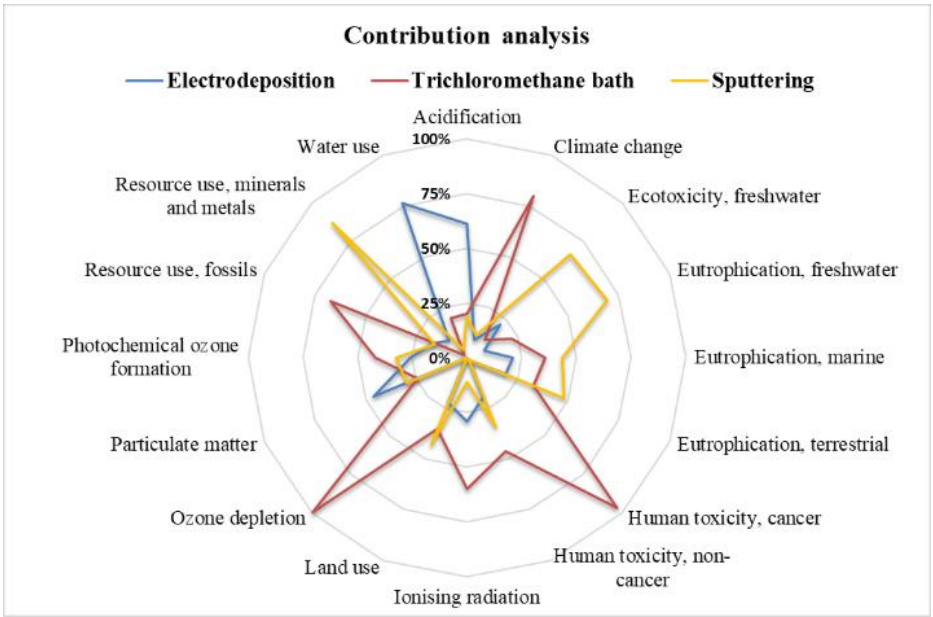

Fig. 5.28 *Contribution analysis of NiFeP/3*

5.6 Conclusions

This study explores the performance of nanostructured NiFeP alloy electrodes, synthesized through template electrosynthesis, for water electrolysis. The electrodes, consisting of approximately 79% iron and 6-8% phosphorus, were evaluated as both cathodes and anodes in a 30% w/w KOH solution. The results were compared with those obtained in a previous work about the behaviour of NiFe NWs. CV, QSSP, and galvanostatic methods were used to analyze the electrochemical behaviour of the electrodes. Stability assessments were carried out through medium- and long-term galvanostatic tests at a current density of ±50 mA/cm² for durations of 6 hours and 125 hours, respectively. After the long-term tests, chemical and physical characterization was performed to detect any potential changes in electrode morphology and composition. The best ternary is individuated and to further assess its suitability for seawater electrolysis, long-term stability test was conducted in

a KOH solution with the addition of 0.5 M NaCl, and the results were compared with those from tests in a pure KOH solution. Findings reveal that the NiFeP nanostructured electrodes exhibit effective catalytic activity for both HER and OER. The addition of NaCl appears not to impact the electrode's stability in the short or long term. Performance in the KOH + NaCl solution was very similar to that in the KOH solution alone. Moreover, the electrodes showed robust mechanical and chemical stability during both medium- and long-term gas evolution phases. For this reason, electrochemical tests were repeated in a simulated seawater electrolyte with a various anions and cations present in seawater. Results are very promising because the current/potential behaviour in the various tests is very similar to that obtained in the solution of only KOH. Two tests were also conducted to evaluate stability under intermittent conditions, and once again, the results are very interesting suggesting the idea of using these electrodes in a SWE powered by energy from renewable sources.

These nanostructured electrodes were also tested for overall water splitting in a lab-scale electrolyzer, demonstrating good performance and confirming the results obtained when electrodes were tested individually. In the future, it would be ideal to test these electrodes in the electrolyser prototype using simulated sea water first and then real sea water samples which have undergone a desalination treatment process to study their efficiency and stability for cycles of longer operation in order to facilitate the transition between laboratory tests and pilot plants.

Additionally, the environmental impact of NiFeP electrodes was assessed using the life cycle assessment (LCA) methodology, examining three scenarios with varying phosphorus precursor concentrations. Results indicated that an increase in phosphorus precursor concentration led to only a slight rise in environmental impact. Contribution analysis showed that

electrodeposition has the lowest impact across most environmental categories. Given the increasing relevance of such technologies, this work could provide a basis for future LCA studies on other electrode types used in electrolyzers.

References

[1] F. Wang, X. Yang, B. Dong, X. Yu, H. Xue, e L. Feng, «A FeP powder electrocatalyst for the hydrogen evolution reaction», *Electrochemistry Communications*, vol. 92, pp. 33–38, lug. 2018, doi: 10.1016/j.elecom.2018.05.020.

[2] C. Du, M. Shang, J. Mao, e W. Song, «Hierarchical MoP/Ni $_2$ P heterostructures on nickel foam for efficient water splitting», *J. Mater. Chem. A*, vol. 5, fasc. 30, pp. 15940–15949, 2017, doi: 10.1039/C7TA03669H.

[3] S. Anantharaj, S. R. Ede, K. Sakthikumar, K. Karthick, S. Mishra, e S. Kundu, «Recent Trends and Perspectives in Electrochemical Water Splitting with an Emphasis on Sulfide, Selenide, and Phosphide Catalysts of Fe, Co, and Ni: A Review», *ACS Catal.*, vol. 6, fasc. 12, Art. fasc. 12, dic. 2016, doi: 10.1021/acscatal.6b02479.

[4] D. Li, H. Liu, e L. Feng, «A Review on Advanced FeNi-Based Catalysts for Water Splitting Reaction», *Energy Fuels*, vol. 34, fasc. 11, pp. 13491–13522, nov. 2020, doi: 10.1021/acs.energyfuels.0c03084.

[5] H. Ooka, J. Huang, e K. S. Exner, «The Sabatier Principle in Electrocatalysis: Basics, Limitations, and Extensions», *Front. Energy Res.*, vol. 9, p. 654460, mag. 2021, doi: 10.3389/fenrg.2021.654460.

[6] R. Li *et al.*, «Electrodeposition: Synthesis of advanced transition metal-based catalyst for hydrogen production via electrolysis of water», *Journal of Energy Chemistry*, vol. 57, pp. 547–566, giu. 2021, doi: 10.1016/j.jechem.2020.08.040.

[7] G. Barati Darband, M. Aliofkhazraei, S. Hyun, e S. Shanmugam, «Pulse Electrodeposition of a Superhydrophilic and Binder-Free Ni–Fe–P Nanostructure as Highly Active and Durable Electrocatalyst for Both Hydrogen and Oxygen Evolution Reactions», *ACS Appl. Mater. Interfaces*, vol. 12, fasc. 48, Art. fasc. 48, dic. 2020, doi: 10.1021/acsami.0c13648.

[8] F. Ganci *et al.*, «Ni alloy nanowires as high efficiency electrode materials for alkaline electrolysers», *International Journal of Hydrogen Energy*, vol. 46, fasc. 72, Art. fasc. 72, ott. 2021, doi: 10.1016/j.ijhydene.2020.11.208.

[9] O. Dragos, H. Chiriac, N. Lupu, M. Grigoras, e I. Tabakovic, «Anomalous Codeposition of *fcc* NiFe Nanowires with 5–55% Fe and Their Morphology, Crystal Structure and Magnetic Properties», *J. Electrochem. Soc.*, vol. 163, fasc. 3, pp. D83–D94, 2016, doi: 10.1149/2.0771603jes.

[10] Q. Han, L. Fan, e H. Wan, «Recent Development of Metal Alloy Nanostructures for Electrochemical Hydrogen Generation»,

International Journal of Electrochemical Science, vol. 14, fasc. 12, pp. 10549–10559, dic. 2019, doi: 10.20964/2019.12.21.

[11] S. Cartagena, F. E. Bedoya-Lora, e J. A. Calderón, «Enhancement of Anodically Treated Stainless Steel by NiFeP-Catalyst Electrodeposition as Bifunctional Electrodes for Water Electrolysis», *J. Electrochem. Soc.*, vol. 169, fasc. 4, p. 044501, apr. 2022, doi: 10.1149/1945-7111/ac5ff1.

[12] T. Armbruster e R. M. Danisi, A c. di, *Highlights in mineralogical crystallography*. Berlin Boston: Walter de Gruyter GmbH, 2016.

[13] H. Li, F. Chen, X. Wu, D. Wang, Y. Ren, e Y. Li, «Improved HER/OER Performance of NiS2/MoS2 Composite Modified by CeO2 and LDH», *Materials*, vol. 17, fasc. 19, p. 4876, ott. 2024, doi: 10.3390/ma17194876.

[14] J. Lian, Y. Wu, H. Zhang, S. Gu, Z. Zeng, e X. Ye, «One-step synthesis of amorphous Ni–Fe–P alloy as bifunctional electrocatalyst for overall water splitting in alkaline medium», *International Journal of Hydrogen Energy*, vol. 43, fasc. 29, Art. fasc. 29, lug. 2018, doi: 10.1016/j.ijhydene.2018.05.107.

[15] F. Schröper, D. Brüggemann, Y. Mourzina, B. Wolfrum, A. Offenhäusser, e D. Mayer, «Analyzing the electroactive surface of gold nanopillars by electrochemical methods for electrode miniaturization», *Electrochimica Acta*, vol. 53, fasc. 21, pp. 6265–6272, set. 2008, doi: 10.1016/j.electacta.2008.03.068.

[16] F. Yu, L. Yu, I. K. Mishra, Y. Yu, Z. F. Ren, e H. Q. Zhou, «Recent developments in earth-abundant and non-noble electrocatalysts for water electrolysis», *Materials Today Physics*, vol. 7, pp. 121–138, dic. 2018, doi: 10.1016/j.mtphys.2018.11.007.

[17] W. Xu, R. Qiu, X. Mao, X. Yang, B. Peng, e Y. Shen, «One-step fabrication of amorphous Ni-Fe phosphated alloys as efficient bifunctional electrocatalysts for overall water splitting», *Journal of Non-Crystalline Solids*, vol. 587, p. 121598, lug. 2022, doi: 10.1016/j.jnoncrysol.2022.121598.

[18] N. A. Khan *et al.*, «Recent Development of Nanostructured Nickel Metal-Based Electrocatalysts for Hydrogen Evolution Reaction: A Review», *Top Catal*, vol. 66, fasc. 1–4, pp. 149–181, gen. 2023, doi: 10.1007/s11244-022-01706-2.

[19] H.-M. Zhang, J.-J. Wang, Y. Meng, e J. Sun, «Recent advances in amorphous metal phosphide electrocatalysts for hydrogen evolution reaction», *International Journal of Hydrogen Energy*, vol. 47, fasc. 85, pp. 36084–36097, ott. 2022, doi: 10.1016/j.ijhydene.2022.08.184.

[20] J. Mohammed-Ibrahim, «A review on NiFe-based electrocatalysts for efficient alkaline oxygen evolution reaction», *Journal of Power Sources*, vol. 448, p. 227375, feb. 2020, doi: 10.1016/j.jpowsour.2019.227375.

[21] Q. Liang, G. Brocks, e A. Bieberle-Hütter, «Oxygen evolution reaction (OER) mechanism under alkaline and acidic conditions», *J. Phys. Energy*, vol. 3, fasc. 2, p. 026001, apr. 2021, doi: 10.1088/2515-7655/abdc85.
[22] H.-M. Zhang, J.-J. Wang, Y. Meng, e J. Sun, «Recent advances in amorphous metal phosphide electrocatalysts for hydrogen evolution reaction», *International Journal of Hydrogen Energy*, vol. 47, fasc. 85, Art. fasc. 85, ott. 2022, doi: 10.1016/j.ijhydene.2022.08.184.
[23] Y. Li *et al.*, «A review: Target-oriented transition metal phosphide design and synthesis for water splitting», *International Journal of Hydrogen Energy*, vol. 46, fasc. 7, pp. 5131–5149, gen. 2021, doi: 10.1016/j.ijhydene.2020.11.030.
[24] C. Zhang *et al.*, «Ternary nickel iron phosphide supported on nickel foam as a high-efficiency electrocatalyst for overall water splitting», *International Journal of Hydrogen Energy*, vol. 43, fasc. 15, pp. 7299–7306, apr. 2018, doi: 10.1016/j.ijhydene.2018.02.157.
[25] M. C. Biesinger, B. P. Payne, A. P. Grosvenor, L. W. M. Lau, A. R. Gerson, e R. St. C. Smart, «Resolving surface chemical states in XPS analysis of first row transition metals, oxides and hydroxides: Cr, Mn, Fe, Co and Ni», *Applied Surface Science*, vol. 257, fasc. 7, pp. 2717–2730, gen. 2011, doi: 10.1016/j.apsusc.2010.10.051.
[26] S. Dresp *et al.*, «Direct Electrolytic Splitting of Seawater: Activity, Selectivity, Degradation, and Recovery Studied from the Molecular Catalyst Structure to the Electrolyzer Cell Level», *Adv. Energy Mater.*, vol. 8, fasc. 22, Art. fasc. 22, ago. 2018, doi: 10.1002/aenm.201800338.
[27] «UNI EN ISO 14040 (2006). Environmental Management – Life Cycle Assessment –Principles and Framework».
[28] «UNI EN ISO 14044 (2006). Environmental Management – Life Cycle Assessment –Requirements and Guidelines»,.
[29] G. Wernet, C. Bauer, B. Steubing, J. Reinhard, E. Moreno-Ruiz, e B. Weidema, «The ecoinvent database version 3 (part I): overview and methodology», *Int J Life Cycle Assess*, vol. 21, fasc. 9, pp. 1218–1230, set. 2016, doi: 10.1007/s11367-016-1087-8.

6. Fabrication and Characterization of Ni Based-High Entropy Alloys

The fabrication and characterization of High Entropy Alloys for alkaline water splitting was carried out in collaboration with “INSTITUT DE RECERCA EN ENERGIA DE CATALUNYA -IREC” under the supervision of Prof. Andreu Cabot.

6.1 Introduction

In recent years, high entropy alloys (HEAs), a new class of alloys known for their corrosion, hardness, wear, and creep resistance, have garnered increasing interest. Research suggests that HEAs possess outstanding catalytic activity due to their four key effects: the high entropy effect in thermodynamics, lattice distortion in structure, sluggish diffusion in dynamics, and the cocktail effect in properties. Due to their high mixing entropy, HEAs are less prone to forming intermetallic compounds. Still, they tend to crystallize into simple face-centered cubic or body-centered cubic phases and potentially even amorphous states. In typical HEAs, the elemental content of each component is relatively close to equimolar, which facilitates tuning the composition of the alloy to optimize catalytic activity while maintaining stability. The synergistic interaction among components in multi-component catalysts has been recognized as an effective strategy for enhancing catalytic efficiency. Additionally, porous nanostructures are known to offer larger surface areas, which further improves performance. Nano-porous high entropy alloys (HEAs) show great promise as electrocatalysts due to their impressive catalytic performance and stability [1], [2]. Currently, the fabrication of high entropy alloys is mainly achieved through physical techniques [3]. HEAs composed of 3d transition metals are among the most researched. The CrMnFeCoNi alloy, a well-known example, can be produced using methods

such as sputtering, arc melting, and plasma sintering. However, these techniques often require high temperatures or costly equipment with limited production capacity, making them less suitable for cost-effective manufacturing [4], [5]. Moreover, the varying properties of different elements (such as their melting points or volatility) often constrain the selection of alloy compositions when using these methods, even when working with the same mixture of elements. Recently, the electrodeposition technique has been explored for producing nanomaterials and alloys. This method has several advantages, such as excellent bonding strength, high density, and strong potential for large-scale application and production. Nevertheless, due to the differing attractions of ions to charges, electrodeposition can be challenging. Achieving a high-quality alloy coating depends on selecting the right complexing agent, adjusting the concentration of metal ions, and optimizing the electrodeposition parameters [6]. In this chapter, to harness the synergistic effect of different metals, various tests were carried out to optimize the electrodeposition of high-entropy alloys first onto a nickel foam and then in the nanowire shape.

6.2 Fabrication and Characterization of NiFeCoMnCr alloy on Nickel Foam

The electrodeposition solution contains all the metal ions necessary to obtain the desired alloy. The electrodeposition was carried out in a standard three-electrode cell at room temperature. A Pt wire was used as a counter electrode, and an Ag/AgCl was used as a reference. Linear Sweep Voltammetry (LSV) at 1 mV s^{-1} and Cyclic Voltammetry measurements were carried out in 1 M KOH at room temperature. A Chi76E potentiostat was used for all electrochemical measurements. Before electrodeposition, NF was cleaned ultrasonically firstly with 2 M HCl for 30 minutes, then with Ethanol also for

30 minutes. Finally, it was rinsed several times with Mill-Q water and dried in the air. Several tests were made by varying both the operating conditions and the composition of the electrodeposition solution. In particular, different solutions with the same concentration of all reagents, 0.25, 0.1, 0.05 M of **Fe**Cl_2*4H_2O, **Co**Cl_2*6H_2O, **Mn**Cl_2*4H_2O, **Cr**Cl_3*6H_2O, **Ni**Cl_2*6H_2O were used. It was found that a concentration of 0.05 M was sufficient to uniformly coat the substrate and obtain a dense coating. In addition, it was established that the optimal content of Chromium was **0.02 M** to avoid its excessive deposition. Initially, the electrodepositions were performed through galvanostatic methods by applying different current densities and for different deposition times. **Figure 6.1** shows an example of galvanostatic electrodeposition at 50 mA cm^{-2} for different times. By applying this current, a reduction potential of the species of approximately -1.2 V is obtained. SEM images **(Figure 6.2**), show the formation of a dense deposit with a clod morphology, like dry mud. It was found that a long deposition time, 60 and 30 minutes, is not suitable for obtaining a uniform coating on Ni foam. In fact, according to [7], also for potentiostatic deposition, as electrodeposition time increases, the formation of agglomerates becomes more pronounced, which tends to easily detach from the foam, leaving uncovered areas. For this reason, the deposition time was reduced to 15 minutes.

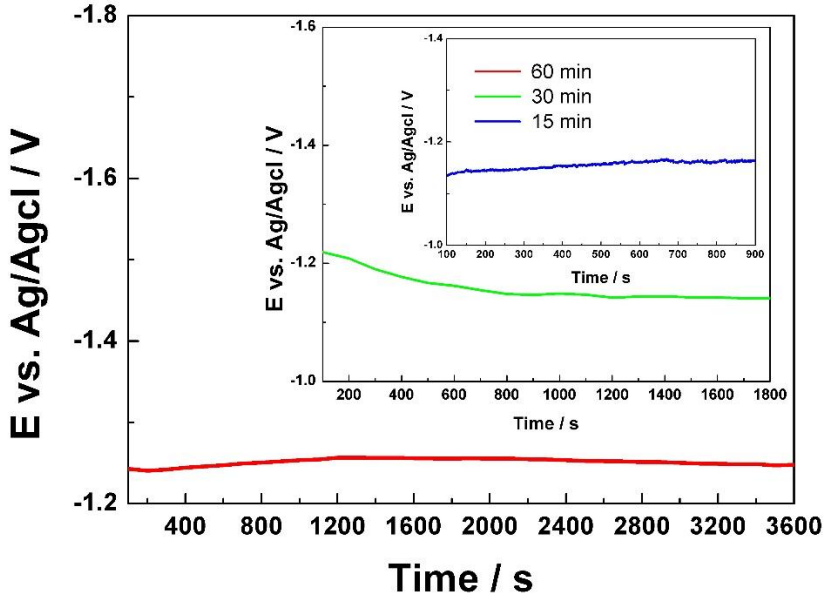

Fig. 6.1 *Galvanostatic Electrodeposition of NiFeCoMnCr alloy at 50mA cm^{-2} for 60 min (red curve), 30 min (green curve) and 15 min (blue curve)*

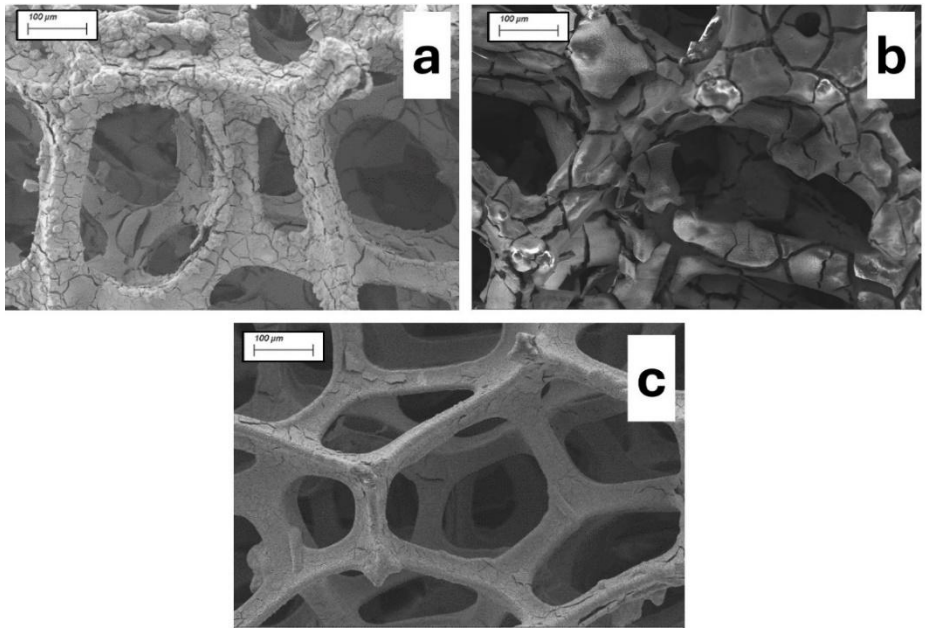

Fig. 6.2 *SEM images of samples obtained by Galvanostatic technique for 60 min (**A**), 30 min (**B**) and 15 min (**C**)*

In addition, since an accurate estimation of the real area of the foam immersed in solution was not always possible, the potentiostatic mode was chosen, applying the potential of -0.9, -1.2, -1.4 V vs Ag/AgCl. These values were selected from the galvanic deposition tests. Initial investigations have shown that at -0.9 V, the deposit is not uniform, so -1.3, -1.4, -1.5 V potential values were investigated. The following **figure 6.3** shows the potentiostatic electrodeposition of this alloy for 15 minutes. As observed, for each applied potential, j reaches a steady value after approximately 200 seconds of transient behaviour.

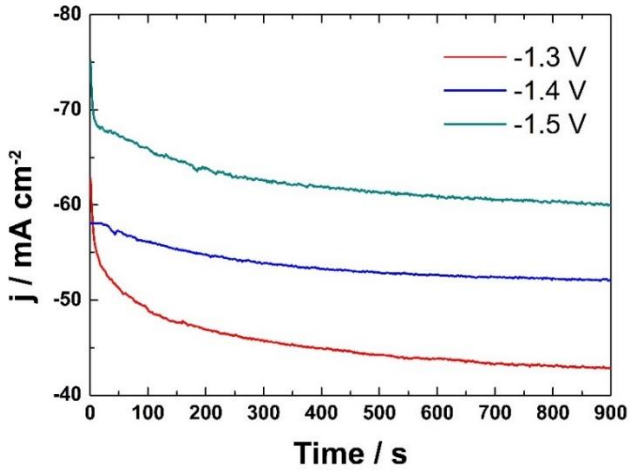

Fig. 6.3 *Potentiostatic Electrodeposition of NiFeCoMnCr alloy at different potentials for 15 minutes*

Then, to optimize the electrodeposition process and improve the adhesion of the coating to the foam, boric acid and citric acid were added to the electrodeposition bath, both acting as stabilizers, leveling, and complexing agents [8]. Their concentration (0.1-0.01 M) was varied to achieve the optimal solution composition. It was found the best concentration of 0.01 M for both acids.

The SEM images, **figure 6.4**, provide a comparison of the coating obtained without and with the addition of acids in the deposition bath, applying a potential of -1.4 V vs. Ag/AgCl for 900 s. The samples obtained with boric and citric acid in solution show fewer cracks and discontinuities that can negatively impact the adhesion properties of the coating on the foam substrate [9]. Notably, electrodeposition is more pronounced at the edges of the NF cavities, **fig. 6.4C,** due to the concentration of a local current density [10], which enhances deposition. **Table 6.1** provides the composition of two different samples by EDS analysis. The presence of all elements is confirmed. It is not possible to evaluate the exact composition of the alloy by EDS analysis due to the presence of nickel both in the alloy and in the foam substrate.

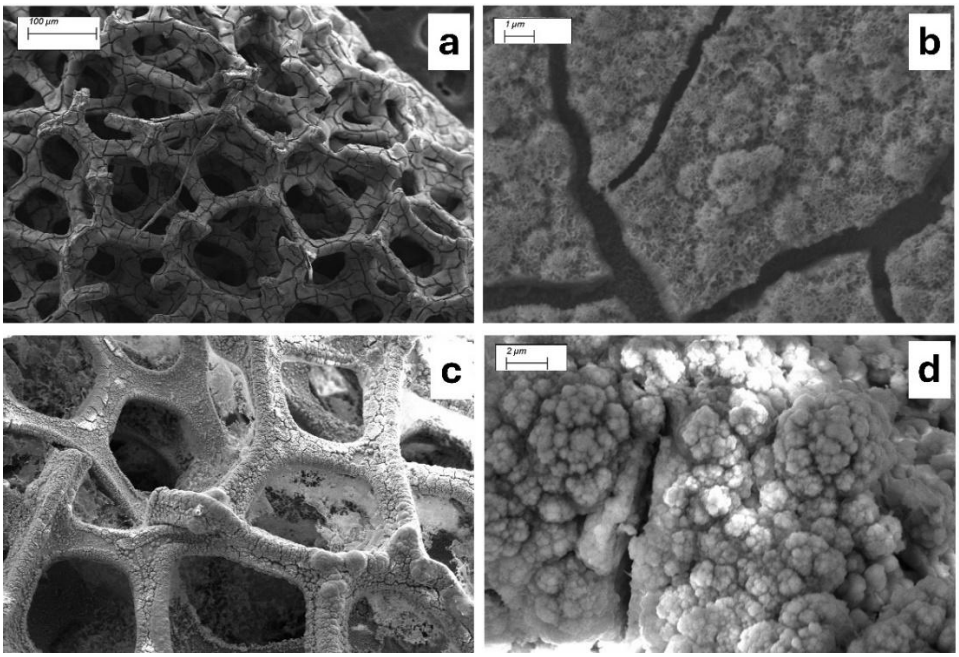

Fig. 6.4 *SEM images of* NiFeCoMnCr/NF *obtained* at -1.4 V vs. Ag/AgCl for 900 s *with* ***(A, B)*** *and without* ***(C, D)*** *acids*

Table 6.1 *EDS analysis of* NiFeCoMnCr/NF *obtained with and without acid*

	Ni ***%***	***Fe*** ***%***	***Co*** ***%***	***Mn*** ***%***	***Cr*** ***%***
Acid	63.3	16.86	11.11	2.72	5.99
No Acid	40.34	23.24	10.99	4.39	21.04

The sample obtained at -1.4 V vs. Ag/AgCl for 900 s was characterized by XRD. **Figure 6.5** shows the XRD pattern of NiFeCoMnCr/NF of for comparison also the patterns of NF and NiFeCoMnCr powder.

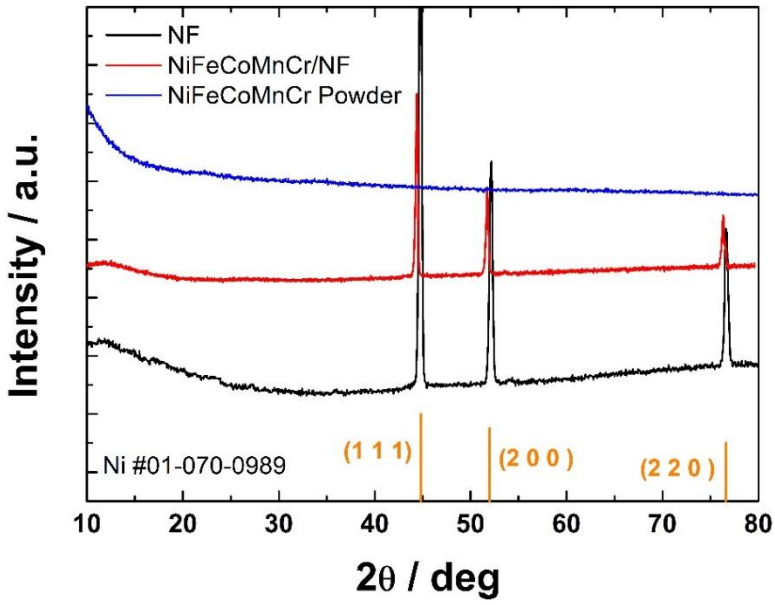

Fig. 6.5 *XRD pattern of Foam (black), NiFeCoMnCr/NF (red) and NiFeCoMnCr powder (blue)*

In the XRD patterns of both coated and uncoated foam, only the nickel peaks (JCPDS 01-070-0989) [11] are identified. According to the literature, the diffraction peaks of the alloy are not identified due to the amorphous state or

low crystallinity of the coating [12]. Moreover, the presence of an alloy with at least five elements often leads to peak shifts and decreased intensity. The Ni peaks have a lower intensity compared to those of the foam. This is due to a screening of the amorphous deposit that lowers the foam diffraction peaks. In addition, the peak intensities were not only much lower compared to those of pure Ni foam, but the decline in intensity was more pronounced at high angles than at low angles. Due to the high level of randomness in the distribution of different-sized atoms at lattice points, based on statistical average probability, the crystal structures of these multi element alloys were substantially distorted, leading to irregular atomic planes. During X-ray diffraction, this severe distortion caused significant X-ray scattering on the uneven Bragg planes, reducing the detectable diffraction signals intrinsic lattice distortion disrupted the crystal structure's perfection, enhancing the scattering effect and likely contributing to the simplified XRD patterns and reduced peak heights [13]. For comparison also the pattern of the NiFeCoMnCr powder was reported. The powder was obtained by washing ultrasonically the foam in isopropanol to detach the deposit from the substrate. The resulting solution was then placed in the support and left to allow the solvent to evaporate before performing the XRD analysis. In this pattern no peaks are present, confirming the amorphous nature of the alloy.

As observed in the previous SEM images, the coating deposited on Ni foam is composed of spherical particles uniformly covering the NF surface. This increase the electrochemical surface area (ECSA) of the electrode enhancing the HER [14]. To evaluate it, CVs curves were carried out from 20 to 100 mV s^{-1} in a non-faradic region for both NF (**figure 6.6A**) and *NiFeCoMnCr/NF (***figure 6.6B**).

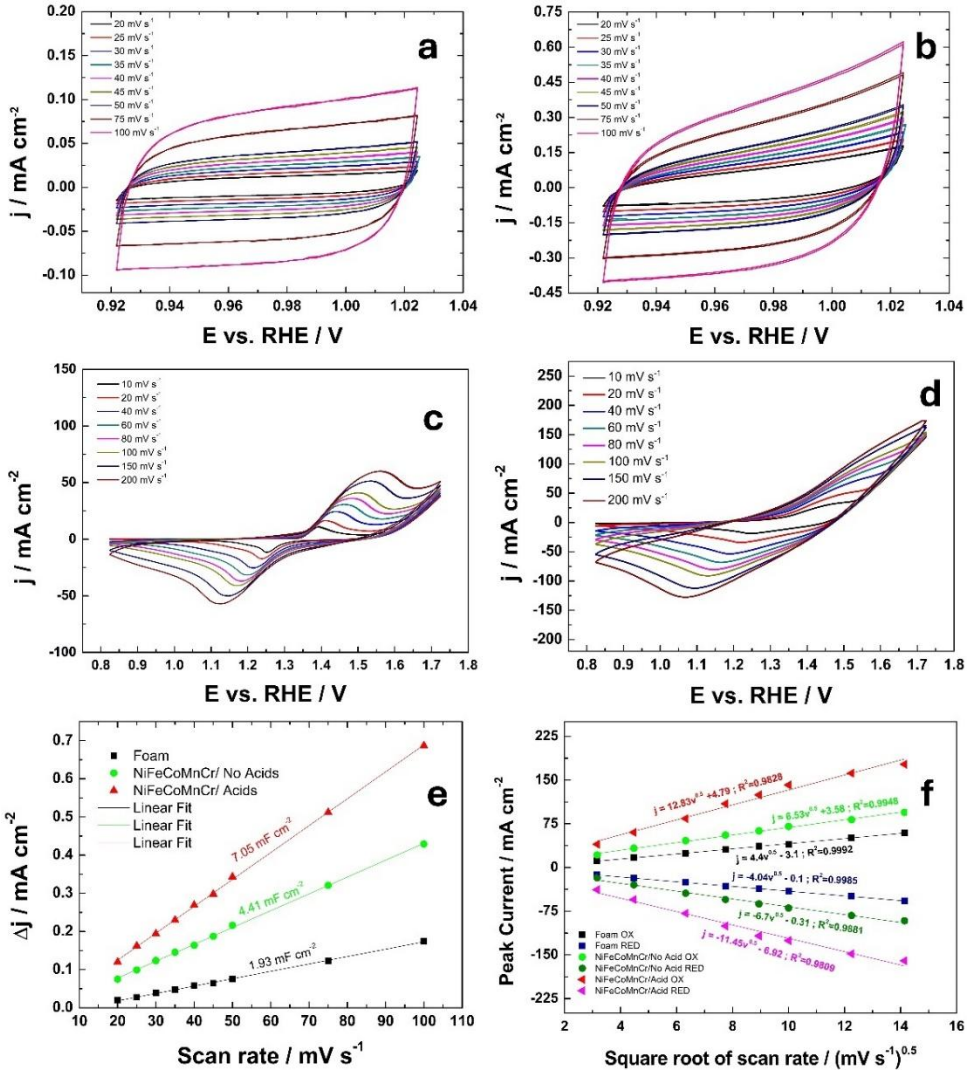

Fig. 6.6 *CVs in a non-faradic-region of (A) NF and (B)NiFeCoMnCr/NF; CVs of (C) NF and (C)NiFeCoMnCr/NF; (E) Specific capacitance of the electrodes is evaluated by double layer capacitance method; (D) Linear relationship between anodic and cathodic peak with the square root of the scan rate*

The specific capacitance, using the double-layer capacitance method, was then estimated because it is correlated with the ECSA. To date, CVs were performed ranging from 0.92 to 1.02 V compared to RHE, where no reactions occurred. For each scanning rate, the difference between anodic and cathodic

current density at 0.97 V vs. RHE was calculated and then plotted against the scan rate. **Figure 6.6E** shows the linear fitting of NF and the catalyst obtained with and without acids. The slope of NiFeCoMnCr/NF with acid is greater than that of the NF and catalyst without acids. This is a good result imputable to the very large surface area of the electrodeposited catalysts. This attribute is expected to enhance electrocatalytic performance. In addition, **figure 6.6C** and **6.6D** show CVs, in a large potential range, obtained at increasing scan rates, which aligns with findings in the literature [15], [16]. All the CV curves exhibit well-defined redox peaks, which indicate the Faradic dominant behavior of Ni based electrodes. The foam with the catalysts has a high current response. Focusing on CV profile of NiFeCoMnCr/NF, according to the literature, the oxidation and reduction peaks are not symmetric, which can be attributed to the kinetic irreversibility of the redox reactions occurring on the electrode surface. As expected, slight shift in the oxidation and reduction peaks is noticed as the scan rate increases [17]. Both oxidation and reduction current peaks exhibit a linear relationship with the square root of the scan rate, as shown in **figure 6.6F**, indicating a diffusion-controlled process. The larger slope for NiFeCoMnCr/NF obtained with acid in solution indicates a better diffusion processes [18].

The NiFeCoMnCr/NF electrodes obtained varying the deposition potential were tested for both HER and OER. In **Figure 6.7** (A-B) a comparison between these electrodes and uncoated NF was shown. The higher activity was obtained for electrodes obtained at a potential of -1.4 V. According to CV tests when acids are inserted into the solution, the electrode activity increases (Figure 6.7 (C-D)). The overpotential at 10 mA cm^{-2} for OER is about 116 mV compared to 356 mV obtained for NF. These performances are better or comparable to literature data concerning this type of alloy [19].

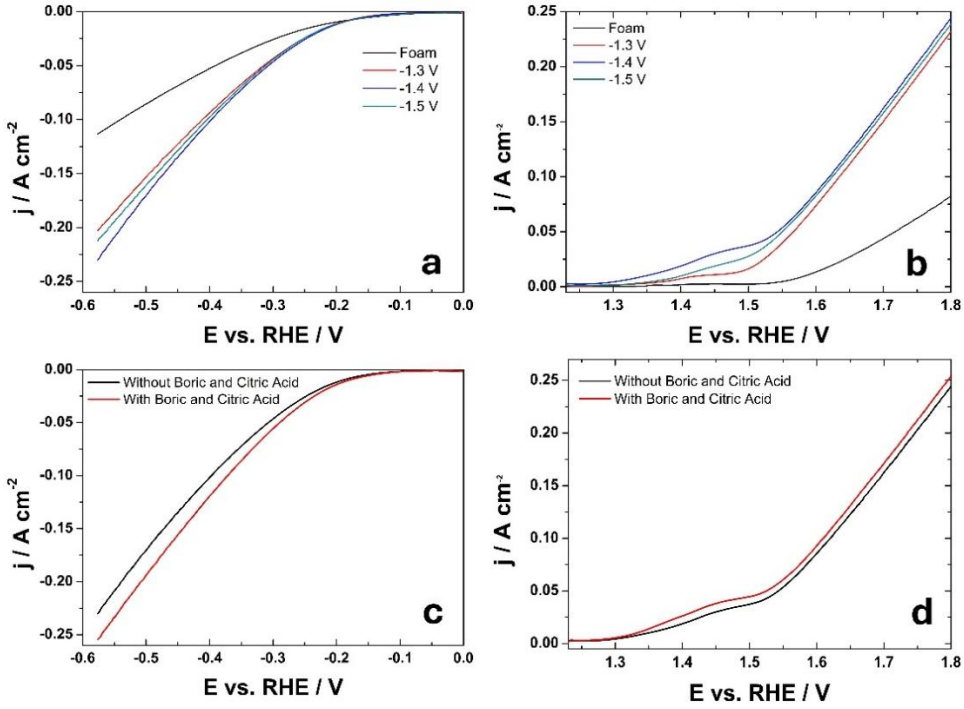

Fig. 6.7 *LSV curves of NiFeCoMnCr/NF obtained at different potentials (A) HER and (B) OER; Comparison of LSV curves of NiFeCoMnCr/NF obtained with and without acids (C) HER and (D) OER*

6.3 Fabrication and Characterization of NiFeCoMnCu alloy on Nickel Foam

Considering the good results obtained with the NiFeCoMnCr alloy, the NiFeCoMnCu alloy was also studied. The NiCu-based is considered a good electrocatalyst for alkaline HER, attributed to its enhanced electrocatalytic activity [20], excellent corrosion resistance [21] , and strong stability [22].

A solution with 0.05 M of $FeSO_4*7H_2O$, $CoSO_4*7H_2O$, $NiSO_4*6H_2O$, $MnSO_4*H_2O$ and 0.01 M of boric and citric acid was used. In this solution, different concentrations (0.05. 0.025, 0.01, 0.005 M) of $CuSO_4*5H_2O$ were added. The optimized conditions of the NiFeCoMnCr alloy were applied (-1.4

V for 900 s). Initial tests have shown that a deposition time of 600 s is sufficient to obtain a uniform coating on the NF substrate. The presence of all elements is confirmed by EDS analysis, **Figure 6.8.**

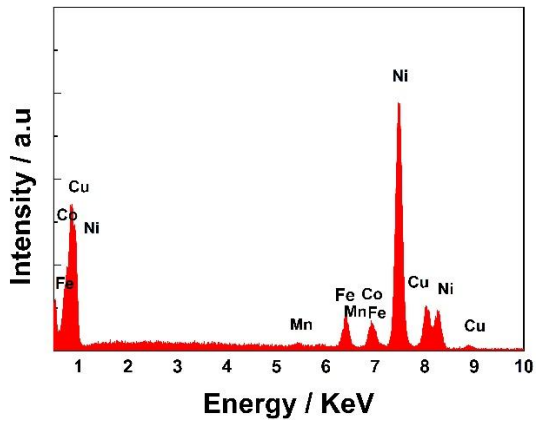

Fig. 6.8 *EDS spectrum of NiFeCoMnCu/NF(using 0.005 M of Cu precursor)*

Table 6.2 *EDS analysis of NiFeCoMnCu/NF electrodes*

Cu precursor [M]	***Ni %***	***Fe %***	***Co %***	***Mn %***	***Cu %***
0.05	12.79	0.39	0.23	0	86.59
0.025	20.43	13.54	12.68	4.27	49.08
0.01	26.63	26.01	17.98	9.07	20.315
0.005	39.91	24.68	20.19	5.77	10.45

It was not easy to optimize the concentration of the Cu precursor numerous tests were carried out because, due to the high noble redox potential of copper. When a medium-high concentration of copper precursor is present in the deposition solution, its deposition is more favored than the other elements. In fact, at 0.05 M, practically the coating consists of only copper (see **Table 6.2**).

According to K. Ngamlerdpokin [23], to compensate for the less favorable thermodynamics of Ni^{2+} reduction and ensure the co-deposition of Ni and Cu, a higher concentration of Ni^{2+} than Cu^{2+} in the solution is necessary.

SEM images of *NiFeCoMnCu/NF* with 0.005 M of Cu precursor in the solution are shown in **figure 6.9**. The foam appears entirely covered by the alloy. The morphology is similar to that of the multimetallic alloys reported in the literature [2], [24]. The coating consists of particles of varying sizes uniformly distributed on the foam surface. High magnification images show that the particles exhibit a cauliflower-like shape.

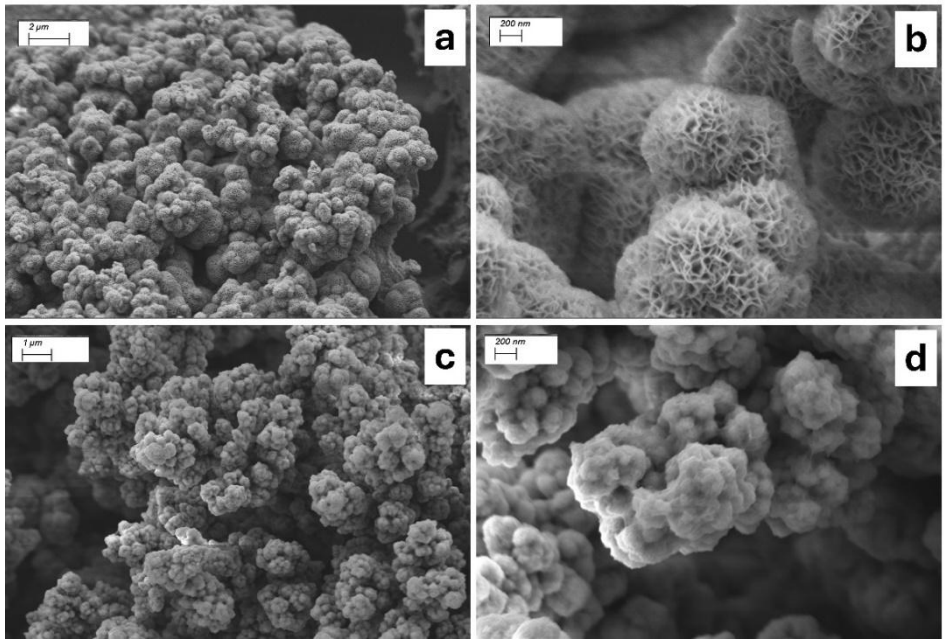

Fig. 6.9 *SEM images of NiFeCoMnCu/NF(using 0.005 M of Cu precursor) at different magnification*

In addition, **Figures 6.10A** and **B** show the SEM images of the samples obtained at different concentrations of copper precursor (0.025 and 0.005 M)

in the deposition solution. A high amount of copper promotes the formation of larger agglomerates, leading to a smaller surface area.

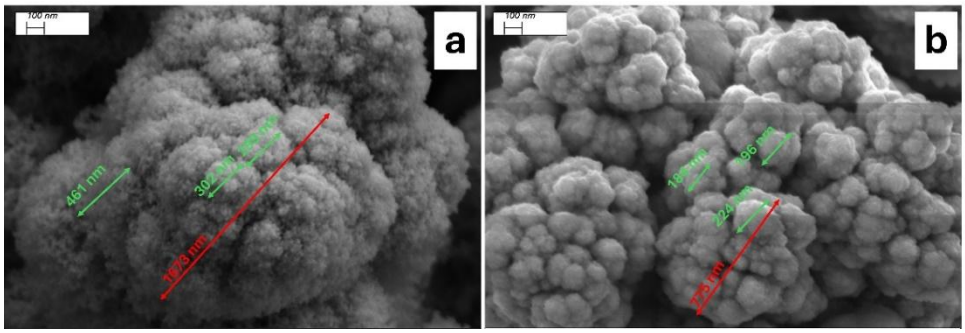

Fig. 6.10 *SEM images of* NiFeCoMnCu/NF obtained with (A) 0.025 M and (B) 0.005 M of Cu precursor

The different *NiFeCoMnCu/NF* electrodes were tested by CVs and LSV at 1 mV s^{-1} (see **figure 6.11**) in KOH 1 M, to identify the best alloy. **Figure 6.11A** shows the CVs in a non-Faradic potential range for the alloy obtained with a concentration of Cu precursor of 0.005M and **figure 6.11B** provides the specific capacitance values for all the alloys and pure NF. The NiFeCoMnCu/NF alloys have specific capacitance values higher than those obtained with the previous alloy. Respect the un-coated NF, in the presence of NiFeCoMnCu alloy, very high j values are recorded. These results highlight the significant impact of the electrodeposition process on the modification of the electrochemical active surface area [7]. When the copper content in the alloy decreases, the specific capacitance increases, suggesting a higher electrochemical surface area and, thus, a possible higher activity. This is in agreement with the previous SEM images (fig. 6.10) and it is confirmed by the LSV curves (**fig. 611 C** and **6.11D**) showing that the best performance is obtained with the alloy obtained with 0.005 M of copper sulphate precursor.

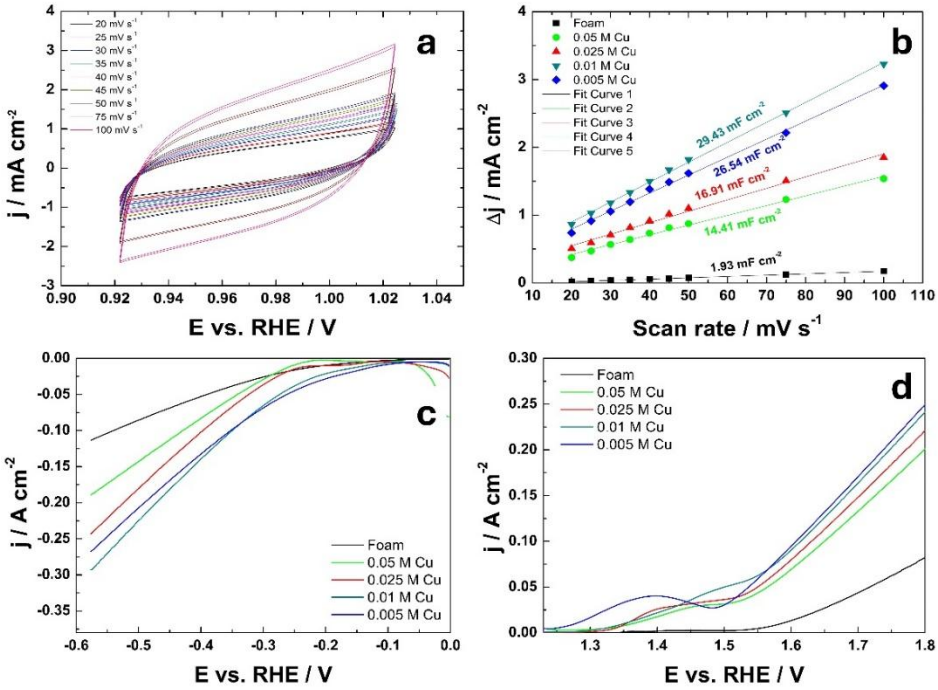

Fig. 6.11 *(**A**) CVs in a non-faradic-region of NiFeCoMnCu/NF (with 0.005M Cu precursor); (**B**) Specific capacitance of NF and NiFeCoMnCu/NF electrodes evaluated by double layer capacitance method; LSV curves of NiFeCoMnCu/NF electrodes for (**C**) HER and (**D**) OER*

6.4 Fabrication and characterization of NiFeCoMnCu-NWs

Starting from the results obtained in the previous chapter, the optimal solution of NiFeCoMnCu alloy is used to obtain NWs by template pulsed electrodeposition. Several attempts were made to optimize the deposition potentials and the number of cycles. The operating conditions that led to the more efficient electrode are -0.65;-1.35 V vs. SCE for 100 and 80 cycles (named **NWs 100c** and **NWs 80c**). Some cycles of the deposition are shown in the following **figure 6.12**

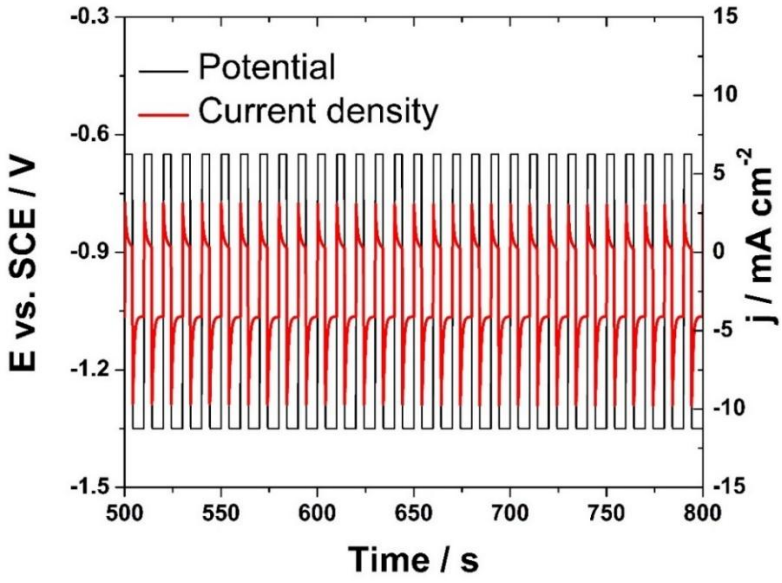

Fig. 6.12 *Pulse potential and measured current density vs. time plots for NiFeCoMnCu NWs electrodeposition*

From SEM images, **figure 6.13**, nanowire morphology is confirmed and the chosen deposition parameters allowed for achieving a uniform distribution of NWs, with a length practically constant, around 12-13 μm. It is visible in the **fig. 6.13C**. In addition, the presence of all desired elements is shown in the EDS spectrum in **fig. 6.13D.**

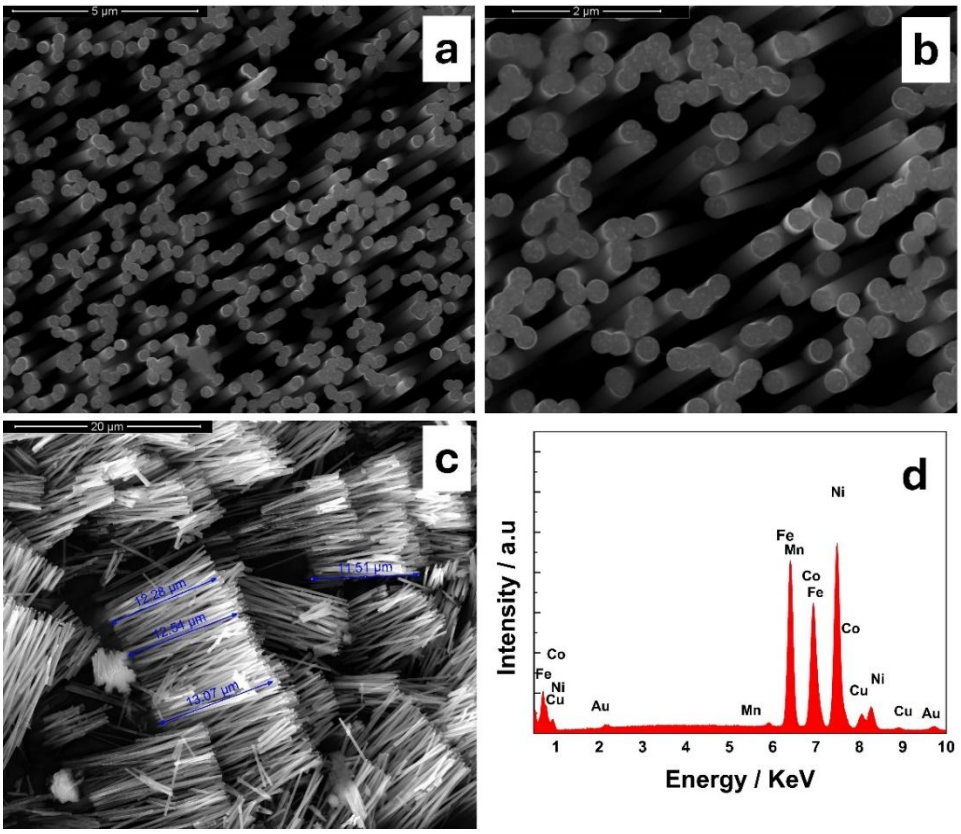

Fig. 6.13 *SEM images (A,B,C) and EDS spectrum (D) of NiFeCoMnCu NWs 80c*

NWs 100c and NWs 80c were electrochemically characterized by QSSP (0.167 mV s^{-1}), Galvanostatic step polarization and Galvanostatic-Stability Test in KOH 30% w/w aqueous solution at room temperature. Their performances were compared with those obtained covering a NF with this alloy. Compared to the results obtained in the previous section 6.3, to ensure a better comparison between these nanowires and those obtained earlier, the electrodes were retested under the same conditions, both in terms of the electrolyte solution and the operational parameters of the techniques used. In

addition, to also evaluate the effect of the foam porosity, two different foams (both with a thickness of 0.5 cm) were used with an average pore size of 800 µm and an average pore size of 1.80 mm. From here, NiFeCoMnCu on Foam 800 µm NiFeCoMnCu on Foam 1.80 mm are simply named **Foam 800 µm** and **Foam 1.80 mm.**

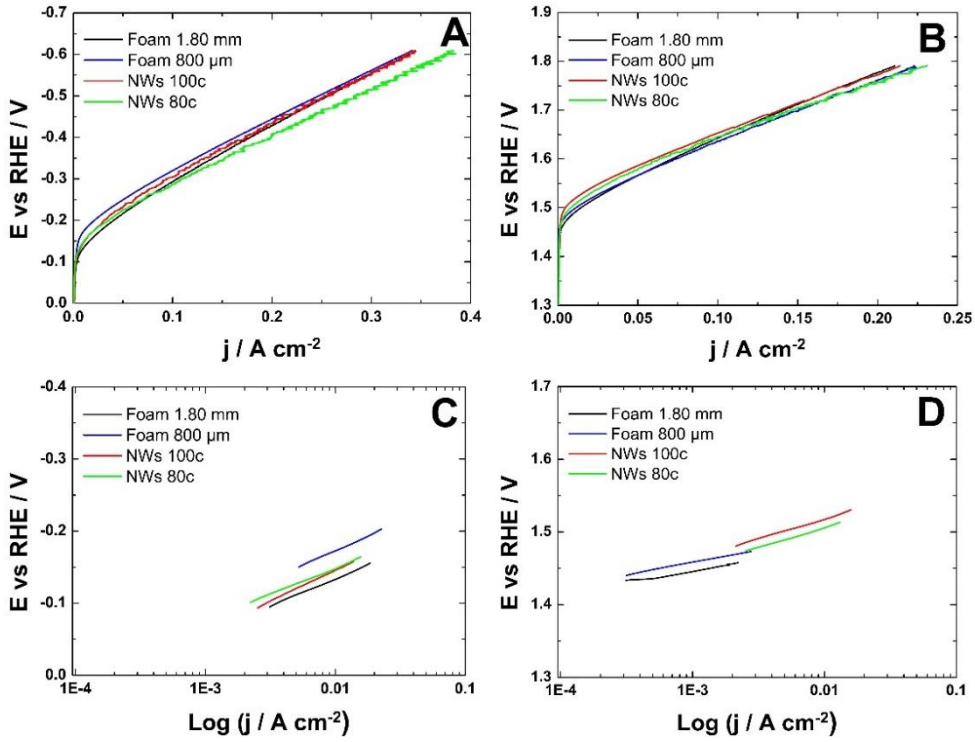

***Fig. 6.14** QSSP and Linearity range of QSSP curves for (**A,C**) HER and (**B,D**)*

QSSP and linearity range are shown in **figure 6.14**. The fitted Tafel's parameters are listed in the **table 6.3**. All the electrodes provide a good excellent activity. At lower current density, the performance is comparable but at higher current density, especially for HER, NWs 80c have shown lower overpotential probably due to the ability of nanowires to facilitate the release of a large amount of gas bubbles that form at high j. The lower Tafel slope is

obtained with Foam 1.80 mm and NWs 80c. For HER, their values are comparable, a Tafel slope of -0.072 V means that the HER kinetics follow the Volmer-Heyrovsky mechanism. This value is better or comparable with other multi-metallic catalysts in the literature [25], [26]. The Tafel slope value for OER is very low and it is better than most catalysts in literature. Typical b values of NiCoFeMoMn are in the range 37-59 mV [27], [28], [29].

Table 6.3 *Fitted Tafel's parameters for HER and OER*

Electrocatalyst	***HER***			***OER***		
	a (V)	**b (V)**	**R^2 (%)**	**a (V)**	**b (V)**	**R^2 (%)**
Foam1.80 mm	-0.284	-0.075	99.86	1.539	0.031	98.14
Foam 800 µm	-0.332	-0.079	99.87	1.561	0.034	99.89
NWs 100c	-0.316	-0.085	99.96	1.627	0.054	99.81
NWs 80c	-0.292	-0.072	99.87	1.613	0.053	99.78

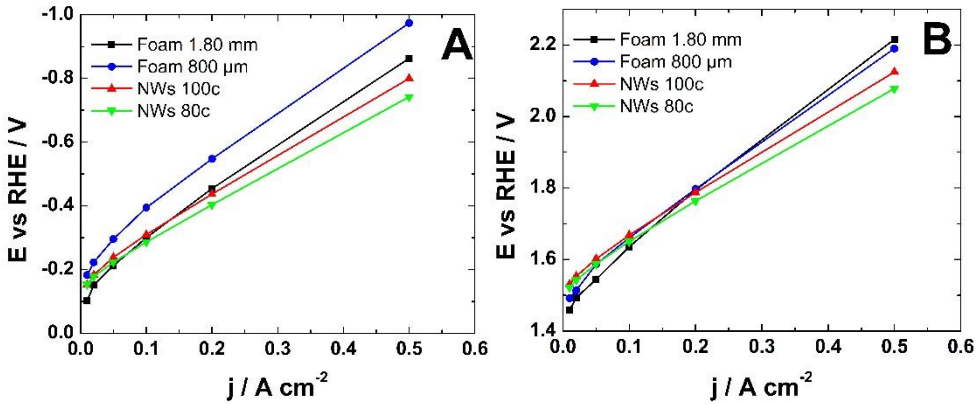

Fig. 6.15*. Galvanostatic-step polarization for (**A**) HER and (**B**) OER*

Galvanostatic step polarization curves are shown in the **figure 6.15**. The trend of QSSP curves is confirmed. The foam shows the worst performance at high j. In the low-mid range of current density, the overpotential values are comparable. The stability is studied initially for 6 hours, as shown in the **figure 6.16**. Results are good especially, for the cathodic side, all the electrodes show excellent performance, with a potential value almost constant during all the test. Since the global performance of NWs 100 c is not satisfactory overall, the long-term stability test is studied only for the two foam and for NWs 80c, **figure 6.17**.

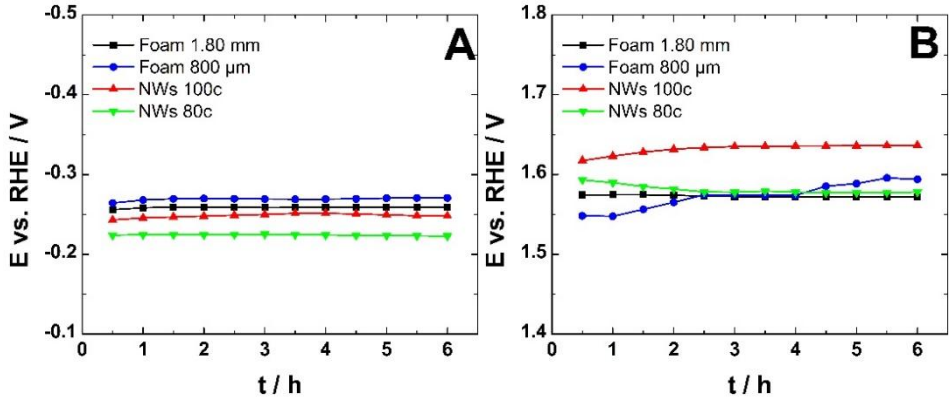

Fig. 6.16 *Mid-term stability test for 6 hours for (**A**) HER at −50 mA/cm² and **B**) OER at 50 mA/cm²*

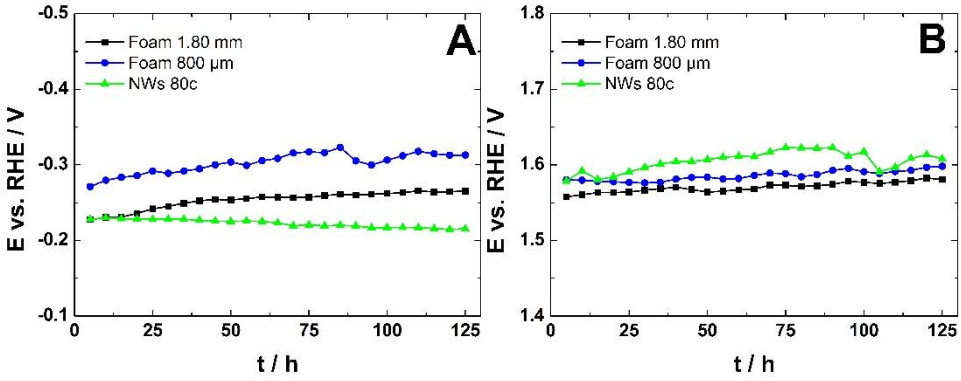

Fig. 6.17. *Long-term stability test for 125 hours for (**A**) HER at −50 mA/cm² and **B**) OER at 50 mA/cm²*

The lower overpotential was measured in the case of Foam 1.80 mm and NWs 80c. In particular, for HER, the initial potential is around -0.22 V and it ends at -0.266V. The greatest loss of activity occurs within the first 24 hours. For NWs, the overpotential is almost constant during all the tests. For OER, the best performance is given by Foam 1.80mm with an overall increase in potential of 22 mV. Comparing the two foams, the more compact one shows worse performance. If the bubbles are confined and cannot be removed, the cell potential will increase because the electrode area is blocked by the bubbles, reducing the active area and hindering hydrogen production [30].

The combination of alloy composition and morphology plays a key role in the catalysis of HER and OER reactions [31]. In this case, nanowires morphology with a composition 1.6% Mn, 40.09% Fe, % 34.86 Co, %10.81 Ni, %12.64 Cu is the best for HER; instead, the more porous foam with around 39% Ni, 23% Fe, 24% Co, 5.8%Mn 8.5% Cu (underlining that the composition of the foam is not as precise as that of the nanowires because the amount of nickel also comes from the substrate) is the best for OER.

6.5 Conclusions

High entropy alloys (HEAs), also known as multicomponent alloys, are formed by combining five or more elements in equal or near-equal molar ratios. These alloys are drawing significant attention from the scientific community for their distinctive structures and exceptional properties. Among the different techniques, electrodeposition has gained prominence due to its cost-effectiveness, simplicity, and ability to precisely control the material properties. This preliminary work explores the production of HEA from aqueous solutions using galvanostatic and potentiostatic electrodeposition on NF as substrate. This technique offers a simple, cost-effective, and scalable

method for fabricating HEAs. By adjusting key parameters such as potential, current density, bath concentration, pH, and temperature, the structural and morphological properties of the resulting deposits can be precisely controlled, making this approach a highly versatile and efficient route for HEA synthesis. The existing literature on electrodeposited HEAs is limited, with the majority of studies utilizing non-aqueous media for their synthesis. After numerous attempts, varying different operating conditions, the most promising alloy found was the one composed of Ni, Fe, Co, Mn and Cu. After identifying the optimal solution composition, the alloy was deposited onto two foams with different porosities. Subsequently, nanowires of this alloy were fabricated. Several electrochemical tests were conducted, yielding satisfactory results when compared to the ternary alloy discussed in the previous chapter. In the future, more in-depth studies will be conducted to further optimize the fabrication of the nanowires, test their performance in simulated seawater, and ultimately in an alkaline lab-electrolyzer prototype.

References

[1] C. Lee *et al.*, «Lattice distortion in a strong and ductile refractory high-entropy alloy», *Acta Mater.*, vol. 160, pp. 158–172, nov. 2018, doi: 10.1016/j.actamat.2018.08.053.

[2] H. Bian *et al.*, «Facile electrodeposition synthesis and super performance of nano-porous Ni-Fe-Cu-Co-W high entropy alloy electrocatalyst», *Surf. Coat. Technol.*, vol. 459, p. 129407, apr. 2023, doi: 10.1016/j.surfcoat.2023.129407.

[3] P. Zhou *et al.*, «Corrosion engineering boosting bulk Fe50Mn30Co10Cr10 high-entropy alloy as high-efficient alkaline oxygen evolution reaction electrocatalyst», *J. Mater. Sci. Technol.*, vol. 109, pp. 267–275, mag. 2022, doi: 10.1016/j.jmst.2021.09.003.

[4] L. Zendejas Medina, L. Riekehr, e U. Jansson, «Phase formation in magnetron sputtered CrMnFeCoNi high entropy alloy», *Surf. Coat. Technol.*, vol. 403, p. 126323, dic. 2020, doi: 10.1016/j.surfcoat.2020.126323.

[5] P. Zhou *et al.*, «Anodized AlCoCrFeNi high-entropy alloy for alkaline water electrolysis with ultra-high performance», *Sci. China Mater.*, vol. 66, fasc. 3, pp. 1033–1041, mar. 2023, doi: 10.1007/s40843-022-2234-5.

[6] Z. Zhu, H. Meng, e P. Ren, «CoNiWReP high entropy alloy coatings prepared by pulse current electrodeposition from aqueous solution», *Colloids Surf. Physicochem. Eng. Asp.*, vol. 648, p. 129404, set. 2022, doi: 10.1016/j.colsurfa.2022.129404.

[7] I. A. Poimenidis *et al.*, «Electrodeposited Ni foam electrodes for increased hydrogen production in alkaline electrolysis», *Fuel*, vol. 342, p. 127798, giu. 2023, doi: 10.1016/j.fuel.2023.127798.

[8] M. Pushpavanam e K. Balakrishnan, «Zinc-nickel alloy deposition in the presence of citrate ions», *J. Appl. Electrochem.*, vol. 26, fasc. 10, ott. 1996, doi: 10.1007/BF00242202.

[9] L. Ji, F. Chen, H. Huang, X. Sun, Y. Yan, e X. Tang, «Preparation of nickel–graphene composites by jet electrodeposition and the influence of graphene oxide concentration on the morphologies and properties», *Surf. Coat. Technol.*, vol. 351, pp. 212–219, ott. 2018, doi: 10.1016/j.surfcoat.2018.07.083.

[10] Konstantin I. Popov, Miomir G. Pavlovic, and Predrag M. Zivkovic, «CURRENT DENSITY DISTRIBUTION IN ELECTROCHEMICAL CELLS». [Online]. Disponibile su: https://knowledge.electrochem.org/encycl/art-d03-curr-distr.htm

[11] Y. Song *et al.*, «Synthesis of a High-Capacity NiO/Ni Foam Anode for Advanced Lithium-Ion Batteries», *Adv. Eng. Mater.*, vol. 22, fasc. 11, p. 2000351, nov. 2020, doi: 10.1002/adem.202000351.

[12] J. Lian, Y. Wu, e J. Sun, «High current density electrodeposition of NiFe/Nickel Foam as a bifunctional electrocatalyst for overall water splitting in alkaline electrolyte», *J. Mater. Sci.*, vol. 55, fasc. 31, pp. 15140–15151, nov. 2020, doi: 10.1007/s10853-020-05080-w.

[13] J.-W. Yeh, S.-Y. Chang, Y.-D. Hong, S.-K. Chen, e S.-J. Lin, «Anomalous decrease in X-ray diffraction intensities of Cu–Ni–Al–Co–Cr–Fe–Si alloy systems with multi-principal elements», *Mater. Chem. Phys.*, vol. 103, fasc. 1, pp. 41–46, mag. 2007, doi: 10.1016/j.matchemphys.2007.01.003.

[14] X. Yin *et al.*, «A novel structure of Ni-(MoS 2 /GO) composite coatings deposited on Ni foam under supergravity field as efficient hydrogen evolution reaction catalysts in alkaline solution», *Electrochimica Acta*, vol. 249, pp. 52–63, set. 2017, doi: 10.1016/j.electacta.2017.08.010.

[15] X. Liu *et al.*, «One-step synthesis and energy-storage application of Ni–Se–S/nickel foam nanoarrays with high areal specific capacitance», *Appl. Nanosci.*, vol. 11, fasc. 6, pp. 1805–1815, giu. 2021, doi: 10.1007/s13204-021-01858-9.

[16] H. Du *et al.*, «Silver nanowire/nickel hydroxide nanosheet composite for a transparent electrode and all-solid-state supercapacitor», *Nanoscale Adv.*, vol. 1, fasc. 1, pp. 140–146, 2019, doi: 10.1039/C8NA00110C.

[17] N. Joseph, P. M. Shafi, J. S. Sethulakshmi, R. Karthik, A. C. Bose, e J.-J. Shim, «Three dimensional NiO nanonetwork electrode for efficient electrochemical energy storage application», *Electrochimica Acta*, vol. 399, p. 139392, dic. 2021, doi: 10.1016/j.electacta.2021.139392.

[18] J. Wang *et al.*, «Fabrication of nanoscale NiO/Ni heterostructures as electrocatalysts for efficient methanol oxidation», *J. Mater. Chem. A*, vol. 5, fasc. 20, pp. 9946–9951, 2017, doi: 10.1039/C7TA01982C.

[19] R. He *et al.*, «A CrMnFeCoNi high entropy alloy boosting oxygen evolution/reduction reactions and zinc-air battery performance», *Energy Storage Mater.*, vol. 58, pp. 287–298, apr. 2023, doi: 10.1016/j.ensm.2023.03.022.

[20] R. Solmaz, A. Döner, e G. Kardaş, «Electrochemical deposition and characterization of NiCu coatings as cathode materials for hydrogen evolution reaction», *Electrochem. Commun.*, vol. 10, fasc. 12, pp. 1909–1911, dic. 2008, doi: 10.1016/j.elecom.2008.10.011.

[21] W. Z. Friend e M. Cohen, «Corrosion of Nickel and Nickel-Base Alloys», *J. Electrochem. Soc.*, vol. 127, fasc. 8, pp. 421C-421C, ago. 1980, doi: 10.1149/1.2130025.

[22] R. Solmaz, A. Döner, e G. Kardaş, «The stability of hydrogen evolution activity and corrosion behavior of NiCu coatings with long-term electrolysis in alkaline solution», *Int. J. Hydrog. Energy*, vol. 34, fasc. 5, pp. 2089–2094, mar. 2009, doi: 10.1016/j.ijhydene.2009.01.007.

[23] K. Ngamlerdpokin e N. Tantavichet, «Electrodeposition of nickel–copper alloys to use as a cathode for hydrogen evolution in an alkaline media», *Int. J. Hydrog. Energy*, vol. 39, fasc. 6, pp. 2505–2515, feb. 2014, doi: 10.1016/j.ijhydene.2013.12.013.

[24] S. Staroń, P. Ledwig, e B. Dubiel, «Electrodeposited Ni-Cu Coatings with Hierarchical Surface Morphology», *Metall. Mater. Trans. A*, vol. 53, fasc. 6, pp. 2071–2085, giu. 2022, doi: 10.1007/s11661-022-06649-7.

[25] S. Ding *et al.*, «Plasma-regulated two-dimensional high entropy oxide arrays for synergistic hydrogen evolution: From theoretical prediction to electrocatalytic applications», *J. Power Sources*, vol. 520, p. 230873, feb. 2022, doi: 10.1016/j.jpowsour.2021.230873.

[26] G. Zhang *et al.*, «High entropy alloy as a highly active and stable electrocatalyst for hydrogen evolution reaction», *Electrochimica Acta*, vol. 279, pp. 19–23, lug. 2018, doi: 10.1016/j.electacta.2018.05.035.

[27] H. Liu *et al.*, «A freestanding nanoporous NiCoFeMoMn high-entropy alloy as an efficient electrocatalyst for rapid water splitting», *Chem. Eng. J.*, vol. 435, p. 134898, mag. 2022, doi: 10.1016/j.cej.2022.134898.

[28] P. Li *et al.*, «A Single-Phase FeCoNiMnMo High-Entropy Alloy Oxygen Evolution Anode Working in Alkaline Solution for over 1000 h», *ACS Catal.*, vol. 12, fasc. 19, pp. 11667–11674, ott. 2022, doi: 10.1021/acscatal.2c02946.

[29] K. Huang *et al.*, «Cathodic plasma driven self-assembly of HEAs dendrites by pure single FCC FeCoNiMnCu nanoparticles as high efficient electrocatalysts for OER», *Chem. Eng. J.*, vol. 425, p. 131533, dic. 2021, doi: 10.1016/j.cej.2021.131533.

[30] H. Cui, G. Cao, S. Zhu, J. Mu, X. Liu, e X. Chou, «Foaming performance evaluation of frother emulsions in the slime flotation: Foamability, foam stability, and foam flow», *Colloids Surf. Physicochem. Eng. Asp.*, vol. 638, p. 128310, apr. 2022, doi: 10.1016/j.colsurfa.2022.128310.

[31] J. Du, X. Zhang, F. He, e Y. Xie, «Modulation of the morphology, composition, and oxidation state of the spinel high-entropy oxides to boost their bifunctional catalytic activity for overall water splitting», *Electrochimica Acta*, vol. 461, p. 142599, set. 2023, doi: 10.1016/j.electacta.2023.142599.

Conclusions and Future Perspectives

This research work regards the fabrication and characterization of different nanostructured electrodes particularly focusing on Ni-based alloys for hydrogen production through seawater electrolysis. Ni-Fe NWs were successfully obtained by template electrosynthesis. Electrochemical tests performed in KOH+NaCl solution are good, and it can be stated that the presence of NaCl did not significantly impact the electrocatalytic performance. Electrodes demonstrated good stability even at temperatures higher than ambient. NiFeP NWs were fabricated to improve the performance of the binary alloy. Considering the improved performance compared to the binary alloy, electrochemical tests were carried out in a simulated seawater solution with a various anions and cations present in seawater. The results are highly promising, as the current/potential behavior observed in the various tests closely matches that obtained in the pure KOH solution. Additionally, two stability tests under intermittent conditions were conducted, yielding similarly intriguing results. These findings support the potential use of these electrodes in seawater electrolysis powered by renewable energy sources. A scale-lab alkaline electrolyzer was constructed to test the overall water splitting where NiFe and NiFeP NWs were used as anodes and cathodes. Their effectiveness as bifunctional catalyst in an alkaline electrolyzer prototype reinforces their potential for practical applications in renewable energy. Key parameters, such as current density, electrolyte temperature, and cell voltage, were monitored to assess the operational stability and efficiency of the system. The reproducibility of the electrode performance highlights the precision of the cell's engineering and the reliability of its design. These results provide valuable insights for scaling up the prototype and optimizing the full-stack configuration, making it a viable candidate for sustainable hydrogen production. Future research will aim to further refine the electrode materials

and operating parameters, focusing on long-term stability and energy efficiency improvements. At the end of this research work, with the aim of developing increasingly high-performing electrodes, a multimetallic alloy was successfully obtained both on the nickel foam and in the form of nanowires. Preliminary studies show better performance compared to previous alloys, but further research and deeper investigations are needed to assess the feasibility of using these electrodes as catalysts for seawater electrolysis. With the pressing need for renewable energy solutions, seawater electrolysis has the potential to answer part of the demand for hydrogen production. The section, therefore, reserved for discussing future research related to this technology, shall concern pilot-scale testing, integration in commercial systems, and collaboration efforts with industry partners. Pilot-scale testing is a fundamental process for validating feasibility and efficiency aspects in seawater electrolysis technologies. Translation of laboratory-scale results to pilot systems can inform researchers about the practical-operational stability, energy efficiency, and performance of electrolysis within actual conditions. Successful transition from experimental setup to commercial system involves research based on modular electrolysis units that are easily scalable to any location and as appropriate for the demand level. This modularity would allow the implementation strategies across different applications - small-scale remote community installations as well as the large offshore hydrogen production facilities-to be flexible and adapted. Partnerships should then be established which will bridge between the theoretical advance and practical implementation and the data/information gained during pilot tests would be shared among the industry players. This is a good accelerator of the acceptance of seawater electrolysis solutions into hydrogen-utilizing applications and is a source for innovation.

Research Results Dissemination

National Conference

- **S. Carbone**, R. L. Oliveri, B. Patella, R. Miceli, F. Pellitteri, A. O. Di Tommaso, G. Aiello, R. Inguanta, *Ternary alloys of Ni-Fe-P for alkaline electrolyzer, Poster at GEI 2023, Cefalù, September 17-21, 2023*
- Oliveri, R., **Carbone, S**., Patella, B., Geraci, S., Aiello, G., Pellitteri, F., ... & Inguanta, R. *Nickel alloy electrodes for the evolution reaction of hydrogen and oxygen in a water-alkaline electrolyser*, *Poster at GEI 2023, Cefalù, September 17-21, 2023*
- S. Geraci, **S. Carbone**, L. Oliveri, B. Patella, R. Miceli, F. Pellitteri, M.Caruso , G. Aiello, R. Inguanta, *Fabrication of Ni-alloy nanostructured elecrodesfor alkaline electrolizers, Poster at GEI 2023, Cefalù, September 17-21, 2023*
- **S. Carbone** , A. Caruso, B. Patella, R. Miceli, F. Pellitteri, P. Mandin, G. Aiello, R. Inguanta, *Ni-Fe-P alloy nanostructured electrodes for alkaline electrolyzer,* Oral Presentation at ICheaP16, Napoli, May 21-24, 2023
- **S. Carbone**, F. Bonafede, F.Ganci, B. Patella, G. Aiello, R.Inguanta, *Nanostructured nickel–zinc alloy electrodes for hydrogen evolution reaction in alkaline electrolyzer*, Oral Presentation at GRICU 2022, Ischia, (Italy), July 3-6, 2022

International Conference

- R. L, Oliveri, **S. Carbone**, B. Patella, S. Geraci, N. Moukri, G. Aiello, F. Pellitteri, N. Campagna, R. Miceli, S. Longo, A. Affranchi, M. Cellura, R. Inguanta *Design of Zero-Gap Alkaline Electrolyzer with Nanostructured Electrodes for Hydrogen Production***,** Poster at ISE 2024, Manchester, 8-11/09/2024
- S. Geraci, **S. Carbone**, L. Oliveri, B. Patella, R. Miceli, F. Pellitteri, M.Caruso , G. Aiello, R. Inguanta, *Ni-Fe-S alloy nanostructured electrodes for alkaline electrolyser,* Presentation at HydrogenDays 2024 , 20-22/03/2024

- S. Geraci, **S. Carbone**, L. Oliveri, G. Micciché, B. Patella, R. Miceli, F. Pellitteri, M.Caruso , G. Aiello, R. Inguanta, *Performance of Nickel-Iron nanostructured electrodes at different temperatures,* Presentation at Catalysis 2023, 26-28/10/2023
- Oliveri, R., Patella, B., **Carbone, S**., Geraci, S., Aiello, G., Pellitteri, F., ... & Inguanta, R. (2024). *Performance of Nanostructured Ni Alloy Electrodes for Hydrogen and Oxygen Evolution Reaction in Water-Alkaline Electrolyzer*. Poster at Catalysis 2023, 26-28/10/2023
- **S. Carbone**, F. Bonafede, F. Ganci, B. Patella, R. Miceli, F. Pellitteri, G. Aiello, G. Inturri, R.Inguanta, *Ni-Fe alloy nanostructured electrodes for seawater electrolyzers*, Oral Presentation at HYPOTHESIS Hydrogen Power Theoritical & Engineering XVII, 26-29/09/2022
- **S. Carbone**, F. Bonafede, F. Ganci, B. Patella, G. Aiello, R. Inguanta, *Nanostructured Nickel alloy electrodes for alkaline electrolysers*, Poster at 73rd of Annual Meeting of ISE 2022, 12-16/09/2022
- **S. Carbone**, F. Bonafede, F. Ganci, B. Patella, G. Aiello, R. Inguanta, *Ni alloy nanowires for alkaline electrolysers*, Oral Presentation at World Online Conference on Sustainable Technologies 2022, 21/03/2022

Publications

- **S. Carbone**, R.L Oliveri, B.Patella, G. Aiello, M. Scopelliti, N.Campagna, F. Pellitteri, R. Miceli S. Longo, A. Affranchi, M. Cellura, R. Inguanta. *Optimized NiFeP alloy for overall water-splitting,* Submitted in Renewable Energy
- B. Patella, N. Moukri, F. Mazzara, **S. Carbone**, R.L. Oliveri, G. Aiello, M. Russo, C. Torino, A. Vilasi, V. Juska, A. O'Riordan, R. Inguanta. *Sensitive electrochemical detection of total sugars in food using NiFe alloy nanowires, Submitted in Food Chemistry*
- **Carbone, S**., Proietto, F., Bonafede, F., Oliveri, R. L., Patella, B., Ganci, F., ... & Inguanta, R. (2023). *Behavior of a forest of NiFe*

nanowires in KOH and NaCl solution for water electrolysis. Electrochimica Acta, 467, 143120, https://doi.org/10.1016/j.electacta.2023.143120.

- **Carbone, S**., Caruso, A. G., Patella, B., Miceli, R., Pellitteri, F., Caruso, M., ... & Inguanta, R. (2023). *Nanostructured Ni-Fe-P Alloy for Alkaline Electrolyzer*. Chemical Engineering Transactions, 100, 649-654, https://doi.org/10.3303/CET23100109
- Patella, B., **Carbone, S**., Oliveri, L. R., Caruso, M., Pellitteri, F., Mandin, P., ... & Inguanta, R. (2023). *Nanostructured Ni-Fe-S Based Electrode for Hydrogen Production by Water Electrolysis.* Chemical Engineering Transactions, *105*, 37-42. https://doi.org/10.3303/CET23105007
- Zanca, C., **Carbone, S**., Patella, B., Lopresti, F., Aiello, G., Brucato, V., ... & Inguanta, R. (2022). *Composite Coatings of Chitosan and Silver Nanoparticles Obtained by Galvanic Deposition for Orthopedic Implants.* Polymers, 14(18), 3915, https://doi.org/10.3390/polym14183915
- Patella, B., Di Vincenzo, S., Moukri, N., Bonafede, F., Ferraro, M., Lazzara, V., **S. Carbone**... & Pace, E. (2024). *Gold nanowires-based sensor for quantification of H2O2 released by human airway epithelial cells*. Talanta, 272, 125772. https://doi.org/10.1016/j.talanta.2024.125772
- Patella, B., Zanca, C., Ganci, F., **Carbone, S**., Bonafede, F., Aiello, G., ... & Inguanta, R. (2023). *Pd–Co-Based electrodes for hydrogen production by water splitting in acidic media*. Materials, 16(2), 474. https://doi.org/10.3390/ma16020474